roceedings of the Indian Academy of Sciences

(Earth and Planetary Sciences)

Volume 97, 1988

CONTENTS

emistry of calcic amphiboles from the area around Terakanambi, southern
rnataka . . . . *N Shadakshara Swamy and B Mahabaleswar* 1

iasi-static deformation of a layered half-space by a long strike-slip
ılt. . . . . *Nat Ram Garg and Sarva Jit Singh* 11

ı the observed synoptic variability in the thermal structure of the upper
rthern Bay of Bengal during MONEX-79 . . *R R Rao and Basil Mathew* 21

stribution of particulate organic carbon in the central Arabian Sea. . . .
. . . . *N B Bhosle, V M Dhople and A B Wagh* 35

there an attractor for the Indian summer monsoon?. . . . . . . *V Satyan* 49

asonal cycle of surface circulation in the coastal North Indian Ocean . .
. . . . *S R Shetye and S Satheesh Chandra Shenoi* 53

ɔherent rainfall zones: Case study for Karnataka . . . .
. . . . *Sulochana Gadgil, R Gowri and Yadumani* 63

agnetic studies on the remanence carriers in igneous rocks of different ages
. . . . *C Radhakrishnamurty, S D Likhite and G S Murthy* 81

ydroclimatic fluctuations of the Upper Narmada catchment and its
sociation with break-monsoon days over India . . . .
. . . . *Nityanand Singh, M K Soman and K Krishna Kumar* 87

te Cretaceous mafic dykes in the Dharwar cration. . . . .
. . . . *Anil Kumar, Y J Bhaskar Rao, V M Padma Kumari,*
A M Dayal and K Gopalan 107

ınouncements. 115

ɔsmic-ray production rates of neon isotopes in meteorite minerals. . . . .
. . . . *N Bhandari* 117

Northward propagation of the 30–50 day mode in the Indian monsoon region
. . . . *R N Keshavamurty, V Krishnakumar and S V Kasture* 127

Spectra of different fluxes over the arid and semiarid zones of northwest India during MONEX 1979 . . . . *U S Singh, Daya Shanker and R K Singh* 137

Satellite-tracked drifting buoy observations in the south equatorial current in the Indian Ocean . . . . *S R Shetye and G S Michael* 149

Retrieval of cloud classification parameters using two-dimensional fast Fourier transform . . . . *M Mohan, Lakshmi Bhaduri and Vijay K Agarwal* 159

Spectral width parameter for wind-generated ocean waves . . . .
. . . . *C V K Prasada Rao* 173

Water characteristics and transport of the antarctic circumpolar current in the Indian Ocean . . . . *P M Muraleedharan and Basil Mathew* 183

Erratum 192

Subject Index 193

Author Index 196

oc. Indian Acad. Sci. (Earth Planet. Sci.), Vol. 97, No. 1, July 1988, pp. 1-10 © Printed in India.

hemistry of calcic amphiboles from the area around Terakanambi, uthern Karnataka

N SHADAKSHARA SWAMY and B MAHABALESWAR
Department of Geology, Bangalore University, Bangalore 560 056, India

MS received 4 February 1987; revised 13 July 1988

Abstract. Chemial analyses of twelve amphiboles from the area around Terakanambi are presented. Results indicate that they are ferro-hornblende and ferro-pargasitic hornblende types in banded iron formations; magnesio hornblende in ultramafic rocks and edenite; and ferroan pargasite and ferroan pargasitic hornblende types in calcamphibolites. Titanium content in the amphiboles of the present study is relatively low compared to results from similar zones elsewhere. The lower titanium content of the amphiboles may be attributed to either bulk chemical composition or to low oxygen fugacity. Mg/Fe ratios vary considerably and it is mainly controlled by host rock composition. The plots of calcic amphiboles on (100 Na/Ca + Na)/(100 Al/Si + Al) and Al^{IV}/Al^{VI} diagrams indicate that they are of medium to low pressure type.

Keywords. Calcic amphiboles; Terakanambi; high grade terrain; chemical analyses.

Introduction

nphiboles are ubiquitous in a wide variety of regionally metamorphosed rocks. They nerally occur as recrystallised phases or as products of breakdown reaction between o different minerals. The study of the chemistry of amphiboles is considered crucial it is related to the intensity of metamorphism under which they are formed (Raase 74; Anantha Iyer and Narayanan Kutty 1976; Raase *et al* 1986; Boyle 1986). The esent study attempts to elucidate the chemical characteristics of amphiboles curring in different supracrustal lithounits of the Terakanambi area.

Geology of the area

ne area around Terakanambi (figure 1) forms the southern part of the Sargur terrain southern Karnataka (Shadakshara Swamy 1983). The supracrustal rocks occur as ge rafts within the gneisses of 2800 to 3400 Ma age (Janardhan *et al* 1986). The pracrustal rocks include varied sequence of metasediments like quartzites, iron rmations, manganiferous horizons, calc-silicate rocks, amphibolites and components layered complex. They are highly deformed and metamorphosed under upper nphibolite facies conditions. The amphiboles discussed in this paper are from banded on formations, calc-amphibolites and olivine-bearing ultramafic rocks.

1 *Amphiboles*

the Precambrian terrains calcic amphibole appears to be a common mineral in the

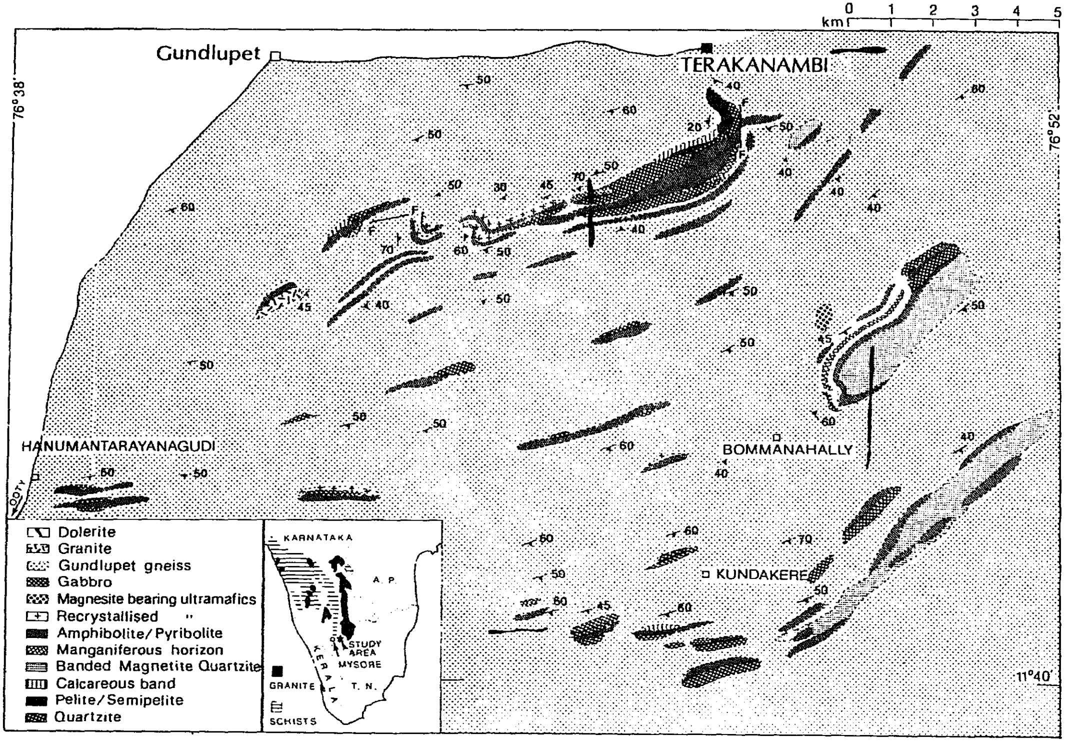

Figure 1. Geological map of the area around Terakanambi. Location of samples: 1 and 2—from BIF, 2·5 km NNE of Bommanahally; 3 and 4—from BIF, 3 km east of Kundagere; 5, 6 and 7—from calc-silicate rocks, 2 km south of Terakanambi; 8—from calc-silicate rock, 1·5 km south of Kundagere; 9 and 10—from calc-silicate rocks. 4·5 km S 35° east of Gundlupet; 11—from an ultramafic rock, 1·5 km south of Kundagere; 12—from an ultramafic rock, 6 km S 50 east of Gundlupet.

ash 1981; Sharma 1982), banded iron formations (Klein 1983; Mahabaleshwar 1984; Hall 1985), and ultramafic rocks (Evans 1977; Srikantappa *et al* 1985). hiboles from the calc-amphibolites of the present study occur either as discrete ns or as grains rimming clinopyroxene. Green-coloured hornblende of the calcic generally pseudomorphs grunerite in the banded iron formations. Tremolite is the r amphibole occurring in association with the green hornblende in the ultramafic s of the study area. Textural studies clearly indicate that the green hornblendes are clino- or orthopyroxenes in the ultramafic rocks.

nalytical methods

erals were analysed with an ARL electron mircoprobe using energy dispersive ction at the Department of Geophysical Sciences, University of Chicago, Chicago Prof. A S Janardhan. In each sample two to three grains were analysed and the age was taken. The operating voltage was 15 kV and the sample current was ^{7} amp with a 1 μm beam spot. Synthetic standards were used. Analyses of the dards were generally reproducible to $\pm 0{\cdot}1$ wt% of each oxide component, and yses in the tables are given only to this precision.

hemistry

analyses of twelve amphiboles are listed in tables 1 and 2. The structural formulae alculated on the basis of 23 oxygen atoms and they satisfy Leake's (1978) criteria defining calcic amphiboles, having $(\mathrm{Ca}+\mathrm{Na})_B \geqslant 1{\cdot}34$ and $\mathrm{Na}_B < 0{\cdot}67$. Calcic hiboles from the banded iron formations belong to ferrohornblende and ferro-asitic hornblende type; calcic amphiboles from the ultramafic rocks are magnesio blendes; and calcic amphiboles from the calc-amphibolites belong to edenite, an pargasite and ferroan pargasitic hornblende types.

ne Al substitution for the tetrahedral site ranges from 1·019 to 1·740 in the blendes of the present study. Leake (1971) documented calcic amphiboles with a imum of about 1·4 Al in octahedral position. In the present study Al ranges from 4 to 0·748.

tanium content of the hornblendes of the present study varies considerably. Many cers (Raase 1974; Raase *et al* 1986) have shown that the titanium content of the hiboles increases systematically with the metamorphic grade. Ti ranges from 0·04 16 with an average of 0·1 in the hornblendes from the calc-amphibolites of the ent study. In the hornblendes of the ultramafic rocks Ti averages 0·1 and, in banded formations, Ti is totally absent. The average Ti content of the calcic amphiboles the Terakanambi area is distinctly lower compared to the Ti content of the hiboles from the ultramafic rocks of the hornblende granulite zone reported by se *et al* (1986). The relatively lower value of Ti may possibly be due to the non-istence of hornblendes with the minerals having excess Ti phase as substantiated aase *et al* (1986). $\mathrm{TiO_2}$ is totally absent in hornblendes of banded iron formations. may be attributed either to bulk composition or to the preferential entry of Ti into netite during metamorphism under low oxygen fugacity conditions as explained by len (1980) and Mahabaleswar and Vasant Kumar (1983).

lany workers (Raase 1974; Hermann *et al* 1980; Spear 1981) have suggested that th

Table 1. Chemistry of calcic amphiboles from the Terakanambi area.

	1	2	3	4	5	6	7	8	9	10	11	12
SiO_2	40·78	42·05	43·67	42·05	41·72	40·72	46·63	46·93	45·62	47·97	48·77	48·07
TiO_2	—	—	—	—	1·26	1·40	0·62	0·36	0·73	—	1·09	0·89
Al_2O_3	11·41	11·07	11·00	11·46	13·99	13·79	10·61	9·34	10·26	9·39	11·08	10·75
FeO*	25·78	25·89	25·75	26·87	17·67	18·22	16·32	17·28	17·86	17·84	6·62	6·89
MnO	—	—	—	—	—	—	—	0·63	0·45	—	—	0·21
MgO	5·87	5·51	5·49	5·71	9·29	8·98	11·24	10·21	10·01	11·18	17·66	17·95
CaO	10·26	10·19	10·33	10·98	11·76	11·68	12·23	12·28	12·51	12·11	12·97	12·66
Na_2O	1·08	0·98	0·73	1·25	1·59	1·31	1·22	0·72	1·32	0·96	0·60	0·62
K_2O	0·81	0·80	0·96	0·85	0·73	0·77	0·22	0·76	0·51	—	0·15	0·15
Cr_2O_3	—	—	—	—	—	—	—	0·20	0·15	—	0·33	0·37
Total	95·99	96·49	97·93	99·17	98·01	96·87	99·09	98·71	99·42	99·45	99·27	98·56

FeO* = Total iron as FeO.

Table 2. Structural formulae on the basis of 23 oxygen atoms.

	1	2	3	4	5	6	7	8	9	10	11	12
Si	6·486	6·628	6·745	6·494	6·260	6·178	6·797	6·934	6·730	6·981	6·775	6·746
Al	1·514	1·372	1·255	1·506	1·740	1·822	1·203	1·066	1·230	1·019	1·225	1·254
ΣT	8·000	8·000	8·000	8·000	8·000	8·000	8·000	8·000	8·000	8·000	8·000	8·000
Al	0·625	0·684	0·748	0·580	0·634	0·643	0·621	0·561	0·554	0·592	0·589	0·524
Ti	—	—	—	—	0·142	0·160	0·068	0·040	0·081	—	0·114	0·094
Cr	—	—	—	—	—	—	—	0·023	0·020	—	0·036	0·042
Mg	1·393	1·295	1·263	1·314	2·077	2·031	2·442	2·248	2·199	2·426	3·655	3·754
Fe	2·982	3·021	2·989	3·106	2·147	2·166	1·869	2·148	2·146	1·982	0·606	0·586
ΣC	5·000	5·000	5·000	5·000	5·000	5·000	5·000	5·000	5·000	5·000	5·000	5·000
Fe	0·447	0·392	0·342	0·363	0·070	0·146	0·120	0·003	0·058	0·189	0·163	0·223
Mn	—	—	—	—	—	—	—	0·078	0·057	—	—	0·024
Ca	1·749	1·721	1·709	1·817	1·890	1·899	1·910	1·944	1·977	1·889	1·931	1·905
Na	—	—	—	—	0·400	—	—	—	—	—	—	—
ΣB	2·196	2·113	2·051	2·180	2·000	2·045	2·030	2·025	2·092	2·078	2·094	2·152
Na	0·339	0·299	0·217	0·373	0·423	0·386	0·346	0·207	0·378	0·271	0·162	0·169
K	0·165	0·161	0·188	0·167	0·139	0·148	0·220	0·144	0·094	—	0·026	0·027
ΣA	0·504	0·460	0·405	0·540	0·562	0·534	0·566	0·351	0·472	0·271	0·188	0·196

1 to 4 = Calcic amphiboles from banded iron formation.
5 to 10 = Calcic amphiboles from calc-amphibolite.
11 to 12 = Calcic amphiboles from ultramafic rocks.

content of hornblende will not increase with increase in temperature conditions. Therefore the variation in Ti content of hornblendes from different lithounits of the Terakanambi area, which are metamorphosed under the same PT conditions, may be a bulk compositional control or due to low fO_2 conditions. Hence, using Ti content as an indicator of grade of metamorphism needs a careful scrutiny.

The potassium content of the calcic hornblendes increases with the metamorphic grade and this may be attributed to the increase in temperature which favours the introduction of potassium into the amphibole structure (Raase *et al* 1986). The introduction of potassium may be either during metamorphism or metasomatism. The average potassium content in the hornblendes of the present study is 0·128, which is relatively higher compared to that in the amphiboles from the low grade terrains elsewhere.

The average $Mg/Mg + Fe^t$ values are 0·279, 0·505 and 0·826 respectively for the hornblendes of banded iron formations, calc-amphibolites and ultramafic rocks. The values clearly indicate that there is a close spatial relationship between the $Mg/Mg + Fe^t$ ratio of hornblendes and that of the host rock. This is in accordance with the observations made by Leake (1965), Grapes *et al* (1977) and Kamineni (1986) for the calcic amphiboles elsewhere. Leake (1968) reported that the low Mg/Fe ratio in Al-rich calcic amphiboles is mainly due to the change in the partitioning related to co-existing minerals, whereas Kamineni (1986) attributed the same to the amounts of Fe and Mg available in the host rock. In the hornblendes of the present study, Al_2O_3 ranges from 9·34 to 13·99% with an average of 11·29% and Mg/Fe ratios also vary considerably. It seems probable that the host rock composition must have played a dominant role in determining the Mg/Fe ratio of hornblendes of the present study and this is clearly substantiated by the presence of higher ratios in the hornblendes of the ultramafic rocks relative to that of hornblendes from the banded iron formations.

In terms of Al^{IV} and Al^{VI} (figure 2) the plots of the hornblendes of Terakanambi area

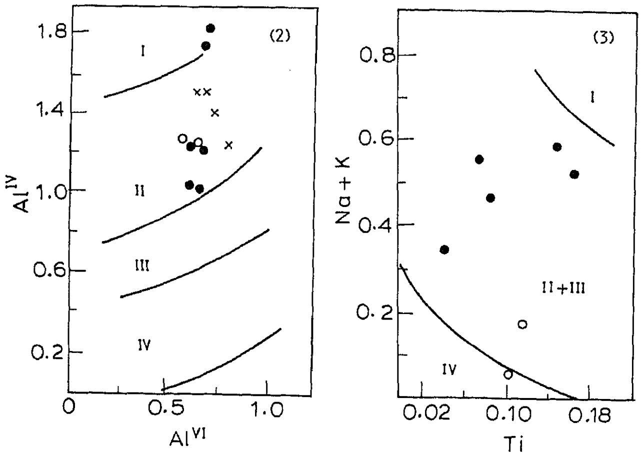

Figures 2 and 3. Al^{IV}–Al^{VI} and Ti/(Na + K) diagram. Fields after Yurkova *et al* (1985): I—Granulite facies, II—Amphibolite facies, III—Epidote amphibolite facies and IV—Greenschist facies, × —amphiboles from the banded iron formations, ●—amphiboles from calc-amphibolites and ○—amphiboles from ultramafic rocks. In figure 3 amphiboles from the banded iron formations are not plotted as they do not contain Ti.

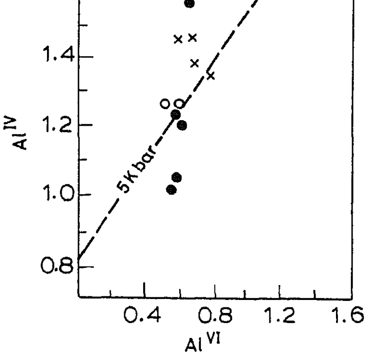

Figure 4. Al^{IV}–Al^{VI} diagram after Raase (1974). Note that the plots of amphiboles fall around the 5 kbar line.

fall well within the field of amphibolite facies of Yurkova *et al* (1985) except for the two plots which fall in the field I of granulite facies. On the (Na + K)/Ti diagram (figure 3) the plots fall in the field II + III assigned for the amphibolite and epidote amphibolite facies. One plot of hornblende from the ultramafic rock falls in the greenschist facies field and this may be attributed to the regressive metamorphic origin of hornblende by the replacement of high temperature orthopyroxene.

Leake (1965), Raase (1974), Brown (1977) and Raase *et al* (1986) have shown that the amphibole composition, in particular the Al and Na contents can be used as a pressure indicator. On the Al^{IV}/Al^{VI} diagram (figure 4) the plots fall around the 5 kbar line of Raase (1974) indicating that the hornblendes of the present study were formed under medium to low pressure conditions. It is generally argued that the Al^{IV} content of the calcic amphiboles increases with Al^{VI} with increasing grade of metamorphism. Plots of hornblendes of the study area on Al^{IV}/Al^{VI} diagram (figure 4) show no substantial increasing or decreasing trends. It also shows that the main governing factors are the amount of Si available and the total value of Al^{IV} substitution for the octahedral site. Spear (1981) suggested that higher Al^{IV} and Al^{VI} contents in hornblendic calcic amphiboles generally favour higher pressures. Though the Al^{IV} and Al^{VI} contents of the hornblendes of the present study are rather high they tend towards low to medium pressure fields on different diagrams (figures 4 and 5). On the diagram (figure 5) of Laird and Albee (1981) plots of hornblendes of the present study fall in and around the low to medium pressure fields.

Grapes and Graham (1978) and Kamineni (1986) have shown the compositional variations for a large number of calciferous amphiboles in terms of Si/Al^{VI}, $(Na + K)/Al^{VI}$ and $(Na + K)/Al^{IV}$. Klein (1969) and Cooper and Lovering (1970) have used these plots to suggest a compositional miscibility gap in the calcic amphiboles. However, similar plots for the calcic hornblendes of the Terakanambi region show compositional continuity in the $(\sum Fe/(\sum Fe + Mg))/Al^{IV}$ (figure 6) and $(Na + K)/Al^{IV}$ (figure 7) diagrams.

5. Conclusions

Calcic amphiboles of the present study are of metamorphic origin and they are of medium to low pressure type. The variation in the titanium content of the hornblendes

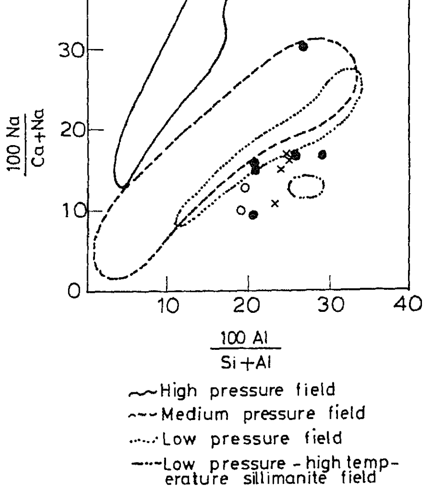

Figure 5. Plots of calcic amphiboles on 100 Na/(Ca + Na) – 100 Al/(Si + Al) diagram. Fields are after Laird and Albee (1981). All the plots fall in and around low to medium pressure fields.

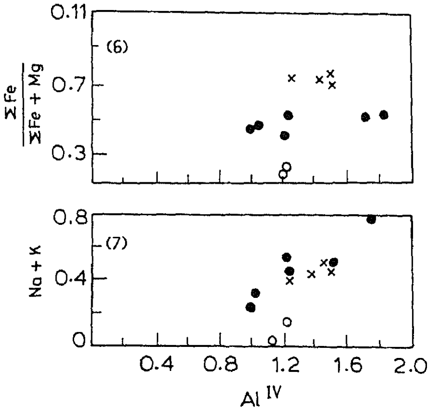

Figures 6 and 7. Plots of amphiboles on (ΣFe/(ΣFe + Mg))/Al^{IV} and (Na + K)/Al^{IV} diagrams after Boyle (1986).

may be attributed to the bulk composition control or to the low fO_2 conditions. Potassium content of the amphiboles of the present study is relatively higher compared to that of the amphiboles from the low grade terrains elsewhere. Whole rock chemistry and temperature conditions of formation are the two important factors that govern the higher Al, Ti and K contents in the calcic amphiboles of the Terakanambi area.

Acknowledgements

The authors are thankful to Prof. C Naganna for encouragement and to Prof. A S Janardhan for the microprobe analyses.

nantha Iyer G V and Narayanan Kutty T R 1976 Geochemistry of amphiboles from the Precambrian of Karnataka; *J. Geol. Soc. India* **17** 17–36

oyle A P 1986 Metamorphism of basic and pelitic rocks at Sulitjelma, Norway; *Lithos* **19** 113–128

rown E H 1977 The crossite content of Ca amphibole as a guide to pressure of metamorphism; *J. Petrol.* **18** 53–72

oolen J J M 1980 Chemical petrology of the Furua granulite complex, southern Tanzania; *GUA pap. Geol. 1* **13** 1246

ooper A F and Lovering J F 1970 Greenschist amphiboles from Haast river, New Zealand; *Contrib. Mineral. Petrol.* **27** 11–24.

vans B W 1977 Metamorphism of Alpine peridotite and serpentinite; *Annu. Rev. Earth Planet. Sci.* **5** 397–447

rapes R H and Graham C M 1978 The actinolitehornblende series in metabasites and the so-called miscibility gap: A review; *Lithos* **11** 85–97

rapes R H, Hashimoto S and Miyashita S C 1977 Amphiboles of a metagabbro amphibolite sequence, Hidaka metamorphic belt, Hokkaido; *J. Petrol.* **18** 285–318

all R P 1985 Mg-Fe-Mn distribution in amphiboles, pyroxenes and garnets and implications for conditions of metamorphism of high grade early Archaean iron formation, Southernwest Greenland; *Mineral. Mag.* **49** 117–128

elz R T 1973 Phase relations of the basalts in their melting range at pH_2O—5 kbar as a function of oxygen fugacity. Part I. Mafic phases; *J. Petrol.* **14** 249–306.

ormann P K, Raith M, Raase P, Ackermand D and Seifert F 1980 The granulite complex of Finnish Lapland: Petrology and metamorphic conditions in the Ivalojoki-Inarijarvi area; *Geol. Surv. Finland Bull.* **308** 1–55

nardhan A S, Shadakshara Swamy N and Capdevila R 1986 Banded iron formation and associated manganiferous horizons of the Sargur supracrustals, southern Karnataka; *J. Geol. Soc. India* **28** 179–188

amineni D C 1986 A petrochemical study of calcic amphiboles from the East Bull lake anorthositegabbro layered complex, District of Algoma, Ontario; *Contrib. Mineral. Petrol.* **93** 471–481

lein C 1969 Two amphibole assemblages in the system actinolite-hornblende-glaucophane; *Am. Mineral.* **54** 212–237

lein C 1983 Diagenesis and metamorphism of Precambrian banded iron formation in *Iron formations; Facts and problems* (eds) A F Trendall and R C Morris, (Amsterdam; Elsevier) 417–469

rishnanath R 1981 Coexisting humite-chondrodite-spinel-magnesium calcite assemblages from the calc-silicate rocks of Ambasamudram, Tamil Nadu, India; *J. Geol. Soc. India* **22** 235–242

aird J and Albee A L 1981 Pressure, temperature and the time indicators in mafic schists; their application to reconstructing the polymetamorphic history of Vermount; *Am. J. Sci.* **281** 127–175

eake B E 1965 The relationship between tetrahedral aluminium and the maximum possible octahedral aluminium in natural calciferous and subcalciferous amphiboles; *Am. Mineral.* **50** 843–851

eake B E 1968 A catalogue of analysed calciferous and subcalciferous amphiboles together with their nomenclature and associated minerals; *Geol. Soc. Am. Spec. paper* **68** 1–210

eake B E 1971 On aluminous and edenitic hornblendes; *Mineral. Mag.* **38** 389–407

eake B E 1978 Nomenclature of amphiboles; *Am. Mineral.* **63** 1023–1053

ahabaleswar B and Vasant Kumar I R 1983 Mineral chemistry of hornblendes from the charnockites of Karnataka, India; *Acta Miner. Petrol.* **26** 115–123

ahabaleswar B, Ananthamurthy K S and Basavanna M 1984 Pressure-temperature estimates of the iron formations of Sivasamudram area, Karnataka; *J. Geol. Soc. India* **25** 564–569

aase P 1974 Al and Ti contents of hornblende, indicators of pressure and temperature of regional metamorphism; *Contrib. Mineral. Petrol.* **45** 179–203

aase P, Raith M, Ackermand D and Lal R K 1986 Progressive metamorphism of mafic rocks from greenschist to granulite facies in the Dharwar craton of South India; *J. Geol.* **94** 261–282

ce J M 1977 Progressive metamorphism of impure dolomitic limestone in the Marysville aureole, Montana; *Am. J. Sci.* **277** 1–24

adakshara Swamy N 1983 Petrology and structure of the metasediments and the associated gneisses around Terakanambi, southern Karnataka; Unpublished PhD thesis, University of Mysore

arma R S 1982 Petrology of a scapolite bearing rock from Karera, District Bhilwara, Rajasthan; *J. Geol. Soc. India* **23** 319–329

Sivaprakash C 1981 Petrology of calc-silicate rocks from Koduru, Andhra Pradesh, India; *Contrib. Mineral. Petrol.* 77 121–128

Spear F S 1981 An experimental study of hornblende stability and compositional variability in amphibolite; *Am. J. Sci.* **281** 697–734

Srikantappa C, Raith M and Ackermand D 1985 High grade regional metamorphism of ultramafic and mafic rocks from the Archaean Sargur terrane, Karnataka, South India; *Precambrian Res.* **30** 189–219

Yurkova R M, Peyve A A, Zinkevich V P and Cherkashin V I 1985 Amphibolites of the Shirshov ridge, Bering Sea; *Int. Geol. Rev.* **27** 1051–1068

Quasi-static deformation of a layered half-space by a long strike-slip fault

NAT RAM GARG and SARVA JIT SINGH
Department of Mathematics, Maharshi Dayanand University, Rohtak 124001, India

MS received 1 April 1987; revised 30 November 1987

Abstract. Theoretical expressions for the surface displacement and shear stress caused by a long strike-slip dislocation in an elastic layer overlying an elastic half-space are derived and the correspondence principle is used to obtain the quasi-static response when the half-space is Maxwell-viscoelastic. Variation of the surface displacement and shear stress with horizontal distance is studied for various times and vertical extents of the fault. It is seen that the quasi-static response differs significantly from the corresponding elastic response.

Keywords. Correspondence principle; strike-slip fault; Maxwell model; quasi-static deformation; surface displacement; shear stress.

1. Introduction

In quasi-static deformation, the inertial terms in the stress equations of equilibrium can be ignored. The study of quasi-static deformation of a viscoelastic model of the earth caused by a shear dislocation is important to understand the post-seismic deformation following large earthquakes. Singh and Rosenman (1974) derived analytical expressions for the quasi-static surface displacements due to a finite vertical strike-slip fault in a Voigt or Maxwell viscoelastic half-space by applying the correspondence principle of linear viscoelasticity. Rosenman and Singh (1973a, b) obtained the corresponding expressions for the quasi-static surface strains, tilts and stresses. Nur and Mavko (1974) studied the characteristics of time-dependent deformation following an earthquake by considering the problem of a fault in an elastic layer overlying a viscoelastic half-space. Mukhopadhyay and Mukherji (1979) and Mukherji *et al* (1980) studied the stress accumulation near an earthquake fault by considering the antiplane strain problem of a finite displacement dislocation in an elastic layer lying over a Maxwell viscoelastic half-space, in which the shear stress is maintained far away from the fault by tectonic forces.

In our previous paper (Singh and Garg 1985, referred to as paper I hereafter), we discussed the two-dimensional problem of a long displacement dislocation in a multilayered half-space with the help of the Thomson-Haskell matrix method. Explicit expressions for the surface displacements due to dip-slip and strike-slip faults were given.

In the present paper, we first obtain the surface elastostatic field, using the results of paper I, due to a long vertical strike-slip fault in a homogeneous isotropic elastic layer lying over a homogeneous isotropic elastic half-space. The correspondence principle of linear viscoelasticity is then used to find the quasi-static response when the half-space is

Maxwell viscoelastic. In this model, the elastic layer represents the lithosphere and the Maxwell viscoelastic half-space represents the asthenosphere. Curves for surface displacement and shear stress are obtained. These curves differ significantly from the corresponding curves for the elastic case when the vertical extent of the fault is large.

2. Theory

We consider a model consisting of a homogeneous isotropic elastic layer of thickness H lying over a homogeneous isotropic Maxwell viscoelastic half-space. We place the origin of a cartesian coordinate system (x, y, z) at the free surface and the z-axis is drawn into the medium. Let a long vertical strike-slip fault, with strike along the x-axis, be situated on the z-axis at a depth h, $0 \leqslant h \leqslant H$, below the free surface. We first calculate the surface displacement and shear stress due to a long strike-slip fault situated in the corresponding elastic model. The correspondence principle of linear viscoelasticity is then used to obtain the quasi-static response.

2.1 *Elastostatic solution*

In equation (5.9) of paper I, we obtained the surface displacement $u_1(0)$ due to a long strike-slip fault situated in a multilayered elastic half-space. In the present paper, we follow the notation used in paper I. We have

$$u_1(0) = \frac{1}{\pi}\mu B_1 \int_0^\infty \left(\frac{V_{12}E_{21} - V_{22}E_{11}}{E_{21}}\right) \sin ky \, \mathrm{d}k, \tag{1}$$

where the matrices $[E]$ and $[V]$ are defined in paper I. μ is rigidity of the source layer and $B_1 = \Delta u_1 \, \mathrm{d}h$ where Δu_1 is the dislocation and $\mathrm{d}h$ the fault width.

For an elastic layer over an elastic half-space, equations (3.29) and (3.31) of paper I yield the following elements for the matrix $[E]$:

$$\begin{aligned}
E_{11} &= [\mathrm{ch}\,(kH) + \beta\,\mathrm{sh}\,(kH)]\exp(-kH),\\
E_{12} &= [\mathrm{ch}\,(kH) - \beta\,\mathrm{sh}\,(kH)]\exp(kH),\\
E_{21} &= -\mu_1[\mathrm{sh}\,(kH) + \beta\,\mathrm{ch}\,(kH)]\exp(-kH),\\
E_{22} &= \mu_1[\beta\,\mathrm{ch}\,(kH) - \mathrm{sh}\,(kH)]\exp(kH),
\end{aligned} \tag{2}$$

where μ_1 is the rigidity of the layer, μ_2 the rigidity of the half-space and

$$\beta = \mu_2/\mu_1. \tag{3}$$

Similarly, the matrix $[V]$ reduces to

$$[V] = \begin{bmatrix} \mathrm{ch}\,(kh) & -\mu_1^{-1}\,\mathrm{sh}\,(kH) \\ -\mu_1\,\mathrm{sh}\,(kh) & \mathrm{ch}\,(kh) \end{bmatrix}. \tag{4}$$

Equations (1), (2) and (4) yield

$$u_1 = \frac{B_1}{\pi}\int_0^\infty \left[\frac{\mathrm{ch}\,(kH - kh) + \beta\,\mathrm{sh}\,(kH - kh)}{\mathrm{sh}\,(kH) + \beta\,\mathrm{ch}\,(kH)}\right] \sin ky \, \mathrm{d}k. \tag{5}$$

$$u_1 = \frac{B_1}{\pi}\int_0^\infty \exp(-kh)\left[\frac{1 + r\exp\{-2k(H-h)\}}{1 - r\exp(-2kH)}\right]\sin ky\,dk, \tag{6}$$

where

$$r = (1-\beta)/(1+\beta) = (\mu_1 - \mu_2)/(\mu_1 + \mu_2). \tag{7}$$

Expanding the denominator in (6) in a power series and integrating term by term, we obtain

$$u_1 = \frac{B_1}{\pi}\left[\frac{y}{y^2+h^2} + \sum_{n=1}^{\infty} r^n\left\{\frac{y}{y^2+(2nH-h)^2} + \frac{y}{y^2+(2nH+h)^2}\right\}\right]. \tag{8}$$

Equation (8) gives the surface displacement parallel to the fault caused by a long vertical strike-slip fault situated in an elastic layer of thickness H lying over an elastic half-space.

The displacement due to a finite vertical strike-slip fault with vertical extent $0 \leqslant h \leqslant d \leqslant H$ (figure 1) is obtained from (8) by integrating with respect to h from 0 to d. We find

$$u_1 = \frac{\Delta u_1}{\pi}\left[\tan^{-1}\left(\frac{d}{y}\right) + \sum_{n=1}^{\infty} r^n \times\left\{\tan^{-1}\left(\frac{2nH+d}{y}\right) - \tan^{-1}\left(\frac{2nH-d}{y}\right)\right\}\right]. \tag{9}$$

The corresponding shear stress is given by

$$p_{12} = \mu_1\frac{\partial u_1}{\partial y} = \frac{\Delta u_1}{\pi}\mu_1\left[\frac{-d}{y^2+d^2} + \sum_{n=1}^{\infty} r^n \times\left\{\frac{2nH-d}{y^2+(2nH-d)^2} - \frac{2nH+d}{y^2+(2nH+d)^2}\right\}\right]. \tag{10}$$

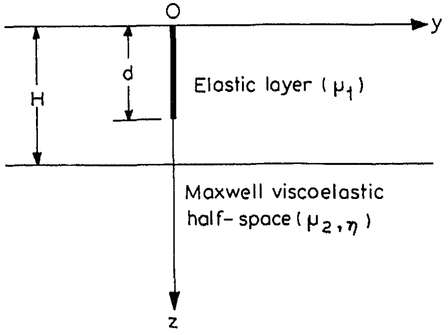

Figure 1. Section of the model by the plane $x = 0$.

We write (9) and (10) in the form

$$u_1 = \frac{1}{\pi}\left[N_0 \tan^{-1}(d/y) + \sum_{n=1}^{\infty} N_n \tan^{-1}\left(\frac{2dy}{y^2 + 4n^2H^2 - d^2} \right)\right], \tag{11}$$

$$p_{12} = \frac{1}{\pi}\left[N_0\left(\frac{-d}{y^2+d^2} \right) + \sum_{n=1}^{\infty} N_n \times \left\{ \frac{2nH-d}{y^2+(2nH-d)^2} - \frac{2nH+d}{y^2+(2nH+d)^2} \right\}\right], \tag{12}$$

where

$$N_0 = \Delta u_1, N_n = \Delta u_1 \left(\frac{\mu_1 - \mu_2}{\mu_1 + \mu_2} \right)^n. \tag{13}$$

We now use the correspondence principle (Fung 1965) to obtain the quasi-static deformation field for a model consisting of an elastic layer lying over a Maxwell viscoelastic half-space. For the elastic layer

$$p_{12} = 2\mu_1 e_{12}. \tag{14}$$

For the Maxwell viscoelastic half-space

$$\dot{e}_{12} = (1/2\mu_2)\dot{p}_{12} + [(1/\eta)p_{12}], \tag{15}$$

where η is the viscosity and the dot ($\dot{}$) signifies time-differentiation. Taking the Laplace transform of (15), we obtain

$$s\bar{e}_{12} = (s/2\mu_2)\bar{p}_{12} + [(1/\eta)\bar{p}_{12}], \tag{16}$$

where s is the Laplace transform variable. We may write (16) in the form

$$\bar{p}_{12} = 2\mu_2^* \bar{e}_{12}, \tag{17}$$

where

$$\mu_2^* = s\mu_2/(s + 2\tau^{-1}), \tag{18}$$

is the transform rigidity and $\tau = \eta/\mu_2$ is the relaxation time. Time dependence of the dislocation source is taken to be a step-function, i.e.

$$\Delta u_1(t) = U_0 H(t), \tag{19}$$

where U_0 and $H(t)$ are respectively the dislocation and the Heaviside step function. Then

$$\overline{\Delta u_1(t)} = U_0/s. \tag{20}$$

In order to obtain the Laplace transformed solution of the viscoelastic problem, it is only necessary to replace μ_2 and Δu_1 by μ_2^* and $\overline{\Delta u_1}$ respectively in the corresponding stic solution. From (11) and (12) we notice that μ_2 and Δu_1 appear only in the ressions for N_0 and N_n. Therefore, the Laplace transformed solution of the coelastic problem is obtained from (11) and (12) on replacing N_0 and N_n by $\bar{N}_0$ and respectively, where, from (13), (18) and (20)

$$\bar{N}_0 = (U_0/s), \quad \bar{N}_n = U_0 G_n(s), \tag{21}$$

$$G_n(s) = (Bs + A)^n / s(s + A)^n, \tag{22}$$

$$A = 2\mu_1/(\mu_1 + \mu_2)\tau, \quad B = (\mu_1 - \mu_2)/(\mu_1 + \mu_2). \tag{23}$$

n order to find the inverse Laplace transform of $G_n(s)$, we use a transform integral ed in Erdélyi (1954). We find that

$$L^{-1}[G_n(s)] = 1 + \exp(-At) \sum_{m=1}^{n} \frac{F_{2m}(-A)}{(n-m)!(m-1)!} t^{n-m}, \tag{24}$$

ere

$$F_{2m}(s) = (d^{m-1}/ds^{m-1})[(Bs + A)^n/s]. \tag{25}$$

ations (11), (12), (21) and (24) yield ($t > 0$)

$$u_1 = \frac{U_0}{\pi}\left[\tan^{-1}\left(\frac{d}{y}\right) + \sum_{n=1}^{\infty}\left\{1 + \exp(-At) \sum_{m=1}^{n} \frac{F_{2m}(-A)}{(n-m)!(m-1)!} t^{n-m}\right\} \times \tan^{-1}\left(\frac{2dy}{y^2 + 4n^2H^2 - d^2}\right)\right], \tag{26}$$

$$p_{12} = \frac{U_0}{\pi}\mu_1\left[\frac{-d}{y^2 + d^2} + \sum_{n=1}^{\infty}\left\{1 + \exp(-At) \sum_{m=1}^{n} \frac{F_{2m}(-A)}{(n-m)!(m-1)!} t^{n-m}\right\} \times \left\{\frac{2nH - d}{y^2 + (2nH - d)^2} - \frac{2nH + d}{y^2 + (2nH + d)^2}\right\}\right]. \tag{27}$$

Putting $\mu_1 = \mu_2$ in (27), we get the solution obtained by Bonafede *et al* (1984) for the ar stress p_{12} as a particular case.

Particular case

t $\qquad \mu_1 = \mu_2 = \mu$ (say). $\qquad$ (28)

en $\qquad A = \tau^{-1}, \quad B = 0,$ $\qquad$ (29)

d $\qquad F_{2m}(-A) = -(m-1)!/\tau^{n-m}.$ $\qquad$ (30)

ations (26) and (27) give ($t > 0$)

$$u_1 = \frac{U_0}{\pi}\left[\tan^{-1}(d/y) + \sum_{n=1}^{\infty}\left\{1 - \exp(-t/\tau) \sum_{k=0}^{n-1} \frac{(t/\tau)^k}{k!}\right\} \times \tan^{-1}\left(\frac{2dy}{y^2 + 4n^2H^2 - d^2}\right)\right], \tag{31}$$

$$p_{12} = \frac{}{\pi}\mu\left[\frac{}{y^2+d^2} + \sum_{n=1}\left\{1 - \exp(-t/\tau)\sum_{k=0}\frac{}{k!}\right\}\right.$$

$$\left.\times\left\{\frac{2nH-d}{y^2+(2nH-d)^2} - \frac{2nH+d}{y^2+(2nH+d)^2}\right\}\right]. \tag{32}$$

Equations (31) and (32) give respectively the quasi-static surface displacement parallel to the fault and the horizontal shear stress caused by a long vertical strike-slip fault $(-\infty < x < \infty, 0 \leqslant z \leqslant d \leqslant H)$ in an elastic layer lying over a Maxwell viscoelastic half-space.

The case $t = 0$ corresponds to the elastic problem. Equations (7), (9), (10) and (28) then yield

$$u_1 = \frac{U_0}{\pi}\tan^{-1}(d/y), \quad p_{12} = \frac{U_0}{\pi}\mu\left(\frac{-d}{y^2+d^2}\right), \tag{33}$$

where $\Delta u_1 = U_0$.

Since we have taken $\mu_1 = \mu_2 = \mu$, (33) gives the field due to a long vertical strike-slip fault $(-\infty < x < \infty, 0 \leqslant h \leqslant d)$ situated in an elastic half-space.

4. Numerical results

We wish to study the variation of the displacement and the stress fields generated by a long strike-slip fault in an elastic layer lying over a Maxwell viscoelastic half-space. In (31) and (32), we have obtained the expressions for the parallel quasi-static displacement and the shear stress. For numerical computation, we define the dimensionless quantities α, T, Y, U_1 and P_{12} through the relations

$$d = \alpha H, \quad t = T\tau, \quad y = YH,$$

$$u_1 = (U_0/\pi)U_1, \quad p_{12} = (U_0\mu/\pi H)P_{12}. \tag{34}$$

Using (34), equations (31) and (32) yield $(T > 0)$

$$U_1 = \tan^{-1}(\alpha/y) + \sum_{n=1}^{\infty}\left[1 - \exp(-T)\sum_{k=0}^{n-1}\frac{T^k}{k!}\right]$$

$$\times\tan^{-1}\left(\frac{2\alpha Y}{Y^2+4n^2-\alpha^2}\right), \tag{35}$$

$$P_{12} = \frac{-\alpha}{Y^2+\alpha^2} + \sum_{n=1}^{\infty}\left[1 - \exp(-T)\sum_{k=0}^{n-1}\frac{T^k}{k!}\right]$$

$$\times\left[\frac{2n-\alpha}{Y^2+(2n-\alpha)^2} - \frac{2n+\alpha}{Y^2+(2n+\alpha)^2}\right], \tag{36}$$

where U_1, P_{12}, T and Y are respectively the dimensionless displacement, shear stress, time and horizontal distance. In the elastic case, (33) gives

$$U_1 = \tan^{-1}(\alpha/y), \quad P_{12} = -\alpha/(Y^2+\alpha^2). \tag{37}$$

ce

$$\left[\exp(-T)\sum_{k=0}^{n-1}\frac{T^k}{k!}\right] < 1$$

all n and $T > 0$, it is obvious that the infinite series appearing on the right hand side 35) converges at least as rapidly as the infinite series $\sum(1/n^2)$. Similarly, noting that

$$\frac{2n-\alpha}{Y^2+(2n-\alpha)^2} - \frac{2n+\alpha}{Y^2+(2n+\alpha)^2} = \frac{2\alpha\{4n^2-(Y^2+\alpha^2)\}}{[Y^2+(2n-\alpha)^2][Y^2+(2n+\alpha)^2]}$$

infinite series appearing on the right hand side of (36) also converges at least as idly as the infinite series $\sum(1/n^2)$. In our numerical computation, we found that the t 10 terms of the infinite series are adequate.

Figures 2–4 show the variation of the dimensionless surface displacement U_1 allel to the fault with the dimensionless horizontal distance Y from the fault for three ues of the vertical extent of the source namely $d = H$, $H/2$ and $H/10$ and three values the dimensionless time $T(T = 0, 1$ and $10)$. For all values of d and T, $U_1 = \pi/2$ when $= 0$ (see equations (35) and (37)). The graphs for $T = 0$ correspond to the elastic case. om (37), we find that, in the elastic case, the parallel horizontal displacement $U_1 \to 0$ all values of d as $Y \to \infty$. We note that the deviation of the viscoelastic solution from elastic solution increases as d increases for a given value of Y. Similarly, the viation of the viscoelastic solution from the elastic solution increases as Y increases a fixed value of d.

Figures 5–7 exhibit the variation of the dimensionless horizontal shear stress P_{12} h the dimensionless horizontal distance Y from the fault for three values of the tical extent of the source, namely, $d = H$, $H/2$, $H/10$ and different values of the mensionless time T. The graphs for $T = 0$ correspond to the elastic case for which $_2 = -H/d$ when $Y = 0$. Also, $P_{12} \to 0$ as Y approaches infinity [see equation (37)]. or $d = H$, the graphs for $T = 1$ and $T = 5$ are quite different from the graph for the stic case (figure 5). For $d = H/2$, there is only a slight difference between the graphs

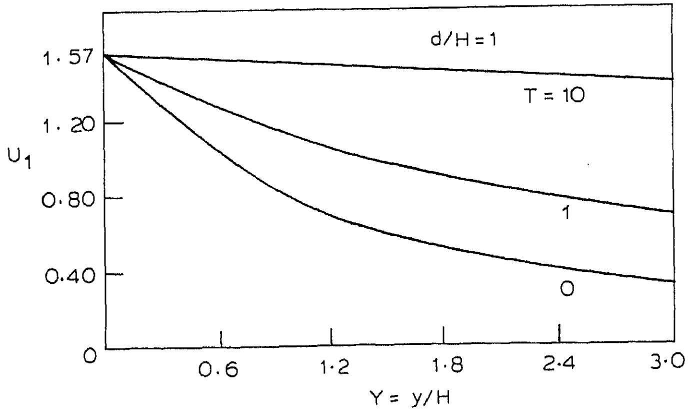

Figure 2. Variation of parallel displacement U_1 with horizontal distance Y when $d = H$.

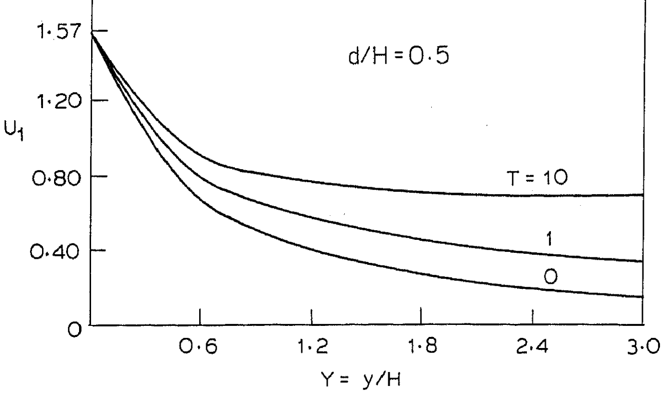

Figure 3. Variation of parallel displacement U_1 with horizontal distance Y when $d = H/2$.

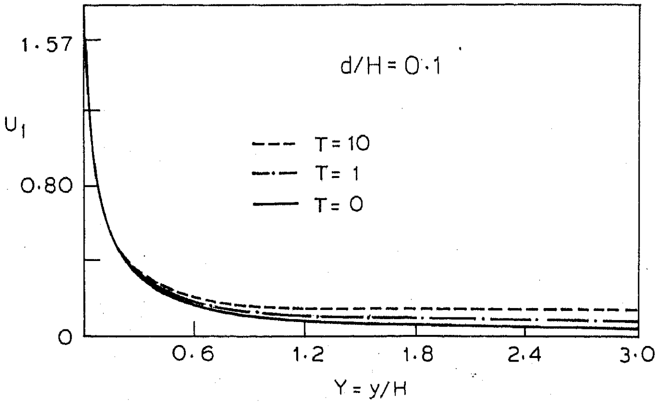

Figure 4. Variation of parallel displacement U_1 with horizontal distance Y when $d = H/10$.

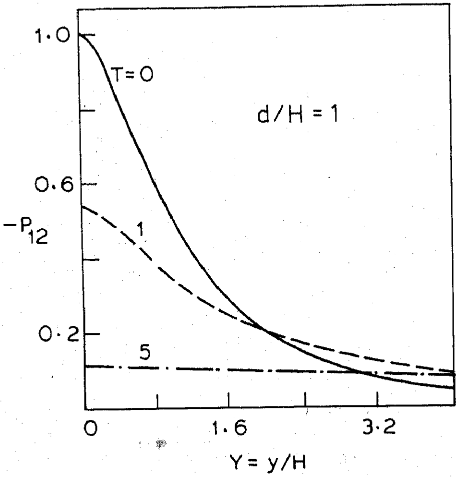

Figure 5. Variation of shear stress $-P_{12}$ with horizontal distance Y when $d = H$.

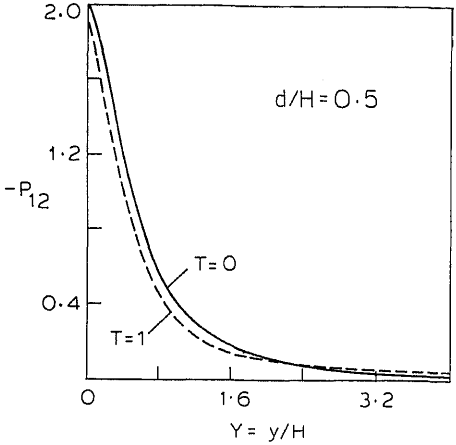

Figure 6. Variation of shear stress $-P_{12}$ with horizontal distance Y when $d = H/2$.

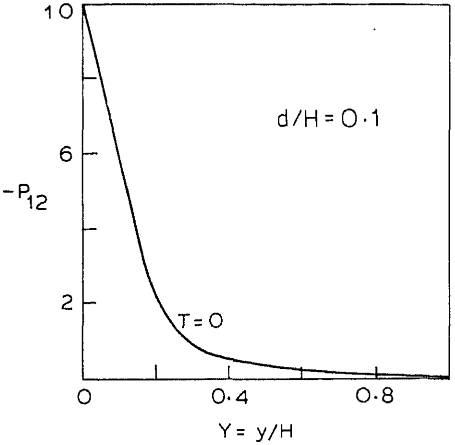

Figure 7. Variation of shear stress $-P_{12}$ with horizontal distance Y when $d = H/10$.

r the viscoelastic case and the elastic case (figure 6). For $d = H/10$, the graphs for the scoelastic case almost coincide with the corresponding graph for the elastic case gure 7).

Discussion

juations (9) and (10) give the surface displacement and the surface shear stress spectively caused by a long vertical strike-slip fault in a homogeneous isotropic layer thickness H lying over a homogeneous isotropic elastic half-space. These results are complete agreement with the corresponding results of Rybicki (1971) who used the ethod of images to obtain these results while we have obtained them directly. The vantage of our method is that it can also be used when there is more than one layer ng over the half-space.

We have used the correspondence principle of linear viscoelasticity to obtain the asi-static displacement and stress fields for a model consisting of an elastic layer lying er a Maxwell viscoelastic half-space. Our results are particularly useful for studying the time-dependent post-seismic deformation associated with large earthquakes. Mukhopadhyay and Mukherji (1979) and Mukherji *et al* (1980) discussed the problem of a long strike-slip fault in an elastic layer lying over a viscoelastic half-space without using the correspondence principle. In addition, these authors included the effect of initial stress and assumed that the shear stress is maintained far away from the fault by tectonic forces. The results of Mukhopadhyay and Mukherji (1979) and Mukherji *et al* (1980) are useful for studying the stress accumulation near an earthquake fault. The correspondence principle is normally applicable if the material is stress-free and strain-free before the fault movement, and we have made this assumption in our model. Similarly, since our main interest was to determine the displacement and the stress fields generated by the fault movement, we have not considered the shear stress maintained far away from the fault by tectonic forces.

Acknowledgement

One of the authors (SJS) is grateful to the Council of Scientific and Industrial Research, New Delhi for financial support.

References

Bonafede M, Boschi E and Dragoni M 1984 A dislocation model of microplate boundary ruptures in the presence of a viscoelastic asthenosphere; *Geophys. J. R. Astron. Soc.* **76** 515–529

Erdélyi A 1954 *Tables of integral transforms* (New York: McGraw-Hill) Vol. 1

Fung Y C 1965 *Foundations of solid mechanics* (New Jersey: Prentice Hall)

Mukherji P, Pal B P, Sen S and Mukhopadhyay A 1980 On stress accumulation near a continuously slipping fault in a two-layered model of the lithosphere; *Bull. Indian Soc. Earthq. Tech.* **17** 29–38

Mukhopadhyay A and Mukherji P 1979 On stress accumulation and fault slip in the lithosphere; *Mausam* **30** 353–358

Nur A and Mavko G 1974 Post-seismic viscoelastic rebound; *Science* **183** 204–206

Rosenman M and Singh S J 1973a Quasi-static strains and tilts due to faulting in a viscoelastic half-space; *Bull. Seismol. Soc. Am.* **63** 1737–1752

Rosenman M and Singh S J 1973b Stress relaxation in a semi-infinite viscoelastic earth model; *Bull. Seismol. Soc. Am.* **63** 2145–2154

Rybicki K 1971 The elastic residual field of a very long strike-slip fault in the presence of discontinuity; *Bull. Seismol. Soc. Am.* **61** 79–92

Singh S J and Garg N R 1985 On two-dimensional elastic dislocations in a multilayered half-space; *Phys. Earth Planet. Inter.* **40** 135–145

Singh S J and Rosenman M 1974 Quasi-static deformation of a viscoelastic half-space by a displacement dislocation; *Phys. Earth Planet. Inter.* **8** 87–101

On the observed synoptic variability in the thermal structure of the upper northern Bay of Bengal during MONEX-79

R R RAO and BASIL MATHEW
Naval Physical and Oceanographic Laboratory, Cochin 682004, India

MS received 8 June 1987; revised 25 February 1988

Abstract. The short-term variability observed in the near surface meteorological parameters and in the vertical thermal structure of the upper layers of the northern Bay of Bengal during a weak monsoonal regime is examined with the aid of time series measurements. The variability of the mixed layer depth is interpreted in terms of forced mixing caused by the surface wind stress and free mixing by buoyancy flux, Ekman pumping controlled by the curl of the surface wind stress, convergence associated with a clockwise gyral circulation and stratification caused by freshwater discharges from rivers. The daily-averaged current vectors in the upper layers indicate the presence of clockwise gyral circulation in the polygon area.

Keywords. Heat budget; thermal structure; mixed layer; heat content; clockwise gyre; synoptic variability.

1. Introduction

In the tropics, northern Bay of Bengal is a unique semi-enclosed basin experiencing seasonal reversing monsoons, depressions, severe cyclonic storms and consequently receives a large amount of rainfall and river run-off. The upper layers of the sea are therefore expected to respond to the hydrometeorological forcing through mass, momentum and heat inputs. Hence it is anticipated that the physical properties of the upper layers as temperature, salinity and currents would also exhibit large variability in the space-time domain. However, very few systematic investigations on the observed variability in the northern Bay of Bengal have been carried out, mainly due to paucity of data sets. Utilizing a variety of data sets, Wyrtki (1971), Colborn (1975), Hastenrath and Lamb (1979), Robinson *et al* (1979), Ramesh Babu and Sastry (1981) reported the seasonal variability of the thermal structure of the upper layers of the Bay of Bengal in the spatial domain. The corresponding information on the short-term variability is relatively meagre.

Prior understanding of the short-term variability in the thermal structure of the upper layers is extremely important in the fields of weather forecasting, fisheries exploration and underwater surveillance operations etc. Information on the thermal variability in the upper layers of the northern Bay of Bengal on the diurnal and synoptic scales is extremely sparse due to lack of systematic time series measurements. Fortunately the field measurement programmes of the recent summer monsoon experiments (MONSOON-77 and MONEX-79) conducted at selected stations over the northern Bay of Bengal afforded an unique opportunity to examine this problem in some detail for a limited period during the summer monsoon season. Rao *et al* (1981) formation of a monsoon depression. In another study, utilizing the bathythermograph (BT) data collected from an Indian ship, Rao *et al* (1983) described the upper oceanic thermal structure observed at selected stations in the northern Bay of Bengal for selective periods during May, June and July 1979 under the summer monsoonal forcing. In the present study an attempt was made to explain the observed short-term variability in the thermal structure of the upper layers of northern Bay of Bengal under a weak monsoonal regime utilizing time series data sets collected from USSR ships during MONEX-79.

2. Data

During 11 to 23 July 1979 four USSR ships formed a stationary polygon (figure 1) in the northern Bay of Bengal to monitor the characteristics of the upper air and upper ocean and to study the genesis and growth of monsoon depressions. Although no depression formed during this period, the collected data sets possibly provided some clues on the non-formation of any depression. Time series of all the standard marine meteorological elements including solar radiation were measured at hourly intervals. BT profiles provided six-hourly temperature data in the vertical upto about 200 m depth. These profiles usually contained data at 10 to 25 non-standard depths. However, as the BT data were not reported at standard depths, a cubic spline technique was adopted to generate data at every 5 m interval in the vertical below the mixed layer. Hydrocasts conducted at three-hourly interval provided salinity data except at the eastern location where the observational interval was 6 h. Daily averages or totals of meteorological and oceanographic elements were used in this study. In the following discussion the observational stations are designated as N, E, S and W corresponding to northern, eastern, southern and western locations of the polygon.

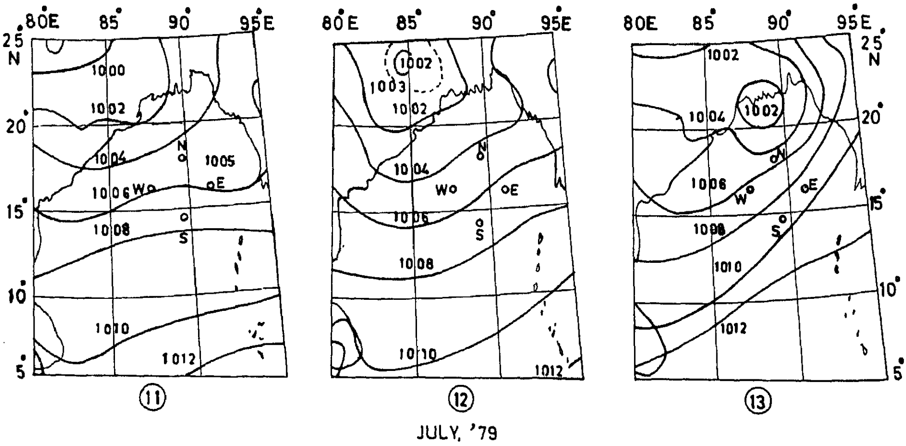

Figure 1. Station locations and daily surface pressure analysis from 11–13 July 1979 (contour interval 2 mb).

Weather

brief summary of the weather extracted from Indian Daily Weather Reports is ported here. A low pressure area moved across the Arakan coast into northeastern Bay 4 July and concentrated into a depression on 6 July. This depression crossed the ast on 8 July and moved west-northwest to the central parts of India by 10 July. By 15 ly it moved as a low pressure area upto Rajasthan and merged with the seasonal low 20 July. On 13 July, another low pressure area developed over the northern Bay gure 1). It moved rapidly northwest on 14 July and merged with the monsoon trough er Bihar. With this the eastern end of the monsoon trough shifted northwards using heavy rains over the foothills. The monsoon westerlies weakened resulting in ak monsoon conditions over the central parts of India. After this an east-west trough lower and middle tropospheres formed across the sourthern peninsula on 21 July. is slowly shifted northwards and became well organised by 27 July when a low essure area formed on its eastern end and moved westwards. At this stage the asonal trough also shifted southwards and the low pressure area merged with it wards the end of July.

Results and discussion

assess the role of heat exchange terms at the air-sea interface on the short-term riability of the SST and mixed layer depth (MLD) an attempt was made to budget ese terms. The daily values of the observed meteorological parameters such as surface essure (PR), scalar wind speed (FF), total cloud cover (TCL), dry bulb temperature B), dew point temperature (DP) and sea surface temperature (SST) utilized for heat dget computation are presented in figure 2. The heat budget equation

$$Q = Q_I + Q_L + Q_S + Q_E,$$

ere Q is the net ocean surface heat gain (W/m^2), Q_I the net insolation after applying rrection for albedo (W/m^2), Q_L the net long wave radiation (W/m^2), Q_S the sensible at flux (W/m^2) and Q_E the latent heat flux (W/m^2). The positive values indicate heat in to the ocean. The Q_I values were only measured directly while all the other terms re estimated (Rao *et al* 1985). The results are portrayed in figure 3. The Q_I at the rface varied between 100 and 300 W/m^2 with the exception of N and E during the itial disturbed days, where the values were < 50 W/m^2. Cloud cover was the most ominent element which influenced the short-term variability of Q_I. The day-to-day riation in cloud cover was reflected in Q_I. However, the correspondence may not be act as the cloud cover was not measured with any instrument and hence may contain me subjective bias.

The net long wave radiation Q_L was controlled by SST, moisture in the atmosphere d cloud cover. Q_L did not exhibit strong variations but varied around -42 W/m^2. $_S$, determined by air (at 10 m above sea surface) and sea temperature difference and the alar wind speed, was almost negative throughout with relatively higher magnitude at and E during initial disturbed period. The negative values imply heat loss to the ean under the unstable regime. The highest value of Q_S never exceeded 30 W/m^2

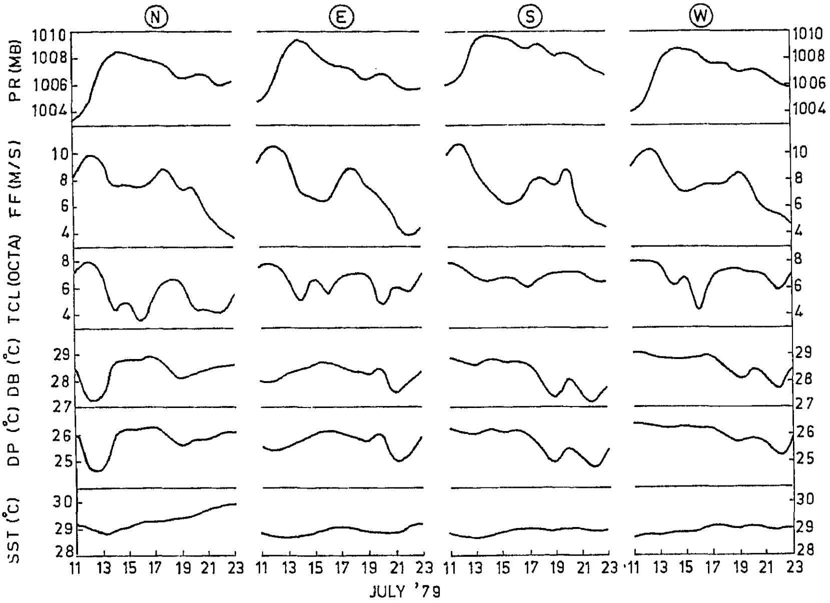

Figure 2. Daily march of surface meteorological parameters at the stationary locations.

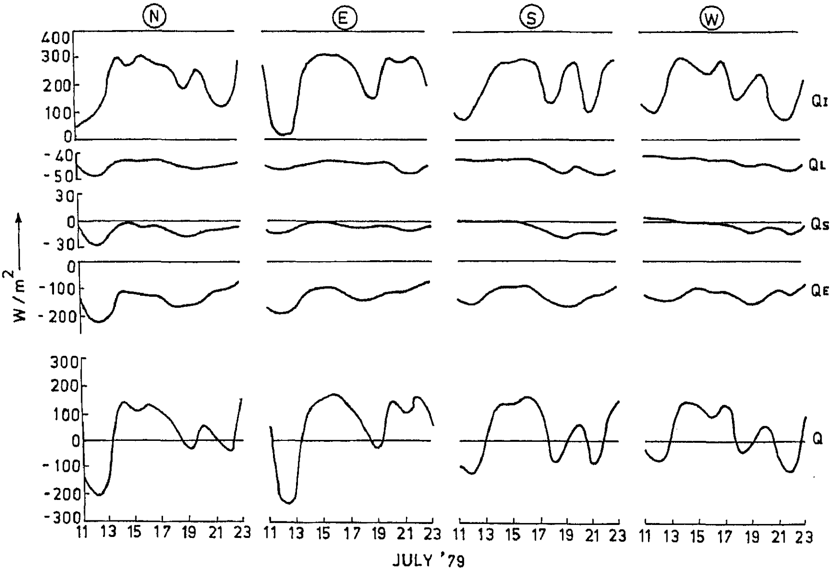

Figure 3. Daily march of surface heat budget estimates at the stationary locations.

vertical vapour pressure gradient and scalar wind speed ranged between − 100 and − 200 W/m² and were higher during the initial disturbed period. A gradual decline in Q_E is noticed at all the locations after the initial disturbed period. The balance between disturbed period. The ocean mostly gained heat from 13/14 to 18 July 1979 at all the locations. Towards the end of the observational period the regime of Q mostly fluctuated around zero line. In view of the absence of large fluctuations in the loss terms, the overall patterns of Q and Q_I resembled each other.

The synoptic scale variability in the near surface mixed layer depth (MLD) was governed by the forced mixing caused by wind and wave action and free mixing caused by buoyancy flux and Ekman pumping produced by the vertical component of curl of the surface wind stress under the stabilizing influence of stratified pycnocline below the mixed layer. An attempt was made to qualitatively relate the variability of MLD with these processes. Following Haney *et al* (1981) the forced mixing was represented by$U_*^3[U_* = (\tau/\rho_w)^{1/2}]$ where U_* is the friction velocity, τ the surface wind stress and ρ_w the density of mixed layer. The net heat gain/loss at the sea surface approximately corresponds to the buoyancy flux. The vertical component of the surface wind stress curl $(\nabla \times \tau)_z$ was estimated with the aid of wind data collected from the four ships. Here $(\nabla \times \tau)_z$ corresponds to the polygon area while U_*^3 and Q correspond to the individual stations. The vertical density gradient (BLG) below the mixed layer was taken as a measure of stability. The daily march of these parameters is shown in figure 4. At all the locations there were strong vertical salinity gradients (figure 5), and the halocline was observed at shallower depths than the thermocline. Hence, MLD was determined from the daily averaged vertical profile of $\sigma_t[\sigma_t = (\rho_t - 1)\ 1000$, where ρ_t is the in situ density]. The MLD was defined as the depth where σ_t at sea surface $-0{\cdot}3\,\mathrm{kg\,m^{-3}}$ occurred in the daily averaged vertical σ_t profile, which roughly correspond to the σ_t

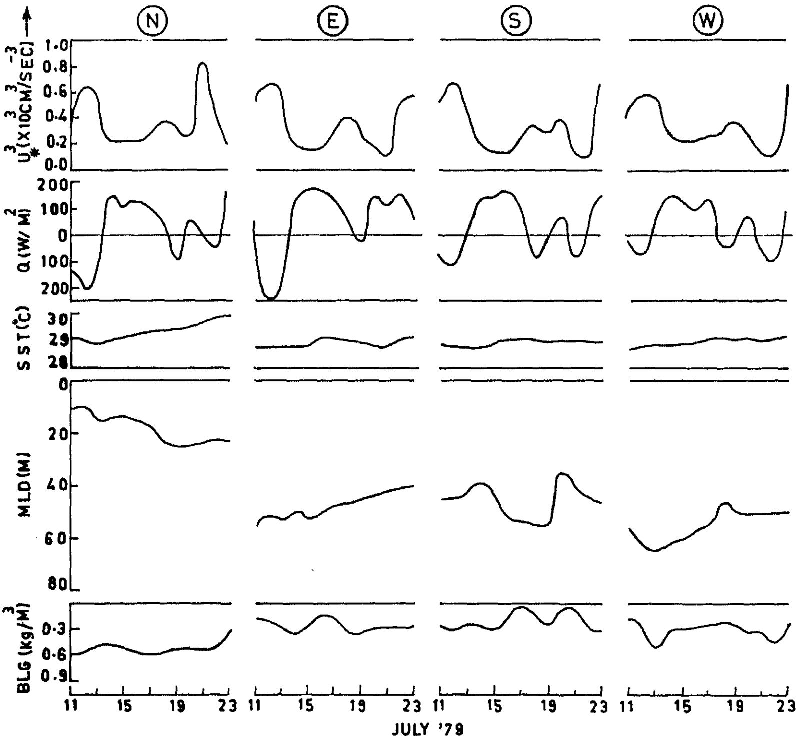

Figure 4. Daily march of U_*, Q, SST, MLD and BLG at the stationary locations.

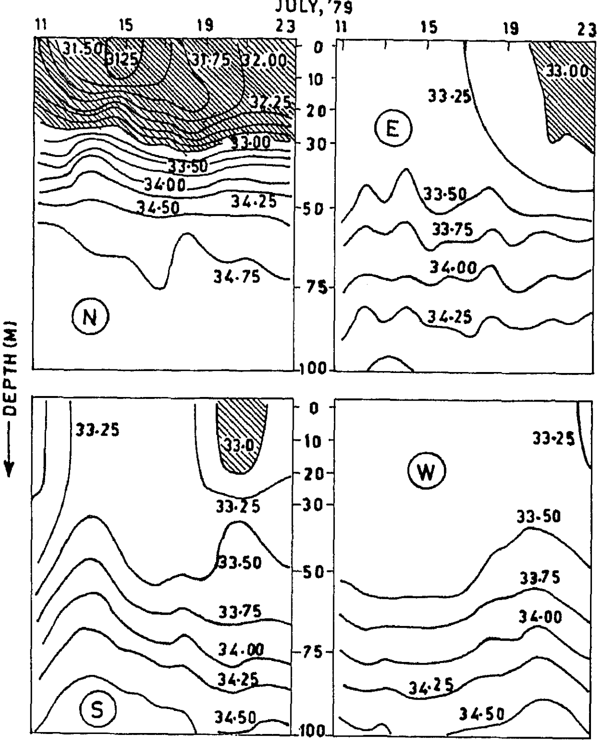

Figure 5. Daily averaged vertical salinity field at the stationary locations (contour interval 0·25‰).

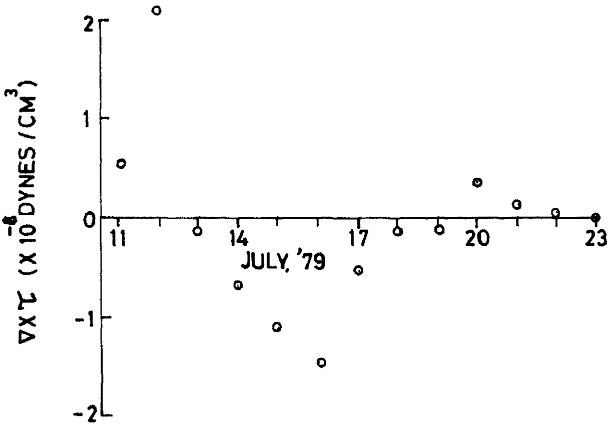

Figure 6. Daily march of vertical component curl of surface wind stress in the polygon area.

change associated with 1°C drop in the vertical thermal profile. In general MLD was relatively shallower at N and deeper at the other stations mainly due to the decrease in the bottom layer stratification away from the Head Bay. A strong halocline in the upper layers produced by the freshwater discharges from Ganges is responsible for the

Table 1.

Location	Correlation between MLD and U_*^3	Correlation between MLD and net heat gain
N	0·12	−0·17
E	0·17	0·42
S	−0·09	−0·15
W	0·26	0·21

meridional variation in BLG. For instance, BLG at N was almost double that of any other three stations (figure 4) where the freshwater influence was maximum. In general the mixed layer deepened at N, shoaled at E and W and was oscillatory at S. From the distribution of $\nabla \times \tau$ (figure 6) a shoaling tendency during initial period ($\nabla \times \tau < 0$) and deepening tendency thereafter until 19 July ($\nabla \times \tau > 0$) are to be anticipated in the MLD distribution. On the whole no such alternating trends were noticed in the MLD except at S. The U_*^3 was distinctly larger during the beginning and ending days at all the locations. Deepening rates of the layer should also be higher during these corresponding periods. However, no such one-to-one correspondence was noticed in the distribution of U_*^3 and MLD. The net heat gain was by and large negative only during the beginning and ending days (figure 3) and was positive at all the locations. The total heat gain varied between $0{\cdot}6 \times 10^8$ J/m^2 at E and $0{\cdot}18 \times 10^8$ J/m^2 at N. This type of heat accumulation lead to mixed layer shoaling. However, such a correspondence was noticed only at E and to a lesser extent at W. In order to obtain a more quantitative relationship between MLD and free and forced mixing the respective correlation coefficients were computed (table 1). At all locations the correlation between MLD and net heat gain was not significant with maximum value of 0·42 at E. The contribution of forced mixing also appears to be very less as evidenced by the correlation coefficient. Rao *et al* (1981) found a good relationship between MLD and net heat gain nearly in the same area in August 1977. However, they did not consider the influence of salinity which showed considerable changes with depth and also with time (Rao and Sanil Kumar 1988) during the observational period. At all the locations the isothermal layer was much deeper than the isohaline layer and the synoptic variations in the salinity field were more conspicuous than that of the thermal structure.

During July a clockwise gyral circulation was noticed in the northern Bay of Bengal (US Navy Atlas 1976). This clockwise circulation can also modify the topography of the mixed layer depth. The divergence pattern from the observed current vectors from four ships at different depths was estimated to identify any such relationship. The day-to-day variability of divergence is shown in figure 7. The positive values imply divergence which is noticed during the first few days only at 25 m and 50 m depths followed by a switchover to convergence showing an increasing tendency with time. However, no such switching-over was noticed at 100 m, 150 m and 200 m depths. From the same data set Swallow (1983) inferred a weak clockwise eddy 400–500 km across, centred near

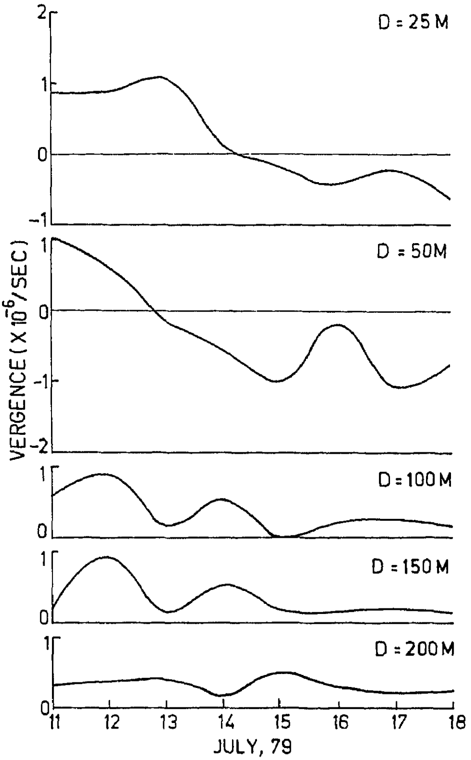

Figure 7. Daily march of divergence field in the polygon area.

14°N and 89°E where the 20°C isotherm was depressed 30 m. A clockwise eddy s
result in convergence near its centre. However, no such anticipated deepening ter
of the mixed layer due to convergence was noticed at the S location. An attempt
a possible relationship between the layer depth and current shear below the mixe
did not yield positive results.

Though, during the observational period, the contribution of saltification/d
caused by evaporation and rainfall was negligible in the polygon area (Rao anc
Kumar 1988), the salinity in the upper layers at all locations showed consic
variability (figure 5). The surface layer salinity at N showed a progressive decre
15 July and thereafter increased while at E and W a gradual fall was r
throughout. At S the salinity increased till 16 July and showed an oscillatory
thereafter. Since the contribution on salinity due to local evaporation/precip
was negligible due to break monsoon conditions, advection seemed to be th
factor responsible for the considerable changes in the salinity regim
increase/decrease in the freshwater discharge from Ganges and Brahmaputra
and its spreading into the four locations might have caused the observed variat

except at N till 15 July (figures 4 and 5). The MLD at N showed a deepening tendency throughout, while the salinity in the upper layers decreased till 15 July and then increased. On the other hand the MLD at E and W shoaled where the salinity in the upper layers decreased. Both the MLD and the salinity field showed an oscillatory nature at S. Such close resemblence between the variability observed in MLD and salinity distribution probably implies that the MLD was governed by the stratification caused in the upper layers due to time-varying freshwater discharges into the Head Bay and its subsequent diffusion and circulation. Under a weak monsoonal spell, the influence of stratification caused by freshwater discharges seems to outweigh the contribution due to forced mixing, free mixing, Ekman pumping or divergence in regulating MLD in the polygon area.

The depth-time (daily-averaged) temperature fields drawn for all the four stations are shown in figure 8. Isotherms were drawn at 1°C interval by computer through linear interpolation. The presence of isothermal layer capped over stratified thermocline is evident at all the locations. The thickness of the isothermal layer was not of equal magnitude within the polygon area. Accumulation of heat within the mixed layer is clearly evident in the latter half of the observational period with the exception of W. The location and thickness of maximum vertical thermal gradient below mixed layer also differed within the polygon area. The phase-averaged distribution of this gradient will be discussed later to highlight this aspect. The short period waves might be viewed as the manifestation of inertial oscillations.

The phase-averaged BT profiles (11–23 July 1979) corresponding to the four stations (figure 9) clearly reveal the nature and magnitude of the horizontal variability prevailing in this area. The horizontal temperature differences in the top 30 m layer are insignificant. Below the isothermal layer the horizontal gradient was stronger in the north-south than that of in the east-west. Further, the gradient was not uniform in the vertical. For instance, in the north-south the temperature difference was over 5°C around 75 m depth and decreased on either side. This large spatial difference resulted mostly due to unequal mixed layer depths at the northern and southern locations.

The averaged profiles of the vertical thermal gradient for all the locations are shown in figure 10. Very weak gradients within the surface mixed layer are evident. Below this, the gradient gradually built up reaching a maximum in the depth range 90–120 m with the only exception N. At N the gradients sharply shot up reaching a peak value of 2·5°C/10 m around 45 m depth. The fall in the gradient below 45 m was less sharp compared to that reported above. At N, on the whole, the slab with $\partial T/\partial z > 1°\mathrm{C}/10\,\mathrm{m}$ persisted from 35 m to 85 m. Such a strong and thick stratified layer acts as an insulator for the vertical exchange of heat and salt. This would lead to trapping of the surplus heat energy in the mixed layer resulting in an anomalous increase of its heat content. The frequent formation of the meteorological disturbances during the summer monsoon season over the Head Bay of Bengal must therefore have some link with the growing mixed layer heat content. Rao *et al* (1981) reported such a possibility at this area during MONSOON-77. When the mixed layer heat content exceeds certain threshold limit it might infuse instability in the overlying monsoonal flow leading to the formation of a disturbance.

The daily march of the cyclonic heat potential ($\mathrm{HP}_{28} = \rho C_p \int_0^{D_{28}} (T - 28)\,\mathrm{d}z$) i.e. heat

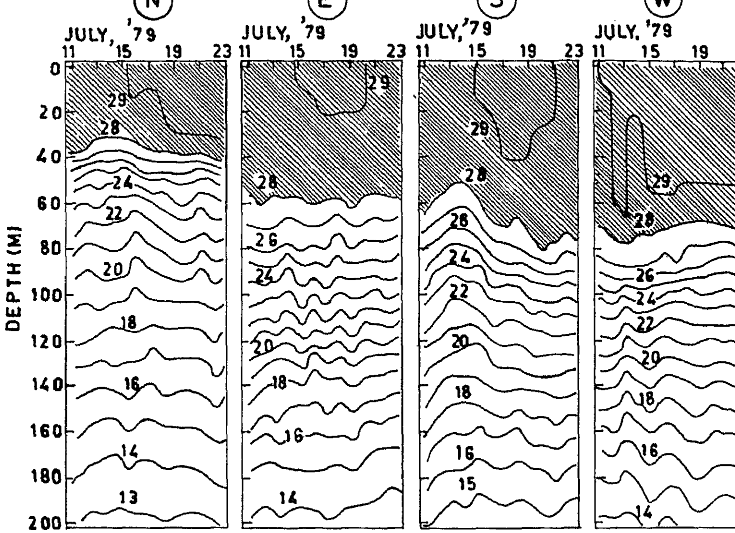

Figure 8. Daily averaged vertical temperature field at the stationary locations
interval 1°C).

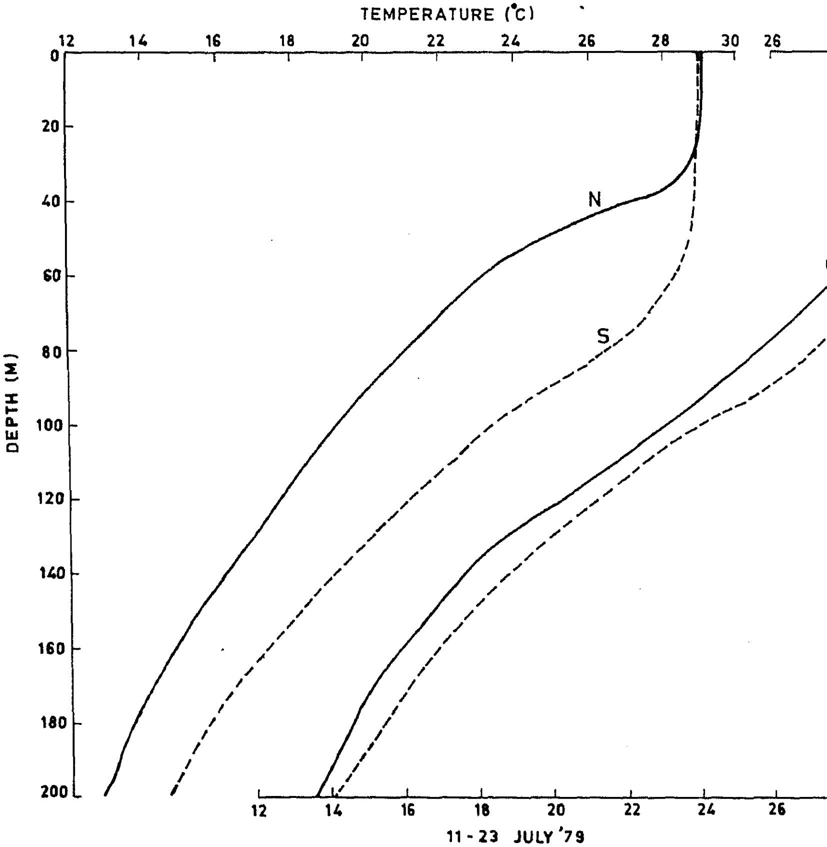

Figure 9. Phase averaged vertical temperature field at the stationary locations.

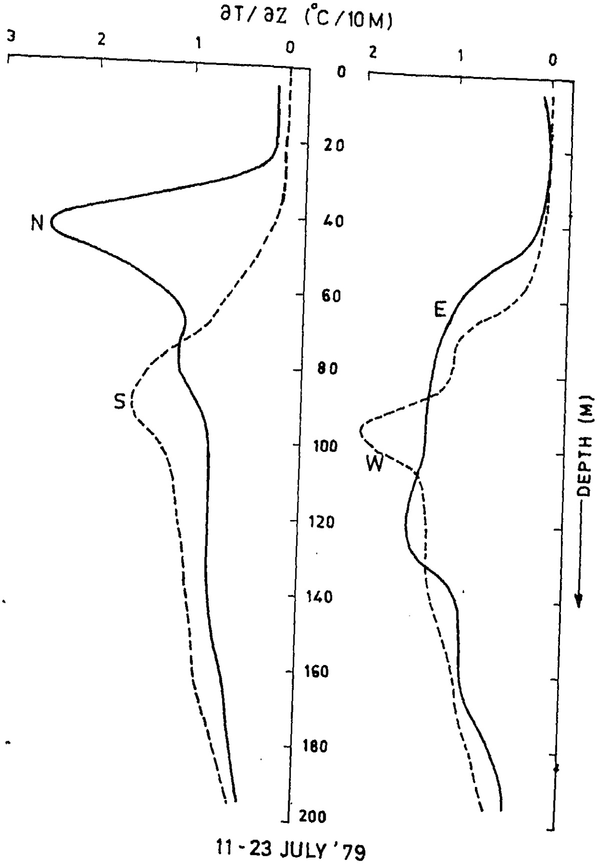

Figure 10. Phase averaged vertical temperature gradients at the stationary locations.

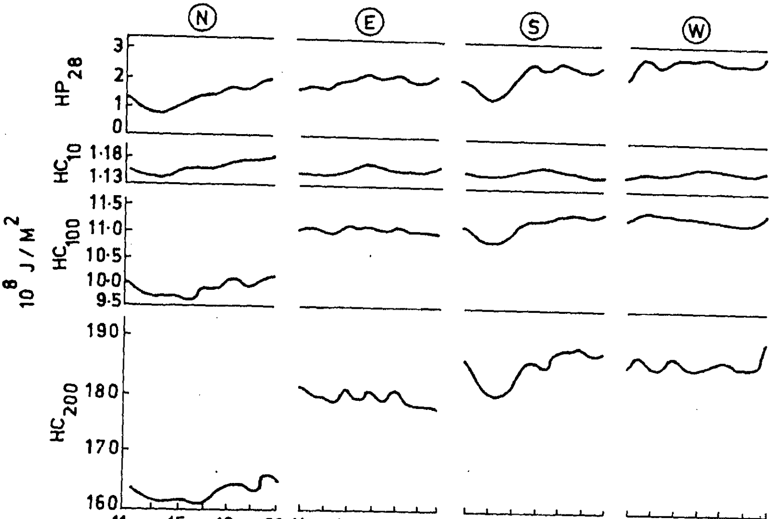

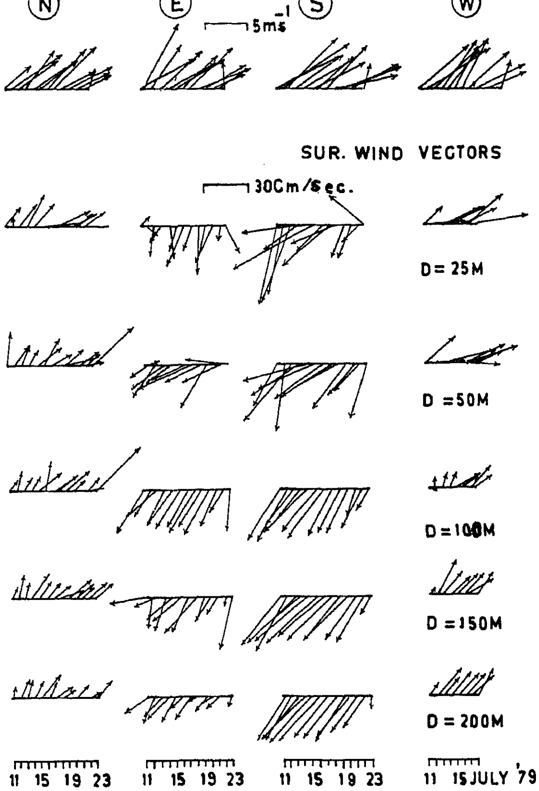

Figure 12. Daily averaged surface wind (m s^{-1}) and sub-surface current (cm s^{-1}) vectors at the stationary locations.

between N and W ($1{\cdot}2 \times 10^8$ J/m^2). In general all the locations registered an increase of about 10^8 J/m^2 over this two-week period. This increase cannot be explained in terms of the surface heat flux alone (figure 4) but the contribution of advective heat is also to be considered. Evaporative heat loss at -250 W/m^2, this area can sustain a meteorological disturbance for a 5-day period. The heat content pattern of the top 10 m layer roughly corresponded with that of SST. However, the heat content of the top 100 m and 200 m layers showed some interesting spatial variations. The lowest value of heat content prominent at N might be attributed to weak downward heat transfer on account of strong stratification caused by freshwater discharge. The temporal trends in heat content indicate increase/decrease of heat probably caused by baroclinic movement of the water in the upper thermocline.

The distribution of daily-averaged current vectors observed at standard depths for all the locations is shown in figure 12. In general the flow was towards northeast at N and W and towards southwest at E and S implying the presence of clockwise circulation in the polygon area. But the surface winds at all the locations were mostly from southwest with an average speed of 7 m/s. The observed circulation does not appear to be driven only by the local wind forcing. The strong spatial differences in the thermo-haline fields and the massive river discharges also appear to contribute to the circulation pattern. In the presence of north-south thermal gradient heat advection may become important in the variability of the heat content of the layer. Warm water advection along the northwest limb and cold water advection along the southeast limb of the polygon is to be anticipated. This should result an increase in the heat content at N and a decrease at S. Observations support the speculation only for N and not for S. The increase of heat content at S may have to be viewed in terms of downward advection of heat probably caused by clockwise eddy circulation. The descent of isotherms (figure 9) and stronger currents throughout the top 200 m water column at S also favour this.

5. Conclusions

(i) As the monsoonal flow was mostly weak during the observational period (11–23 July 1979) fair weather conditions produced a mild heating in the surface layers due to net oceanic heat gain.

(ii) Mixed layer depth was minimum at the northern location compared to other locations due to stronger below layer stratification caused by freshwater river discharge. The day-to-day variability of MLD did not appear to have been controlled by forced and free mixing or Ekman pumping but seemed to have been influenced by stratification caused by the river discharges.

(iii) Analysis of the observed daily averaged current vectors indicated the presence of a clockwise eddy in the polygon area.

(iv) The horizontal thermal gradient in the upper thermocline was stronger in the north-south compared to that of east-west. Advection of heat in the horizontal and also in the vertical seems to have contributed to the observed increase in the heat content at the northern and southern stations respectively.

Acknowledgement

Thanks are due to the Director, India MONEX Management Committee (IMMC), New Delhi, who made available all the data sets utilized in this study.

Appendix

1. The daily averaged vertical component of surface wind stress curl $(\nabla \times \tau)_z$ was computed using the formula

$$(\nabla \times \tau)_z - \frac{\partial \tau_y}{\partial x} - \frac{\partial \tau_y}{\partial y}, \qquad (1)$$

where $\tau = \rho_a C_D U^2$ in the surface wind stress (dynes cm^{-2}), τ_x the zonal component of τ, τ_y the meridional component of τ, ρ_a the density of air (g/cc), C_D the drag coefficient $1{\cdot}20 + 0{\cdot}00025\,U$ (Kondo 1975) and U the daily averaged wind speed (cm s^{-1}).

2. The daily averaged divergence was computed using the formula

$$D = (\partial u/\partial x) + (\partial u/\partial y), \qquad (2)$$

where u and v are the zonal and meridional

$(\mathrm{cm\,s^{-1}})$.

For numerical computation, the finite difference scheme is employed. Thus

$$(\Delta \times \tau)_z = \frac{\Delta \tau_y}{\Delta x} - \frac{\Delta \tau_x}{\Delta y},$$

$$D = \frac{\Delta u}{\Delta x} + \frac{\Delta v}{\Delta y},$$

where Δx and Δy are the geographical distance between stations in the zonal a meridional directions. Since the stations are located in the tropical belt, correction due to convergence of meridians with latitude is ignored.

References

Colborn J G 1975 *The thermal structure of the Indian Ocean. IIOE oceanographic monographs* N (Honolulu: University Press) pp 173

Haney R L, Risch M S and Heise G C 1981 Wind forcing due to synoptic activity over the north Pa Ocean; *Atmos. Ocean* **19** 128–147

Hanstenrath S and Lamb P J 1979 *Climate atlas of the Indian Ocean* (Wisconsin: University Press) V and 2

Kondo J 1975 Air-sea bulk transfer coefficients in diabatic conditions; *Boundary-Layer Meteorol.* **9** 91

Ramesh Babu V and Sastry J S 1981 Heat storage in the Andaman Sea; *Mausam* **32** 145–150

Rao R R and Sanil Kumar K V 1988 Salinity variability in the upper layers of the Arabian Sea and Ba Bengal during summer monsoon experiments (unpublished)

Rao R R, Gopalakrishna V V and Babu S V 1981 A case study on the northern Bay of Bengal sub-sur thermal structure and ocean mixed layer depth in relation to surface energy exchange processes du MONSOON-77; *Mausam* **32** 85–92

Rao R R, Rao D S, Murthy P G K and Joseph M X 1983 A preliminary investigation on the sum monsoonal forcing on the thermal structure of upper Bay of Bengal during MONEX-79; *Mausam* **34** 2 250

Rao R R, Ramam K V S, Rao D S and Joseph M X 1985 Surface heat budget estimates at selected area North Indian Ocean during MONSOON-77; *Mausam* **36** 21–32

Robinson M K, Bauer R A and Schroeder E H 1979 *Atlas of North Atlantic Indian Ocean; monthly m temperature and mean salinities of the surface layer.* Naval Oceanographic Office Reference Publica 18, Dept of the Navy (Washington DC) pp. 213

Swallow J C 1983 Eddies in the Indian Ocean: in *Eddies in marine science* (ed.) A R Robinson (Be Springer-Verlag) p. 200

U S Navy 1976 *Marine climatic atlas of the world.* Vol III Indian Ocean (US Navy) pp. 348

Wyrtki K 1971 *Oceanographic atlas of the International Indian Ocean expedition* (Washington DC) pp.

Distribution of particulate organic carbon in the central Arabian Sea

N B BHOSLE, V M DHOPLE and A B WAGH
National Institute of Oceanography, Dona Paula 403 004, India

MS received 25 September 1987; revised 22 June 1988

Abstract. Particulate organic carbon (POC) of 161 water samples collected from 8 depths (surface to 1000 m) at 21 stations was measured. The POC concentrations ranged from 154 to 554 μg per litre at the surface and decreased in the upper 300 m water column. At greater depths (> 300 m), POC concentrations increased and were similar (145 to 542 $\mu g\, l^{-1}$) to those observed at surface. Deep water POC maximum was embedded within the oxygen minimum layer and was also associated with high phosphate-phosphorus. The POC contents increased, whereas oxygen decreased as the distance away from the shore increased. Phytoplankton biomass was a major source of POC. The observed pattern of POC is discussed with respect to some physicochemical and biological factors.

Keywords. Particulate organic carbon; chlorophyll *a*; dissolved oxygen; Arabian Sea.

1. Introduction

In the open ocean, particulate organic matter (POM) is mostly derived from surface primary production by phytoplankton and consists of autotrophic and heterotrophic organisms and their detritus. Therefore, POM constitutes a major part of the total suspended material in the surface waters of the ocean (Lal 1977). It plays an important role in the vertical transport of organic and inorganic materials and also serves as a sink for some trace components such as heavy metals and organic pollutants (Lal 1977; Sackett 1978; Simpson 1982). POM consists of large particles such as fecal pellets (Urrere and Knauer 1981) and marine snow (Asper 1987), which rapidly settles to the sea floor. Recent studies based on Carbon-14 data suggest that these rapidly sinking particles are not the major source of organic carbon for organisms in deep waters (Pearcy and Stuiver 1983). Such particles are rare in the seawater (McCave 1975), and therefore, poorly collected by conventional water samplers. They are, however, collected more effectively by sediment traps or filtering large volumes of seawater at depths (McCave 1975). The other type comprises slowly sinking small particles (< 50 μm) that dominate the standing stock of POM. These small particles are generally collected using conventional water samplers.

Studies on the distribution and composition of small particles, collected by water sampling bottles, have been carried out in many seas and oceans (Riley 1970; Menzel 1974; Copin-Montegut and Copin-Montegut 1983; Gordon and Cranford 1985). Earlier studies on the distribution of POM showed that it varies little and is refractory below a depth of 300 m (Menzel 1974). Later studies reported that both particulate organic carbon (POC) and nitrogen (PON) varied spatially and temporally (Riley 1970; Gordon *et al* 1979), and decreased with depth (Copin-Montegut and Copin-Montegut 1983; Gordon and Cranford 1985). It was also observed that deep water concentrations

1977; Gordon and Cranford 1985).

Compared to large POC data collected over the years from different oceanic regions, very little information is available on the POC distribution in the waters of the Arabian Sea. Studies made so far are restricted to the euphotic zone (Radhakrishna *et al* 1978a, b; Bhattathiri and Devassy 1979).

Recently, we reported the distribution of POC in the central Bay of Bengal (Nandakumar *et al* 1987). In continuation of our studies on the distribution of POC in the northern Indian Ocean, we present here the POC data from the oceanic waters of the Arabian Sea. The general features emerging from the results are discussed with respect to some physicochemical and biological parameters.

2. Materials and methods

Seawater samples (161) were collected using Niskin water samplers (5–10 l) from eight depths (0 to 1000 m) at 21 stations during 13 B cruise of *ORV Sagar Kanya* in the central Arabian Sea from 14 February to 14 March 1985 (figure 1). Samples were immediately filtered through pre-combusted (450°C 3 h) 47 mm GF/C (1·0 μm pore size) glass filters. Filters were stored at −20°C until the analysis was completed. Particulate matter left on the filters was analysed for POC and chlorophyll *a* (Chl *a*). As the filters were not preweighed, suspended matter could not be determined on these samples.

POC was analysed spectrophotometrically after wet oxidation of carbon by acid dichromate (Parsons *et al* 1984). Chl *a* was estimated spectrofluorometrically after extracting the filters with 90% acetone (Boto and Bunt 1978). Dissolved oxygen was determined by Winkler method (Carpenter 1965). Inorganic phosphate-phosphorus was analysed on a six-channel autoanalyser (Skalar) on board the vessel. The precision of these methods was better than ± 6%.

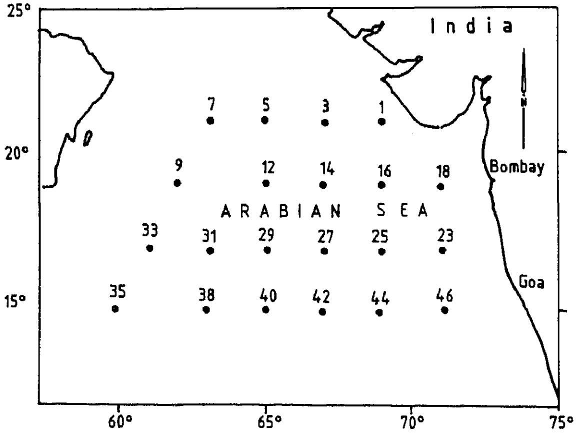

Figure 1. Location of sampling sites in the Arabian Sea.

3. Results and discussion

Vertical profiles of POC, dissolved oxygen and inorganic phosphate-phosphorus are shown in figures 2 to 5. These data are also given in appendix 1. The range of minimum and maximum concentrations of these parameters for all the stations along with standard deviations and coefficients of variation are given in tables 1–3.

Surface POC concentrations ranged from 154–554 $\mu g\, l^{-1}$ ($\bar{x} = 368 \pm 125\, \mu g\, l^{-1}$; $n = 21$). These values are in the same range as those reported earlier from the surface waters of the Arabian Sea (Radhakrishna *et al* 1978a, b; Bhattathiri and Devassy 1979) as well as from other areas (Romankevich 1984). With some exceptions the concentrations of POC generally decreased with increasing depth in the upper 300 m water column (figures 2 to 5). This probably suggests loss of carbon during descent due

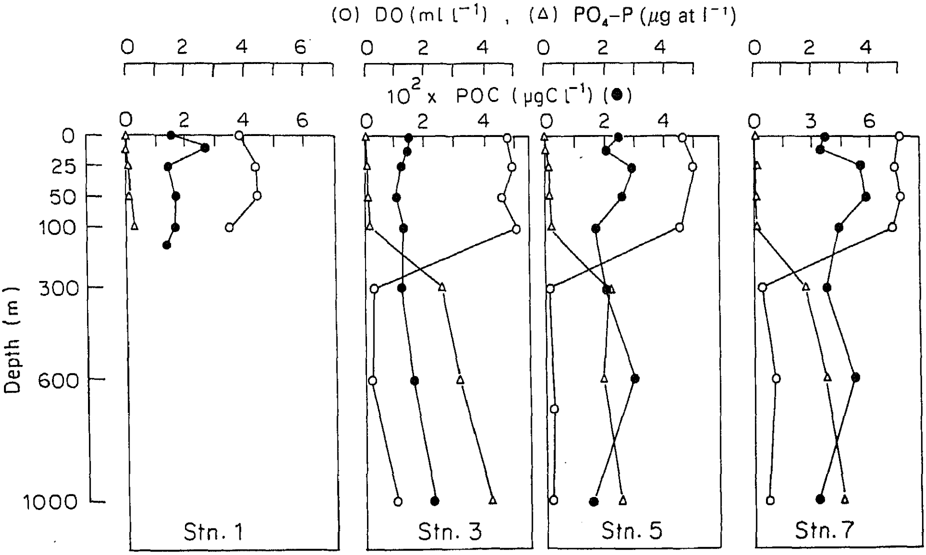

2

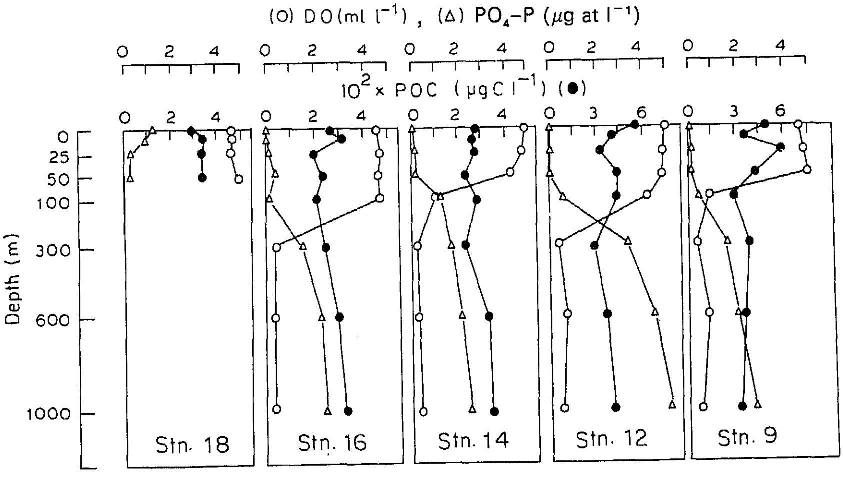

3

Figures 2–3. For caption, see next page.

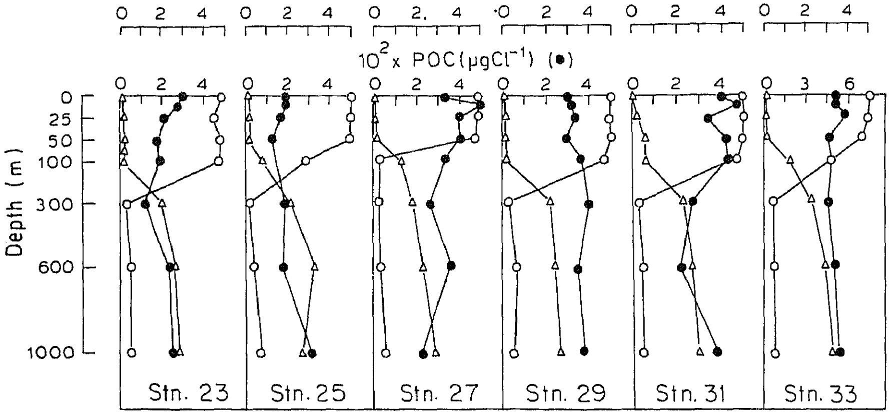

4

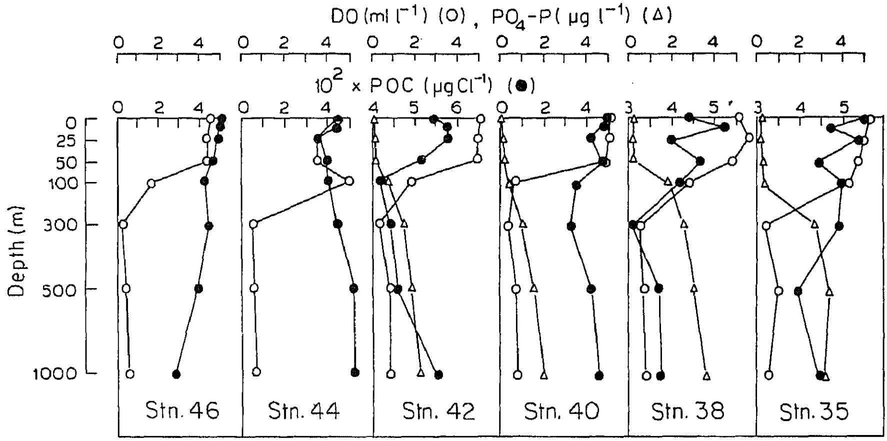

5

Figures 2–5. Concentration of POC, dissolved oxygen (DO) and inorganic phosphate-phosphorus (PO_4) vs depth profiles in the Arabian Sea.

Table 1. Distribution of particulate organic carbon (μgC l^{-1}) at different stations in the Arabian Sea.

Depth (m)	Range	Mean	SD	CV %	*n*
0	155–554	368	125	33·96	21
10	149–568	373	118	31·63	21
25	105–581	359	143	39·83	21
50	103–581	350	132	37·71	21
100	124–490	323	116	35·91	20
300	109–481	307	109	35·50	19
600	155–510	343	99	28·86	19
1000	145–542	340	105	30·88	19

SD, standard deviation; CV, coefficient of variation; *n*, number of samples.

Table 2. Distribution of dissolved oxygen (ml l^{-1}) at different stations in the Arabian Sea.

Depth (m)	Range	Mean	SD	CV %	*n*
0	3·99–5·22	4·81	0·27	5·61	21
10	—	—	—	—	—
25	4·30–5·50	4·85	0·27	5·56	21
50	4·31–5·10	4·72	0·22	4·66	21
100	0·20–5·07	3·25	1·62	49·84	20
300	0·07–0·36	0·23	0·09	39·31	19
600	0·19–0·87	0·44	0·20	45·45	19
1000	0·12–1·06	0·43	0·19	44·18	19

SD, standard deviation; CV, coefficient of variation; *n*, number of samples;—, no data.

Table 3. Distribution of inorganic phosphate-phosphorus (μg at l^{-1}) at different stations in the Arabian Sea.

Depth (m)	Range	Mean	SD	CV %	*n*
0	tra–1·30	0·12	0·28	233·30	19
10	—	—	—	—	—
25	tra–0·38	0·10	0·12	120·00	19
50	tra–0·57	0·15	0·16	106·60	19
100	tra–1·74	0·56	0·47	83·92	18
300	0·93–3·30	2·00	0·54	27·00	17
600	1·39–4·40	2·56	0·68	26·56	17
1000	1·90–5·00	2·90	0·74	25·51	17

SD, standard deviation; CV, coefficient of variation; *n*, number of samples; —, no data; tra, traces below detection limit.

to remineralization, ingestion and assimilation by mid-water organisms. Throughout the water column, POC varied by about a factor of 5 (table 1). This probably indicates uniform supply of organic matter as a result of diatom bloom during the period of sampling. Diatom blooms are generally observed in February/March in the Arabian Sea (Kelkar, personal communication).

At most of the stations, after an initial decrease in the upper 300 m water column, the POC concentrations generally increased, especially from 600 to 1000 m depth (figures 2 to 5), and were more or less similar to those observed at the surface (table 1). These deep water POC concentrations observed for the Arabian Sea are higher than those reported from other areas (Wangersky 1976; Copin-Montegut and Copin-Montegut 1983; Romankevich 1984; Gordon and Cranford 1985). Nevertheless, these values are in the same range as those reported recently for the Bay of Bengal (Nandakumar *et al* 1987). Higher concentrations of POC observed here are probably due to higher surface primary production in the area (Qasim 1977).

concentrations decreased very little and are homogeneous below a depth of 300 m. In contrast to this, Gordon and Cranford (1985) suggested that POC decreased with depth. The present result disproves both and implies that POC distribution in Arabian Sea is more complicated than that reported from other regions (Menzel 1974; Wangersky 1976; Copin-Montegut and Copin-Montegut 1983; Gordon and Cranford 1985). Probably some physicochemical and biological conditions prevailing during sampling in the Arabian Sea play an important role in influencing the distribution of POC in these waters.

Sinking rates of organic detrital particles depend on the particle density and viscosity of fluid medium. Rapid changes in temperature and salinity are reported from Arabian Sea waters (Sengupta and Naqvi 1984) which may alter the density and decrease the sinking rate of organic detritus particles causing probably an accumulation (Karl *et al* 1976). However, in that case we would expect the accumulation of POC in the upper 100 to 200 m water column where density gradients were maximum (Sengupta and Naqvi 1984).

A second mechanism that might explain the observed pattern of POC distribution involves a relaxation of upwelling followed by subsequent injection of surface-derived particulate matter into the mesopelagic zone. Garfield *et al* (1979) proposed such a model to account for subsurface peaks in suspended protein at 200 to 250 m depth. In our present study we were unable to resolve any subsurface peaks in POC; thus, it seems unlikely that we have observed temporally uncoupled patches of organic matter originating at the surface.

The secondary peak observed for POC (figures 2 to 5) might also be due to chemolithotrophic microbial growth and carbon production at these depths (Karl and Knauer 1984). However, such a mechanism has been contested by others (Betzer *et al* 1984).

Migrating zooplankton populations have been implicated in the removal and transfer of organic matter. It was observed that zooplankton abundance is larger in the top 200 m than at greater depths (Paulinose and Arvindakshan 1977). There was no significant difference in the zooplankton biomass between the hauls taken from 200 to 0 m and 900 to 0 m implying that the organisms are largely confined to upper 200 m and tend to avoid the oxygen-deficient layer below 300 m. This pattern of zooplankton distribution is very well reflected in the POC distribution. Thus, it is likely that the secondary POC peak observed at 600 to 1000 m depth is due to dearth of zooplankton at these depths.

Alternatively, this secondary POC peak was due to lateral transport of organic matter from the productive shelf. In order to check this possibility we have integrated the POC values in the depth range of 0 to 100 m, 300 to 600 m and 1000 m and plotted them against distance away from the shore (figure 6). A simple regression analysis was also used to assess the significance of this relationship. Throughout the water column, POC concentrations increased as the distance away from the shore increased. A positive correlation coefficient was observed which was significant ($P \leqslant 0{\cdot}001$). However, the r values were slightly low. This positive relationship between POC and the distance away from the shore suggests lateral transport of POC from the productive shelf waters and might be the possible process for the accumulation of POC in deep waters.

Elevated POC values in low oxygenated waters could also be the result of conversion of dissolved organic carbon to POC. In any case a secondary POC maximum exists

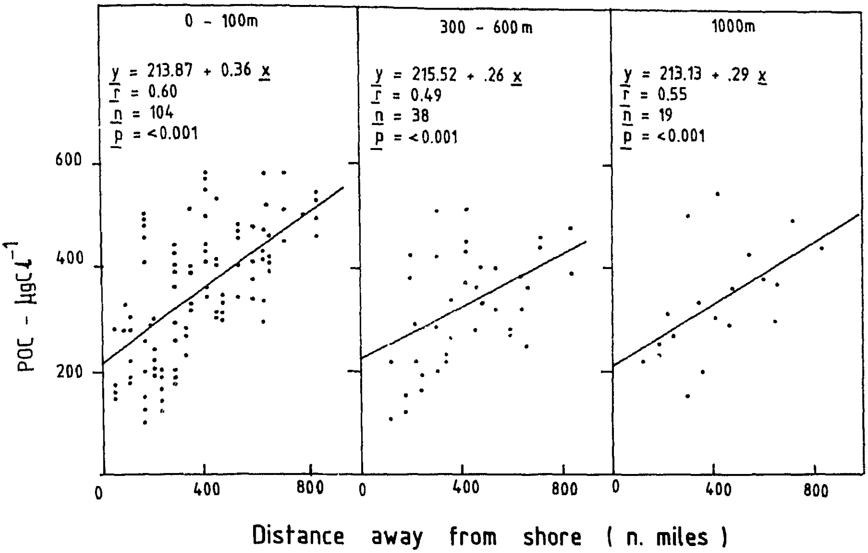

Figure 6. Relationship between POC and distance away from shore.

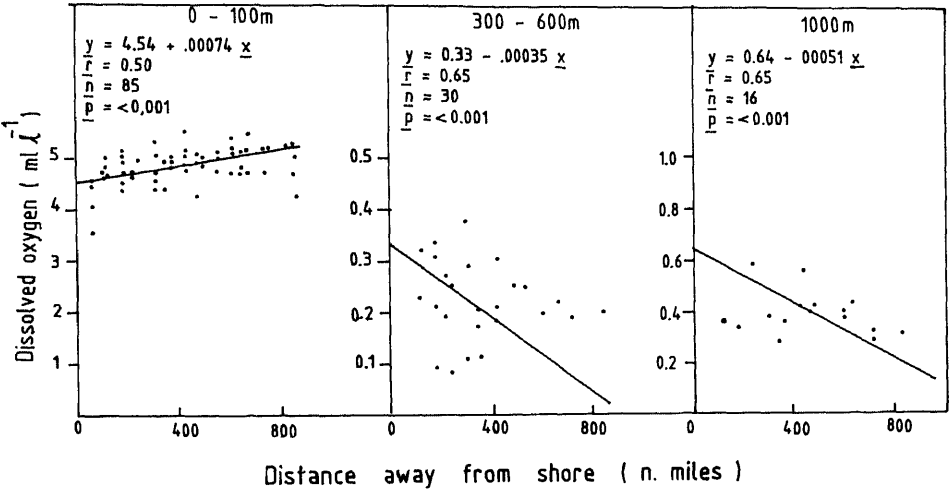

Figure 7. Relationship between dissolved oxygen and distance away from shore.

because the supply of POC to these depths exceeds the loss, because of either increased supply or decreased loss.

The *in situ* concentration of dissolved oxygen represent a balance between vertical and horizontal diffusion and advection and biological utilization (Riley 1951). Distribution of dissolved oxygen in the study area is shown in figures 2 to 5. A mean decreased as the distance away from the shore increased (figure 7). An oxygen minimum layer extending from 300 to 1000 m was very conspicuous (figures 2 to 5, table 2). A deep water POC maximum was found embedded within this layer. Once the organic matter gets accumulated as mentioned above, it is oxidised, thus depleting the oxygen concentration. This is evident from the inverse distribution pattern of dissolved oxygen and POC (figures 2 to 5), probably suggesting biological utilization.

At 300 m, however, this is not the case as low oxygen concentration is generally accompanied by a minimum of POC content at most of the stations (figures 2–5). This can probably be explained as follows. The high salinity water in the Persian Gulf characterized by σt values of 26·6 flows throughout the Hormuz Strait and the Gulf of Oman into the Arabian Sea and maintains its density level at about 300 m depth (Sengupta and Naqvi 1984). More or less in the same depth range the intensive zone of denitrification has been reported (Sengupta and Naqvi 1984). As the oxygen concentration is very low, nitrate ions are the next abundant source of free energy for the oxidation of organic matter (Richards 1965). Probably this is what is happening at this depth. Thus, low POC concentrations observed at 300 m and subsequent nitrite maximum at more or less same depth (Sengupta and Naqvi 1984) suggests the possibility that low POC concentration at 300 m is the result of POC oxidation using nitrate as the electron acceptor.

Below this depth (> 300 m), the dissolved oxygen is minimum and POC maximum and inorganic phosphate-phosphorus also start increasing (figures 2 to 5). Phosphate-phosphorus was low in the surface waters (0·12 μg at l^{-1}) and increased rapidly with depth to a maximum of 2·90 μg at l^{-1} (table 3). The microbial decomposition of accumulated organic matter proceeds with utilization of oxygen and release of phosphate-phosphorus (figures 2 to 5). It is reported that phosphate-phosphorus maximum usually lies close to oxygen minimum and CO_2 maximum (Riley and Chester 1971). In the Arabian Sea CO_2 maximum lies in the O_2 minimum zone, although the phosphate-phosphorus maximum is slightly below O_2 minimum zone (Sengupta and Naqvi 1984).

In oceanic waters, POM is mostly derived from the surface primary production by phytoplankton and consists of autotrophic and heterotrophic organisms and their detritus. Chl *a* has been used as an indicator of phytoplankton biomass. Detailed distribution of Chl *a* will be dealt seperately (Pant, personal communication). Here, these data are only used to assess the contribution of Chl *a* carbon to POC. A regression analysis was used to find out the relationship between these two parameters. A significant relationship between these two parameters ($P \leqslant 0{\cdot}001$) was found ($r = 0{\cdot}62$; $n = 82$; $Y = 223{\cdot}82 + 15{\cdot}28\,X$), indicating that phytoplankton carbon comprised a fairly constant percentage of total carbon.

Acknowledgements

The authors thank Dr B N Desai for constant encouragement. We also thank Dr A Pant for providing us unpublished Chl *a* data and to Shri N S Parabhu for his help on

Appendix 1. Concentrations of POC, DO and $PO_4 - P$ at various stations in the Arabian Sea.

Station	Depth (m)	POC $\mu gC\ l^{-1}$	DO $ml\ l^{-1}$	$PO_4 - P$ μg at l^{-1}
1	0	154·94	3·99	0·05
	10	276·46	4·02	0·01
	25	148·86	4·36	0·01
	50	173·16	4·38	tra
	100	164·05	3·56	0·32
	150	142·94	—	—
3	0	154·94	4·71	0·12
	10	148·86	—	—
	25	115·44	4·97	tra
	50	103·29	4·64	0·16
	100	124·56	5·07	0·22
	300	124·30	0·31	2·63
	600	154·94	0·21	3·12
	1000	227·85	1·06	4·17
5	0	261·27	4·71	tra
	10	206·58	—	tra
	25	288·61	5·10	0·21
	50	264·34	4·71	0·25
	100	174·16	4·50	0·20
	300	197·47	0·11	1·95
	600	285·57	0·22	2·07
	1000	145·82	0·12	2·49
7	0	364·55	4·98	tra
	10	336·20	—	—
	25	550·19	4·78	tra
	50	581·27	5·10	tra
	100	441·52	4·77	0·07
	300	372·41	0·18	1·97
	600	510·38	0·62	2·45
	1000	303·80	0·42	2·99
9	0	477·97	4·60	0·08
	10	342·28	—	—
	25	581·27	4·82	0·14
	50	421·27	5·03	0·16
	100	293·67	0·80	0·45
	300	376·71	0·34	1·60
	600	338·23	0·80	2·33
	1000	303·80	0·45	2·85
12	0	534·69	5·09	tra
	10	405·07	—	—
	25	311·90	4·94	tra
	50	423·29	4·92	tra
	100	415·19	4·25	0·50
	300	275·45	0·36	3·30
	600	358·48	0·65	4·40
	1000	394·67	0·40	5·00

(Appendix 1. Continued)

14	0	281·02	4·95	0·05
	10	265·83	—	—
	25	273·42	4·89	0·05
	50	232·41	4·37	0·36
	100	279·50	1·06	1·15
	300	227·85	0·17	1·80
	600	318·99	0·20	2.18
	1000	332·66	0·28	2·54
16	0	264·31	4.66	0·01
	10	305·32	—	—
	25	189·88	4·74	tra
	50	235·45	4·66	0·40
	100	200·51	4·71	tra
	300	240·00	0·27	1·50
	600	293·17	0·19	2·10
	1000	308·36	0·23	2·30
18	0	281·02	4·60	1·30
	10	329·62	4·65	0·92
	25	325·07	4·56	0·34
	50	329·62	4·45	0·30
23	0	303·80	4·76	0·02
	10	282·53	—	—
	25	215·70	4·50	tra
	50	182·28	4·77	tra
	100	192·91	4·66	0·10
	300	109·37	0·23	1·90
	600	215·70	0·41	2·40
	1000	233·29	0·35	2·60
25	0	191·40	4·89	0·10
	10	197·47	—	—
	25	159·50	4·90	0·20
	50	123·04	4·87	tra
	100	139·75	2·82	0·70
	300	185·32	0·07	2·00
	600	159·50	0·25	3·20
	1000	273·42	0·58	2·70
27	0	320·51	4·88	tra
	10	507·35	—	—
	25	391·90	4·97	tra
	50	399·50	4·76	0·10
	100	326·59	0·20	1·20
	300	258·23	0·11	1·70
	600	343·29	0·20	2·20
	1000	208·10	0·35	2·80
29	0	297·72	4·99	0·02
	10	306·84	—	—
	25	335·70	4·98	0·27
	50	290·13	5·01	0·10
	100	349·37	4·76	0·19
	300	397·98	0·25	2·11
	600	331·14	0·51	2·40
	1000	355·45	0·42	2·50

(Appendix 1. Continued)

31	0	389·31	5·10	tra
	10	478·48	—	—
	25	343·29	5·09	0·38
	50	410·13	5·00	0·57
	100	422·28	4·69	0·60
	300	282·53	0·20	2·36
	600	265·83	0·42	2·77
	1000	376·71	0·39	2·97
33	0	508·86	5·10	0·28
	10	508·86	—	—
	25	580·26	5·08	0·18
	50	452·66	4·71	0·26
	100	476·97	3·31	1·35
	300	443·55	0·30	2·30
	600	461·71	0·47	2·93
	1000	492·16	0·33	3·15
35	0	554·43	5·22	0·31
	10	464·81	—	—
	25	528·61	4·97	0·15
	50	461·78	4·7[illegible]	0·20
	100	490·64	4·22	0·32
	300	481·52	0·20	2·67
	600	385·83	0·87	3·22
	1000	435·95	0·33	2·92
38	0	432·92	5·01	0·06
	10	519·50	—	—
	25	393·42	5·50	0·10
	50	461·78	4·77	0·13
	100	410·13	2·72	1·74
	300	252·15	0·36	2·39
	600	363·04	0·52	2·93
	1000	366·08	0·60	3·45
40	0	481·52	4·97	tra
	10	472·40	—	—
	25	402·53	5·00	tra
	50	464·81	4·72	tra
	100	340·26	0·65	0·52
	300	320·51	0·34	0·93
	600	401·02	0·69	1·39
	1000	431·40	0·60	1·95
42	0	531·65	5·00	tra
	10	568·10	—	—
	25	569·62	4·98	tra
	50	504·31	4·44	—
	100	397·98	4·95	—
	300	422·28	0·29	—
	600	508·86	0·38	—
	1000	499·75	0·38	—
46	0	501·27	4·50	—
	10	490·64	—	—
	25	478·48	4·30	—
	50	458·74	4·31	—
	100	411·65	1·53	—

Asper V L 1987 Measuring the flux and sinking speed of marine snow aggregates; *Deep Sea Res.* **34** 1–17

Betzer P R, Showers W J, Laws E A, Winn C D, DiTullio G R and Kroopnick P M 1984 Primary productivity and particulate fluxes on a transect of the equator at 150° W in the pacific ocean; *Deep Sea Res.* **31** 1–11

Bhattathiri P M A and Devassy V P 1979 Biological characteristics of the Laccadive Sea (Lakshadweep); *Indian J. Mar. Sci.* **8** 222–226

Boto K G and Bunt J S 1978 Selective excitation fluorometry for the determination of chlorophylls and pheophytins; *Anal. Chem.* **50** 392–395

Carpenter J H 1965 The accuracy of the Winkler method for dissolved oxygen; *Limmnol. Oceanogr.* **10** 135–140

Copin-Montegut C and Copin-Montegut G 1983 Stoichiometry of the carbon, nitrogen and phosphorus in marine particulate matter; *Deep Sea Res.* **30** 31–46

Garfield P C, Packard T T and Codispati L A 1979 Particulate protein in the Peru upwelling system; *Deep Sea Res.* **26/6A** 623–629

Gordon D C 1977 Variability of particulate organic carbon and nitrogen along the Halifax-Bermuda section; *Deep Sea Res.* **24** 257–270

Gordon D C and Cranford P J 1985 Detailed distribution of dissolved and particulate organic matter in the Arctic Ocean and comparison with other oceanic regions; *Deep Sea Res.* **32** 1221–1232

Gordon D C, Wangersky P J and Sheldon R W 1979 Detailed observations on the distribution and composition of particulate organic material at two stations in the Sargasso Sea; *Deep Sea Res.* **26** 1083–1092

Karl D M and Knauer G A 1984 Vertical distribution, transport and exchange of carbon in the northeast Pacific Ocean: Evidence for multiple zones of biological activity; *Deep Sea Res.* **31** 221–243

Karl D M, LaRock P A, Morse J W and Sturges W 1976 Adenosine triphosphate in the north Atlantic Ocean and its relationship to the oxygen minimum; *Deep Sea Res.* **23** 81–88

Lal D 1977 The oceanic microcosm of particles; *Science* **198** 997–1008

McCave I N 1975 Vertical flux of particles in the ocean; *Deep Sea Res.* **22** 491–502

Menzel D W 1974 in *The sea* (ed.) E D Goldberg (New York: Interscience) pp. 659

Nandakumar K, Venkat K and Bhosle N B 1987 Distribution of particulate organic carbon in the central Bay of Bengal; *Proc. Indian Acad. Sci.* (*Earth Planet Sci.*) **96** 189–193

Parsons T R, Matai Y and Lalli C M 1984 *A manual of chemical and biological methods of sea water analysis* (Oxford: Pergamon) pp. 63–104

Paulinose V T and Arvindakshan P N 1977 Zooplankton biomass, abundance and distribution in the north and northeastern Arabian Sea; *Proc. Symp. warm water zooplankton Specl. Publ.* Natl. Inst. Oceanogr. Goa, pp. 132–136

Pearcy W G and Stuiver M 1983 Vertical transport of carbon-14 into deep sea food webs; *Deep Sea Res.* **30** 427–440

Qasim S Z 1977 Biological productivity of the Indian Ocean; *Indian J. Mar. Sci.* **6** 122–137

Radhakrishna K, Devassy V P, Bhattathiri P M A and Bhargava R M S 1978a Primary productivity in the northeastern Arabian Sea; *Indian J. Mar. Sci.* **7** 137–139

Radhakrishna K, Devassy V P, Bhargava R M S and Bhattathiri P M A 1978b Primary production in the northern Arabian Sea; *Indian J. Mar. Sci.* **7** 271–275

Richards F A 1965 Anoxic basins and fjords, in *Chemical oceanography* (eds) J P Riley and G Skirrow (London: Academic Press) pp. 611–645

Riley G A 1951 Oxygen, phosphate and nitrate in the Atlantic Ocean; *Bull. Bingham Oceanogr. Collect. Yale University* 13 1–126

Riley G A 1970 Particulate organic matter in sea water; *Adv. Mar. Biol.* **8** 1–118

Riley G P and Chester R 1971 *Introduction to marine chemistry* (London: Academic Press) pp. 465

Romankevich E A 1984 *Geochemistry of organic matter in the ocean* (Berlin: Springer-Verlag) pp. 4–273

Sackett W M 1978 Suspended matter in seawater, in *Chemical oceanography* (eds.) J P Riley and R Chester (London: Academic Press) pp. 127–172

Sengupta R and Naqvi S W A 1984 Chemical oceanography of the Indian Ocean, north of the equator—a review; *Deep Sea Res.* **31** 671–706

Simpson W R 1982 Particulate matter in the ocean—sampling methods, concentrations, size distribution and particle dynamics; *Oceanogr. Mar. Biol. Annu. Rev.* **20** 119–172

Urrere M A and Knauer G A 1981 Zooplankton fecal pellet fluxes and vertical transport of particulate organic material in the pelagic environment; *J. Plankton Res.* **3** 369–387

Wangersky P J 1976 Particulate organic carbon in the Atlantic and Pacific Oceans; *Deep Sea Res.* **23** 457–465

Is there an attractor for the Indian summer monsoon?

V SATYAN
Physical Research Laboratory, Navrangpura, Ahmedabad 380 009, India

MS received 5 October 1987; revised 21 March 1988

Abstract. Aperiodicity in the time series of Indian summer rainfall for 116 years is analysed using the phase space approach. The question whether a low-dimensional strange attractor is associated with the chaotic behaviour of the monsoon system is investigated. It is found that a strange attractor of dimensionality around 5·1 exists and the system has 12 relevant degrees of freedom.

Keywords. Monsoon climate and variability; deterministic chaos; strange attractors; phase space analysis.

1. Introduction

The seasonal event of southwest summer monsoon over the Indian region is well known for its variability on a wide range of time scales, especially its large variability on the interannual time scale. Conventional periodicity analysis (Mooley and Parthasarathy 1984) of time series of monsoon rainfall during the last 100 years or so reveals two cycles (2·8-year and 14-year) but these are seen only during the last 30 years of the data record. Thus, there appears to be a large aperiodic component in monsoon fluctuations. It is important to know whether this non-periodic part is due to the intrinsic variability of the system (Lorenz 1984). We try to understand whether there is a strange attractor underlying the evolution of the monsoon and determine its topological characteristics. To examine this question, we have analysed a long-term monsoon rainfall record. This is the all-India summer monsoon rainfall for the period 1871–1986 (Mooley and Parthasarathy 1984). We have used the recently developed techniques in nonlinear dynamics (Packard *et al* 1980; Grassberger and Procaccia 1983). More precisely, we obtain the dimensionality d of the attractor for the monsoon system, and a quantitative estimate of the minimum number of variables n_c necessary to characterize a long-term monsoon rainfall record, and the long-term behaviour of the monsoon system that it represents.

2. Theory

For a multivariable nonlinear system such as the monsoon, an extremely useful approach is the description of its dynamics in phase space. Recent advances (Packard *et al* 1980; Grassberger and Procaccia 1983) in nonlinear dynamics enable us to obtain information about the behaviour of the system in phase space without explicit knowledge of the dynamical equations for the system, or their actual solutions. If one knows the behaviour of the system in phase space, it may be possible to model its nonlinear dynamics by an iterative map. Recent studies using the phase space approach have shown that strange attractors underlie the dynamics of global paleoclimate (Nicolis and Nicolis 1984), the southern oscillation (Hense 1987) and some mid-latitude systems (Fraedrich 1986).

For dissipative dynamical systems it is clear that there should be an attractor—that is a region in phase space, where the system spends all its time after the transient phenomena have died down. It is well-known that the attractor can be a fixed point (static situation), a limit cycle (periodic motion) or a strange attractor (chaotic motion). In terms of topological properties the attractors are characterized by their dimensionality. The dimensionality d is zero for a fixed point, $d = 1$ for a limit cycle while a strange attractor has non-integer dimensionality.

The crucial point for our purposes is that the dimensionality of the attractor as well as the long term phase space description of the multivariable system, can be deduced by analysing a time series in one variable. We summarize here the algorithm for the calculation of dimensionality proposed by Grassberger and Procaccia (1983).

Consider a time series in which some variable is measured as a function of time for a long period. For the summer monsoon system one such variable is a long record of seasonal rainfall averaged over the monsoon region. From such a time series one samples n points separated by a fixed time interval τ so that one obtains points $X(t)$, $X(t+\tau)$, $X(t+2\tau)\cdots X(t+(n-1)\tau)$. By an appropriate choice of τ, these points are expected to be linearly independent. We denote the n points by a vector $\mathbf{X}(t)$. Let us next consider M different instants of time t_i, $i = 1, M$ and for each t_i we obtain from the time series the vector $\mathbf{X}_i = \mathbf{X}(t_i)\ i = 1 \cdots \mathrm{M}$. From these M vectors one calculates a correlation function of the attractor

$$C(r) = \frac{1}{M^2}\sum_{\substack{i,j=1\\ i\neq j}}^{M} \Theta(r - |\mathbf{X}_i - \mathbf{X}_j|), \tag{1}$$

where $|\mathbf{X}_i - \mathbf{X}_j|$ is the distance between the two points i and j in the n dimensional vector space and r is an arbitrary distance parameter. It should be noted that the points we have chosen on the attractor are random in time. However, they are spatially correlated as they all lie on the attractor. Thus $C(r)$ is a global measure of this spatial correlation. Θ is the Heaviside function, $\Theta(x) = 1$ if $x > 0$, $\Theta(x) = 0$ if $x < 0$. Thus $C(r)$ simply counts the number of pairs of points whose distance $|\mathbf{X}_i - \mathbf{X}_j|$ is less than r. It has been shown (Grassberger and Procaccia 1983) that the dimensionality d of the attractor is related to $C(r)$ by the relation

$$C(r) = r^d \text{ (for small } r\text{)}. \tag{2}$$

The basic idea here is that the number of points (and hence $C(r)$) of a d-dimensional attractor inside a n-dimensional ball of radius r ($d \leqslant n$) scales as r^d. Thus, the slope of the curve log $C(r)$ plotted against log r gives the dimensionality d. In practice, one evaluates d for different number n of components for each vector $\mathbf{X}_i$. Then if the dynamics is governed by a low-dimensional attractor the slope d saturates beyond a critical value n_c. n_c then gives the minimum number of dynamic variables that would be necessary to characterize the motion in phase space. It should also be pointed out that if one analyses a series with "pure noise" then there would be no saturation in slope beyond reasonable values of n_c

We closely follow these ideas and obtain d and n_c from a time series of monsoon rainfall. For time series we have taken the 116-year record (Mooley and Parthasarathy 1984) of the all-India summer monsoon (June to September) rainfall for the period 1871 to 1986. We chose a range of values of the shift parameter τ and carried out the following computations for each τ. The correlation function for the time series was computed according to (1) beginning in a two-dimensional phase space (i.e. $n = 2$) and for a range of values of the prescribed distance r. This procedure was repeated for increasing values of the embedding phase space dimension ($n = 2$ to 20). Figure 1 shows the variation of $\ln(N(r))$ with variation in $\ln(r)$ in each phase space. Here we show the results for $n = 2$ to 10 only. For convenience we have displayed the plots of $\ln(N(r))$ vs $\ln(r)$ instead of $\ln(C(r))$ vs $\ln(r)$, where $N(r)$ is M^2 times $C(r)$. Next, for each curve with a particular value of n, we determine its slope in the linear region of the curve using a regression procedure. This slope gives the dimensionality of the attractor according to (2). The variation of this dimensionality as n is varied is shown in figure 2. The above results are not sensitive to the choice of τ. We see that the dimensionality saturates to a limiting value. This saturation is seen to be around 5·1 which implies that the dynamics represented by the rainfall time series can be characterized by a strange attractor having a fractal dimensionality 5·1. The fractal dimensionality points to the fact that the observed aperiodicity comes essentially from the intrinsic variability of the system. Furthermore we see that the critical value of the embedding phase dimension n beyond which d saturates is around 12. This implies that at least twelve collective variables would be involved in a dynamical description of the monsoon system whose behaviour is represented by the rainfall time series.

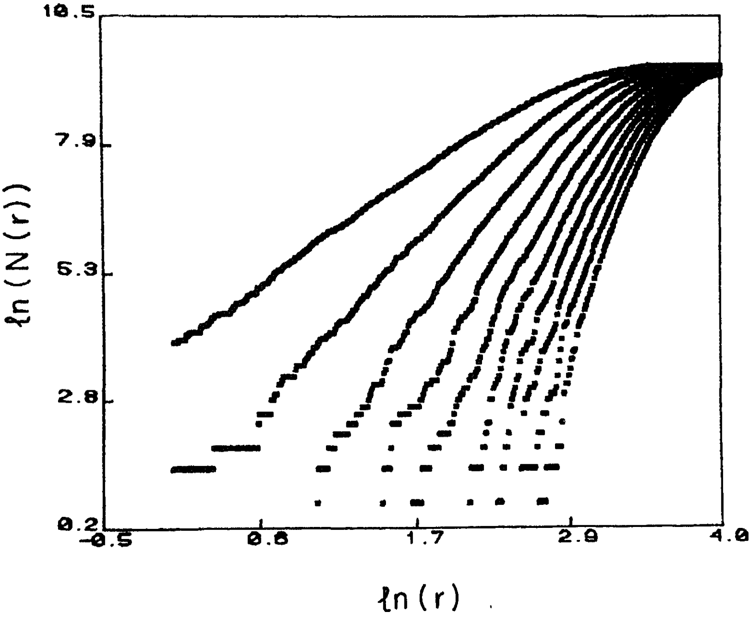

Figure 1. Dependence of $\ln(N(r))$ on $\ln(r)$ for embedding dimensions 2–10. Curves on the extreme left and extreme right correspond to dimensions 2 and 10 respectively.

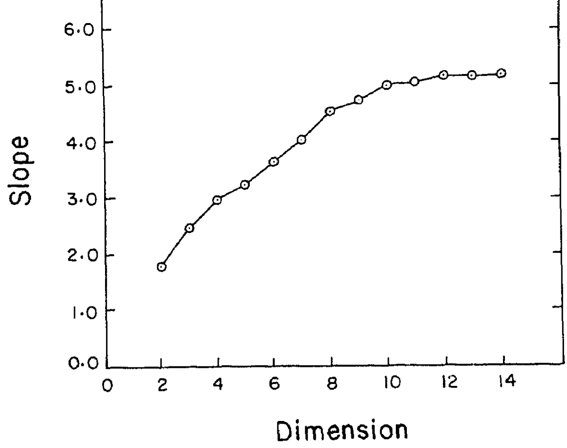

Figure 2. Slope of ln$(N(r))$ vs ln(r) curves for embedding dimensions 2–14.

4. Conclusions

We have investigated the question whether there is an attractor underlying the evolution of monsoon climate over the last 116 years. For this purpose we have analysed the corresponding monsoon rainfall time series in the system phase space and evaluated a correlation function for the attractor. We find that a strange attractor of dimensionality around 5·1 exists and the system has 12 relevant degrees of freedom.

Acknowledgement

The author is thankful to Dr B Parthasarathy for providing the rainfall data for the period 1871–1986.

References

Fraedrich K 1986 Estimating the dimensions of weather and climate attractors; *J. Atmos. Sci.* **43** 419–432
Grassberger P and Procaccia.I 1983 Characterization of strange attractors; *Phys. Rev. Lett.* **50** 346–349
Hense A 1987 On the possible existence of a strange attractor for the southern oscillation; *Beitr. Phys. Atmos.* **60** 34–47
Lorenz E N 1984 Irregularity—a fundamental property of the atmosphere; *Tellus* **36A** 98–110
Mooley D A and Parthasarathy B 1984 Fluctuations in all-India summer monsoon rainfall during 1871–1978; *Climatic Change* **6** 287–301
Nicolis C and Nicolis G 1984 Is there a climatic attractor? *Nature (London)* **311** 529–532
Packard N H, Crutchfield J P, Farmer J D and Shaw R S 1980 Geometry from a time series; *Phys. Rev. Lett.* **45** 712–716

Seasonal cycle of surface circulation in the coastal North Indian Ocean

S R SHETYE and S SATHEESH CHANDRA SHENOI
National Institute of Oceanography, Dona Paula 403 004, India

MS received 13 November 1987; revised 23 May 1988

Abstract. Monthly-mean winds and currents have been used to identify the driving mechanisms of seasonal coastal circulation in the North Indian Ocean. The main conclusions are: (i) the surface circulation off Arabia is typical of a wind-driven system with similar patterns of longshore current and wind stress; (ii) circulation off the west coast of India is consistent with the dynamics of a wind-driven eastern boundary current only during the southwest monsoon. During the northeast monsoon it is possible that the influence of the interior flow is important. (iii) There are at least three mechanisms that influence the surface circulation off the east coast of India: wind-stress, influence of fresh-water run off and contribution of the interior flow. It is difficult at present to assess the relative importance of these three processes.

Keywords. Coastal currents; wind stress; Sverdrup transport; Munk layer; monsoons; North Indian Ocean.

1. Introduction

The North Indian Ocean is one of the few oceanic regimes that come under the influence of the annual cycle of the monsoonal winds. Under its influence, the coastal circulation in the region exhibits a well-marked seasonal cycle. This special feature has prompted study of the circulation off Somalia, where the annual cycle is the most pronounced (Schott 1983). Little is, however, known about the nature of the coastal circulation over the rest of the North Indian Ocean and still lesser about the causes behind it. In this note we examine this problem by looking at two sets of readily available maritime data: monthly-mean winds and monthly-mean surface currents. The latter are based on ship-drift values.

Our approach is similar to that used by Wooster *et al* (1976) to study the coastal circulation along the east coast of the N. Atlantic. Since the longshore component of the local wind stress (τ_l) has been identified as one of the principal forcing function for the longshore coastal currents (V_l), we begin by comparing the annual cycles of τ_l and V_l. In the area where the two match, we conclude that the local winds dominate the surface coastal circulation. If they do not, we examine possible alternatives. As the circulation off Somalia has been a topic of considerable attention, this coast has not been included in the discussion. The rest of the coastline has been divided into three subareas—the Arabian Coast, the West Coast and the East Coast of India.

2. Seasonal variation of τ_l and V_l

The KNMI Atlas (1952) gives the monthly-mean ship-drift values on a two degree-grid over the Indian Ocean. Figures 1a, b based on the atlas, give the drifts for grids located

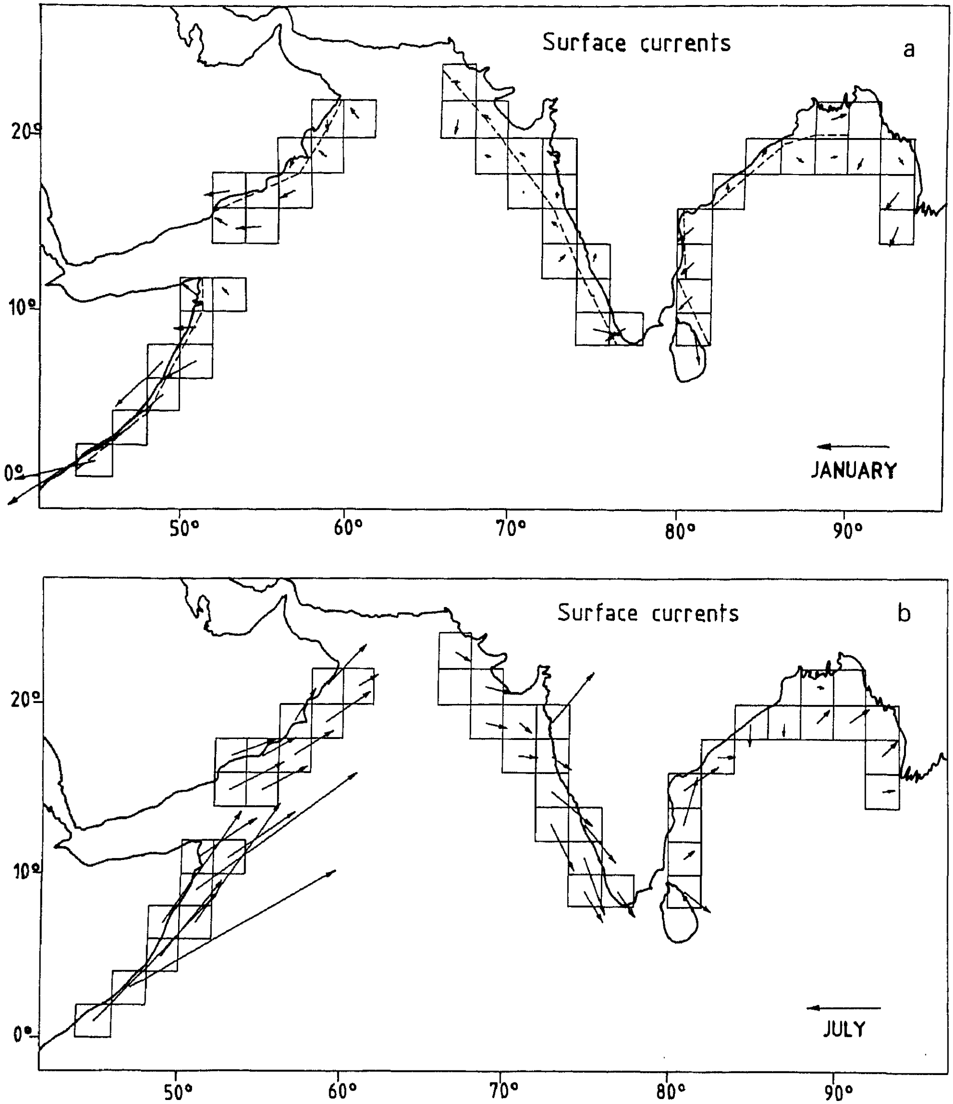

Figure 1. Monthly-mean ship drift in the North Indian Ocean based on KNMI Atlas (1952) for (**a**) January and (**b**) July. Arrow at the lower right hand corner of each figure has a magnitude of 50 cm/s.

in the North Indian coastal areas for January and July. The monthly mean longshore component of the surface currents has been computed by taking the component of the monthly-mean ship-drift along the straight line shown in each two-degree square in figure 1a. The 60-year climatology of monthly-mean resultant winds on a one-degree grid in the Indian Ocean has been given by Hastenrath and Lamb (1979). Using these data we first computed the monthly-mean wind for each grid in figure 1. These were then used to compute wind stress according to

$$\tau = \rho_a C_D W \mathbf{W},$$

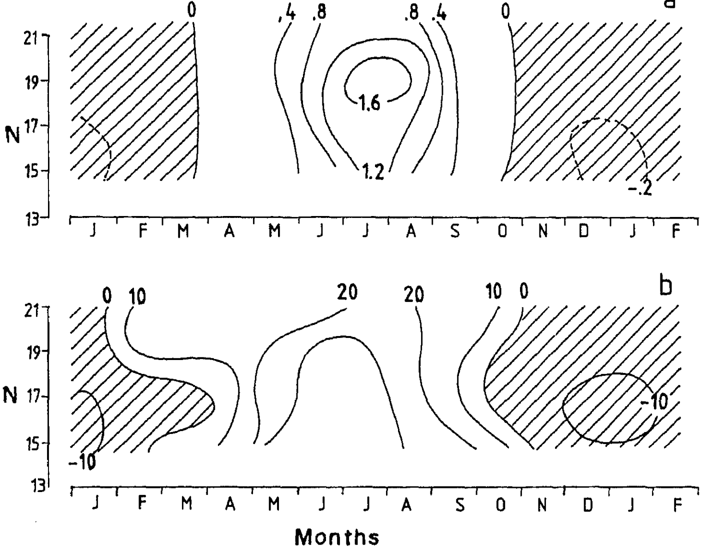

Figure 2. Monthly variation of longshore component of (**a**) wind stress τ_l (dyne/cm^2) and (**b**) surface velocity V_l along the coast of Arabia. A positive value indicates that wind stress or velocity is pointed away from the equator.

where τ is the stress (Newton/m^2), ρ_a, the density of air (1·175 kg/m^3), C_D an empirical drag coefficient taken to be $1{\cdot}3 \times 10^{-3}$, **W** the observed resultant wind and W the speed. τ_l for a two-degree square was computed by taking the component of τ along the line shown in each square of figure 1. Shetye *et al* (1985) used a similar procedure to define the annual cycle of monthly-mean wind stress in the coastal North Indian Ocean.

The first of the three subareas, the Arabian Coast, covers the coastline from 15 to 21°N. The second, the West Coast of India, covers the latitudes 9–23°N whereas the third, the East Coast of India, covers the region 9–21°N. The area east of 90° E has not been considered in the discussion. The sign convention is: τ_l is positive when the Ekman drift is offshore. This makes τ_l positive when poleward along a western boundary (i.e. coast of Arabia and the East Coast of India); τ_l is positive when equatorward along an eastern boundary (West Coast of India). The same sign convention is used for v_l.

As seen in figures 2a, b τ_l off the coast of Arabia is negative during November–March and positive during April–October. The behaviour of V_l shows a similar pattern. In particular, reversals in τ_l and V_l coincide. Earlier, Prell and Streeter (1982) pointed out that upwelling in this region is in phase with τ_l.

Along the West Coast of India τ_l is positive (i.e. equatorward) throughout the year (figure 3a). V_l, on the other hand, is poleward between October and January (figure 3b). Hence, during the northeast (NE) monsoon the coastal current flows against the wind. During the rest of the year there is a fair resemblance between the two patterns.

The two patterns in figures 4a, b show some marked contrasts. τ_l is positive between March and October. V_l on the other hand is positive between February and August. V_l reverses direction in the middle of the southwest (SW) monsoon season when τ_l is close to its peak annual value. The reversal of the currents thus precedes the winds by a couple of months and occurs when the winds are at their strongest. τ_l shows a marked

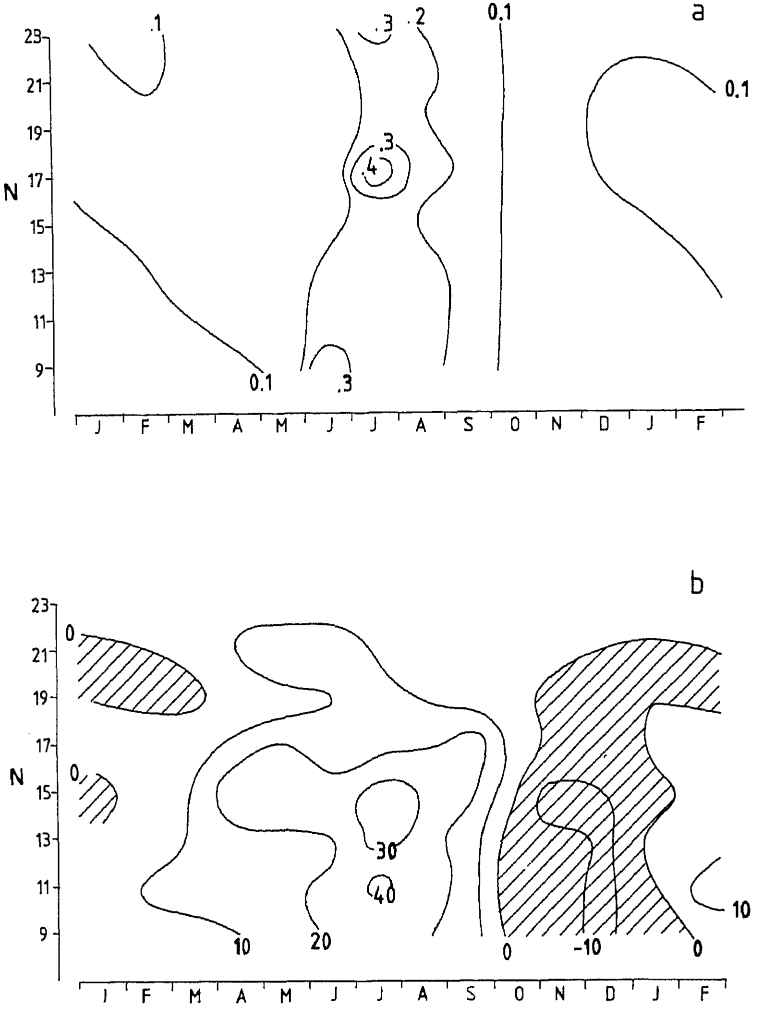

Figure 3. Monthly variation of longshore component of (**a**) wind stress τ_l (dyne/cm^2) and (**b**) surface velocity V_l along the West Coast of India. A positive value indicates that wind stress or velocity is pointed towards the equator.

peak around 17 N in July, whereas the currents do not show any such behaviour. V_l during August–January shows a systematic decrease in magnitude towards the north, a feature not seen in τ_l pattern. The reversal in the direction of V_l around January precedes the reversal in winds by about a month.

3. Sverdrup transport in the North Indian Ocean

Currents along the western boundary of a basin are influenced by the interior Sverdrup flow. It is therefore worthwhile to examine the nature of the Sverdrup transport

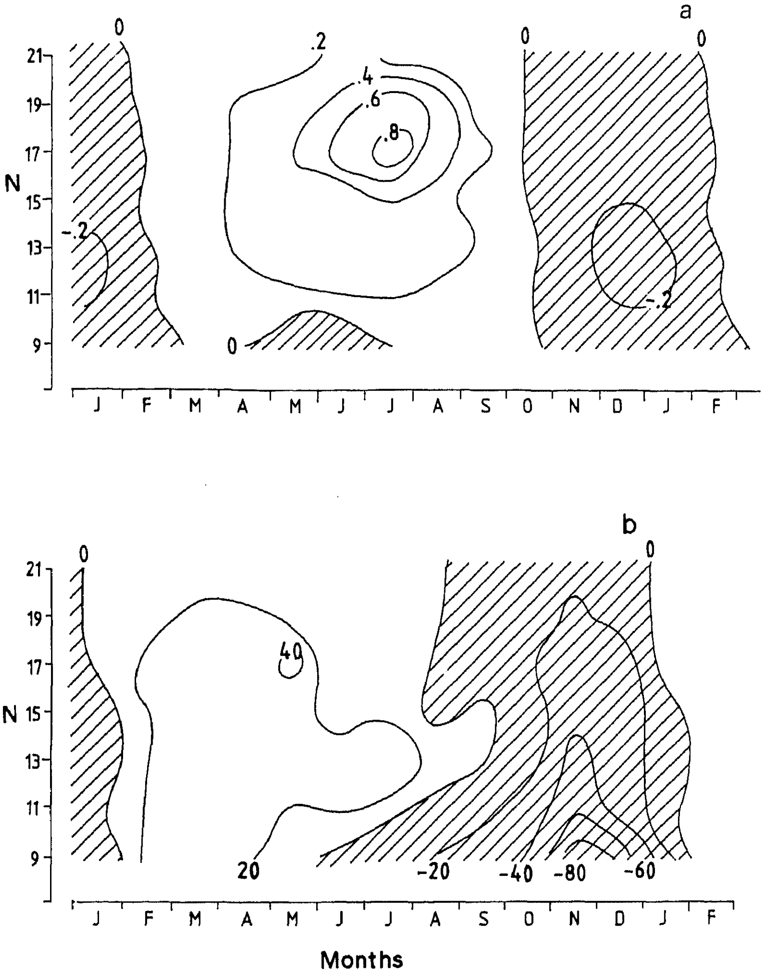

Figure 4. Same as figure 2, but for the East Coast of India.

mfunction (ψ) given by

$$\partial\psi/\partial x = (1/\rho_0\beta)\,\mathrm{curl}\,\tau,$$

e τ is the wind stress, β the rate of meridional variation of Coriolis parameter and e mean density of water (taken to be $1{\cdot}0\,\mathrm{g/cm^3}$). ψ has been determined for two :hs: January, representative of the NE monsoon and July, representative of the SW soon. The curl of the wind stress given by Hastenrath and Lamb (1979) has been except for one change. Hastenrath and Lamb (1979) use $2{\cdot}8 \times 10^{-3}$ for the value of rag coefficient C_D. This value is more than twice the usual norm of approximately 10^{-3}. The value of curl used in our computation has therefore been obtained after plying by 0·46 the value given by Hastenrath and Lamb. The computed ψ is n in figures 5a, b. A Munk layer is needed along the western boundary to close the lation depicted in these figures. The strength of such a layer would be about 15 Sv porting mass northward along the coast of Somalia in July and approximately

2 Sv southward in January. Along the coast of Arabia the contribution to Munk layer in January is negligible and it is of the order of 6 Sv equatorward in July. In the Bay of Bengal the contribution of the Munk layer is important only between 15° and 20°N, the magnitude and the direction of the flow being 3 Sv equatorward in July and 3 Sv poleward in January.

Bruce (1983) earlier computed the Sverdrup transport for the Arabian Sea. The pattern of transport given there agrees well with ours; however, the magnitudes are higher than ours because of the lower value of C_D used in our computations.

4. Discussion

The general agreement between τ_l and V_l patterns off Arabia suggests that the surface circulation off Arabia is driven primarily by the local winds. This observation is consistent with that of Prell and Streeter (1982) who concluded that the monthly mean upwelling in the region is controlled by τ_l. Hence, the Arabian coastal circulation appears similar to the classical wind-driven circulation along the eastern boundaries. But, we have the implication of figure 5b that there has to be a southward flow of approximately 8 Sv in the Munk layer along this coast. Bruce (1983) also observed a similar disagreement between the Sverdrup transports computed from wind stress and the near surface transport computed from hydrographic observations. To reconcile with these apparently contrasting views we need to hypothesize the following structure for the flow: an "eastern-boundary-like" flow confined near the surface and controlled by local τ_l alone; and a deeper flow arising due to a Munk layer. The magnitude of the latter is controlled by the curl of wind stress east of the coast.

Off the west coast of India during the SW monsoon, when τ_l is at its peak, there is fair resemblance between the patterns of τ_l and V_l. Hence we conclude that during this season it is τ_l that primarily controls V_l. During November–January the surface current flows against τ_l. This has also been pointed out by Pankajakshan and Rama Raju (1987). During this season the coastal current moves with the coastal pressure gradient (see charts 364 and 369 from Wyrtki (1971)). This is in contrast to the behaviour generally attributed to a wind-driven eastern boundary current. The poleward flow along the West Coast of India appears when τ_l is at its weakest, and hence it is safe to conclude that it is not forced by the latter.

A mechanism that has been suggested earlier to explain this current during November-January is the thermohaline forcing due to the poleward increase of surface density (Shetye 1984). Godfrey and Ridgeway (1985) pointed out that the poleward flowing Leeuwin current off the coast of West Australia, flows against τ_l and with the longshore surface pressure gradient. McCreary *et al* (1986) showed that the Leeuwin current can be driven by the alongshore poleward density increase arising due to the poleward temperature decrease in the interior regime off the West Coast of Australia. Such a density decrease is of course a manifestation of the large scale interior circulation off the Australian coast.

The magnitude of the alongshore density gradient off the West Coast of India varies seasonally, but always increases towards the north. The change in σ_t from 10°N to 20°N is approximately 1·1 g/cm^3 in January–February, it reduces to 0·12 in July–August and is at its annual peak (1.4 g/cm^3) during November–December. Hence the density gradient is the strongest when τ_l is the weakest. Note that the change in

τ_l from 25 to 35°S off the West Coast of Australia is approximately 1·4 g/cm^3 producing density gradient of approximately $1{\cdot}3 \times 10^{-11}$ g/cm^4 and is constant throughout the ear. τ_l along this coast has a maximum of 1 dyne/cm^2 in November–January and anishes in June.

In short, the annual cycle of the surface current along the West Coast of India appears be controlled by two opposing forcing functions: τ_l which tends to drive the surface ow towards the equator; and, longshore density gradient which tends to drive the urrent poleward. τ_l dominates during the SW monsoon season whereas the density radient dominates during the NE monsoon season.

The coastal density gradient along the west coast arises mainly due to variation in ılinity (see charts 38–57 in Wyrtki (1971)). This is in contrast to conditions generally bserved elsewhere in the world (West Coast of Australia, for example) where the ensity gradient is normally due to temperature variation. The northern end of the rabian Sea is connected to the Persian Gulf. The salinity in this mediterranean basin anges between 37 and 41 ppt. Salinities higher than 36 ppt observed towards the orthern end of the West Coast of India can be attributed to the presence of the Persian ulf. Salinity near the southern end of the west coast ranges between 33 and 34 ppt and typical of the low salinity waters of the eastern North Indian Ocean. The west coast ıus lies at the interface between these two waters with marked salinity differences.

There are two major differences between the τ_l and V_l patterns brought out by figures a and b. The first of these is the absence of a "cell-like" maximum at approximately 7°N around July in the τ_l pattern. The second is that the distinct increase in V_l towards ıe southern end of the East Coast of India is not seen in the τ_l pattern. As seen below ıere are two possible explanations for these differences: contribution of the Sverdrup ow, and the influence of freshwater run off on the coastal currents.

The Sverdrup flow in the Bay of Bengal during July and January is shown in figure 5. he wind stress curl over the northern bay is positive during July. The resulting Munk yer along the coast of India would therefore be required to transport about 3 Sv outhward. During January the wind stress curl is negative. The expected transport is Sv northward. At present it is not known to what extent the Munk transport ıfluences the surface flow along the East Coast. However, it is a potential candidate to xplain the absence of the maximum in V_l observed at 17°N around July.

The importance of freshwater run off as a driving mechanism for coastal currents as been highlighted by Royer (1979). Royer (1982) pointed out that the precipitation in ıe coastal mountains of the northeast Pacific produces a freshwater discharge with an nnual average of 23,000 m^3/s. The water enters the sea by way of numerous small rivers nd streams, forming a "line-source" of low density water. The freshwater creates a ross shelf density gradient that drives a longshore geostrophic baroclinic jet moving ith the land to the right of it. Royer (1982) estimated that the width of the jet is less ıan 25 km, and has speeds in excess of 100 cm/s, and transport in excess of 1·3 10^6 m^3/s. It was also suggested that the flow is maintained as a narrow current djacent to the coast by the wind stress that causes downwelling conditions.

The Bay of Bengal is a region which experiences evaporative loss varying from 3 to mm water/day (Hastenrath and Lamb 1979). The bay, however, receives considerable

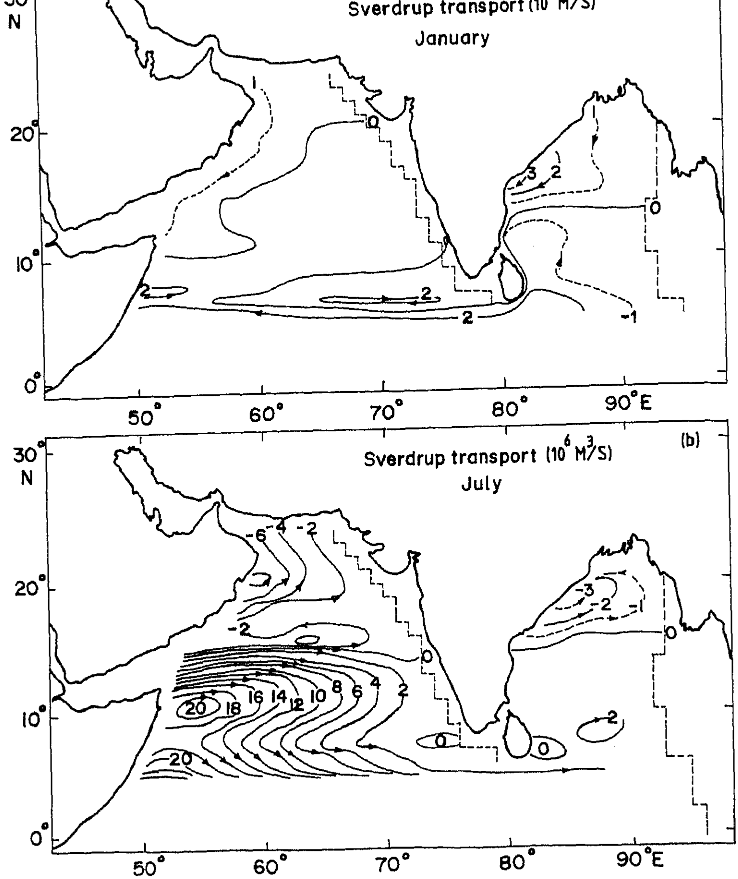

Figure 5. Sverdrup transport: ψ ($10^6\,m^3/s$) in the North. Indian Ocean north of 5°N in (**a**) January and (**b**) July. The dashed line in the figure gives the 'eastern boundary' where ψ has been set to zero.

large fraction of this run off occurs during the four months of the SW monsoon season. In addition to these rivers there are others which discharge freshwater along the East Coast of India. These include the Mahanadi, the Godavari, the Krishna and the Cauvery. Figures on freshwater contribution of these rivers to the Bay are not available. It is known, however, that the peak discharge in Mahanadi, Godavari and Krishna generally occurs during August. The mean discharge during this month at gauging station Kaimundi on Mahanadi has been reported to be $7710\,m^3/s$ (Anon 1969). The corresponding figures at Dowlaishwaram on Godavari and at Vijayawada on Krishna are $11{,}900\,m^3/s$ and $6{,}550\,m^3/s$ (Anon 1969). Towards the southern end of the east coast peak rainfall occurs later, generally in November. The peak discharge at Vellore on Pennar occurs in November (Anon 1969). Rao (1979) reported that the mean annual flow in Cauvery basin is $6{,}600\,m^3/s$.

On the whole, despite the uncertainties in the present estimates of freshwater run off, it is safe to assume that the total freshwater run off along the East Coast of India is well in excess of 30,000 m^3, and that a large fraction of this occurs during the four months of the SW monsoon. Comparing this figure with that for the Alaska coast, it appears that the coastal freshwater input is a strong candidate for driving the coastal circulation. It is possible that the freshwater run off is related to the differences between the τ_l and V_l patterns that were pointed out earlier. During the SW monsoon the freshwater run off is at a peak in the northern part of the coast. This can set up a cross-shore salinity and density gradient. The resulting baroclinic pressure gradient would tend to drive an equatorward geostrophic flow along the coast, opposing the poleward current that τ_l could set up. The hydrographic observations (Gopalakrishna and Sastry 1985) do show a cross-shore density gradient resulting from the increasing salinities away from the coast. During the NE monsoon the freshwater influx increases towards the southern end. This could drive an equatorward baroclinic current whose magnitude would increase towards the south, because the freshwater influx is higher there. τ_l at this time is equatorward. The winds would therefore tend to converge the freshwater near the coast, creating a situation similar to the one off Alaska.

5. Conclusions

(i) The surface circulation off the coast of Arabia is typical of a wind-driven coastal current, with τ_l and V_l exhibiting similar patterns.

(ii) Circulation off the West Coast of India is consistent with the dynamics of a wind-driven eastern boundary current only during the SW monsoon. During the NE monsoon it is possible that the influence of the interior flow as envisioned by McCreary *et al* (1986) is important.

(iii) There appears to be at least three competing mechanisms that influence the surface circulation off the East Coast of India: wind-stress, influence of freshwater run off and contribution of a Munk layer driven by Sverdrup flow. It is not possible at present to assess the relative importance of these three processes.

One of the primary objectives behind undertaking this study was to generate hypotheses regarding the dynamics of coastal circulation in the North Indian Ocean, more importantly along the coast of India, so that future studies can be aimed at testing these hypotheses. In view of this, it is worthwhile to list some of the specific questions which need to be addressed: (a) During the NE monsoon, is the interior circulation in the Arabian Sea consistent with that necessary to drive the eastern boundary current according to the mechanism outlined by McCreary *et al* (1986)? (b) What are the spatial and temporal variations of the freshwater run off along the coasts of India? (c) It would also be worthwhile to examine the dynamics of coastal currents that are driven by both wind and freshwater influx.

References

Anonymous 1969 Discharge of selected rivers of the world, UNESCO, Paris

Bruce J C 1983 The wind field in the Western Indian Ocean and the related ocean circulation; *Mon. Weather Rev.* **111** 1442–1452

Bumgartner A and Reichel E 1975 *The world water balance mean annual global, continental and maritime precipitation evaporation and run off*, (Amsterdam; Elsevier) p. 179

Godfrey J S and Ridgeway K R 1985 The large-scale environment of the poleward-flowing Leeuwin current, Western Australia: longshore steric height gradients, wind stresses and geostrophic flow; *J. Phys. Oceanogr.* **15** 481–495

Gopalakrishna V V and Sastry J S 1985 Surface circulation over the shelf off the East Coast of India during the southwest monsoon; *Indian J. Mar. Sci.* **14** 62–65

Hastenrath S and Lamb P J 1979 *Climatic atlas of the Indian Ocean, Parts 1 and 2: Surface climate and atmospheric circulation*, (Madison: Wisconsin University Press)

KNMI (Koninklijk Nederlands Meteorolgisch Institut) 1952 *Indische ocean oceanographische en meteorologische gegevens*, 2 edn. Publication No. 135

McCreary J P, Shetye S R and Kundu P K 1986 Thermohaline forcing of eastern boundary currents: With application to the circulation off the west coast of Australia; *J. Mar. Res.* **44** 71–92

Pankajakshan T and Rama Raju D V 1987 Intrusion of Bay of Bengal water into Arabian Sea along the West Coast of India during northeast monsoon. *Contribution in marine sciences. Dr S Z Quasim Sastyabdapurthi felicitation volume* (eds) T S S Rao, R Natarajan, B N Desai, G N Swami and S R Bhat (Dona-Paula, Goa: National Institute of Oceanography) p. 237–244

Prell W L and Streeter H F 1982 Temporal and spatial patterns of monsoonal upwelling along Arabia: A modern analogue for the interpretation of quarternary SST anomalies; *J. Mar. Res.* **40** 143–155

Rao K L 1979 *India's water wealth: Its assessment uses and projection* (New Delhi Orient Longmans) p. 267

Royer T C 1979 On the effect of precipitation and run off on coastal circulation in theGulf of Alaska; *J. Phys. Oceanogr.* **9** 71–79

Royer T C 1982 Coastal freshwater discharge in the northeast Pacific; *J. Geophys. Res.* **87** 2017–2021

Schott F 1983 Monsoon response of the Somali current and associated upwelling, in *Progress in oceanography* (eds) M V Angel and J O' Brien (New York: Pergamon Press) vol. 12, pp. 357–382

Shetye S R 1984 Seasonal variability of the temperature field off the southwest coast of India; *Proc. Indian Acad. Sci. (Earth Planet. Sci.)* **93** 399–411

Shetye S R, Shenoi S S C, Antony M K and Kumar V K 1985 Monthly-mean wind stress along the coast of the North Indian Ocean, *Proc. Indian Acad. Sci. (Earth Planet. Sci.)* **94** 129–137

Wooster W, Bakun A and Mc Lain D 1976 The seasonal upwelling cycle along the eastern boundary of the North Atlantic; *J. Mar. Res.* **34** 131–141

Wyrtki K 1971 *Oceanographic atlas of the International Indian Ocean expedition*, National Science Foundation, US (Washington DC: Government Printing Office)

Coherent rainfall zones: Case study for Karnataka

SULOCHANA GADGIL, R GOWRI and YADUMANI
Centre for Atmospheric Sciences, Indian Institute of Science, Bangalore 560012, India

MS received 3 February 1988; revised 28 July 1988

Abstract. Generally average rainfall over meteorological subdivisions is used for assessment of the variability of monsoon rainfall. It is shown here that variations of seasonal rainfall over the meteorological subdivisions of interior Karnataka are not coherent. A methodology for delineating coherent rainfall zones is developed in this paper and applied to derive such zones for the State of Karnataka.

Keywords. Monsoon variability; coherent rainfall zones.

1. Introduction

The major problem in monsoon meteorology is understanding the nature of the variability of the monsoon rainfall on different spatial and temporal scales. Over the monsoonal regions there is a large interannual variability of rainfall from droughts to years with a good monsoon. The severity of droughts can be assessed either in terms of the deficit of the rainfall in a season/year or in terms of the impact on critical resources such as agriculture. Generally droughts are defined in terms of the deficit of rainfall because it is not easy to assess quantitatively the impact on specific resources. Large anomalies in seasonal or annual rainfall generally occur simultaneously over regions which are hundreds of kilometers in extent because the monsoon is a planetary scale phenomenon. Hence the average rainfall over regions of this spatial scale viz the meteorological subdivisions (figure 1), is used by the India Meteorological Department for assessment of the monsoon performance in a specific year or a season.

It is clear that such an assessment is meaningful only if the variations of the rainfall for the period of interest are coherent over each of the meteorological subdivisions. Otherwise, even when the subdivisional average rainfall is normal, parts of the subdivision may experience drought while the rainfall may be normal or in excess over the rest. Our analysis of the time series of monthly rainfall over the State of Karnataka (figure 1) has revealed that two of the three meteorological subdivisions of the State are not coherent with respect to the variation of annual and seasonal rainfall. This implies that the subdivisional average does not reflect the experience of the subregions within these subdivisions and the availability of critical resources such as agricultural produce and water may not be related to the quantity of the subdivisional rainfall. For a meaningful assessment of the variability of rainfall it is necessary to use zones over which rainfall variations are coherent over the time scale of interest. Such coherent rainfall zones have to be identified for defining the occurrence of droughts, estimating their impact and for planning remedial measures. Clearly, coherent zones should form the basic unit for deriving the detailed statistics of rainfall variation during the

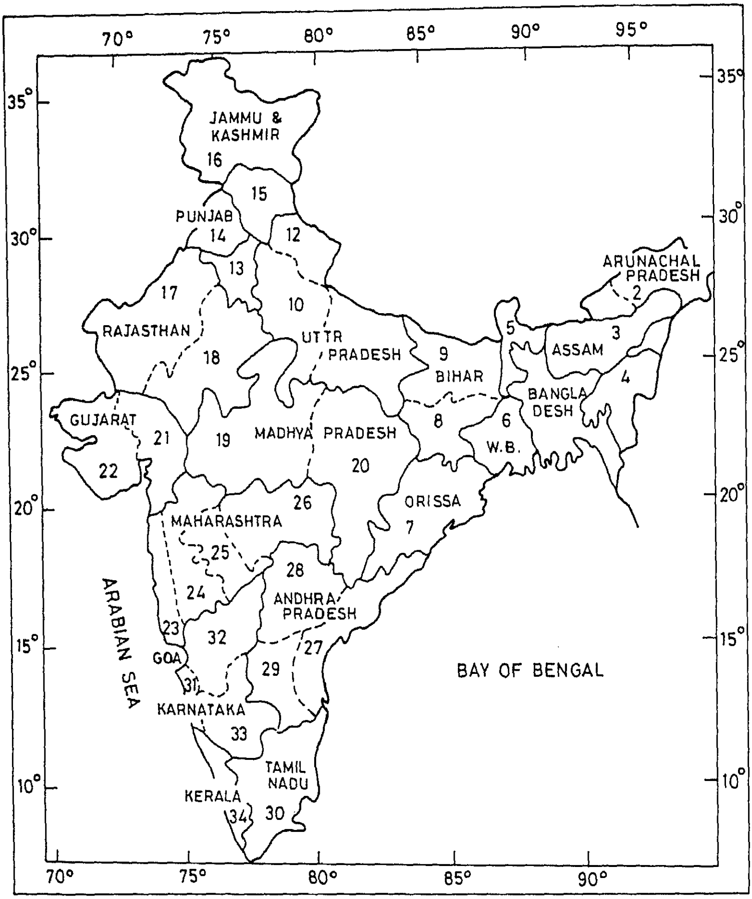

Figure 1. Meteorological subdivisions of India (after Rao 1976).

timescale chosen (such as the dependable rainfall at different probability levels) which is necessary for proper planning of the utilization of water resources and for determining the optimal agricultural strategy.

In this paper we illustrate the methodology we have developed for identification of coherent rainfall zones by delineating these zones for the State of Karnataka. In § 2 the basic data and the nature of the variation of rainfall over the study region are described. The measures of coherence used and the methodology developed for identification of coherent regions are discussed in §§ 3 and 4 respectively. The delineation of the coherent zones of the State of Karnataka is discussed in § 5. The extent to which the zones thus derived are coherent with respect to the occurrence of large anomalies in seasonal and annual rainfall is estimated in § 6 and the implications of the different definitions of meteorological droughts are discussed in § 7.

2. Rainfall in Karnataka: basic features

The data analysed comprise monthly rainfall during 1901–1985 at 50 well-distributed

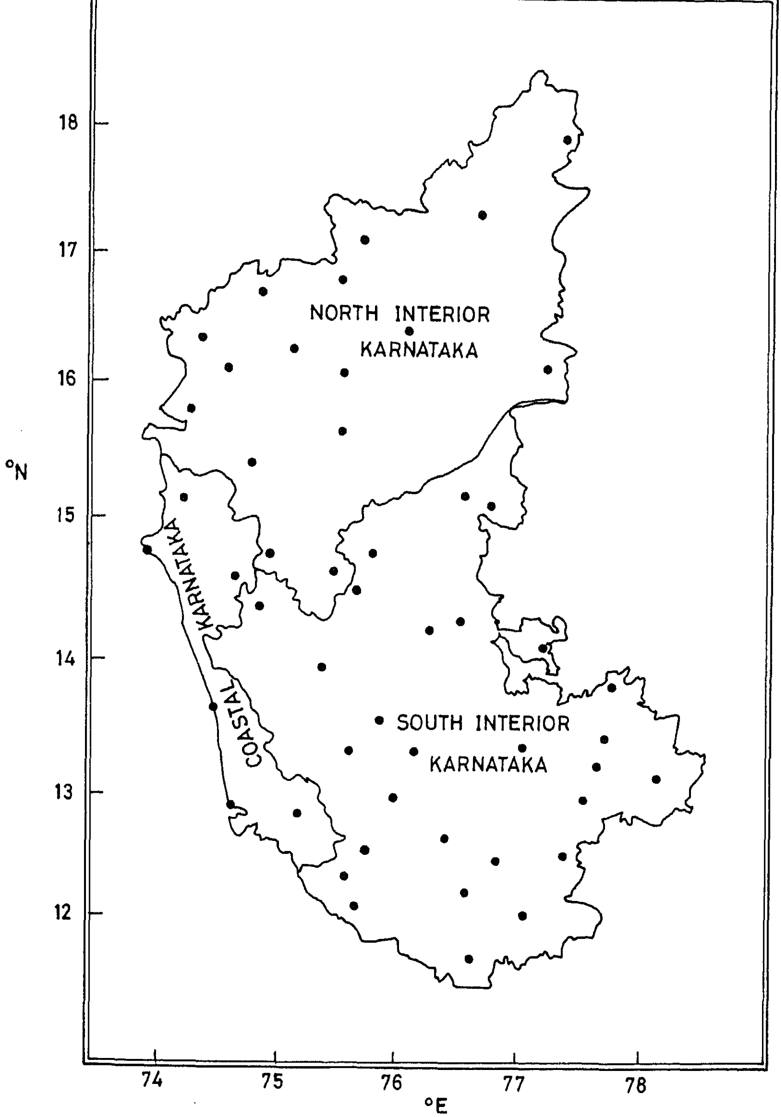

Figure 2. Meteorological subdivisions of Karnataka and the network of stations used.

vork of stations used are shown in figure 2. There is considerable variation in the
:age annual rainfall as well as the average rainfall pattern i.e. the distribution of
fall within the year, across the State (figure 3). Most of the rainfall occurs during
seasons viz the summer monsoon (June–September) and the post-monsoon
tober–December). In addition, some rainfall is also received during the pre-
ısoon season i.e. March–May. Our aim is to delineate zones of the State which are
erent with respect to the variations in the annual rainfall and rainfall in the two
or rainy seasons. In fact the zones so determined also turn out to be coherent for
ation of rainfall in each of the major rainy months.

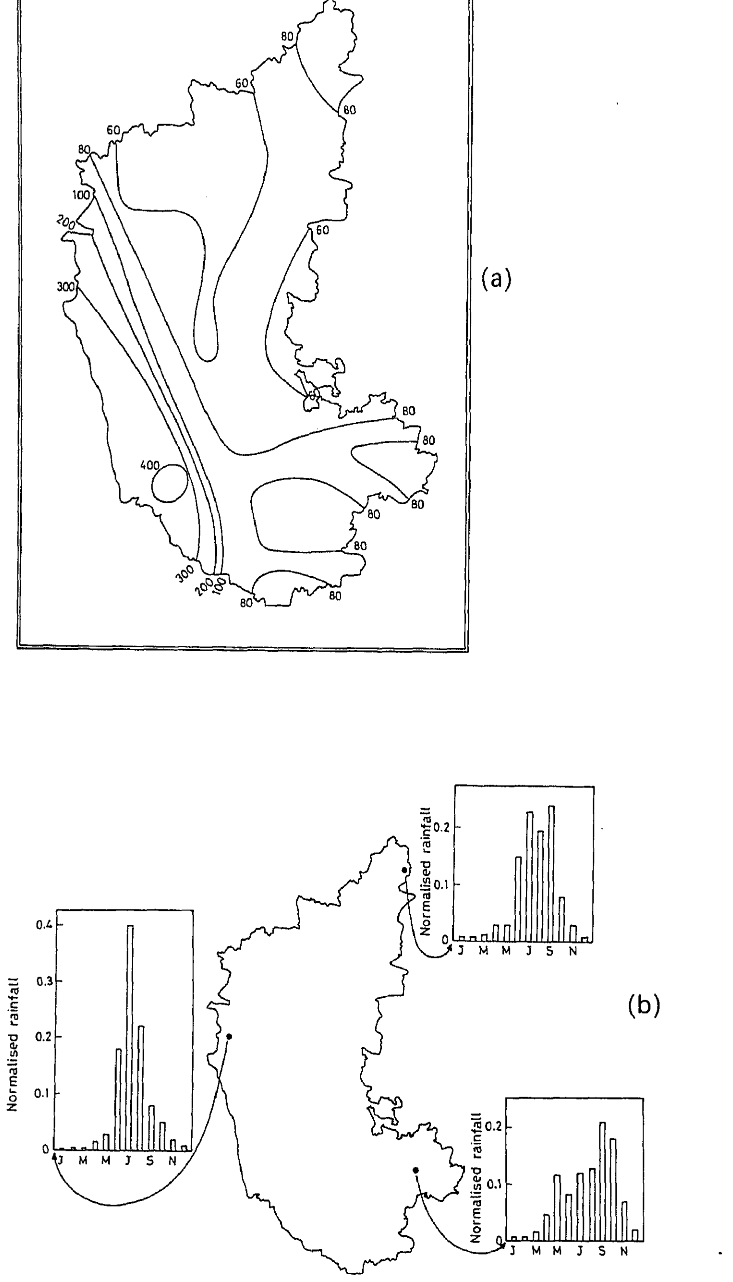

Figure 3. (**a**) Mean annual rainfall at different stations. (**b**) Mean monthly rainfall at three different stations: Supa (15·16°N, 74·3°E) near the west coast; Bidar (17·55°N, 77·32°E) in the northeastern part; and Devanahalli (13·15°N, 77·42°E) in the southeastern part.

The degree to which the variations in the rainfall at one station are related to that at another station can be estimated by the cross-correlation. When the cross-correlation of the annual rainfall is high, the anomalies in the annual rainfall i.e. drought or excess rains are likely to occur simultaneously over the two stations. Obviously, the correlation between any two stations in a coherent zone has to be statistically significant for the rainfall over the time-scales of interest such as seasonal, annual etc. Whether this condition is satisfied by the existing meteorological subdivisions can be easily tested. Tables 1–3 show the correlations of the different stations of the meteorological subdivisions of Karnataka relative to the one arbitrarily chosen station in each. It is seen that the correlations are not significant at 5% level for several stations. Thus the existing meteorological zones cannot be considered to be coherent even for variations of annual rainfall and it is necessary to determine anew the coherent zones of the State.

Table 1. Meteorological subdivision: South Karnataka (central station: Kolar).

Stations	Correlations				Mean disparity index
	Annual	Pre monsoon	Summer monsoon	Post monsoon	
Devanhalli	0·74	0·41	0·69	0·75	0·20
Bangalore	0·71	0·60	0·66	0·76	0·19
Chikaballapur	0·63	0·39	0·55	0·69	0·21
Bagepalli	0·61	0·40	0·51	0·59	0·23
Harihar	0·57	0·48	0·48	0·47	0·29
Tumkur	0·56	0·31	0·50	0·67	0·23
Kadur	0·55	0·30	0·29	0·51	0·29
Challakere	0·53	0·17	0·43	0·40	0·30
Chitradurga	0·53	0·20	0·38	0·55	0·26
Kanakapura	0·52	0·54	0·36	0·68	0·22
Arsikere	0·52	0·23	0·36	0·63	0·25
Pavagada	0·52	0·18	0·55	0·60	0·26
Hospet	0·51	0·31	0·44	0·51	0·28
K. R. pet	0·48	0·29	0·49	0·54	0·27
Hassan	0·48	0·30	0·43	0·45	0·28
Kollegal	0·47	0·35	0·52	0·56	0·24
Gundlupet	0·46	0·22	0·59	0·53	0·29
Bellary	0·45	0·27	0·50	0·42	0·28
Mysore	0·41	0·31	0·32	0·56	0·25
Mandya	0·40	0·21	0·61	0·51	0·25
Harpanahalli	0·38	0·20	0·38	0·40	0·27
Chikmagalur	0·31	0·24	0·25	0·38	0·30
Shimoga	0·17	0·28	0·10	0·46	0·36
Somwarpet	0·07	0·16	0·04	0·44	0·44
Sorab	0·07	0·27	0·08	0·35	0·46
Mercara	0·05	0·26	0·00	0·54	0·45
Virajpet	0·02	0·22	0·07	0·34	0·43

Correlations which are not significant at 5% level have been underlined.

Stations	Correlations Annual	 Pre monsoon	 Summer monsoon	 Post monsoon	Mean disparity index
Bidar	0·49	0·53	0·49	0·57	0·21
Indi	0·46	0·23	0·49	0·44	0·26
Raichur	0·46	0·54	0·49	0·42	0·23
Bijapur	0·42	0·63	0·49	0·50	0·26
Chikodi	0·41	0·21	0·42	0·44	0·32
Muddebihal	0·41	0·32	0·54	0·43	0·27
Bagalkot	0·35	0·31	0·37	0·48	0·29
Gokak	0·34	0·27	0·44	0·43	0·32
Ron	0·33	0·27	0·36	0·45	0·29
Athni	0·26	0·31	0·36	0·39	0·30
Mudhol	0·22	0·22	0·32	0·43	0·29
Ranebennur	0·14	0·25	0·05	0·30	0·34
Hangal	0·12	0·24	0·02	0·36	0·35
Dharwar	0·09	0·26	0·10	0·44	0·31
Belgaum	0·08	0·05	0·11	0·28	0·37

Correlations which are not significant at 5% level have been underlined.

Table 3. Meteorological subdivision: West Coast (central station: Sirsi).

Stations	Correlations Annual	 Pre monsoon	 Summer monsoon	 Post monsoon	Mean disparity index
Supa	0·73	0·68	0·75	0·67	0·10
Beltangady	0·64	0·73	0·66	0·52	0·13
Karwar	0·53	0·73	0·54	0·50	0·20
Mangalore	0·40	0·72	0·40	0·37	0·20
Coondapur	0·35	0·65	0·41	0·40	0·18

We use the cross-correlation of annual rainfall as an important measure of the coherence of the variations of rainfall at a pair of stations. The starting point of our analysis is, therefore, the correlation matrix of the annual rainfall for the 50 raingauge stations computed by utilizing the 85-year data set. Since our aim is to identify zones which are coherent not only with respect to annual rainfall but with respect to seasonal rainfall as well, in addition to the cross-correlation for annual rainfall we also have to take into account the coherence of the monthly rainfall pattern. For this, another measure of similarity (or rather disparity) of monthly patterns of the rainfall is used. The rainfall pattern at a given station during a specific year can be represented as a point in the twelve-dimensional space of monthly rainfall. We define the Euclidean distance between the points representing the rainfall patterns at the stations of interest as the disparity index between the stations for the specific year chosen. Since the

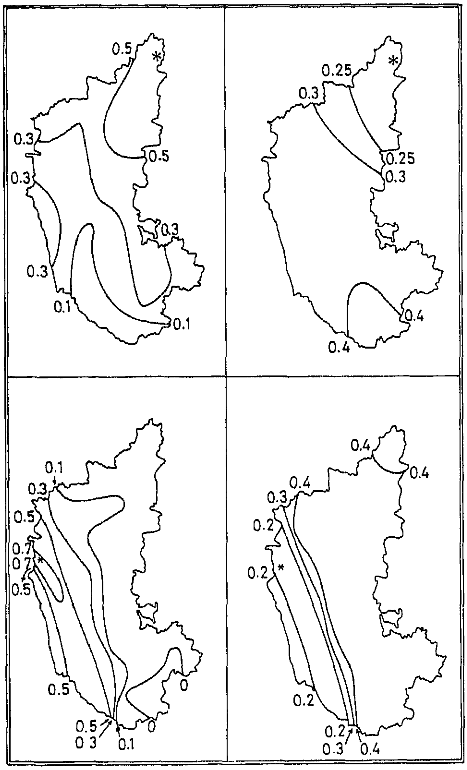

Figure 4. Correlation of annual rainfall and mean disparity index with respect to two representative stations viz Supa and Bidar.

rence of the total quantum of rainfall received duing the year is assessed by the
-correlation of annual rainfall, we use normalized rainfall pattern (i.e. the fraction
infall received in each month) in computing the disparity index. Various measures
e disparity between the patterns at a given pair of stations, such as the mean,
e etc. can be calculated from the 85-year data set. The cross-correlation of annual
all and the mean value of the disparity index are used as measures of coherence and
ck of coherence respectively in our method for delineating the coherent zones.
ever the same results are obtained if the mode of the 85-year distribution of the
rity index is used instead of the mean.

e spatial variation of the correlation of the annual rainfall and the mean disparity
x relative to two representative stations viz. Bidar in the northeastern parts and
near the west coast are shown in figure 4. It is seen that the coherence relative to
decreases rapidly in the eastward direction (figures 4c, d) across the Western
ts and becomes statistically insignificant over the interior parts of the State. The
n with maximum coherence relative to this station is a zone parallel to the west

Bidar in the northeastern region (figures 4a, b) indicates that the interior itself is not a coherent zone since the annual rainfall over the southern part of interior Karnataka is poorly correlated with that over the northeastern part. Thus it is clear that at least three zones are necessary; whether three zones are adequate will be determined in this study. Even in the event of three zones being adequate, they have to be delineated anew since the existing meteorological subdivisions of interior Karnataka are not coherent. We consider next the methodology for delineation of coherent zones.

4. Delineation of coherent zones

4.1 *The approach*

The number of coherent zones depends on the degree of coherence demanded within each zone. The minimum requirement is that the cross-correlation for the rainfall over the time scale of interest between any pair of stations within a coherent zone be statistically significant. We seek to delineate coherent zones which satisfy the condition that the correlation of the annual rainfall as well as the rainfall in the two major rainy seasons of summer monsoon and post-monsoon, between any two stations within a zone is significant at 5% level (i.e. $\geqslant 0{\cdot}21$ for a sample of 85 years assuming a Gaussian distribution). We are interested in determining the minimum number of coherent zones in which the State can be divided, such that the minimum requirement of coherence is satisfied for each zone. It is clear from figure 4 that the State as a whole cannot be considered as a coherent zone because stations within the State are poorly correlated even on the annual scale. The upper limit on the number of coherent zones is obviously provided by the trivial case of each station being considered as an independent zone when maximum coherence is achieved within each zone.

The problem of delineation of coherent zones is somewhat complex because all measures of coherence such as the cross-correlation refer to relationship between variations at a pair of stations. Thus the problem is akin to the analysis of the distribution of points when the co-ordinates are not known but the matrix of interpoint distance is known. In this situation, it is not easy to analyse the distribution of the points to identify the clusters or groups of coherent stations. However, relative to a given central station, the stations at which the variations are sufficiently coherent (i.e. with values of correlation coefficients above and disparity index below specified thresholds) can be readily identified. Thus if a network of central stations which represent the entire gamut of the observed variation can be identified objectively, coherent zones can be delineated by assigning stations appropriately to the different central stations or seed points. This is the approach we have adopted in this study.

In order to determine the minimum number of zones into which the State can be divided, we begin by investigating the possibility of having only two zones. As expected from the discussion at the end of the last section, we find that these zones cover only a part of the State, the rest of the State comprising a large number of stations which cannot be assigned to either of these zones without violating the imposed condition on the minimum correlation within a zone. As the number of zones is increased, the number of stations which cannot be assigned to any zone decreases until the final stage at which the entire State is covered. We consider next the methodology for choosing the ıbvious choice for the first two central stations/seed points is the pair of stations :he lowest value of correlation of annual rainfall. For the stations analysed here ıinimum correlation turns out to be negative i.e. $-0{\cdot}15$ between Supa near the coast and Devanahalli in the southeastern part. It is clear that these two stations ɔt be assigned to the same zone. The next seed point is chosen as that station which st poorly correlated with each of the seed points chosen earlier. This would be gous to seeking the point which is farthest from the chosen seed points in the sis of the spatial distribution of points. Specifically, the station with the minimum of the maximum correlation relative to the seed points already chosen is selected : next seed point. The process of selection of the seed points can be illustrated by ibing the identification of the third seed point after the first two have been chosen ɔse with a minimum value of the cross-correlation viz. Supa and Devanahalli. Let ɔrrelation of a station i of the remaining 48 stations, with Supa and Devanahalli be .d r_{D_i} respectively. We consider only the maximum correlation relative to the dy chosen seed points, R_i which is given by

$$R_i = \text{Maximum of } r_{\mathrm{S}_i} \text{ and } r_{\mathrm{D}_i}.$$

ʼalue of R_i will be large for any station i which is well correlated with either of the :n seed points i.e. Supa or Bidar. A small value of R_i indicates that the station i is y correlated with both the seed points. The minimum value of this maximum lation will occur for a station which is least correlated with the set of seed points :n. This station is chosen as the next seed point. This process is continued until an ıate network of central stations representing the entire gamut of variation in the region is obtained.

Formation of coherent zones

: the seed points/central stations are identified, the assignment of stations to the ı set of central stations to form coherent zones/groups of stations is done as ws. At the first instance, the station which is best correlated with the central station idered, is assigned to it provided that (i) its mean disparity index relative to that :al station is less than that relative to the other central stations and (ii) the mum correlation of annual rainfall within the region so formed exceeds a specified shold viz 0·3. The threshold in the second condition has been chosen to be ɛwhat stringent, implying correlations significant at 1% level, so as to ensure rence on seasonal and monthly scales. Once the group membership increases to or more, it is necessary to ensure that any new station added is better correlated the set of stations included in that group than it is to the set of stations in the other ps. Hence we consider the correlation of each unassigned station with every ıber of the group. If a group consists of stations $1, 2, \ldots, n$, from the correlations of unassigned station i with each member viz r_{ik} for $k = 1, 2, \ldots, n$ we take the mum one i.e. r_{min_i}. We rank all the stations to be assigned according to the value of in descending order. Thus the station with the first rank is characterized by the ɛst value of the minimum correlation relative to the stations already assigned to the .p. Since this station is better correlated with the group as a whole than any other station, it is assigned to that zone provided that conditions (i) and (ii) above are satisfied.

At the first instance, when only two central stations are used, we find that several stations cannot be assigned to either of the two coherent zones without violating one of these conditions. As the number of central stations increases, more and more parts of the State get represented and the number of such unassignable points decreases, until eventually the entire study region is covered. At each stage, the coherence of the seasonal rainfall within the identified zones is also assessed. The final results are the same if a threshold of 0·2 is used in condition (ii); differences arise only in the intermediate stages. The detailed delineation of the coherent zones of Karnataka using the methodology described here is discussed in the next section.

5. Coherent zones of Karnataka

As seen from figure 4 the annual rainfall at stations near the west coast is rather poorly correlated with that over the southeastern part of the State. In fact, the pair of stations with the poorest correlation comprises one station from each of these regions. We consider first the division of the State into two coherent zones using these stations as the central stations or seed points. We find that using the methodology described in the previous section, only 27 of the 50 stations can be assigned to the coherent zones formed (figure 5.I). The remaining 23 stations cannot be assigned to either of the two coherent zones without violating the imposed condition on the minimum correlation between any two stations within a coherent zone. Since the coherent zones cover only a part of the State with a large number of stations in the northern part of the State remaining unassigned, we may conclude that two zones are not adequate. We next consider the possibility of dividing the State into three coherent zones.

Not surprisingly, the third central station appears in the northeastern part of the State (figure 5.II). At this stage the number of unassigned stations is reduced to 17. Of these the majority cannot be assigned without violating the imposed condition of the minimum correlation within a zone. The remaining four stations occur near the boundaries of the zones and cannot be assigned to any of the three zones because the condition that the disparity index must be minimum relative to the central station of the zone to which the station is assigned cannot be satisfied in their case. In other words although each of these stations is better correlated on the annual scale with the stations of one zone, it is closer to another zone on the seasonal and monthly scale. It is seen that even with three coherent zones fairly large regions in the northwestern and southern parts of the State remain unassigned. Hence it is clear that more than three zones are required.

To determine the minimum number of zones into which the State can be divided, we continue this exercise of adding one centre at a time, delineating the corresponding

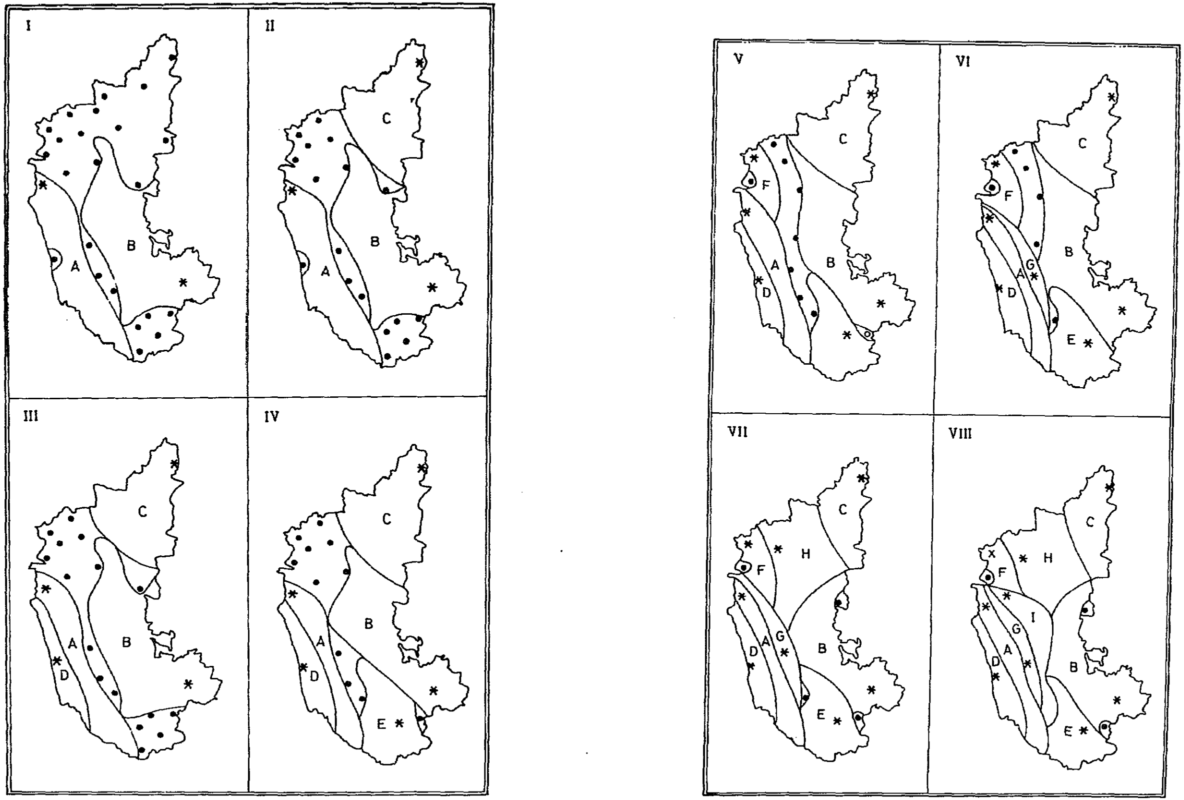

Figure 5. Figures I–VIII represent division of the State into two, three,…, nine zones derived by taking increasing number of seed points—central stations (*).

Table 4. Successive stages of formation of coherent zones.

# of zones	# of stations unassigned	Unassigned because of min. corr. insignificant	Zones	A	B	C	D	E	F	G	H	I	J
2	23	23	# of stations	10	17								
			Monthly*	4	24								
			Seasonal**	7	16								
3	17	13	# of stations	10	17	6							
			Monthly*	4	15	3							
			Seasonal**	5	10	0							
4	17	10	# of stations	6	17	6	4						
			Monthly*	0	18	3	0						
			Seasonal**	0	10	0	0						
5	12	4	# of stations	6	15	6	4	7					
			Monthly*	0	20	3	0	2					
			Seasonal**	0	15	0	0	0					
6	10	3	# of stations	6	14	6	4	7	3				
			Monthly*	0	11	3	0	2	62				
			Seasonal**	0	1	0	0	0	100				
7	8	1	# of stations	5	15	6	4	7	3	3			
			Monthly*	0	11	3	0	2	34	0			
			Seasonal**	0	1	0	0	0	67	0			
8	6	0	# of stations	5	12	3	4	7	3	3	7		
			Monthly*	0	8	0	0	2	10	0	5		
			Seasonal**	0	0	0	0	0	33	0	0		
9	4	0	# of stations	5	10	3	4	7	2	3	7	5	
			Monthly*	0	6	0	0	2	0	0	5	2	
			Seasonal**	0	0	0	0	0	0	0	0	0	
10	2	0	# of stations	5	9	3	4	7	2	3	7	5	3
			Monthly*	0	4	0	0	2	0	0	2	2	0
			Seasonal**	0	0	0	0	0	0	0	0	0	0

*% of pairs of poorly correlated stations within each zone on the monthly scale i.e. % of pairs for which the correlation of monthly rainfall during June–December is not significant at 5% level in the rainy months (June–December).

**Same as *but for the seasonal rainfall during summer monsoon and post-monsoon seasons.

coherent zones, checking the extent of the State covered by these coherent zones, and the coherence within each such zone on seasonal and monthly scales. Detailed results are given in table 4 in which information about the number of unassigned stations at each stage as well as the reason for their unassignability is also included.

It can be seen that in zones A and B formed at the first stage, the correlation on the seasonal and monthly scales is not significant for a few pairs of stations; the number of such pairs being somewhat larger for the sprawling zone B than the coastal zone A. Zone C added at the next stage is more coherent on seasonal and monthly scales. At this point, another central station appears on the west coast, resulting in a splitting of A into two zones which are completely coherent on monthly and seasonal scales. As more centres appear, more zones are formed, the membership of the earlier zones changes and the number of pairs of stations which are not significantly correlated on seasonal and monthly scales reduces. At the final stage (figure 6) the zones are coherent on the seasonal scale and largely so even on the monthly scale.

So far we have considered a zone to be coherent on the timescale of interest if the correlation between any two stations in the zone is significant at 5%. The next task is to determine whether this condition is adequate to ensure that large anomalies of opposite signs do not occur simultaneously over such a zone so that the delineated zones fulfil the original purpose of providing meaningful averages. To ascertain this, it is first necessary to define what constitutes large anomalies. In the case of negative anomalies, this amounts to defining droughts in terms of the deficit in rainfall. We consider this problem next.

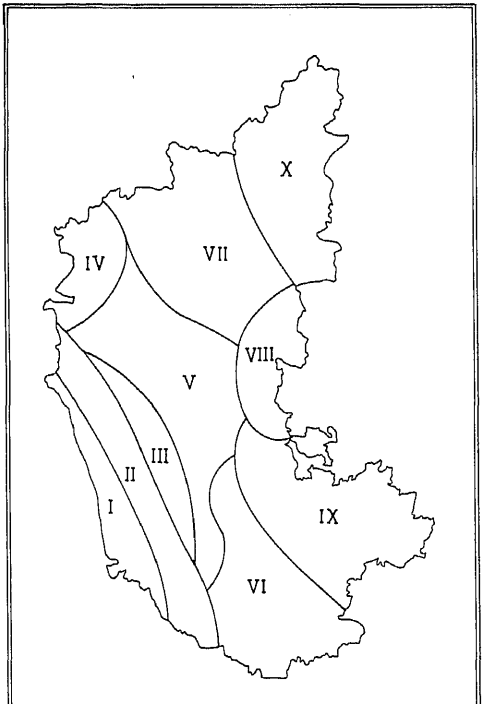

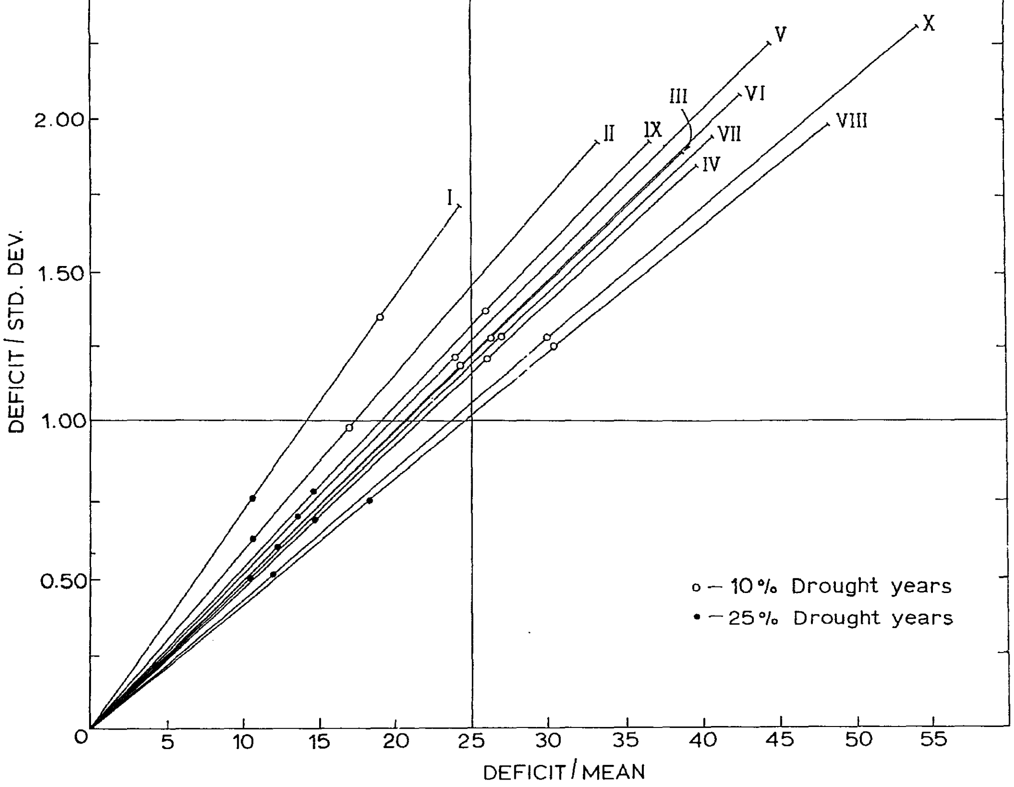

Figure 7. For each zone, during years in which the annual rainfall was less than the mean, the deficit/mean (abscissa) and deficit/standard deviation (ordinate) are plotted to indicate the observed range of variation.

6. Droughts and coherent zones

There is no universally accepted definition of droughts. Obviously meteorological droughts are associated with deficit rainfall. But how large does this deficit have to be for the year/season to be declared as a drought? Logically this should be determined by the nature of the impact of the deficit on the critical resources of the region. If the resource utilization strategy is rational, the impact will not be large unless the rainfall deficit exceeds the expected variation of the rainfall over the region. Hence in one approach to the definition of drought, the deficit is scaled by the simplest measure of variability viz the standard deviation and drought is said to occur when the deficit exceeds the standard deviation or some multiple thereof (e.g. Shukla 1986). The multiplicative factor is often taken to be 1·28 because when the distribution is normal, the probability of the deficit exceeding 1·28 times the standard deviation is 10%. A generalization of this definition to omit the dependence on the nature of the distribution is to define drought as a 10% probability event from the observed distribution of the time variation for the region of interest. In the second approach to the definition of droughts, the yardstick used for assessing the deficit of rainfall is the mean rainfall over the region. Thus according to IMD (1971) drought is said to occur when the rainfall is less than 75% of the mean i.e. the deficit exceeds 25% of the mean rainfall.

The implications of all these definitions of drought for the different zones of figure 6 are shown in figure 7 in which the range of the variation of the deficits in the zonal average annual rainfall during 1901–85 scaled by the mean rainfall (abscissa) and by the standard deviation (ordinate) is shown. The range of the deficits in the 10% and 25% years with lowest rainfall is also indicated therein. It is seen that if the IMD (1971) definition of drought is used, not a single drought occurred during 1901–85 in the coastal zone I, while only three occurred in the adjacent zone II. On the other hand, the frequency of droughts thus defined in zones VII and IX is larger than 10%. For the ramaining zones the IMD criterion implies droughts in about 10% of the years.

If droughts are defined as years with deficits larger than one standard deviation, the frequency in zone II is about 10% whereas it is much larger in all the other zones including the coastal zone. If a factor of 1·28 is used in the definition of droughts, the frequency is close to 10% for all the zones with the exception of zone II in which it is about 5%. Thus if the definition of droughts is to be based primarily on the observed variation of rainfall, it may be best to define it as an event of a given probability e.g. as a chance of 1 in 10 event. Such droughts for the two major rainy seasons in the different zones are shown in figure 8. The minimum value of the deficit characterizing a drought has then to be derived from the observed variation over the region. The same concept can be used in defining the categories of the above normal and the below normal rainfall.

The extent to which the objective of this study viz identification of zones which are sufficiently coherent for identification of droughts or conditions of above or below normal rainfall has been achieved can be assessed once we define precisely what constitutes a drought or a situation with above/below normal rainfall.

Consider first a case in which we take 25% of the years with lowest/highest rainfall to represent the below/above normal rainfall at a particular station. The frequency of simultaneous occurrence of stations with above and below normal rainfall within a zone/region can be taken as a measure of the lack of coherence in that zone/region. We find that for the meteorological subdivisions of interior Karnataka a majority of the

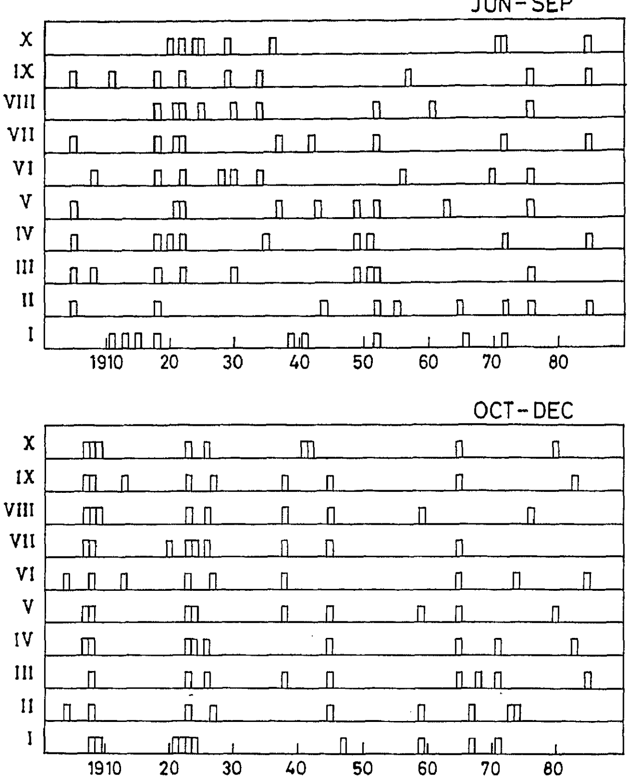

Figure 8. Droughts in the different zones during the two major seasons when drought is defined as a chance of 1 in 10 events.

years (74% for the southern and 54% for the northern subdivision) were characterized by such simultaneous occurrence of above and below normal rainfall. On the other hand, for the rainfall zones determined here, in a vast majority of years (ranging from 71% to 94% for the different zones), the rainfall variations are completely coherent with anomalies of the same sign within each zone i.e. all the stations within a zone experiencing below normal/normal in some years and above normal/normal rainfall in others. Another index of the lack of coherence within a zone for a particular year is the product of the fraction of stations simultaneously experiencing above and below rainfall; this product is zero for years when the zone is completely coherent. The mean value of this product over the 85 years ranged from 0·3% to 1·5% for these zones. Thus the zonal average appears to be a meaningful estimate of the rainfall at the different stations within a zone. We find that for most of the zones when the zonal average rainfall is below normal, the rainfall is not above normal at any of the individual stations comprising the zone. The exceptions are the zones V, VII and IX in which during 2–4% of the station-years, rainfall slightly above normal was recorded when the zonal average was below normal. If we define drought as a 10% probability event and consider the drought years for each zone when the zonal average rainfall is in the lowest 10% category, we find that at no station is the rainfall above normal in any zone. A majority of the stations (ranging from 70% to 82% for the different zones) experience drought during these years. Thus we may conclude that the zones delineated here are sufficiently coherent for estimating the performance of the monsoon and identifying droughts on the seasonal/annual scale.

Acknowledgements

It is a pleasure to thank Prof. R Narasimha and Dr N V Joshi for many stimulating discussions and Prof. R Ananthakrishnan for detailed comments. This research was supported by a grant from ISRO.

References

IMD 1971 *Rainfall and drought in India.* India Meteorological Department Publication, pp. 22–23

Rao Y P 1976 *Southwest monsoon.* Meteorological Monographs, Synoptic Meteorology 1/1976, India Meteorological Department, New Delhi, pp. 367

Shukla J 1986 Interannual variability of monsoon; in *Monsoons* (eds) J S Fein and P L Stephens (New York: Wiley-Interscience)

Magnetic studies on the remanence carriers in igneous rocks of different ages

C RADHAKRISHNAMURTY, S D LIKHITE and G S MURTHY[†]
Tata Institute of Fundamental Research, Bombay 400005, India
[†]Department of Earth Sciences, Memorial University of Newfoundland, St. John's, Canada A1B 3X7

MS received 8 February 1988

Abstract. A critical study on the type of the magnetic grains, both in composition and domain state, in rocks of different ages has been carried out. One simple, fast and non-destructive test, which can provide useful information on the nature of the magnetic grains in freshly collected samples, seems to be the ratio of susceptibilities at 77 and 300 K. This ratio, termed relative susceptibility, ranges from 0·1, for samples containing 70% ulvospinel bearing titanomagnetite (TM70) to 1·50 for cation deficient magnetite bearing ones. The results indicate that the value of 0·1 for TM70 is not greatly affected even if some amount of TM80, which is nonmagnetic at 300 K, is present in a rock sample. However, the coercive force at 77 K will increase considerably for such a sample. The effects of mixed compositions and domain states of magnetic grains on the overall behaviour of basalts are discussed.

Keywords. Domain states; magnetic parameters; basalts; remanence carriers.

1. Introduction

Only a small fraction of the few percent of the iron oxide grains in an igneous rock is responsible for the remanent magnetization of the sample. The remanence carriers could be of the same composition as the bulk of the iron oxide grains or of a different composition. Similarly, the domain state of the carriers could be the same or different from that of the other magnetic grains in the sample. In an ideal situation when a sample contains magnetic grains of a single composition and of one domain state, the character of the remanence carriers can be understood by any simple magnetic method. But more often than not, rock samples contain both mixed composition and domain states (Radhakrishnamurty *et al* 1982) and the procedure to identify them is yet to be evolved. However, the parameter coercive force (H_c) at 77 K of the rock samples is quite dependable for inferring the composition of the magnetic grains, although the domain state may be somewhat uncertain, as was reported by Radhakrishnamurty and Likhite (1987). It may be pointed out in this context that the measurement of any parameter, especially for a mixture, may be subjected to experimental limitations which could be insurmountable. The measured value of a parameter could be the result of those of the different components of the mixture and it may not be possible to separate the value of each of the component. For example, if a sample contains a mixture of low and high coercive force materials, the measured value of this parameter would be the result of the two individual values and would depend on the relative proportions of the components which might not be easy to estimate from the overall behaviour (Radhakrishnamurty and Sahasrabudhe 1965). At best the parameters for a rock sample could lead to qualitative inferences on the nature of the magnetic grains present. Also, it will be ideal if all the parameters could be measured, preferably by some non-destructive methods, on the same core sample that was used for the natural remanent magnetization (NRM) measurements. In this paper, a brief review of the methods for the study of the magnetic grains in rocks, their usefulness and limitations is presented.

2. Magnetic parameters for basalts

NRM studies are usually carried out on standard core samples of 2·5 cm in diameter and about the same length. The susceptibility of the core samples, both at room and liquid nitrogen temperatures, may be measured by the method suggested by Radhakrishnamurty *et al* (1979), either before or after the NRM studies. However, the Curie temperature, saturation intensity and saturation remanence could be determined only after the completion of NRM studies on the cores. These parameters can be obtained on standard core samples by the procedures described by Radhakrishnamurty and Likhite (1970, 1987), though other methods employing smaller samples are more commonly used. Nevertheless, it is important to get as many parameters as possible on the same core sample, so that they could be inter-related. Even then, these parameters could fail to elucidate the actual situation adequately, if the magnetic grains in a sample are of mixed domain states and compositions. This problem was discussed to some extent earlier (Radhakrishnamurty *et al* 1981). Based on the extensive studies on basalts of different ages ranging from less than a million to more than a billion years, and on the general magnetic behaviour of magnetic materials, the following conclusions could be drawn:

(i) The magnetic susceptibility of a dilute sample will depend on the domain state of the grains, even if all the grains are of one uniform composition, as can be inferred from the hysteresis behaviour of multidomain (MD), optimum single domain (SD) and superparamagnetic (SP) particles described by Beans (1955). Although the actual measurements of susceptibility on samples containing different domain states are very few in the literature, it is common knowledge that SD samples will show a minimum value and SP the maximum with MD between these two extremes.

(ii) Saturation intensity of magnetization (J_s) of a sample does not depend on the domain state of the grains provided a sufficiently large field is used for the determination. But the saturation ramanence (J_r) is dependent on the domain state. Thus, the value of the relative remanence (J_r/J_s) will be quite small (0·1) for MD and SP grains, whereas it will be 0·5 for SD grains with uniaxial anisotropy and 0·8 for particles with cubic anisotropy.

(iii) The coercive force (H_c) is highly dependent on the domain state of the grains in the sample; it being very small for MD and SP particles and attaining the optimum value for the SD state for any one magnetic material.

(iv) For determination of the Curie temperature, the two methods generally used are the low-field (susceptibility vs temperature, $\chi - T$) and the high field ($J - T$), whose relative advantages and disadvantages have been discussed by Radhakrishnamurty *et al* (1979). The shape of the $\chi - T$ curve depends considerably on the etic grains in basalts by magnetic methods was proposed (Radhakrishnamurty Also from the extensive magnetic studies on basalts it has been pointed out akrishnamurty and Likhite 1987) that the H_c at 77 K could provide dependable ation on the nature of the iron oxide grains in the sample concerned. For the t study, all the high field properties were measured in a peak field of 500 mT. This might not have saturated all types of samples and hence the symbol J_m enting the maximum intensity of magnetization, instead of J_s, has been used in ting the results.

ults and discussion

1 shows some of the parameters for basalts of different ages, obtained by the use -destructive magnetic methods. However, the ages of the samples have not been as they are not essential for the present discussion. The results have been ted on the basis of an increasing value of relative susceptibility (RS) (ratio of tibilities at 77 and 300 K, χ_{77}/χ_{300}). The main reasons for this emphasis on the RS are (i) very low values of RS (0·1) clearly indicate the presence of titanomagnetite with 60% to 70% of ulvospinel in solid solution with magnetite, abbreviated as and TM70 respectively and (ii) any RS value with the association of a tibility peak at about 120 K, the isotropic point of magnetite will imply the

Table 1. Some magnetic parameters for selected basalt samples.

RS	Peak in χ	H_c (mT) at 300 K	H_c (mT) at 77 K	J_r/J_m at 300 K	J_r/J_m at 77 K	% increase in J_m
0·06	—	2·3	180·0	0·05	0·67	19
0·12	—	4·0	222·8	0·12	0·56	50
0·12	—	16·1	106·0	0·12	0·63	13
0·29	—	10·1	153·0	0·27	0·56	56
0·30	—	4·0	44·4	0·10	0·20	8
0·50	—	27·5	95·0	0·25	0·46	2
0·53	—	9·0	18·5	0·12	0·19	1
0·68	—	19·6	60·0	0·31	0·29	21
0·70	—	32·4	60·0	0·34	0·23	20
1·08	—	39·2	51·0	0·29	0·25	17
1·17	—	16·0	15·9	0·18	0·12	14
1·44	—	23·0	23·0	0·15	0·12	100
1·41	1·52	36·4	27·7	0·43	0·25	17
1·32	1·53	40·9	37·0	0·36	0·46	28
1·30	1·53	10·8	23·0	0·17	0·16	29
1·19	1·43	36·4	32·3	0·41	0·29	28
0·70	1·44	36·4	64·7	0·36	0·36	14
0·47	1·30	13·9	32·4	0·20	0·30	3
0·46	1·36	9·2	36·5	0·08	0·15	28

-relative susceptibility χ_{77}/χ_{300}; peak in χ shows the susceptibility peak at around 120K, if any; H_c, J_r were measured in a peak field of 500 mT; the last column shows the percentage increase in J_m when the is cooled from 300 to 77 K.

presence of multidomain magnetite grains in the sample concerned. It may be mentioned in this context that the studies on basalts of different ages have also indicated that the multidomain magnetite can occur together with some SD magnetite and/or cation deficient magnetite only, and rarely with other titanomagnetites.

Although the RS value between 0·1 and 1·3 seems to have a specific relation with the composition in the case of synthetic titanomagnetites (see Radhakrishnamurty *et al* 1981), it may not often hold good in the case of basalts due to the mixed nature of the iron oxide grains present. As a matter of fact, a mixed domain state and more than one composition of the iron oxide grains in rocks cause non-compatibility among the different magnetic parameters. On the other hand, the very same non-compatibility will indicate the mixed nature of the iron oxide grains. Some of the interesting points that could be visualized from the results presented in table 1 are as follows:

(i) Rock samples showing nearly the same RS value can differ considerably in their H_c values at 77 K (e.g. CR5 and CR68; 262 and M4).

(ii) High values of H_c at 300 K are often associated with high J_r/J_m values (e.g. 21, E24, E21). These features normally indicate the presence of considerable proportion of SD grains in the sample concerned.

(iii) Large increase in the values of H_c and J_r/J_m at 77 K compared to those at 300 K indicates the presence of significant amount of SP fraction in them (e.g. 332, CR23). Such an increase will be limited to a factor of two or less in the case of SD samples (e.g. R21, CR51). Also these large changes pertain to samples containing TM60 to TM70 grains (Radhakrishnamurty *et al* 1981).

(iv) Samples containing MD magnetite (inferred from the presence of a susceptibility peak—E24 downwards in table 1) generally show small changes—increase or decrease—in H_c and J_r/J_m values with temperature.

(v) An increase in J_m for the samples, when cooled from 300 K to 77 K (column 8), will depend on the composition of different TM grains and their relative proportions. The sample CR23 showed the highest H_c (222·8 mT) at 77 K. The coercive force at 77 K for TM68 is 180 mT and for TM80 it is 250 mT and further TM80 is non-magnetic at 300 K (Radhakrishnamurty *et al* 1981). In view of this, a reasonable explanation for the behaviour of CR23 may be that it contains some TM80 grains besides others, whereby the resultant H_c could be as high as 222·8 mT at 77 K. It is interesting to note that this sample, containing even probably some amount of TM80, showed an RS value of 0·12 which is nearly the same as that expected for TM60 and TM70 (Radhakrishnamurty *et al* 1981). An important implication of these observations is that the presence of TM80 grains, in association with TM60 or TM70 in a rock sample, can be deciphered, probably by the measurement of H_c at 77 K only.

(vi) The very large (100%) and quite small (1%) increases in J_m shown by some samples when cooled to 77 K, are somewhat unexpected and difficult to explain and need further investigations for elucidation.

Thus the data presented in table 1 can provide a broad perspective of the limits within which the values of different magnetic parameters of basalts could lie.

In the case of samples from diabase dykes from northwest Greenland, Murthy *et al* (1981) showed that the remanence carriers were essentially SD grains but the overall magnetic behaviour of the samples was soft, probably dominated by other domain states. In another recent study (Smith and Banerjee 1986), ed, the complexity of attempting a correlation between them was discussed. ors stated "it is possible that the TRM-ARM anology is not valid for this y, but it seems likely that some, if not all, of the observed behaviour is due to ". Alteration could thus produce different compositions and domain states e mineral grains which in turn could bring about incompatibility amongst compatible magnetic parameters. The non-destructive methods described ould be useful to identify if a particular rock sample indicates mixed on and domain states or single uniform composition and one domain state.

sions

value of coercive force (> 200 mT) at 77 K shown by a basalt may be used for ng the presence of titanomagnetite grains that are non-magnetic at ambient ratures.

composition and domain states of the magnetic grains commonly present in s may cause incompatibility among otherwise compatible magnetic eters.

s

955 Hysteresis of mixtures of ferromagnetic micro-powders, *J. Appl. Phys.* **26** 1381–1383

, Patzold R and Brown R 1981 Source of stable remanence in certain intrusive rocks; *Phys. Earth nter.* **26** 72–80

hamurty C 1985 Identification of titanomagnetites by simple magnetic techniques and on to basalt studies; *J. Geol. Soc. India* **9** 640–651

hamurty C and Likhite S D 1970 Hopkinson effect, blocking temperature and Curie points in *Earth Planet. Sci. Lett.* **7** 389–396

hamurty C and Likhite S D 1987 A pulsed field technique for study of magnetic grains in rocks; *rth Planet. Inter.* **46** 259–262

hamurty C and Sahasrabudhe P.W 1965 Abnormal hysteresis loops of some magnetic materials s; *Curr. Sci.* **34** 338–340

hamurty C, Deutsch E R and Murthy G S 1979 On the presence of titanomagnetites in basalts; *J.* . **45** 443–446

hamurty C, Likhite S D, Deutsch E R and Murthy G S 1981 A comparison of magnetic es of synthetic titanomagnetites and basalts; *Phys. Earth Planet. Inter.* **26** 37–46

hamurty C, Likhite S D, Deutsch E R and Murthy G S 1982 On the complex magnetic ur of titanomagnetites; *Phys. Earth Planet. Inter.* **30** 281–290

M and Banerjee S K 1986 Magnetic structure of the upper kilometre of the marine crust at Deep ling Project Hole 504B, Eastern Pacific Ocean; *J. Geophys. Res.* **91** 10337–10354

Hydroclimatic fluctuations of the Upper Narmada catchment and its association with break-monsoon days over India

NITYANAND SINGH, M K SOMAN and K KRISHNA KUMAR
Indian Institute of Tropical Meteorology, Pune 411 005, India

MS received 14 March 1988; revised 22 July 1988

Abstract. In this paper, hydroclimatic fluctuations of the Upper Narmada catchment (upto Narmadasagar damsite) have been studied by examining the time series (1901–80) of (i) 1-to 10-day annual extreme rainfall; (ii) seasonal total rainfall between May and October; (iii) the precipitation concentration index (PCI); (iv) a modified version of PCI (MPCI); and (v) parameters of the periods contributing specified percentages of rainfall to annual total. Most of these parameters followed the normal distribution and did not show any significant long-term trend. However, some dominant long period oscillations have been noticed in extreme rainfall, seasonal rainfall, PCI and MPCI series. Influence of break-monsoon days over India during July and August on the rainfall activities of the Upper Narmada catchment has also been investigated and salient findings discussed.

Keywords. Seasonal rainfall; precipitation concentration index; hydrological floods and droughts; rainfall period; break-monsoon days.

1. Introduction

Information on the variability of rainfall processes over an area is vital for a variety of practical problems linked to rainfall. The present study provides such information on the interannual and long term features of the rainfall over Upper Narmada catchment (upto Narmadasagar damsite), where a gigantic multipurpose water resources project is to commence. Realizing the importance of the area, several studies have been undertaken to understand its long term rainfall characteristics.

Ramana Murthy *et al* (1987) examined the time series (1901–80) of monthly and total seasonal rainfall of June through September and annual rainfall exclusively of Upper Narmada catchment for long term trends. They found a rising trend in the seasonal and annual rainfall from the beginning of the century till 1945 and oscillatory changes later around the long term mean. Monthly rainfall values fluctuate around their long term means. Chaturvedi and Srivastava (1981) also reported an 80-year (1891–1970) long series of area-averaged annual rainfall for the entire Narmada catchment but did not discuss the characteristics of the rainfall series. Close similarity between the rainfall series reported in the above two studies is noteworthy.

Using 60 years' (1901–60) data of 230 stations, Parthasarathy and Dhar (1976) presented time series analysis of area-averaged annual rainfall over the eastern Madhya Pradesh (MP) and the western MP separately, and reported an increasing trend in the rainfall of east MP up to 1935 and that up to 1945 in west MP. In the case of annual rainfall, their study suggests a decreasing trend for the eastern MP after 1935 whereas for the western MP the series fluctuates around its mean after 1945.

In a separate study, using data of one raingauge station from each district, Parthasarathy (1984) calculated change in the mean summer monsoon rainfall (June to September) from the period 1871–1924 to the period 1925–1978 over east MP and west MP and found an increase of 5·9% (statistically significant at 10% level) in the rainfall of west MP and a decrease of 4·6% (statistically not significant) in east MP.

These studies, though useful for understanding the climate variability of the area, are of limited practical value. In the present study we propose to examine the finer details of the rainfall processes in addition to seasonal total so that useful information on rainfall characteristics can be provided to the water-based enterprises of the Upper Narmada catchment. The parameters of the rainfall processes over Upper Narmada catchment selected for the study are as follows:

(i) Area-averaged extreme rainfall of durations ranging from 1 to 10 days.
(ii) Area-averaged seasonal total rainfall during May to October, its time distribution characteristics and the combined characteristics of May-October rainfall and its time distribution.
(iii) The starting and the ending dates and the length of different periods contributing to each of 2, 5, 10, 20,... 90 and 95% rainfall to the annual total.

The association between break-monsoon days during the principal monsoon months of July and August (an important regional aspect of summer monsoon circulation) and the rainfall activities over Upper Narmada catchment is also investigated to understand the mechanism of rainfall fluctuations over the area.

2. Physiographic and climatic features

Narmada river originates from the Maikal ranges of the Vindhyas and after traversing a distance of about 1304 km nearly in the east-west direction at latitudes between 20° and 23°N, through the states of MP, Maharashtra and Gujarat—the maximum being in MP, it meets the Arabian Sea near Broach. It is a perennial river and the fifth largest in the country. However, in the present study we have considered the upper part of the catchment, upto Narmadasagar damsite in the downstream (figure 1). The total area of the Upper Narmada catchment is approximately 65,000 km^2 with an average elevation of 500 m above the sea level. Normally, this catchment receives larger rainfall compared to its surroundings. The annual isohyetal pattern displays decreasing magnitude from east to west, except for the two pockets of heavy rainfall (exceeding 1600 mm) in the Maikal ranges and around Pachmarhi (figure 1). The mean annual rainfall over the Upper Narmada catchment is 1252 mm of which 90% is contributed by the southwest monsoon system during June through September.

In general, the rainfall activities over this area are controlled by movement of the low pressure systems (the most common synoptic situation associated with monsoon activity) and depressions, and orography contributes to the enhancement of rainfall (Srinivasan *et al* 1971). According to a rough estimate, 80–90% of the annual rainfall over Narmada catchment occurs in association with disturbances (inclusive of lows, storms and depressions) of the monsoon season (Pant *et al* 1969). However, Raghavan (1973) showed that this anomalous rainfall is not because of orographic effect but primarily due to the presence of the monsoon trough over this area at 700 mb. In the

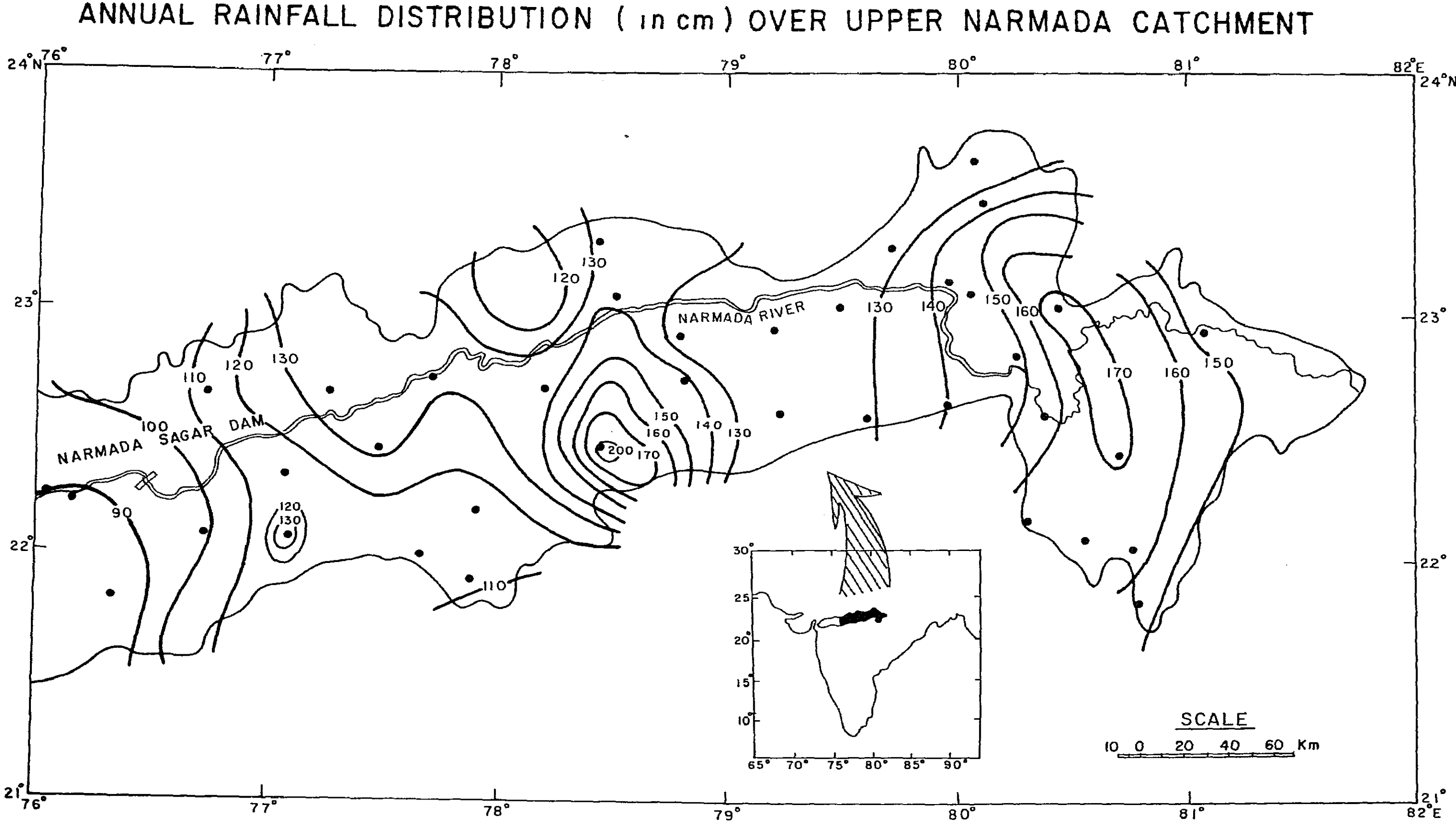

Figure 1. Location of the study area and the network of 38 raingauge stations. Continuous lines are the isopleths of the mean annual rainfall.

layer between 2·1 and 3·0 km (Banerji *et al* 1967). Raghavan (1973) explained that the 700 mb (3 km) level takes maximum advantage of the monsoon trough axis and its associated upward motion and produces greater rainfall around 23°N—the central part of the Upper Narmada catchment. According to Bedekar and Banerjee (1969) a trough zone forms over the central India right from the start of a depression in the Bay of Bengal which produces concentrated rainfall in the longitudinal belt of 80° to 81°E. It seems heavy rainfall results from the interactions between the monsoon trough, the low pressure systems and the orography. But this complicated process is not well understood.

On an average, one storm/depression, which forms over the Bay of Bengal during the monsoon season and moves in a west-northwest direction, passes over the eastern part of the catchment (see Ramage 1971). Narmada catchment lies slightly south of the mean depression path and receives heavy rainfall even from those disturbances whose surface centres are to the north of the catchment. Monsoon storms/depressions produce more rainfall in their southwest and southern sectors (Sikka 1977). Some of the storms/depressions maintain their west-northwesterly course through the catchment and cause severe floods (Pant *et al* 1969). Other physiographic details of the catchment (Mistry and Thatte 1969) and climatology of the area (Srinivasan *et al* 1971; IMD 1981) have been reported earlier.

3. Rainfall data

Location of 38 raingauge stations whose daily data for the period 1901–80 are used in the analysis is given in figure 1. For individual stations the period of record varies from 60 to 80 years. Based on available records, the mean rainfall for the catchment for each calendar date of the period 1901–80 is obtained through arithmetic averaging. From this area-averaged daily rainfall data the proposed parameters to be investigated were evaluated following the procedure given below. The basic statistical features of different parameters are also given.

4. Rainfall parameters and statistical properties

4.1 *1- to 10-day extreme rainfall*

For providing the desired information on rainfall characteristics for hydrologic design purposes as well as for flood severity assessment, characteristics of the extreme rainfall of wide ranging durations from 1 to 10 days have been studied for the Upper Narmada catchment. Extreme rainfall amount for each of 1, 2, 3 up to 10-day durations has been picked up year after year to form the extreme rainfall series of selected durations. The basic statistical properties, viz mean, standard deviation and coefficient of variation of different extreme rainfall series based on 80 years (1901–80) data are given in table 1. The mean of extreme rainfall for 1- to 10-day increases in nonlinear manner from 65 to 258 mm and they exhibit variability (C V) of 21 to 27%. The normality aspect of each extreme series has been tested by employing Fisher's g-statistic test to understand the nature of its frequency distribution. The coefficients of skewness (g_1) and kurtosis (g_2) and error statistics $g_1/\mathrm{SE}(g_1)$ and $g_2/\mathrm{SE}(g_2)$ (SE denotes standard error) for different

Table 1. Statistical parameters of the 1- to 10-day extreme rainfall, May–October total rainfall and PCI for Upper Narmada catc

Parameter	1-day	2-day	3-day	4-day	5-day	6-day	7-day	8-day	9-day	10-day	M–O
Mean (mm)	65·1	105·9	132·9	153·2	170·52	188·1	206·4	223·9	242·2	258·2	1174·4
SD (mm)	15·0	27·8	35·76	41·4	45·05	46·8	47·6	49·8	52·9	54·5	217·5
CV (%)	23·0	26·2	26·9	27·0	26·4	24·9	23·1	22·2	21·8	21·1	18·5
g_1	0·29	0·38	0·72	0·96	0·99	0·88	0·69	0·63	0·63	0·60	0·09
g_2	−0·37	−0·60	0·00	0·64	0·72	0·49	0·02	−0·2	−0·2	−0·3	−0·14
g_1/SE(g_1)	1·07	1·42	2·68*	3·56*	3·67*	3·27*	2·58*	2·33*	2·33*	2·22*	0·34
g_2/SE(g_2)	−0·69	−1·12	0·01	1·20	1·35	0·92	0·04	−0·38	−0·39	−0·56	−0·27

*Statistically significant at 5% level and above.

rainfall series are given in table 1. The test analysis shows that the rainfall series for 1- and 2-day durations follow approximately the normal distribution, whereas it is skewed for longer durations.

4.2 *May to October rainfall*

Over Upper Narmada catchment, the May–October (M–O) rainfall with a mean of 1174·4 mm contributes 93·8% to the annual total and is considered as the period of rainy season. The parameters of the basic statistical features and normality test for M–O rainfall series are given in table 1. This rainfall exhibits a variability of 18·5% and follows the normal distribution.

4.3 *Time distribution of May–October rainfall*

Apart from the total rainfall, features of the time distributions of seasonal rainfall are also equally important. The time distribution of May–October rainfall is quantified here by computing Oliver's precipitation concentration index (PCI) using 3-day (triad) rainfall totals. The index is defined as (Sato *et al* 1985),

$$\mathrm{PCI}_j = \frac{\sum_{i=1}^{N} X_{ji}^2}{(\sum X_{ji})^2} \times 100, \tag{1}$$

where X is the triad rainfall, N the number of triads ($=61$) and j indicates the particular year, i.e. $j = 1, 2, \ldots, 80$.

After experimenting with daily, triad, pentad (5-day), weekly, decade (10-day) and monthly rainfall, 3-day total rainfall has been found optimum for computing PCI for hydrological purposes. Using short period (say daily) rainfall may underestimate the PCI values because of splitting of long and intense rain events into smaller rainfall amounts. On the other hand, longer period rainfall totals may overestimate the PCI because of pooling of smaller rainfall amounts. The characteristic property of PCI is that its high value (more than normal) indicates occurrence of rainfall in concentrated manner whereas a low value (less than normal) indicates well-distributed rainfall in time.

Mean, standard deviation, coefficient of variation and parameters of normality test for PCI series are given in table 1. The PCI series with a mean of 4·93% exhibits variability of 20% and is significantly different from normal distribution as indicated by Fisher's g-statistic test.

4.4 *The modified precipitation concentration index (MPCI)*

In order to assess rainfall of a year as hydrologically flood or drought, an index is evolved by a linear combination of May–October rainfall and its time distribution (PCI). For evaluating the index, firstly the mean of the standardized May–October rainfall and PCI is obtained year after year to form a third series,

$$\mathrm{XPCI}_i = \frac{1}{2}\left[\frac{\mathrm{PCI}_i - \overline{\mathrm{PCI}}}{\sigma_{\mathrm{PCI}}} + \frac{R_i - \bar{R}}{\sigma_{\mathrm{R}}}\right], \tag{2}$$

where XPCI is the element of the third series, $\overline{\text{PCI}}$ and σ_{PCI} are the mean and standard deviation of the PCI series and $\bar{R}$ and σ_R are the mean and standard deviation of the rainfall series respectively. The XPCI series is then normalized to form the series of a new index, designated as the modified precipitation concentration index (MPCI)

$$\text{MPCI}_i = (\text{XPCI}_i - \overline{\text{XPCI}})/\sigma_{\text{XPCI}}. \tag{3}$$

A high value (more than normal) of MPCI indicates the occurrence of high rainfall in few intense spells, whereas its low value (less than normal) indicates the occurrence of a low rainfall in a large number of spells. However, numerous combinations, probably infinite, are possible between different magnitudes of rainfall and PCI.

A large rainfall in a few spells may transform its major portion into run off and may result in floods. Run off component will be drastically reduced if the low rainfall is spread over a larger number of spells causing drought from a hydrological point of view. Depending on the magnitude of MPCI, the flood/drought year has been further categorized as normal, moderate flood/drought, severe flood/drought and disastrous flood/drought by giving arbitrary thresholds of $\pm\frac{1}{2}$, ± 1, ± 2 and $\gtrless \pm 2$ ($+$ denotes flood and-drought) to MPCI. However, there exists a highly significant (at 0·1% level) correlation ($r = 0{\cdot}50$) between May and October rainfall and MPCI, which shows that the seasonal total rainfall is a good indicator for a year to be hydrologically a flood or a drought but MPCI provides more exact information required for the purpose.

The MPCI series for Upper Narmada catchment is significantly different from the normal distribution as indicated by Fisher's g-statistic test.

4.5 *The period contributing specified percentages to annual total*

The different facets of the rainfall season viz its starting and ending dates, its length and its amount exhibit large variability. To demarcate the average period of the rainy season over a station or place numerous criteria can be traced in the literature; there does not appear to be a uniform criterion to demarcate the period of rainy season during a particular year over different rainfall regimes of India (Singh 1986). Rather than demarcate the period of rainy season yearwise over the Upper Narmada catchment, we picked up the period of shortest duration which contributed a fixed percentage of rainfall to the total rainfall of the year. In order to provide information on rainy season for a variety of practical problems we have picked up the rainfall period year after year which has contributed each of 2, 5, 10, 20, ... 90 and 95% rainfall to the annual total and examined the statistical features of their parameters. The procedure for getting the rainfall period for a given percentage of annual total is given below.

The process started by picking 1-day highest rainfall amount of a year and comparing it with 2% value of the annual total. In case the 1-day extreme rainfall fell short of the 2% value of the annual rainfall, the extreme 2-day rainfall was picked up for comparison. As soon as the extreme amount of a certain duration equalled or exceeded the 2% value of the annual rainfall, the starting and ending dates of the period were noted, and the values compared with 5% value of the annual rainfall. The process of hydrology, agriculture and forestry.

The basic statistical properties and parameters of the g-statistic test for starting and ending dates and length for different rainfall periods are given in tables 2, 3 and 4 respectively. The earliest and the latest observed starting and ending dates and the shortest and longest length of each rainfall period are also given in the tables along with the year.

4.5a *Starting date.* The mean starting date of the period contributing rainfall up to 10% to the annual total is in the first or second week of August, but it exhibits standard deviation of 3 weeks, which suggests that the period of occurrence of most intense rainfall activities of the year fluctuates abruptly from one year to another. In extreme cases the 10% rainfall period can start as early as 18th June (1921) and as late as 23rd September (1916). The mean starting date for higher percentages shifts monotonically to July, June and May months with increase of percentage values. The standard deviation of the starting date for the rainfall periods up to 90% is 10–25 days which is quite large. Interestingly, as indicated by g-statistic test the frequency distribution of starting date of the rainfall period up to 80% is, by and large, normal.

4.5b *Ending date.* For lower percentage rainfall periods (say up to 30%) the mean ending date is in the first or second week of August, and for higher percentages it shifts monotonically to the months of September and October. Like the starting date, the ending date of the lower rainfall periods also exhibits large (more than 3 weeks) standard deviation. The frequency distribution of the ending date for rainfall periods up to 80% is normal (table 3).

4.5c *Length of period.* The basic statistics and parameters of the normality test for the length series of different rainfall periods are given in table 4. It may be interesting to note that every year 1-day extreme rainfall contributes at least 2% to the annual total over the Upper Narmada catchment. On an average, 50% of the annual rainfall over the area occurs just in 41 days and up to 80% in 81 days. However, from 80% to 90% it requires an additional 37 days, and from 90% to 95% another 50 days. For 90% (30 days) and 95% (52 days) rainfall periods the standard deviation of the length series is also quite large. Except for 5, 10, 80 and 90% rainfall periods, the frequency distribution of the length series is normal. From the analysis it is inferred that the 80% rainfall period could be considered as the period of reliable rainfall.

In the mean, the 80% rainfall period starts on 24th June and ends on 12th September. In extreme cases, this period can start as early as 2nd June (1938) and end as late as 8th October (1903) and can have shortest length of 35 days (1930) and longest length of 111 days (1916).

5. Time series analysis

In this section, the time series of each of the above mentioned parameters are examined for long term trends. In the investigation student's t-test for difference in the mean between two equal subperiods, and Mann-Kendall (MK) Rank test (τ) for randomness against trend have been employed. These two tests can be applied for detecting linear as

Table 2. Statistical parameters of starting date of different rainfall periods in Upper Narmada catchment.

	Annual rainfall (%)											
Parameter	2	5	10	20	30	40	50	60	70	80	90	95
Mean (date/month)	10/8	8/8	4/8	29/7	26/7	26/7	16/7	8/7	2/7	24/6	11/6	5/5
SD (days)	24·3	24·7	24·0	22·2	20·9	17·2	15·0	12·8	9·9	9·9	22·4	51·0
g_1	0·13	0·09	0·12	0·21	0·05	0·21	0·10	0·05	0·63	0·20	2·80	0·86
g_2	−0·91	−0·81	−1·03	−0·76	−0·93	−0·91	−0·65	−0·17	0·23	−0·27	10·23	−0·81
$g_1/SE(g_1)$	0·47	0·33	0·46	0·79	0·17	0·77	0·36	0·18	2·33*	0·73	10·39*	3·18*
$g_2/SE(g_2)$	−1·72	−1·52	−1·93	−1·43	−1·74	−1·82	−1·22	−0·32	0·44	−0·52	19·23*	−1·53
Earliest	28/6	14/6	18/6	13/6	10/6	21/6	7/6	5/6	2/6	2/6	11/2	2/1
Year	17, 45	19	21	21	10	41	38	38	38	38	07	38
Latest	25/9	24/9	23/9	21/9	4/9	28/8	14/8	5/8	25/7	17/7	5/7	2/7
Year	16	16	16	16	54	54	05	55	34	03	23	23

*Statistically significant at 5% level and above.

Table 3. Statistical parameters of ending date of different rainfall periods in Upper Narmada catchment.

Parameter	Annual rainfall (%)											
	2	5	10	20	30	40	50	60	70	80	90	95
Mean (date/month)	10/8	9/8	7/8	8/8	13/8	18/8	25/8	30/8	4/9	12/9	5/10	18/10
SD (days)	24·3	24·6	24·0	22·8	21·5	18·0	18·0	15·4	12·4	11·7	24·3	27·0
g_1	0·13	0·11	0·16	0·36	0·35	0·38	0·21	0·24	0·01	0·05	1·19	0·87
g_2	−0·91	−0·81	−1·02	−0·60	−0·83	−0·67	−0·88	−0·40	−0·30	−0·15	0·89	0·09
g_1/SE(g_1)	0·47	0·39	0·58	1·33	1·30	1·42	0·77	0·88	0·02	0·18	4·44*	3·23
g_2/SE(g_2)	−1·72	−1·52	−1·92	−1·13	−1·55	−1·25	−1·66	−0·74	−0·56	−0·28	−1·67	0·16
Earliest	28/6	15/6	21/6	23/6	6/7	15/7	24/7	1/8	6/8	12/8	27/8	2/9
Year	17, 45	19	21	21	10	45	6	32	13	30	7	13
Latest	25/9	25/9	26/9	6/10	27/9	1/10	6/10	6/10	6/10	8/10	14/12	26/12
Year	16	16	16	16	49	54	16	16	16	03	67	9

*Statistically significant at 5% level and above.

Table 4. Statistical parameters of length of different rainfall periods in Upper Narmada catchment.

	Annual rainfall (%)											
Parameter	2	5	10	20	30	40	50	60	70	80	90	95
Mean (days)	1	1·5	3·6	10·6	19·3	29·8	41·2	51·6	65·8	80·7	116·8	166·8
SD (days)	—	0·6	1·3	3·1	5·4	7·2	8·9	10·1	10·1	12·2	29·7	51·9
g_1	—	0·68	0·75	0·28	0·24	0·12	0·20	0·06	0·05	0·72	1·12	0·53
g_2	—	−0·51	−0·72	0·15	−0·02	−0·21	0·01	−0·21	0·15	0·63	0·61	−0·68
$g_1/\mathrm{SE}(g_1)$	—	2·52*	2·77*	1·06	0·88	0·44	0·73	0·21	0·20	2·66*	4·18*	1·96
$g_2/\mathrm{SE}(g_2)$	—	−0·95	−0·33	0·28	−0·03	−0·39	0·01	−0·39	0·28	1·19	1·14	−1·28
Shortest	1	1	2	4	8	14	16	28	41	55	79	89
Year				72, 74	74, 79	72, 74	72	72	30	30	72	69
Longest	1	3	7	19	34	49	63	80	94	111	209	297
Year		34, 36, 38, 58	36, 58	17, 36	16	16	16	16	16	16	19	79

*Statistically significant at 5% level and above.

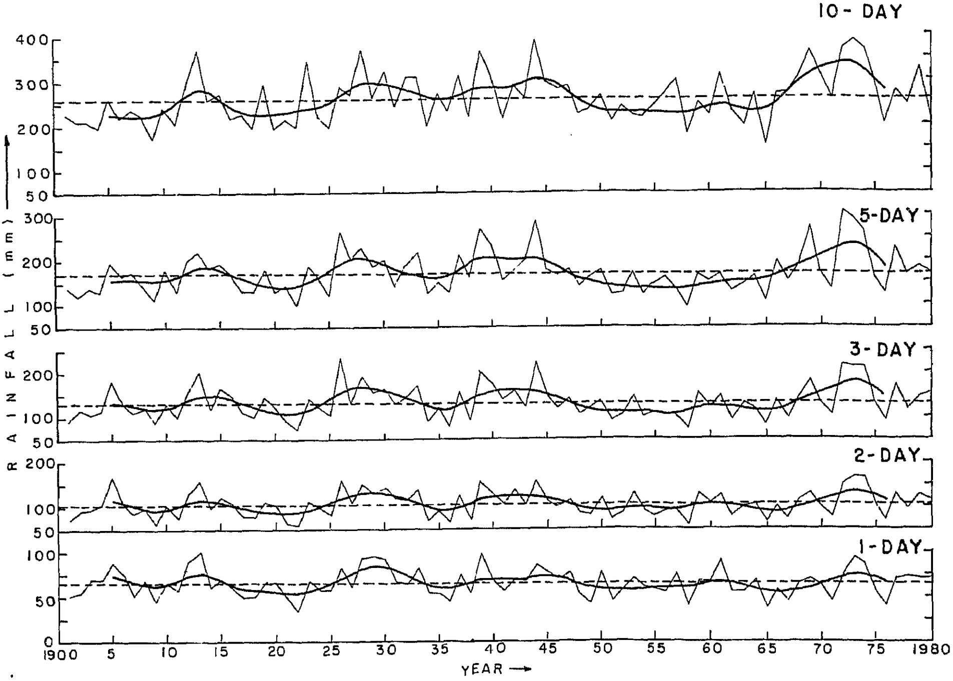

Figure 2. Time series plots of the area-averaged extreme rainfall over Upper Narmada catchment (thin line) for 1, 2, 3, 5 and 10-day durations. Thick line indicates the filtered (9-point gaussian low pass) values of the corresponding series.

well as nonlinear type of trends (WMO 1966). An abstract of the results of the analysis is given below.

5.1 *1- to 10-day extreme rainfall*

Though t and τ tests have been applied to each of the 1- to 10-day extreme rainfall and results discussed, the actual series is presented only for the five chosen, viz 1, 2, 3, 5 and 10-day durations (figure 2). The individual series smoothed by a 9-point gaussian low pass filter (WMO 1966) are also presented in figure 2 along with the actual series. The statistical tests do not show any significant long term trend in extreme rainfall series, and hence there is no indication that the storm rainfall intensity, and consequently severity of floods, over the Narmada catchment undergoes any significant change. However, from the filtered version of different extreme rainfall series four epochs of both the above and the below normal rainfall can be marked. In order to investigate whether there is any dominant periodicity in these extreme rainfall series, spectral analysis has been carried out which is discussed in a separate section.

5.2 *May–October rainfall, PCI and MPCI*

The time series of May–October rainfall, PCI and MPCI for Upper Narmada catchment are presented in figure 3. In MPCI series years with different categories of

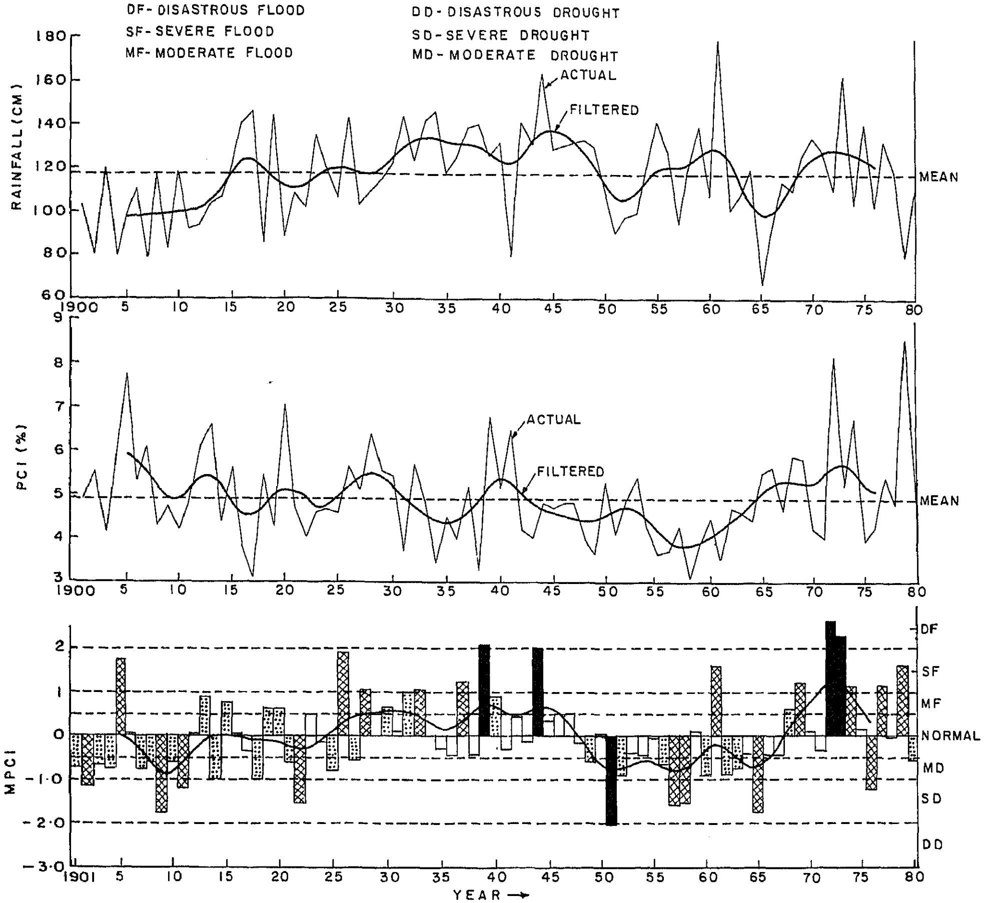

Figure 3. Time series plots of the May–October rainfall, PCI and MPCI. In MPCI series years with different categories of floods/ droughts are shaded differently. Thick line indicates filtered values.

floods/droughts are marked. Smoothing of high frequency waves in each series is done by applying the 9-point gaussian low pass filter and is presented in figure 3 along with the actual series.

Large year-to-year variability in the values of each series can be seen. Application of t and τ tests does not show any significant long term trend, and the three series can be assumed to be homogeneous.

A careful examination of rainfall and PCI series reveals that in general they fluctuate in the opposite manner. The negative correlation ($r = -0{\cdot}495$) between rainfall and PCI is significant at 0·1% level. The opposite association between seasonal rainfall and its time distribution (PCI) suggests that during good rainfall years, the rains will be distributed, by and large, throughout the period of rains. The fluctuation of MPCI, however, is fairly correlated with the seasonal total rainfall ($r = 0{\cdot}502$). Therefore, to a large extent total rainfall is sufficient to identify a year as a flood or drought year even for hydrological purposes.

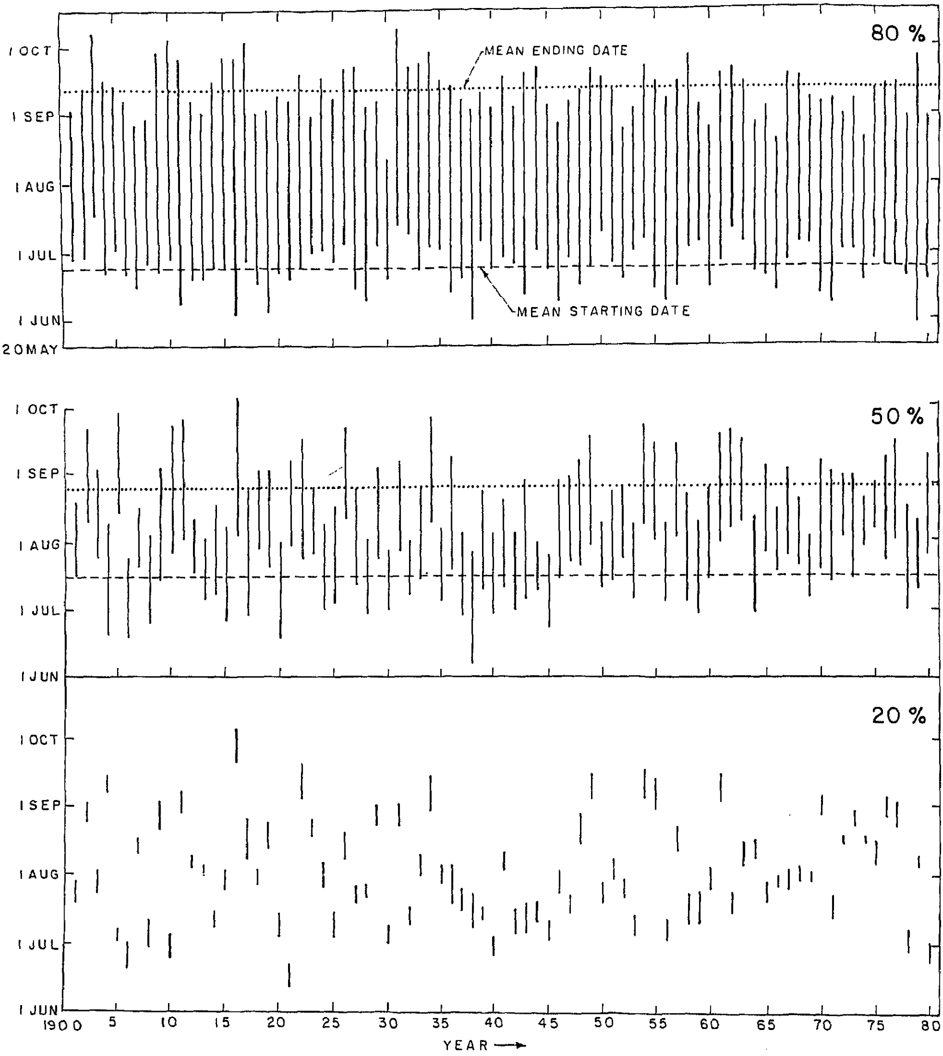

Figure 4. Time series plots of the starting and ending dates and the length of the shortest period contributing 20, 50 and 80% rainfall to the annual total over Upper Narmada catchment. For 50 and 80% rainfall periods the means of starting and ending dates are also presented.

5.3 *Starting and ending dates and length of the rainfall periods*

The time series of starting and ending dates and the length for chosen rainfall periods of 20, 50 and 80% values are presented in figure 4. For a given rainfall period, after marking the starting and ending dates of a particular year they are joined by a thick line to represent the length of period. Student's t and MK τ tests show that the starting and ending dates and the length series of different rainfall periods do not possess any trend.

The parameters of the period of major rainfall activities over the catchment area are stationary and hence no attempt is made to analyse them further.

application. We have adopted here the method based on computing discrete Fourier transform (DFT). It is basically a harmonic analysis followed by some additional statistical manipulation. Details of estimating DFT power spectra and testing them for statistical significance are given by Schickedanz and Bowen (1975).

Normalized, smoothed spectral estimates of the selected extreme rainfall series as well as May–October rainfall, PCI and MPCI series are presented in figure 5. For convenience, the spectra are presented by taking the wave period on logarithmic scale along the abscissa. It is seen from the spectra that considerable power is contained in

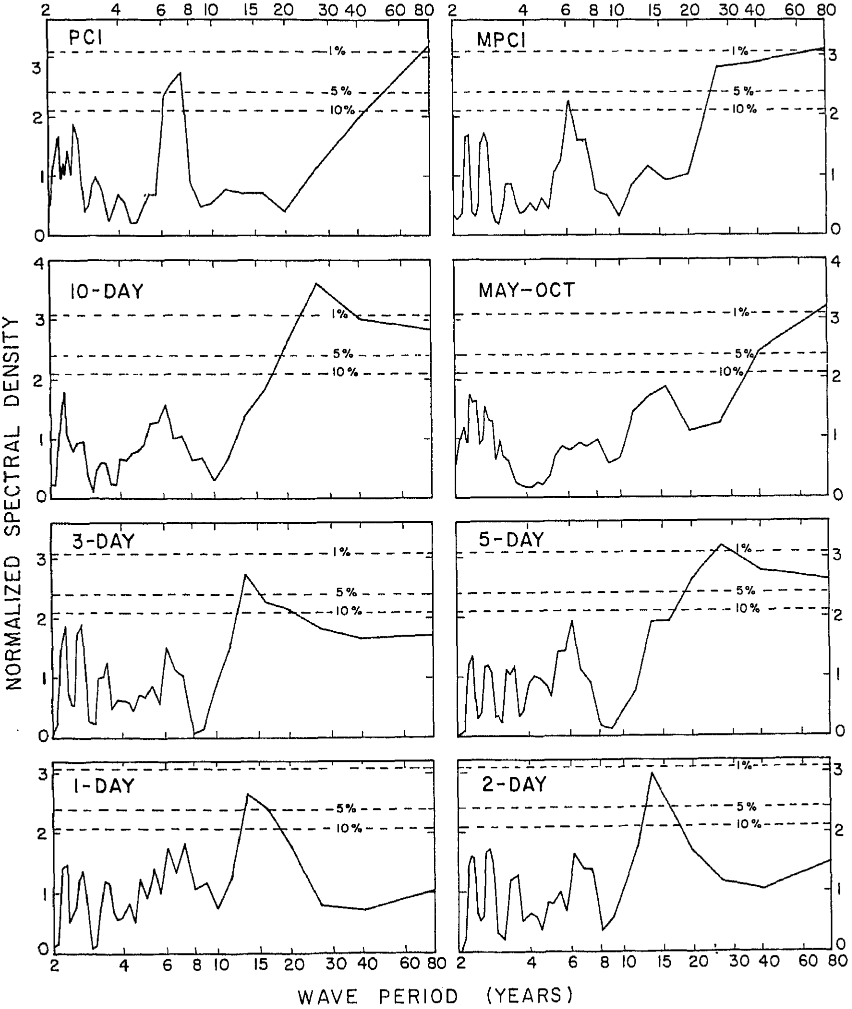

Figure 5. Power spectra of some representative parameters of the rainfall processes over Upper Narmada catchment.

the periods ranging from 13·3 to 16 years for extreme rainfall series of 1- to 3-day durations. However, for longer duration extreme series, the power contained in comparatively low frequency mode (wave period >20 years) became greater and significant. In the May–October rainfall series, the amplitude of 40- and 80-year waves are significant. This also shows that extreme rainfall series and seasonal rainfall series of the same region can have different fluctuation characteristics.

The PCI spectra indicate concentration of power in high frequency waves with periods ranging from 6·7 to 7·3 years and in a low frequency wave of 80- year period. In the case of MPCI, however, the significant periodicities range from 26·7 to 80 years. The dominance of low frequency waves in extreme and seasonal rainfalls and MPCI are indicative of the occurrence of wet and dry epochs in the rainfall fluctuations of the Upper Narmada catchment. This may give sometimes a misleading impression of increasing/decreasing rainfall trend over the area. However, looking into the data limitation, the practical significance of 80-year wave in some hydroclimatic parameters should be interpreted with caution.

7. Rainfall over Upper Narmada catchment and break-monsoon days over India

The most conspicuous feature of the monsoon circulation over the Indian region is the monsoon trough. It is a quasi-permanent planetary scale low pressure area (or trough) in the lower and middle troposphere during the southwest monsoon period. The monsoon trough is fully developed by July and remains active up to the end of August (Raghavan 1973). In the mean, the sea level axis of the monsoon trough passes from Sri Ganganagar to Calcutta through Kanpur and Allahabad. It has a southward tilt in the vertical and at 700 mb, an atmospheric layer with maximum available precipitable water, lies over the eastern part (23°N) of the Narmada catchment. Because of favourable geographical location the Upper Narmada catchment receives larger rainfall than its surroundings. Occurrence and intensification of the monsoon trough at its normal and southerly position and formation of low pressure areas embedded in the trough is a favourable meteorological situation for good rainfall activity over the plains of north India (up to 20°N in the south). Northward shift of the trough axis brings about a dry weather condition over the north Indian plains. When the trough axis lies near the foot of the Himalaya, the northern plains are almost completely deprived of rainfall. This situation is commonly known as break-monsoon condition. During

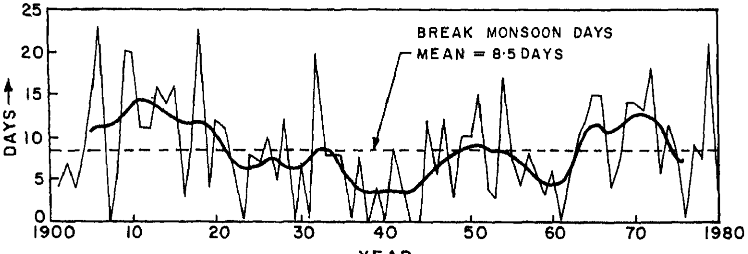

Parthasarathy and Pant (1986) (figure 5). The series displays opposite behaviour with respect to seasonal rainfall over Upper Narmada catchment. The negative correlation coefficient ($r = -0{\cdot}375$) based on 80 data points is statistically significant at 1% level. But the correlation is not as strong as was expected. Sometimes, plains of the northern India (including Narmada catchment) receive ample rains and experience floods after a prolonged dry spell caused by a westward moving Bay depression or storm. This overcomes the rainfall deficiency caused by the break-monsoon condition. This assumption can be supported by the fact that there exists a highly significant positive correlation ($r = 0{\cdot}395$) between break-monsoon days and the precipitation concentration index (PCI), that is during a year with large number of break-monsoon days the total seasonal rainfall will be concentrated in comparatively less number of rainfalls. Therefore, the effectiveness of rainfall activities over the Upper Narmada catchment for hydrological purposes is independent of the number of break-monsoon days over India. The correlation coefficient between the break-monsoon days and the MPCI of the Upper Narmada catchment is 0·018 which indicates the independent nature of the two series.

The break-monsoon condition is known for low or no rainfall activities over the northern plains, but some times deficiency in July and August rainfall due to break-monsoon condition is compensated by the good rainfall activities during June and September caused by the storms/depressions. Of the 22 heavy rainstorms, which occurred over the Narmada catchment during 1930 to 1968, as reported by Pant *et al* (1969), 10 had occurred during June and September. Hence, even if some year happens to be a below-normal rainfall year, it can be a hydrologically flood year because of the concentration of total seasonal rainfall into a few intense rainspells.

8. Summary and conclusions

The important features of hydroclimatic fluctuations of the Upper Narmada catchment and its association with break-monsoon days over India noticed in this investigation are as follows:

(i) The area-averaged extreme rainfall series of Upper Narmada catchment for 1 and 2 days is normally distributed, whereas it is skew distributed for longer durations. The dominant periodicities noticed in different extreme rainfall series vary from 13·3 to 16 years and 26·7 years.

(ii) The frequency distribution of May–October rainfall over the Upper Narmada catchment is normal. But the PCI and MPCI series are significantly different from normal. Some dominant periodicities have been noticed in May–October rainfall (40 and 80 yrs), PCI (6·7 to 7·3 and 80 yrs) and MPCI (26·7 to 80 yrs) series.

(iii) The time series of the starting and ending dates and the length of each of the period contributing 2, 5, 10, 20, . . . 90 and 95% rainfall to the annual total is homogeneous and random. The frequency distribution of these parameters in most cases is normal. The 80% rainfall period can be considered as the period of reliable rainfall over the Upper Narmada catchment. In the mean, this period starts on 24th June and ends on 12th September.

Narmada catchment.

It is expected that the behaviour of the characteristic parameters, viz extreme rainfall, seasonal rainfall, PCI and MPCI, representing features of the rainfall processes over Upper Narmada catchment which are found to observe epochs of high and low values can provide forecasters and water managers a valuable aid for issuing flood forecast and planning long term management of water resources in the basin respectively. Due to data limitation it is suggested that the significance of the dominant 80-year wave in some hydroclimatic parameters should be used with caution.

Acknowledgements

Authors are grateful to Shri D R Sikka for encouragement, to Dr G B Pant and Dr B Parthasarathy for stimulating discussion and critically reviewing the paper.

References

Banerji S, Rao D V L N, Julka M L and Anand C M 1967 Some further results of investigations on quantitative precipitation forecasting over selected areas in North India; *Indian J. Meteorol. Geophys.* **18** 465

Bedekar V C and Banerjee A K 1969 A study of climatological and other rainfall patterns over central India; *Indian J. Meteorol. Geophys.* **20** 23

Chaturvedi M C and Srivastava D K 1981 Study of a complex water resources system with screening and simultaneous models; *Water Resources Res.* **17** 783

India Met. Deptt. 1981 *Climate of Madhya Pradesh.* Office of the Additional Director General of Meteorology (Res.), I M D, Pune, p. 265

Mistry J F and Thatte C D 1969 Floods in river Narmada—August 1968. *Flood control and the use of river water resources*, Symp. held at South Gujarat University, Surat (Surat: South Gujarat University) p. 87

Pant P S, Abbi S D S and Gupta D K 1969 A hydrometeorological study of the heavy floods in Narmada and Tapti. *Flood control and the use of river water resources* Symp. held at South Gujarat University, Surat (Surat: South Gujarat University) p. 151

Parthasarathy B 1984 *Some aspects of large-scale fluctuations in the summer monsoon rainfall over India during 1871–1978*, Ph.D. thesis, University of Poona, Pune, p. 370

Parthasarathy B and Dhar O N 1976 Studies on trends and periodicities of rainfall over Madhya Pradesh; *Proc. Indian Natl. Sci. Acad.* **A42** 73

Parthasarathy B and Pant G B 1986 Summer monsoon rainfall over different regions of India and circulation features during 1981–84. *The diagnosis and prediction of monthly and seasonal atmospheric variations over the globe*, Symp. held at Maryland, USA, during July 1985 WMO No. TD-87, p. 235

Pestiaux P and Berger A 1984 An optimal approach to the spectral characteristics of deep-sea climatic records. *Milankovitch and climate, Part 1* (Dordrecht: D Reidel) p. 417

Raghavan K 1973 Break-monsoon over India; *Mon. Weather Rev.* **101** 33

Ramage C S 1971 *Monsoon meteorology* (New York: Academic Press) p. 61

Ramana Murthy K V, Soman M K and Mulye S S 1987 Long term variations in the rainfall over Upper Narmada catchment; *Mausam* **37** 313

Sato N, Yamada M and Murakami C 1985 Distribution of the precipitation concentration index over east Asia and regional division by its use; 1984 *Jpn. Progr. Climatol.* p. 56

Schickendanz P T and Bowen E G 1975 Computation of climatological power spectra using variable record lengths. *Fourth conference on probability and statistics in atmospheric sciences* held at Tallahassee, Florida, USA, (Boston, USA: American Meteorological Society) p. 102

Sikka D R 1977 Some aspects of the life history, structure and movement of monsoon depressions; *Pure Appl. Geophys.* **115** 1501

Singh N 1986 On the duration of the rainy season over different parts of India; *Theor. Appl. Climatol.* **37** 51

Srinivasan V, Raman S and Mukherji S 1971 Southwest monsoon—Typical situations over Madhya Pradesh and Vidarbha. *FMU* Rep. No. III-3.4, India Meteorol. Deptt., Pune p. 68

WMO 1966 Climatic change WMO Tech. No. 79, WMO-195, TP 100

Late Cretaceous mafic dykes in the Dharwar craton

ANIL KUMAR, Y J BHASKAR RAO, V M PADMA KUMARI, A M DAYAL and K GOPALAN
National Geophysical Research Institute, Hyderabad 500 007, India

MS received 8 April 1988

Abstract. Palaeomagnetic, geochemical and geochronological studies have been conducted on a set of dolerite dykes intruding the Peninsular gneisses near Huliyurdurga town, Karnataka, as a reconnaissance survey indicated a Cretaceous age for them. The dykes are mainly tholeiitic in composition with their 87Sr/86Sr ratios tightly clustered around 0·7045. Their palaeomagnetic data ($D_m = 329°$, $I_m = -55°$) and the corresponding palaeopole coordinates ($\lambda_p = 34°$S, $L_p = 108°$E) are strikingly close to those of the Deccan Traps to the north. Whole rock K-Ar ages of these dykes ranging between 69 and 84 Ma are also similar to the range of K-Ar ages of the Deccan basalts. The chemical, palaeomagnetic and temporal coherence between the dykes and the Deccan basalts indicate that they may indeed be tectonically related events.

Keywords. Cretaceous dykes; Deccan volcanism; geochronology; geochemistry; Palaeomagnetism.

1. Introduction

In an attempt to understand the crustal conditions and stress systems during early-mid Proterozoic times in continental areas, a concerted study of various dyke swarms in Karnataka has been taken up as NGRI and IGCP-257 projects. As part of this programme, systematic sampling was carried out over several selected dyke swarms in parts of Tumkur and Hassan districts. Palaeomagnetic results on two dykes near Huliyurdurga (referred to in this paper hereafter as Huliyurdurga Cretaceous Dykes, HCD) differed markedly from the rest and indicated Cretaceous magnetic signatures. As a quick check on their very young age, we carried out magnetogranulometric tests, which were successfully used by Radhakrishnamurthy and Deutsch (1974) to distinguish Cretaceous and younger basalts from much older ones. The measurements on HCD samples suggested Cretaceous or younger origins.

This finding prompted more intensive geological, palaeomagnetic, geochemical and geochronological studies on HCD to explore the manifestation of Cretaceous magmatism in the south Indian shield. Preliminary findings of these studies are reported here.

2. Geological setting

HCD are a part of a prominent dyke swarm to the east of the Huliyurdurga (Kunigal) schist belt. The swarm comprises mafic dykes of several generations, most of which are believed to be of Proterozoic origin. The HCD (dykes A and B; figure 1) are observed to

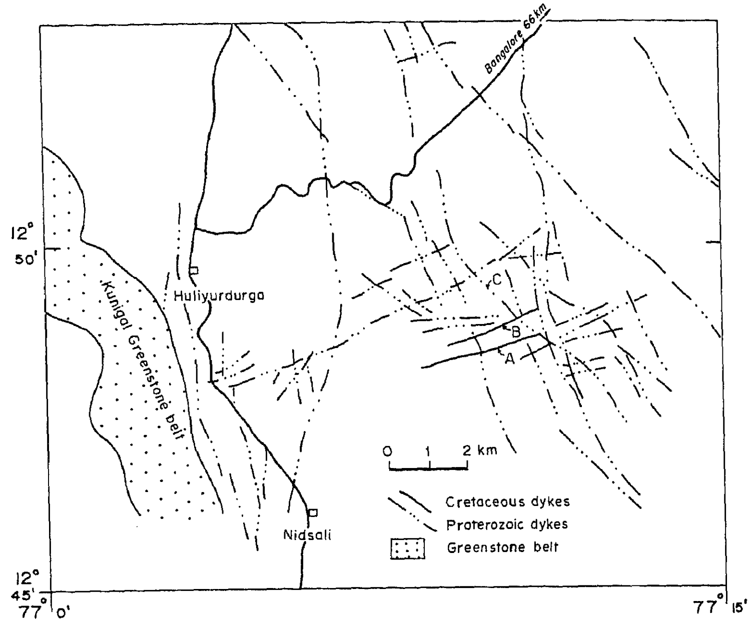

Figure 1. Distribution of dykes in the area.

intrude several of the older dykes and the Archaean gneiss. The contacts with the gneiss are often sharp with a chilled zone. The dykes strike N 70°E and dip vertically with an average width of about ten meters. Field observation of the dyke and its contacts does not show any features indicative of shearing such as brecciation, slicken-sliding along margins or offset of foliations in the country rock along the contacts with the dyke. Therefore, it is inferred that these dykes intrude tensional fractures. There exist a large number of similar dykes in the region whose age and petrological characteristics are not known.

3. Experimental methods

Over twenty fresh samples from dykes A and B and three from dyke C (figure 1) were studied for their magnetic, petrochemical and geochronological signatures. The block samples collected were oriented using a magnetic compass. Cores were later drilled from the block samples and sliced into specimens of nominal dimensions 2·5 cm in diameter × 2·3 cm in height. Three or four cores were usually taken from each block sample and 2 or 3 specimens prepared from each core. The remaining part of the samples was used for geochemical analysis and K-Ar dating.

The intensity and direction of natural remanent magnetization were measured on a model DSM-2 Schonstedt spinner magnetometer with a measurement range from 5 to less than $2{\cdot}5 \times 10^{-7}$ emu, and accuracy of moment better than ± 5% and an angular accuracy of 2°. Of the several core specimens drilled from each block sample, at least one was subjected to detailed alternating field (AF) demagnetization to 1000 Oe (100 mT) using a two-axis tumbling device similar to that described by Creer (1959). An equal number of specimens were thermally demagnetized using a Schonstedt TSD-1 instrument.

Whole-rock Ar analysis was made on about 1 mm chips. A part of this material was ground to less than 200 mesh for potassium analysis. Argon was extracted in an all metal low-blank ($\sim 1 \times 10^{-9}$ cc STP ^{40}Ar at 1500°C) ultrahigh vacuum system and isotopic analysis on a MS-10 mass spectrometer in the static mode. Potassium was determined by flame photometry on an IL443 instrument using lithium as the internal standard. An inter-laboratory standard Mica-mg (phlogopite) was analysed along with HCD samples which yields an age of 533 ± 12 Ma. This agrees to within the experimental error with the recommended value of 522 ± 12 Ma (Govindraju 1979).

The samples were chemically analysed on lanthanum-doped fused pellets using a Philips PW 1400 X-ray fluorescence spectrometer.

4. Results

The dykes are medium-grained in the interior with a decrease in grain size towards the margins. Petrographic studies show ophitic and subophitic textures. The principal mineral constituents are plagioclase and augite, with pigeonite, ilmenite and titanomagnetite as accessories.

The major element composition of six representative samples of the dykes is given in table 1. It can be seen that the rocks have a uniform chemical composition which is

Table 1. Geochemistry of Huliyurdurga dykes.

	HD86/2	HD86/5	HD86/36	HD86/37	HD86/42	HD86/43
SiO_2	50·05	49·73	50·17	49·77	50·35	50·28
TiO_2	3·07	3·03	2·80	2·93	2·98	3·01
Al_2O_3	12·90	12·71	12·34	12·58	12·89	13·37
Fe_2O_3	4·82	5·19	5·44	5·14	4·44	5·01
FeO	10·44	9·92	9·60	9·24	10·60	10·08
MnO	0·22	0·23	0·22	0·21	0·24	0·21
MgO	5·05	4·47	5·10	4·50	5·02	4·86
CaO	9·78	10·03	10·20	10·27	9·79	9·72
Na_2O	2·18	1·77	1·90	1·74	2·00	2·03
K_2O	0·43	0·43	0·39	0·42	0·36	0·42
P_2O_5	0·32	0·33	0·36	0·34	0·35	0·32
Total	99·26	97·84	98·52	97·14	99·02	99·31
			CIPW norms			
q	8·222	11·331	10·516	11·925	9·369	9·623
or	2·560	2·597	2·339	2·555	2·148	2·499
ab	18·584	15·308	16·319	15·157	17·091	17·297
an	24·323	26·027	24·351	26·019	25·379	26·310
wo	9·374	9·447	10·282	10·081	8·919	8·410
en	12·671	11·378	12·892	11·537	12·626	12·188
fs	10·607	9·559	9·054	8·517	11·434	9·859
mt	7·041	7·691	8·006	7·692	6·501	7·314
il	5·874	5·882	5·898	5·729	5·716	5·756
ap	0·764	0·799	0·866	0·829	0·837	0·763

Sample No.	K%	^{40}Ar rad mol./g × 10^{-11}	^{40}Ar rad %	Age Ma
Dyke A				
HD 86/2	0·366	5·2668	55	81 ± 3
HD 86/5	0·384	4·7110	52	69 ± 3
HD 86/42 (a)	0·351	4·4580	57	72 ± 2
HD 86/42 (b)	0·351	4·4730	58	72 ± 3
Dyke B				
HD 86/36 (a)	0·349	5·1601	54	83 ± 2
HD 86/36 (b)	0·349	5·2074	71	84 ± 2
HD 86/22	0·357	4·8777	53	77 ± 3
Dyke C				
HD 86/9	0·353	157·03	95	1596 ± 34

^{40}K decay constants after Steiger and Jager (1977). Errors are 2 sigma.

Table 3. Palaeomagnetic data for Huliyurdurga dykes.

	NRM						Cleaned					
S	N	n	D°	I°	K	A95°	AF	n	D°	I°	K	A95°
Dyke A												
1	4	26	333	−49	393	1·4	20	4	330	−54	614	2·8
2	4	17	11	−48	9	11·2	20	4	329	−54	1500	1·8
3	4	18	339	−44	71	3·9	20	6	329	−56	347	3·1
4	4	19	337	−41	50	4·5	20	8	331	−49	70	5·9
Dyke B												
5	4	16	332	−49	336	1·9	20	5	325	−58	588	2·6
Mean pole position = 107·7°E, 33·9°S; dm = 4·1°, dp = 2·9°.												

Notes: S, Site number; N, number of block samples; n, number of specimens; D, declination; I, inclination; K, precision parameter; A95, radius of circle of confidence at 95% probability; AF, alternating fields established as the end points for samples of that site; dm and dp, semi-axis of ellipse of confidence at 95% probability.

tholeiitic and resembles the composition of the typical Deccan basalts (Mahoney *et al* 1982). 87Sr/86Sr ratios and Sr concentrations of 4 samples have been measured mass-spectrometrically, yielding the following values after age correction which is very small: HD 86/37 0·70486 ± 2, 218 ppm; HD 86/2 0·70414 ± 2, 229 ppm; HD 86/5 0·70572 ± 2, 231 ppm; and HD 86/42 0·70453 ± 2, 232 ppm. The error in Sr ratios is $1\sigma m$ and refers to the last digit, and Sr determinations are accurate to within 1%. The Sr ratios are relative to a mean value of 0·71023 ± 2 measured for NBS 987 Sr standard.

Whole-rock K-Ar dating of HCD samples yields ages in the range 69 to 84 Ma (table 2). Though the samples represented central to marginal parts of the dyke, no

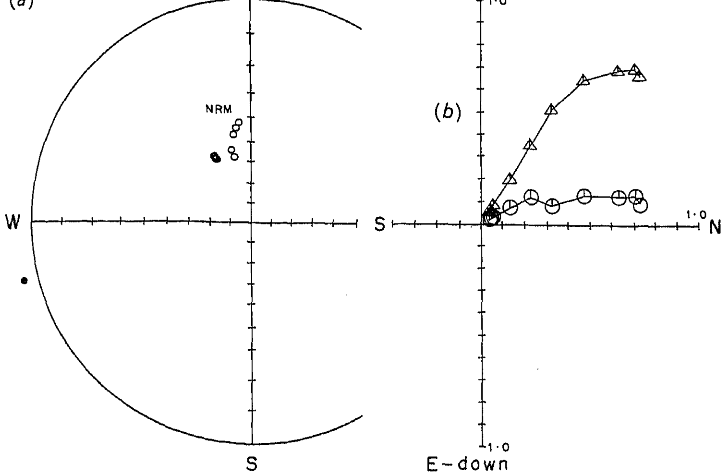

Figure 2. An example of the AF demagnetization characteristics of a specimen from HCD. (**a**) Stereographic projection showing directions of magnetization at successive peak fields (**b**) Zijderveld plots for vectors displayed in (**a**). Circles lie in the horizontal plane, triangles lie in the vertical plane.

systematic differences in age are seen. In order to check if these ages are reset ages caused by a later thermal episode, petrographic and K-Ar analyses of a sample from a prominent older dyke (C) cut by HCD was carried out. Dyke C shows unmetamorphosed and unaltered mineralogy with primary textures and has a much older age of about 1600 Ma. In the light of this result, we believe that the late Cretaceous K-Ar age of HCD represents their time of intrusion.

One site on dyke A and four sites on dyke B (figure 1) were sampled for palaeomagnetic studies with a minimum of four block samples from each site. Natural remanent magnetization (NRM) measurements showed fairly consistent directions (table 3). The angular dispersion further decreased after alternating field demagnetization. Typically by 150 Oe the directions began demagnetizing towards the origin (figure 2). The AF trends were carefully examined with the aid of stereo nets, orthogonal plots and vector subtraction (details of which will be published elsewhere). Based on these analyses, a single, discrete high coercivity component recorded in single domain titanomagnetites has been identified. This normally magnetized component ($D_m = 328{\cdot}9°$, $I_m = -54{\cdot}5°$, $K = 476$, $A95 = 2{\cdot}9°$) is interpreted to be of primary origin and is related to the time of intrusion of the dykes. The dykes yield a palaeomagnetic pole position of latitude 34°S, longitude 108°E ($d_m = 4{\cdot}1°$, $d_p = 2{\cdot}9°$).

5. Discussion

The dykes are tholeiitic in composition and falls within the range of compositions of continental basalts, as shown in figure 3. Since these dykes are relatively small volume intrusions into a Precambrian basement, the possibility of host rock contamination of

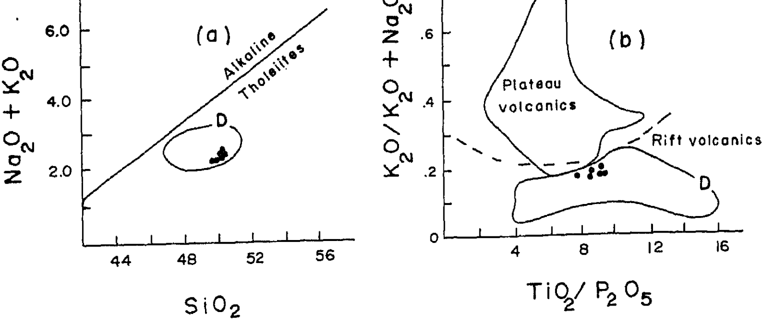

Figure 3. (a) Alkalies vs silica plot showing Huliyurdurga dyke compositions. Field of central Indian Deccan volcanics (D) after Krishnamurthy and Udas (1981). Alkalic and tholeiitic basalt discrimination after Irvine and Barager (1971). (b) Position of Huliyurdurga dyke with relation to plateau volcanics and rift volcanics. Deccan trap data (D) are from Chandrasekharan and Parthasarathy (1978).

the primary magma of the dykes cannot be ruled out. However, the tight cluster of the Sr isotopic ratios around 0·7045 and Sr compositions around 230 ppm suggest that such contamination, if present, is very small. It does not appear to be fortuitous that the Sr isotopic ratios and Sr concentrations of the dykes are almost identical to those of some of the least crustally contaminated Deccan lava flows in the Mahabaleshwar section (Mahoney *et al* 1982). This suggests very similar upper mantle sources for both the HCD's and the Deccan lavas. Nd isotopic compositions of the dykes will help confirm this interpretation.

Another feature of similarity between the HCD and the Deccan basalts is in their emplacement time. The K-Ar ages of HCD's show a spread between 69 and 84 Ma which is outside the analytical uncertainties. The average age is about 76 Ma. Though the conventional K-Ar ages of Deccan basalts show even larger spread from 35 to 85 Ma, there is increasing evidence that the main Deccan volcanism was a relatively sharp event centred around 65 Ma (Venkatesan *et al* 1986; Courtillot *et al* 1986). The HCD ages are only marginally older than this. It is not clear at this stage whether the higher and larger scatter of the HCD ages are mainly due to variable amounts of radiogenic argon inherited from the country rocks during dyke emplacement. While the present data indicate that the HCD and the Deccan basalts have very similar ages, the possibility that the HCD's slightly but distinctly predate the Deccan lavas cannot be ruled out. 40Ar/39Ar dating of some HCD samples is being attempted to resolve this issue.

The remarkable similarity in age and composition between HCD and Deccan basalts is reinforced by the magnetic signatures of both rocks. The primary magnetic composition of the HCDs is strikingly uniform, leading to a closely constrained palaeopole position at 108°E, 34°S. This agrees very well with the overall mean virtual geomagnetic pole for the Deccan traps (106°E, 34°S; Klootwijk 1979), and falls well within the palaeomagnetic data field of the Deccan volcanics as shown in the polar wander path (figure 4). This shows that both the HCDs and the Deccan lavas crystallized in nearly identical ambient magnetic fields.

Cretaceous dyke activity in Peninsular India has also been reported earlier in the

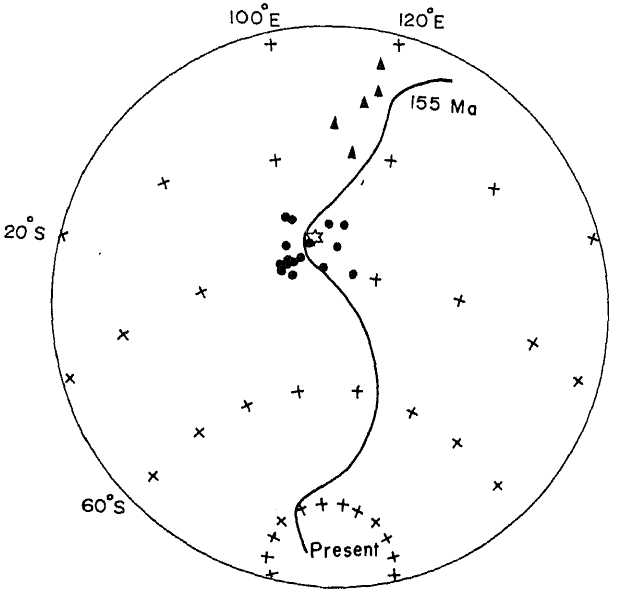

Figure 4. The Mesozoic-Tertiary APWP for India following Klootwijk and Priece (1979). The closed circles represent Deccan trap pole positions and the triangles represent Sylhet/Rajmahal traps (data from Klootwijk 1979). Results with A95 (radius of circle of confidence at 95% probability) less than 10° have been incorporated in the figure from Klootwijk's (1979) synthesis. Star refers to Huliyurdurga dykes pole position.

literature. These are generally from areas in close geographic association with the subaerial flows of the Deccan and Rajmahal provinces (Gondwana dykes 121 to 57 Ma BP, Murty 1985). Away from these provinces, dyke swarms of Cretaceous age have been described from the areas proximal to the subcontinental margin in Kerala state (Radhakrishna *et al* 1985). These apart, Hasnian and Qureshy (1971) reported Cretaceous dykes from Karnataka, one of them located very close to Chitradurga town and two others to the east of Mysore city. These authors correlated them with Deccan volcanism based only on palaeomagnetic and geochemical data.

The Kerala dykes (~ 100–150 Ma) are apparently synchronous with the break-up of the Gondwanaland (~ 125 Ma BP) and with the separation of Madagascar from India ~ 100 Ma BP (Barron 1987). Dykes of similar age (133–158 Ma) are also exposed in the south and southeast continental margins of Africa (Hunter and Reid 1985), India's immediate neighbour in the Gondwana supercontinent. Such dykes may therefore constitute an expression of crustal extension and rifting.

Unlike the Kerala dykes, the Huliyurdurga dykes are fillings into tensional fractures created in the Archean basement far away from zones of intense continental distention and related tectonics. Their strong coherence with the Deccan basalts in terms of

Acknowledgements

The authors are grateful to Prof. V K Gaur for encouragement and to Prof. C Radhakrishnamurty for suggesting the possibility of the very young age of the HCD based on preliminary magnetogranulometric results. They thank Dr R Srinivasan for his help in one of the field trips, Dr M S Bhalla for providing palaeomagnetic laboratory facilities and Dr T V Sivaraman for Sr isotopic analysis.

References

Barron E J 1987 Cretaceous plate tectonic reconstructions; *Palaeogeogr., Paleoclimatol., Palaeoecol.* **59** 3–29

Chandrasekharan D and Parthasarathy A 1978 Geochemical and tectonic studies of the coastal and inland Deccan trap volcanics and a model for the evolution of Deccan trap volcanism; *Nues. Jb. Miner. Abh.* **132** 214–229

Courtillot V, Besse J, Vandamme D, Montigny R, Jaeger J J and Capetta H 1986 Deccan flood basalts at the Cretaceous/Tertiary boundary; *Earth Planet. Sci. Lett.* **80** 361–374

Creer K M 1959 AC demagnetization of Keuper marls; *Geophys. J. R. Astron. Soc.*, **2** 262–275

Govindaraju 1979 Report (1968–1978) on two mica reference samples: biotite mica-Fe and phlogopite mica-Mg; *Geostandards Newsl.* **3** 3–24

Hasnian I and Qureshy M N 1971 Palaeomagnetism and geochemistry of some dykes, Mysore state, India; *J. Geophys. Res* **76** 4786–4795

Hunter D R and Reid D L 1985 Mafic dyke swarms in southern Africa; Int. Conf. mafic dyke swarms, Toronto, Canada (abstracts)

Irvine T N and Baragar W R A 1971 A guide to the chemical classification of the common volcanic rocks; *Can. J. Earth. Sci.*, **8** 523–548

Klootwijk C T 1979 A review of palaeomagnetic data from the Indo-Pakistani fragment of Gondwana land. *Geodynamics of Pakistan* (eds) Abul Farah and Kee A De Jong (Quetta: Geol. Surv. Pakistan)

Klootwijk C T and Priece J W 1979 India's and Australia's pole path since the late Mesozoic and the Indian-Asia collision *Nature (London)* **282** 605–607

Krishnamurthy P and Udas G R 1981 Regional geochemical characters of the Deccan trap lavas and their genetic implications; *Deccan volcanism and related basalt provinces in other parts of the world* (eds) K V Subba Rao and R N Sukeshwale (Bangalore: Geol. Soc. India) Mem. 3

Mahoney J, Macdougall J D, Lugmair G W, Murali A V, Shankar Das M and Gopalan K 1982 Origin of the Deccan Trap flows at Mahabaleshwar inferred from Nd and Sr isotopic and chemical evidence; *Earth. Planet. Sci. Lett.* **60** 47–60

Murthy N G K 1985 Mafic dyke swarms in India; Int. Conf. on mafic dyke swarms, Toronto, Canada (abstracts)

Radhakrishna T, Mitchell J G and Venkatesh R 1985 Multiple emplacement of basic dyke swarms in Kerala and coastal evolution of south India; Int. Conf. mafic dyke swarms, Toronto, Canada (abstracts)

Radhakrishnamurty C and Deutsch E R 1974 Magnetic techniques for ascertaining the nature of iron oxide grains in basalts; *J. Geophys.* **40** 463–465

Rao R U M, Rao G V and Narain H 1976 Radioactive heat generation and heat flow in the Indian shield; *Earth. Planet. Sci. Lett.* **30** 57–64

Singh R N and Negi J G 1982 High Moho temperature in Indian shield; *Tectonophysics* **82** 299–306

Steiger R H and Jager E 1977 Subcommission on geochronology; convention on the use of decay constants in geo and cosmochronology; *Earth Planet. Sci. Lett.* **36** 359–362

Venkatesan T R, Pande K, Gopalan K and Macdougall J D 1986 Time and duration of Deccan volcanism (abstract). Terra Cognita, 6, 182

INTERNATIONAL SYMPOSIUM ON THE STRUCTURE AND DYNAMICS OF INDIAN LITHOSPHERE

CALL FOR PAPERS

A three-day international symposium on the structure and dynamics of the Indian continental and oceanic lithosphere, sponsored by ICL and IASPEI, will be held at the National Geophysical Research Institute, Hyderabad, India, during February 1–3, 1989. We request research contributions in the following areas:

- Structure and tectonics (geophysical, geological and geochemical)
- Intraplate stress regimes
- Kinematics of Indian plate and Indian continent
- Lithosphere—asthenosphere interactions
- Mantle convection and thermal history

Extended abstracts (not exceeding 500 words) with figures (in A-4 size suitable for reproduction) should arrive **before 30 November 1988**.

For further information contact:

Dr R N Singh
Symposium Secretary
National Geophysical Research Institute
Uppal Road
Hyderabad 500007
India

IAGA Meeting, Exeter, U.K.

July 24 to August 4 1989

(6 sessions: $3\frac{1}{2}$ days)

Geophysical anomalies of Gondwana ($\frac{1}{2}$ day)
Magnetic petrology in magnetic anomaly interpretation (1 day)
Magnetic anomalies due to sulphides ($\frac{1}{2}$ day)
Interpretation of long-wavelength anomalies ($\frac{1}{2}$ day)
Tectonic implications of magnetic anomalies in Europe ($\frac{1}{2}$ day)
Poster Session: Magnetic maps and their correlation with other geophysical and geological observations ($\frac{1}{2}$ day)

Those intending to participate in this meeting and contribute papers may communicate with the Chairman, Dr W J Hinze, Department of Earth and Atmospheric Sciences, Purdue University, West Lafayette, Indiana 47907, USA, with a copy to Dr V K Gaur, Director, National Geophysical Research Institute, Hyderabad 500 007, India.

Cosmic-ray production rates of neon isotopes in meteorite minerals

N BHANDARI

NOTE TO SUBSCRIBERS

This volume closes with the issue of this number. An additional number will be published in 1989 to make up for the deficit pages.

Keywords. Meteorites; solar flares; galactic cosmic rays, [redacted]

1. Introduction

The concentration of ^{21}Ne in stony meteorites provides a reliable method of determining their exposure ages and the ratio ^{22}Ne/^{21}Ne is useful in understanding the exposure history of the meteoroid and estimating the atmospheric ablation and shielding depth. Furthermore the three isotopes of neon (20, 21 and 22) provide an accurate method of correcting for any primordial component and identifying grains irradiated by solar flare particles during precompaction stage of the meteoroid. Measurements in mineral separates are sometimes more useful than those in the bulk meteorite because they provide a comparatively clearer picture of the irradiation history of the meteorite. We have therefore calculated the rates of production of ^{21}Ne and ^{22}Ne due to galactic (GCR) and solar (SCR) particles in some common silicate minerals which are abundant in chondrites.

2. Methodology

The isotope production rates due to galactic cosmic rays depend on target element abundances, excitation functions and energy spectra of primary and secondary nucleons which, in turn, depend upon the size of the meteoroid and shielding depth. Here we follow the model of Bhandari and Potdar (1982) for calculating the flux of nucleons as a function of energy at various depths within a meteoroid of a given size. The GCR flux in the interplanetary space of $1\cdot7$ P/cm^2. sec. 4π ster. (> 1 BeV) is used here following Reedy and Arnold (1972). This represents a long-term (10^6–10^7 years) average flux at 1 A.U. near the ecliptic. The energy spectra of nucleons within the experimental work of Bhattacharya *et al* (1980) and Potdar *et al* (1986) who determined this parameter for spherical meteoroids of radii 6, 9, 15, 25, 50 and > 400 cm. Proton and neutron cross-sections for the production of neon isotopes for different target elements at some energies have been measured (Reedy and Arnold 1972 and references therein; Walton 1974; Walton *et al* 1976; Tobailem and Lassus St Genies 1977; Reedy *et al* 1979; Tobailem 1981; Baros and Regnier 1984). Michel *et al* (1986) and Aylmer *et al* (1987) determined some excitation functions from simulated thick target irradiations to proton beams as well as from thin target experiments. The excitation functions used here are the same as those adopted by Bhandari and Potdar (1982). In the case of ^{22}Ne, direct production from various elements as well as via decay of ^{22}Na has been taken into account. There is some uncertainty in the excitation functions because of the lack of measurements, particularly for neutron-induced reactions. In such cases excitation functions for neutron-induced reactions are taken to be the same as those for the analogous proton-induced reactions. This introduces some uncertainty in the production rates but is not serious since the ^{21}Ne and ^{22}Ne/^{21}Ne ratio profiles agree well with the measured values in San Juan Capistrano, St Severin and Keyes meteorites (Bhandari and Potdar 1982). The ^{22}Ne/^{21}Ne profiles also agree with the Berne data (Eberhardt *et al* 1966). However, there is some uncertainty in the estimation of exposure ages of these meteorites. In their work Bhandari and Potdar (1982) used the mean values of the exposure ages—11·2 Ma for St Severin and 19 Ma for San Juan Capistrano and Keyes. New analysis (Graf *et al* 1986) indicates somewhat higher exposure ages. If this is true the production rates given here will have been overestimated by the same factor, although the ^{22}Ne/^{21}Ne ratio would be unaffected. The adopted abundances of Mg, Al, Si and Na, which are the main target elements in silicate minerals, are given in table 1 (Allen and Mason 1973).

A similar procedure is used for calculating the production rates due to solar cosmic rays except that, because of the low energy of primary protons, it is not necessary to consider secondary nucleon production. There is some uncertainty in the estimates of long-term average solar flare proton fluxes. The values of flux $J_s(> 10\,\text{MeV/cm}^2$, sec. 4π ster) and rigidity R_0 (MV) have been determined from studies of lunar rocks (Bhandari *et al* 1975; Kohl *et al* 1978). We use here two sets of energy spectra defined by $(J_s, R_0) =$ (i) (125, 125) and (ii) (100, 100). The solar proton flux, however, depends upon the heliocentric distance, being high near the sun, at the meteoroid perihelion, and decreasing significantly with distance as the meteoroid moves towards its aphelion, where it spends most of its time. The average flux, integrated over the orbit, has been found to be as low as (40, 100) for the St Severin meteorite (Lal and Marti 1977; Bhandari and Potdar 1982).

Table 1. Adopted abundances (%) of main target elements in silicate minerals.

	Mg	Al	Si	Na
Olivine	23·9	0·01	17·8	0·02
Feldspar	0·04	11·0	30·5	7·0
Orthopyroxene	17·7	0·06	26·0	0·03
Clinopyroxene	10·1	0·3	25·3	0·43

3. Results and discussion

The production profiles of ^{21}Ne due to GCR and the ^{22}Ne/^{21}Ne ratio in clinopyroxene, olivine, orthopyroxene and feldspar in meteorites of different radii, i.e. 9, 15, 25, 50 cm and infinitely large (> 400 cm), are shown in figure 1 (a and b). It can be seen that the isotope production rate first increases with depth, with the development of nuclear cascade reaching a maximum around 10–20 cm depth, and then, in larger meteorites, decreasing with subsequent attenuation of nucleons. Typical GCR production rates of ^{21}Ne from different target elements, i.e. Mg, Al and Si, in a spherical meteoroid of 50 cm radius at a depth of 20 cm within the meteoroid are given in table 2 to show their relative importance. The ^{22}Ne/^{21}Ne ratios are given in table 3.

Calculations show that the GCR production profiles of ^{21}Ne and ^{22}Ne in major target elements follow a similar trend with depth, resulting in a monotonously decreasing ^{22}Ne/^{21}Ne profile in olivines and pyroxenes. The ^{22}Na production from Na, which is produced in (*n*, 2*n*) reaction, has a relatively flat profile compared to its production in other target elements. For this reason, in feldspars which contain large amounts of Na, the (^{22}Ne + ^{22}Na)/^{21} Ne ratio increases with depth. Starting around 1·6 near the surface, the ^{22}Ne/^{21}Ne ratio attains a value of 2·4 at a depth of 50 cm in large meteoroids, mainly owing to this reaction. The neon ratio in feldspars is thus, to a first approximation, sensitive to the pre-atmospheric size of the meteoroid. The isotopes ^{21}Ne and ^{22}Ne are also favourably produced in (*n*, alpha) reaction on ^{24}Mg and ^{25}Mg respectively. As ^{24}Mg isotopic abundance (78·99%) is much higher than ^{25}Mg abundance (10%) in olivines, where Mg content is high, the ^{22}Ne/^{21}Ne ratio remains low (between 1·2 and 0·98) for large meteoroids. The lowest production of ^{21}Ne occurs in feldspars and the highest in olivines because of the abundance of Mg which is the main target. The ^{22}Ne/^{21}Ne ratio in olivines and pyroxenes decreases from 1·2 or 1·3 near the surface to a value around 1 at a depth of 50 cm in large meteoroids.

Table 2. GCR production rate of ^{21}Ne (10^{-8} cc STP g. Ma) in various minerals for different target elements in a 50 cm radius meteoroid at a depth of 20 cm.

	Mg	Al	Si	Total
Olivine	0·468	0·00	0·078	0·546
Feldspar	0·001	0·06	0·133	0·194
Orthopyroxene	0·347	0·001	0·144	0·462
Clinopyroxene	0·198	0·002	0·111	0·311

Table 3. Spallation ^{22}Ne/^{21}Ne ratio in various target elements in a 50 cm radius meteoroid.

Shielding depth	Mg	Al	Si
3 cm	1·032	1·25	1·32
At centre	0·96	1·33	1·36

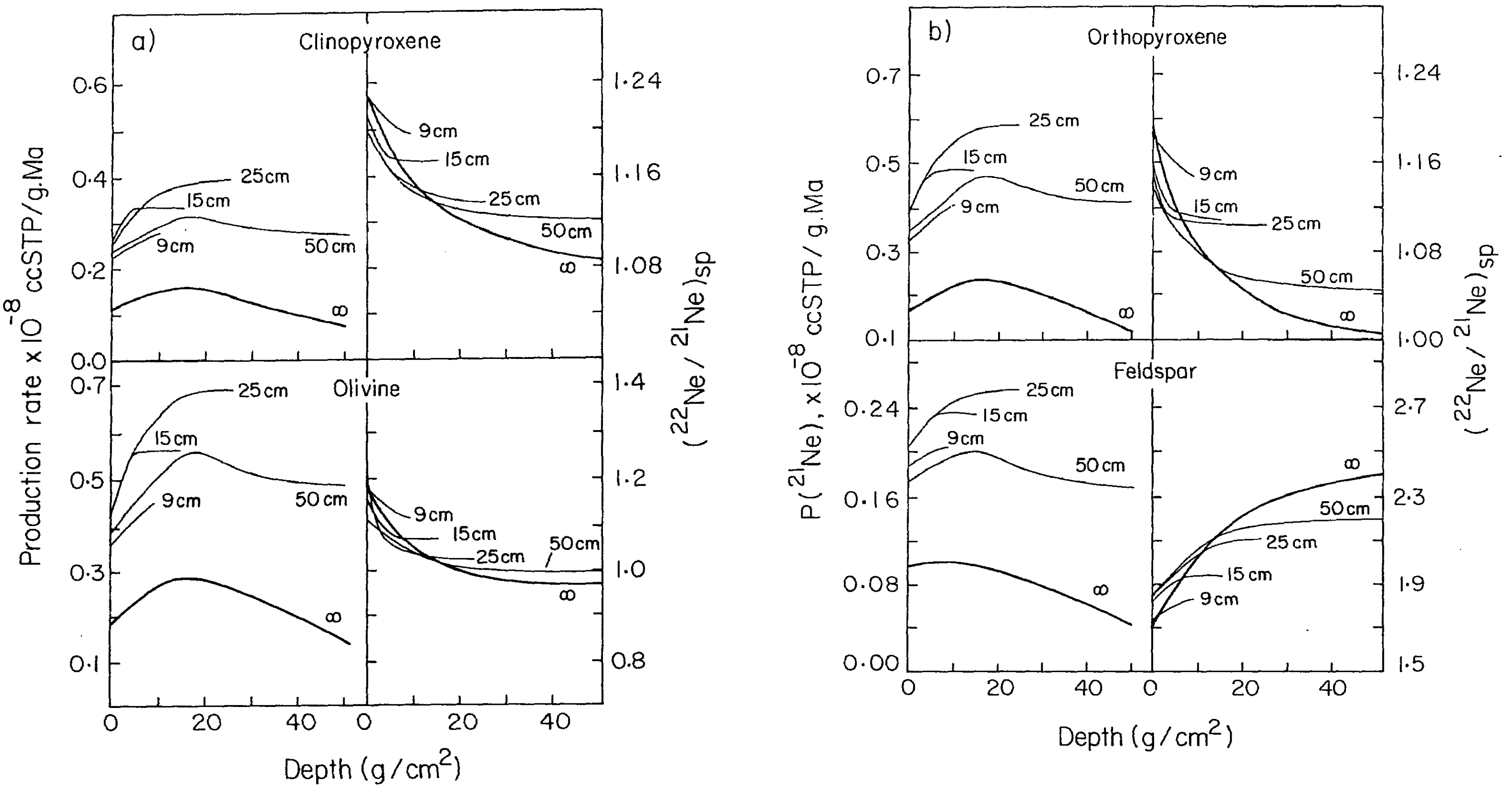

Figure 1. ^{21}Ne production rate (P(^{21}Ne)) due to galactic cosmic rays and (^{22}Ne/^{21}Ne)$_{sp}$ in various minerals as a function of meteoroid radius and depth of sample in (a) clinopyroxene and olivine; (b) orthopyroxene and feldspar.

The solar production profiles in various minerals are shown in figure 2 for $(J_s, R_0) = (100, 100)$ and $(125, 125)$, after the GCR contribution has been added. The total production rates are given in tables 4 and 5 for some selected depths and sizes. In all cases, the ^{22}Ne production rate is higher than that of ^{21}Ne and the ^{22}Ne/^{21}Ne ratio monotonically decreases with depth (figure 2), approaching the pure GCR value at about 5 cm. The high ratio in feldspars of ~ 3 is mainly due to ^{23}Na (p, pn) ^{22}Na reaction, which is very favourable.

The above calculations can be compared with the observed values in minerals separated from chondrites. Bochsler *et al* (1969) and Cressy and Bogard (1976) made measurements of neon isotopes in mineral separates from Bruderheim, Elenovka, etc. Their data show that the ^{22}Ne/^{21}Ne ratio is directly correlated with Si content and inversely with Mg content. In Bruderheim silicates, where Mg/Si varies between 0·5 and 1·2, the ^{22}Ne/^{21}Ne ratio ranges between 1·09 and 1·14. Elenovka feldspars, ^{22}Ne/^{21}Ne = 1·25 for pure Si (Mg/Si = 0). The shielding depths within the meteoroids are however not known. We can obtain some rough estimates of shielding depths from the track density data. Bruderheim was a shower and the fragments, in general, had high ablation, 6–15 cm as estimated in a few cases by Bhandari *et al* (1980). Elenovka was also a multiple fall and the three fragments analysed had shielding depths between 3 and 9 cm (Bhandari *et al* 1980). These observed values can be compared with the calculated ratios given in figures 1 and 2. The calculated ^{22}Ne/^{21}Ne ratio (at shielding depth of 3 cm) in olivines and pyroxenes varies between 0·98 and

Table 4. GCR production rates of ^{21}Ne (10^{-8} cc STP/g Ma) in various minerals as a function of depth and radius, R, of the meteoroid.

		Depth (cm)					
Mineral	R (cm)	10	20	30	40	100	At centre
Olivine	9						0·450
	15	0·562					0·562
	25	0·64	0·688				0·688
	50	0·509	0·546	0·513	0·497		0·494
	∞	0·27	0·276	0·237	0·195	0·079	
Feldspar	9						0·211
	15	0·237					0·237
	25	0·247	0·253				0·253
	50	0·195	0·194	0·179	0·172		0·170
	∞	0·1	0·092	0·076	0·06	0·018	
Clinopx	9						0·278
	15	0·336					0·336
	25	0·372	0·392				0·395
	50	0·296	0·310	0·290	0·280		0·278
	∞	0·155	0·158	0·131	0·108	0·04	
Orthopx	9						0·396
	15	0·486					0·486
	25	0·546	0·583				0·583
	50	0·434	0·461	0·432	0·418		0·415
	∞	0·215	0·232	0·197	0·113	0·063	

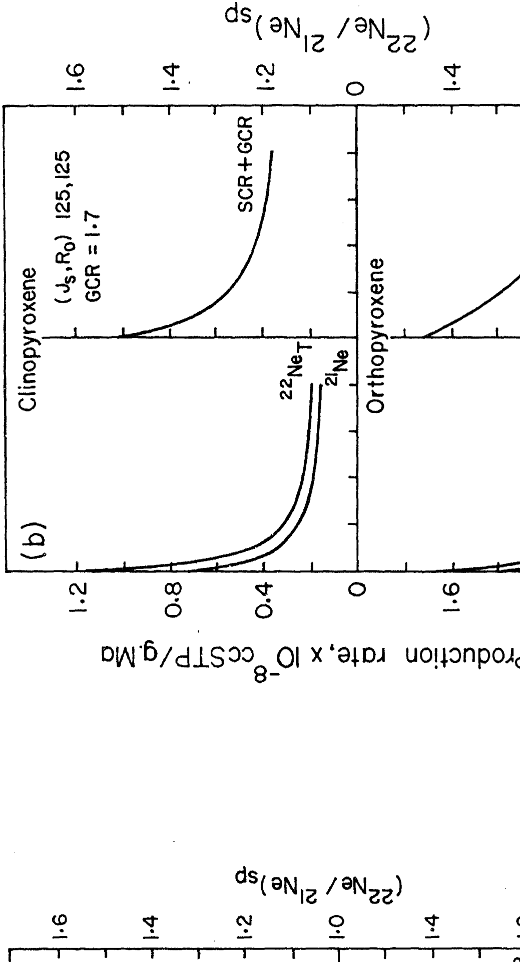
(b)
Clinopyroxene
(J_s, R_0) 125,125
GCR = 1·7
SCR+GCR
22Ne_T
21Ne
Orthopyroxene
(22Ne / 21Ne)sp
1·6
1·4
1·2
0
1·4
1·2
0·8
0·4
0
1·6
roduction rate, x 10-8 ccSTP/g.Ma
(22Ne / 21Ne)sp
1·6
1·4
1·2
1·0
1·4

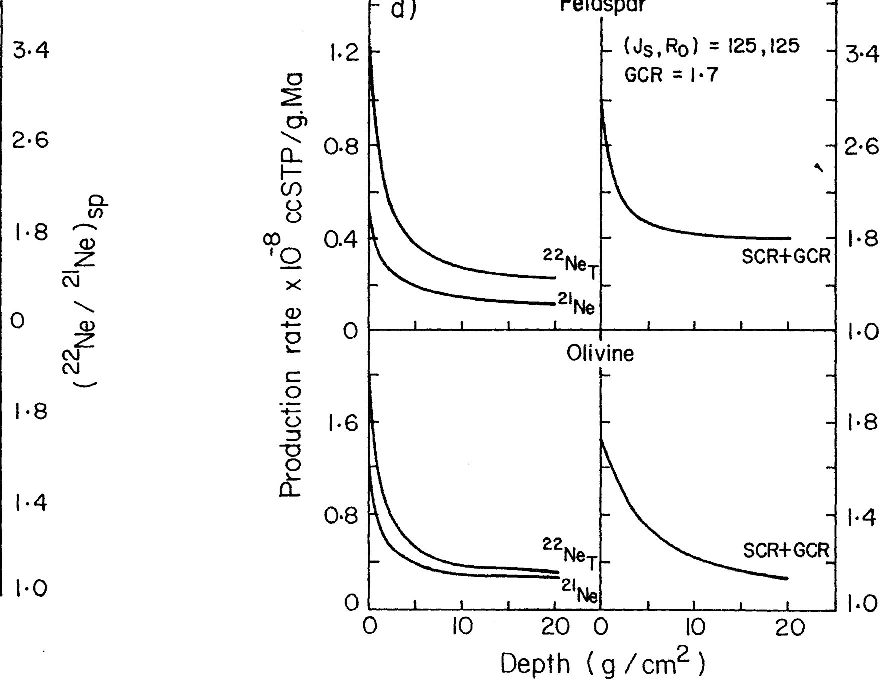

^{21}Ne and ^{22}Ne due to both solar and galactic cosmic rays and $(^{22}Ne/^{21}Ne)_{sp}$ in various minerals located
h^2 sec. 4π ster and SCR flux parameter values of $(J_s, R_0) = (100,100)$ [in figures (a) and (c)] and (125,125)

Table 5. GCR production ratio $^{22}Ne/^{21}Ne$ in various mi
radius, *R*, of the meteoroid.

		Depth		
Mineral	*R* (cm)	10	20	30
Olivine	9			
	15	1·077		
	25	1·042	1·026	
	50	1·041	1·013	1·007
	∞	1·055	0·995	0·976
Feldspar	9			
	15	1·947		
	25	2·052	2·109	
	50	2·058	2·158	2·181
	∞	2·02	2·21	2·312
Clinopx	9			
	15	1·173		
	25	1·152	1·14	
	50	1·151	1·32	1·128
	∞	1·154	1·124	1·107
Orthopx	9			
	15	1·111		
	25	1·082	1·068	
	50	1·081	1·056	1·051
	∞	1·087	1·046	1·024

1·18, which is consistent with the values in Bruderheim quo
$^{22}Ne/^{21}Ne$ ratio of 1·15 also compares favourably with th
in Elenovka pyroxenes. In the case of feldspars, corrected f

References

Allen R O Jr and Mason B 1973 Minor and trace elements in some mete
Acta **37** 1435–1456

Aylmer D, Begemann F, Cloth P, Dragovitsch P, Englert P, Filges D, F
Klein J, Kruse T H, Michel R, Moniot R K, Middleton R, Pe
Tuniz C, Vadja S, Weber H and Wieler R 1987 Monte Carlo model
of the nuclide production in thick stony targets isotropically irrad
ISSN 0366–0885 Kernfirschungsanlage Julich Gmbh

Baros F and Regnier S 1984 Measurement of cross-sections for ^{22}Na,
of Mg, Al, Si, Ca and Fe. Production ratios of some cosmogeni
855–861

Bhandari N and Potdar M B 1982 Cosmogenic ^{21}Ne and ^{22}Ne dept
Sci. Lett. **58** 116–128

Bhandari N, Bhattacharya S K and Padia J T 1975 The surface radi
to solar activity in the past; *Proc. 6th Lunar Sci. Conf. Geochim.*

Bhandari N, Lal D, Rajan R S, Arnold J R, Marti K and Moore
meteorites: a study based on cosmic ray tracks and neon isotope

Bhattacharya S K, Imamura M, Sinha N and Bhandari N 1980 D
activity in chondrites; *Earth Planet. Sci. Lett.* **51** 45–57

Bochsler H, Eberhardt P, Geiss J and Grögler N 1969 Rare gas meas
of the Otis and Elenovka chondrites. In *Meteorite research* (ed)
pp. 857–874

Cressy P J and Bogard D D 1976 On the calculation of cosmic ra
Geochim. Cosmochim. Acta. **40** 749–762

Eberhardt P, Eugster O, Geiss J and Marti K 1966 Rare gas measurem
21 414–440

Graf Th, Signer P and Wieler R 1986 Production rates of light nobl
Meteoritics **21** 376–377

Kohl C P, Murrel M T, Russ G P III and Arnold J R 1978 Evidence
ray flux over the past ten million years: ^{53}Mn and ^{26}Al measu
Geochim. Cosmochim. Acta Suppl. **10** 2299–2310

Lal D and Marti K 1977 On the flux of low energy particles in the s
meteorite; *Nucl. Track Detect.* **1** 127–130

Michel R, Dragovitsch P, Englert P, Peiffer F, Stuck R, Theis S, Begem

Proc. Indian Acad. Sci. (Earth Planet. Sci.), Vol. 97, No. 2, December 19
© Printed in India.

Northward propagation of the 30–50 day mode
region

R N KESHAVAMURTY, V KRISHNAKUM
Physical Research Laboratory, Navrangpura, Ahmedabad

MS received 29 February 1988; revised 11 November 198

Abstract. A highly simplified zonally symmetric system o
the basic mechanism of the northward movement of the 3
monsoon region. Zonally symmetric perturbations are used
Indian region. A two-level model is employed. A simple para
included. An expression is derived for the northward
magnitude for the phase speed is obtained. The northward m
by the basic zonal wind profile and cumulus heating.

Keywords. Northward propagation; 30–50 day oscillatio

1. Introduction

A 30–50 day oscillation in the equatorial region was first
Julian (1971). These were eastward-moving east-west over
height plane. Alexander *et al* (1978) composited active an
slow northward movement. Yasunari (1979, 1980) and
found similar northward propagation in satellite clou
Subrahmanyam (1982) found a northward-propagating mo

motion are

$$\frac{\partial u'}{\partial t}+\left(\frac{\partial U}{\partial y}-f\right)v'=-ku',$$

$$\frac{\partial v'}{\partial t}+fu'=-\frac{\partial \varphi'}{\partial y}-kv'.$$

The thermodynamic energy equation is

$$\frac{\partial}{\partial t}\left(\frac{\partial \varphi'}{\partial p}\right)+\sigma\omega'=-\frac{R}{C_p p}\dot{Q}'-k'\frac{\partial \varphi'}{\partial p}.$$

In these equations u' and v' are the zonal and meridional components of perturbat wind respectively, φ' the geopotential, $\omega = \mathrm{d}p/\mathrm{d}t$, k the coefficient of Rayleigh frict and k' the Newtonian cooling coefficient.

The fact that we have used zonally symmetric perturbations is a limitation. As th is some zonal symmetry in the monsoon region, i.e. the zonal scale of the inter-trop convergence zone (ITCZ) is much larger than the meridional scale, we believe this reasonable approximation. In our future (model) studies we shall retain x-depende in the equations. We assume a highly simplified boundary layer CISK type of hea (Charney and Eliassen 1964)

$$-\frac{R}{C_p p}\dot{Q}'=K\frac{\partial u_3'}{\partial y}.$$

Here $k=k'$ and $K=H\sigma g\rho\,\sin(2\alpha)\,\sqrt{(K_e/2f_0)}$, where $H=1{\cdot}5$; $\alpha=22\frac{1}{2}$d K_e = coefficient of eddy viscosity; f_0 at 10°N; ρ = density of air; σ = static stabil We use a two-level model:

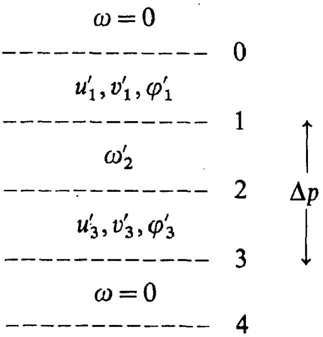

We also use a drastically simplified thermodynamic energy equation

$$\sigma\omega_2'=K\frac{\partial u_3'}{\partial y}.$$

unreasonable approximation. It is not claimed that the temperature fluctuations are totally unimportant but we would like to see the result of this approximation.

The continuity equation is

$$\frac{\partial v'_3}{\partial y} + \frac{0 - \omega'_2}{\Delta p} = 0 \tag{6}$$

$$\omega'_2 = \Delta p \frac{\partial v'_3}{\partial y}. \tag{7}$$

Substituting in the thermodynamic energy equation (at level 2) we get

$$\sigma \Delta p \frac{\partial v'_3}{\partial y} = K \frac{\partial u'_3}{\partial y}. \tag{8}$$

The equations of motion at level 3 are

$$\frac{\partial u'_3}{\partial t} + \left(\frac{\partial U_3}{\partial y} - f\right) v'_3 = -k u'_3 \tag{9}$$

and

$$\frac{\partial v'_3}{\partial t} + f u'_3 + \frac{\partial \varphi'_3}{\partial y} = -k v'_3. \tag{10}$$

Taking $\partial/\partial t$ of (8) and substituting for $\partial u'_3/\partial t$ from (9) we get

$$\sigma \Delta p \left(\frac{\partial}{\partial t} + k\right) \frac{\partial v'_3}{\partial y} = -K \frac{\partial}{\partial y}\left\{\left(\frac{\partial U_3}{\partial y} - f\right) v'_3\right\}. \tag{11}$$

Assuming oscillatory solution

$$v'_3 = V_3 \exp(i\nu t),$$

where ν is the frequency

$$\sigma \Delta p (i\nu + k) \frac{\mathrm{d}V_3}{\mathrm{d}y} = -K\left\{\left(\frac{\partial^2 U_3}{\partial y^2} - \beta\right) V_3 + \left(\frac{\partial U_3}{\partial y} - f\right)\frac{\mathrm{d}V_3}{\mathrm{d}y}\right\}$$

$$\times \left\{K\left(\frac{\partial U_3}{\partial y} - f\right) + (i\nu + k)\sigma \Delta p\right\} \frac{\mathrm{d}V_3}{\mathrm{d}y} = K\left(\beta - \frac{\partial^2 U_3}{\partial y^2}\right) V_3 \tag{12}$$

$$\frac{\mathrm{d}V_3}{V_3} = \frac{K\left(\beta - \dfrac{\partial^2 U_3}{\partial y^2}\right)}{\left\{K\left(\dfrac{\partial U_3}{\partial y} - f\right) + k\sigma \Delta p + i\nu \sigma \Delta p\right\}} \mathrm{d}y. \tag{13}$$

Therefore

$$V = V \exp\left[\int \frac{K\left(\beta - \dfrac{\partial^2 U_3}{\partial y^2}\right)}{} \mathrm{d}y\right].$$

$$= \frac{}{\left[\sqrt{\left(K\left(\frac{\partial U_3}{\partial y}-f\right)+k\sigma\Delta p\right)^2+v^2\sigma^2\Delta p^2}\,\right]}$$

$$\times \exp\left[i\tan^{-1}\left\{\frac{K\left(\frac{\partial U_3}{\partial y}-f\right)+k\sigma\Delta p}{v\sigma\Delta p}\right\}\right]. \tag{14}$$

Writing the exponent as

$$\frac{i}{y}\tan^{-1}\left\{\frac{K\left(\frac{\partial U_3}{\partial y}-f\right)+k\sigma\Delta p}{v\sigma\Delta p}\right\}y$$

we can approximately write

$$C_y=-\frac{v}{l}=\frac{-vy}{\tan^{-1}\left\{\frac{K\left(\frac{\partial U_3}{\partial y}-f\right)+k\sigma\Delta p}{v\sigma\Delta p}\right\}} \tag{15}$$

where l is the meridional wave number.

3. Calculation

We have used the smoothed profiles of zonal wind at 700 mb (U_3) and 200 mb (U_1) given in (Keshavamurty *et al* 1986). We have taken the period of oscillation as 40 days and have calculated the meridional phase speed C_y from (15) with and without friction. A value for friction corresponding to a decay time of 5 days was used. The meridional phase speed values are given in table 1 for the latitudes equator to 29°N. A phase speed of a few metres per second was obtained. In the case with friction there is southward movement in the region from the equator to 9°N. Considering the simplifying assumptions in the theory it is interesting that the theory predicts a reasonable speed.

Table 1. Calculated meridional phase speeds for latitudes equator to 29°N.

Latitude °N	Phase speed ($m\,s^{-1}$) Without friction	With friction
0–4	4·66	−0·53
5–9	1·76	−8·99
10–14	2·18	4·31
15–19	2·74	3·34
20–24	3·32	3·62
25–29	4·06	4·42

4. Wave-CISK

We shall now examine the result of introducing another simple type of cumulus heating, i.e. wave-CISK. Here we shall use the same equations of motion but the thermodynamic energy equation is

$$\frac{\partial}{\partial t}\left(\frac{\partial \varphi'}{\partial p}\right)+\sigma\omega' = -\frac{R}{C_p p}\dot{Q}' - k\frac{\partial \varphi'}{\partial p}$$

$$= K'\frac{\partial v_3'}{\partial y} - k\frac{\partial \varphi'}{\partial p}. \tag{16}$$

The cumulus heating is proportional to the divergence at the lower level. Following Lau and Peng (1987), the value of K' is given by

$$K' = mrLq_{\mathrm{sat}}R/C_p p, \tag{17}$$

where m is the moisture availability factor ($=0{\cdot}8$), r the relative humidity ($=0{\cdot}75$), $q_{\mathrm{sat}}(T_3)$ the saturation specific humidity at temperature T_3 at the lowest model level, L the latent heat of condensation, R the specific gas constant and C_p the specific heat at constant pressure.

Taking $(\partial/\partial t + k)$ of (2) and eliminating $(\partial/\partial t + k)u'$ using (1), we get

$$\left(\frac{\partial}{\partial t}+k\right)^2 v' + f\left(\frac{\partial}{\partial t}+k\right)u' + \left(\frac{\partial}{\partial t}+k\right)\frac{\partial \varphi'}{\partial y} = 0.$$

$$\left(\frac{\partial}{\partial t}+k\right)^2 v' - f\left(\frac{\partial U}{\partial y}-f\right)v' + \left(\frac{\partial}{\partial t}+k\right)\frac{\partial \varphi'}{\partial y} = 0. \tag{18}$$

Taking $\partial/\partial y$ of the thermodynamic energy equation

$$\frac{1}{\Delta p}\left(\frac{\partial}{\partial t}+k\right)\left(\frac{\partial \varphi_3'}{\partial y}-\frac{\partial \varphi_1'}{\partial y}\right)+\sigma\frac{\partial \omega_2'}{\partial y} = K'\frac{\partial^2 v_3'}{\partial y^2}. \tag{19}$$

However, by the continuity equation

$$\omega_2' = \Delta p\frac{\partial v_3'}{\partial y}$$

and $v_1' = -v_3'$.

Therefore by eliminating $(\partial/\partial t)(\partial\varphi'/\partial y)$ eq. (19) reduces to

$$-\frac{2}{\Delta p}\left(\frac{\partial}{\partial t}+k\right)^2 v_3' + \frac{f}{\Delta p}\left[\frac{\partial}{\partial y}(U_1+U_3)-2f\right]v_3' + (\sigma\Delta p - K')\frac{\partial^2 v_3'}{\partial y^2} = 0. \tag{20}$$

Assuming oscillatory solution of the type $v_3' = V_3\exp(i\nu t)$,

$$\frac{d^2 V_3}{dy^2} + n^2(y) V_3 = 0,$$

where

$$n^2(y) = \frac{f\left(\frac{\partial}{\partial y}(U_1 + U_3) - 2f\right) + 2(v^2 - k^2) - 4ikv}{\Delta p(\sigma \Delta p - K')} .$$

Using the same profiles of U_1 and U_3 and considering a period of 40 days, we ha calculated n^2. The values are presented in table 2. If linear friction is not included n negative everywhere and meridional propagation is not possible in this case, as sho in table 3.

Table 2. Calculated values of n^2 and refractive index n (with friction).

Latitude	$n^2 \times 10^{12}\,\mathrm{m}^{-2}$ RP	$n^2 \times 10^{12}\,\mathrm{m}^{-2}$ IP	$n \times 10^{6}\,\mathrm{m}^{-1}$ RP	$n \times 10^{6}\,\mathrm{m}^{-1}$ IP
30S	−1·49387	−0·00261	0·00107	−1·22224
29	−1·38461	−0·00261	0·00111	−1·17669
28	−1·28819	−0·00261	0·00115	−1·13499
27	−1·20380	−0·00261	0·00119	−1·09718
26	−1·12604	−0·00261	0·00123	−1·06115
25	−1·04143	−0·00261	0·00128	−1·02050
24	−0·93422	−0·00261	0·00135	−0·96655
23	−0·85599	−0·00261	0·00141	−0·92520
22	−0·76900	−0·00261	0·00149	−0·87693
21	−0·70078	−0·00261	0·00156	−0·83713
20	−0·63882	−0·00261	0·00163	−0·79926
19	−0·57932	−0·00261	0·00171	−0·76113
18	−0·52235	−0·00261	0·00180	−0·72274
17	−0·44987	−0·00261	0·00194	−0·67073
16	−0·39640	−0·00261	0·00207	−0·62961
15	−0·34605	−0·00261	0·00222	−0·58826
14	−0·28637	−0·00261	0·00244	−0·53514
13	−0·24565	−0·00261	0·00263	−0·49564
12	−0·18639	−0·00261	0·00302	−0·43173
11	−0·14353	−0·00261	0·00344	−0·37888
10	−0·09296	−0·00261	0·00428	−0·30492
9	−0·05623	−0·00261	0·00550	−0·23720
8	−0·06294	−0·00261	0·00520	−0·25092
7	−0·06388	−0·00261	0·00516	−0·25279
6	−0·05474	−0·00261	0·00557	−0·23403
5	−0·03660	−0·00261	0·00681	−0·19143
4	−0·02353	−0·00261	0·00849	−0·15362
3	−0.04260	−0·00261	0·00632	−0·20650
2	−0·02855	−0·00261	0·00771	−0·16913
1	−0·00228	−0·00261	0·02434	−0·05359
0	−0·00062	−0·00261	0·03211	−0·04062
1	−0·00228	−0·00261	0·02434	−0·05359
2	−0·01068	−0·00261	0·01253	−0·10412
3	−0·02637	−0·00261	0·00802	−0·16258

(*Continued*)

(*Table 2 continued*)

Latitude	$n^2 \times 10^{12}\,\mathrm{m}^{-2}$		$n \times 10^{6}\,\mathrm{m}^{-1}$	
	RP	IP	RP	IP
4	−0·03860	−0·00261	0·00664	−0·19658
5	−0·05075	−0·00261	0·00579	−0·22535
6	−0·06922	−0·00261	0·00496	−0·26315
7	−0·08001	−0·00261	0·00461	−0·28289
8	−0·10136	−0·00261	0·00410	−0·31839
9	−0·13419	−0·00261	0·00356	−0·36634
10	−0·17267	−0·00261	0·00314	−0·41555
11	−0·21318	−0·00261	0·00283	−0·46172
12	−0·26270	−0·00261	0·00254	−0·51255
13	−0·31961	−0·00261	0·00231	−0·56535
14	−0·37892	−0·00261	0·00212	−0·61557
15	−0·44827	−0·00261	0·00195	−0·66954
16	−0·51781	−0·00261	0·00181	−0·71959
17	−0·59799	−0·00261	0·00169	−0·77330
18	−0·70128	−0·00261	0·00156	−0·83742
19	−0·78129	−0·00261	0·00148	−0·88391
20	−0·82624	−0·00261	0·00143	−0·90898
21	−0·90458	−0·00261	0·00137	−0·95109
22	−0·93555	−0·00261	0·00135	−0·96724
23	−0·99739	−0·00261	0·00131	−0·99870
24	−1.02254	−0·00261	0·00129	−1·01121
25	−1·10260	−0·00261	0·00124	−1·05005
26	−1·21216	−0·00261	0·00118	−1·10098
27	−1·11461	−0·00261	0·00124	−1·05575
28	−1·06976	−0·00261	0·00126	−1·03429
29	−1·17057	−0·00261	0·00121	−1·08193
30N	−1·37497	−0·00261	0·00111	−1·17259

Table 3. Calculated values of n^2 and refractive index n (without friction).

Latitude	$n^2 \times 10^{12}\,\mathrm{m}^{-2}$	$n \times 10^{6}\,\mathrm{m}^{-1}$
30S	−1·49	1·22i
29	−1·38	1·18i
28	−1·29	1·13i
27	−1·20	1·10i
26	−1·12	1·06i
25	−1·04	1·02i
24	−0·93	0·97i
23	−0·85	0·92i
22	−0·77	0·88i
21	−0·70	0·84i
20	−0·64	0·80i
19	−0·58	0·76i
18	−0·52	0·72i
17	−0·45	0·67i
16	−0·39	0·63i
15	−0·34	0·59i
14	−0·28	0·53i
13	−0·24	0·49i

(*Continued*)

Latitude	$n^2 \times 10^{12}\,\mathrm{m}^{-2}$	$n \times 10^6\,\mathrm{m}^{-1}$
12	−0·18	0·43i
11	−0·14	0·38i
10	−0·09	0·30i
9	−0·05	0·23i
8	−0·06	0·25i
7	−0·06	0·25i
6	−0·05	0·23i
5	−0·03	0·19i
4	−0·02	0·15i
3	−0·04	0·20i
2	−0·03	0·16i
1	0·00	0·03
0	0·00	0·03
1	0·00	0·03
2	−0·01	0·10i
3	−0·02	0·16i
4	−0·04	0·19i
5	−0·05	0·22i
6	−0·07	0·26i
7	−0·08	0·28i
8	−0·10	0·32i
9	−0·13	0·36i
10	−0·17	0·41i
11	−0·21	0·46i
12	−0·26	0·51i
13	−0·32	0·56i
14	−0·38	0·61i
15	−0·45	0·67i
16	−0·52	0·72i
17	−0·60	0·77i
18	−0·70	0·84i
19	−0·78	0·88i
20	−0·82	0·91i
21	−0·90	0·95i
22	−0·93	0·97i
23	−1·00	1·00i
24	−1·02	1·01i
25	−1·10	1·05i
26	−1·21	1·10i
27	−1·11	1·05i
28	−1·07	1·03i
29	−1·17	1·08i
30N	−1·37	1·17i

5. Necessary condition for complex refractive index

$$\frac{d^2V}{dy^2} + n^2 V = 0$$

$$\frac{d^2}{dy^2}(V_r + iV_i) + (n_r^2 + in_i^2)(V_r + iV_i) = 0.$$

We get

$$\frac{d^2V_r}{dy^2}+n_r^2V_r-n_i^2V_i=0 \tag{23}$$

$$\frac{d^2V_i}{dy^2}+n_i^2V_r+n_r^2V_i=0. \tag{24}$$

Multiplying (23) by V_i and (24) by $-V_r$ and adding, we get

$$\frac{d}{dy}\left(V_i\frac{dV_r}{dy}-V_r\frac{dV_i}{dy}\right)-n_i^2(V_i^2+V_r^2)=0. \tag{25}$$

Integrating over a channel y_1 to y_2 and using the boundary condition

$$V_i=V_r=0 \quad \text{at} \quad y=y_1 \quad \text{and} \quad y=y_2$$

we get

$$\int_{y_1}^{y_2} n_i^2(V_i^2+V_r^2)\,dy=0. \tag{26}$$

This is possible only in the case where n_i^2 passes through zero, i.e. changes sign somewhere in the channel. It is seen that in the case of boundary layer CISK (Keshavamurty *et al* 1986 table 2) n_i^2 changes sign at the equator. This is mainly due to the term $(\partial U_3/\partial y-f)$. Since the absolute vorticity changes sign at the equator there is a possibility of n^2 being complex and thus of meridional propagation of the 30–50-day mode.

6. Summary and conclusions

Using a very highly simplified system of equations we have derived an expression for the speed of the northward propagation of the 30–50-day mode. Using July mean wind profile, a calculation of this phase speed yields reasonable values. The northward movement is determined by the basic wind profile and cumulus heating. A necessary condition for the northward propagation is also derived.

References

Alexander G, Keshavamurty R N, De U S, Chellapa R, Das S K and Pillai P V 1978 Fluctuations of monsoon activity; *Indian J. Meteorol. Hydrol. Geophys.* **29** 76–87

Charney J G and Eliassen A 1964 On the growth of the hurricane depression; *J. Atmos. Sci.* **21** 68–75

Keshavamurty R N, Kasture S V and Krishnakumar V 1986 30–50 day oscillation of the monsoon: A new theory; *Beltr. Phys. Atmos.* **49** 443–454

Lau N C and Lau K W 1986 The structure and propagation of intraseasonal oscillations appearing in a GFDL general circulation model; *J. Atmos. Sci.* **43** 2023–2047

Lau K M and Peng L 1987 Origin of low-frequency (intraseasonal) oscillations in the tropical atmosphere. Part I: Basic theory; *J. Atmos. Sci.* **44** 950–972

Madden R A and Julian P R 1971 Detection of a 40–50 day oscillation in the zonal wind in the tropical Pacific; *J. Atmos. Sci.* **28** 702–708

Sikka D R and Gadgil S 1980 On the maximum cloud zone and the ITCZ over Indian longitudes during southwest monsoon; *Mon. Weather Rev.* **108** 1840–1853

Yasunari T 1979 Cloudiness fluctuations associated with the northern hemisphere summer monsoon; *J. Meteorol. Soc. Jpn.* **57** 227–242

Yasunari T 1980 A quasi-stationary appearance of 30–40 day period in the cloudiness fluctuations during the summer monsoon over India; *J. Meteorol. Soc. Jpn.* **58** 225–229

Proc. Indian Acad. Sci. (Earth Planet. Sci.), Vol. 97, No. 2, December 1988, pp. 137–147.
© Printed in India.

Spectra of different fluxes over the arid and semiarid zones of northwest India during MONEX 1979

U S SINGH, DAYA SHANKER and R K SINGH
Department of Geophysics, Banaras Hindu University, Varanasi 221 005, India

MS received 14 March 1988

Abstract. Fluxes of heat, momentum and the kinetic energy over the arid and semiarid regions of Indian Peninsula have been computed. Spectral analysis of these fluxes at 50 mb interval were performed at each level in the vertical up to 300 mb surface. The eddy latent heat transport is governed essentially by short- and long-range periodicities. A 5-day periodicity is generally present in the vertical mean eddy fluxes. Long-range periodic oscillations are more pronounced in the extreme north of the Indian subcontinent. Dominance of medium-range periodicity is observed in all the fluxes except latent heat.

Keywords. Atmospheric flux; periodicity; MONEX; vertical distribution; oscillations.

1. Introduction

The study of different fluxes helps in better understanding of excess and deficit in the budget analysis. Spectral analysis has been widely used to understand the dominant periodicities in meteorological parameters to study the cause of the oscillations. Several investigators (Sankar Rao 1962; Sankar Rao and Ramanadham 1963; Saha 1970; Saha and Bavadekar 1973, 1977; Rao and Ramanamurty 1977; Ghosh *et al* 1978; Bavadekar and Mooley 1978; Rao 1981) attempted to study the fluxes over the Indian region. Singh and Singh (1987) carried out the study of heat and momentum transport over the east and west coasts of India during MONEX 79. The power spectral analysis of useful meteorological variables has been attempted by many workers. Madden and Julian (1972) showed the evidence of a global 5-day pressure wave. Gupta (1972) and Gupta and Singh (1977) observed the 5-day pressure oscillation over the Siberian anticyclone and the 4–5-day pressure oscillation over the Mediterranean regions respectively.

The present study was carried out to throw some light on the significant periodicities in sensible heat fluxes, latent heat fluxes and momentum and kinetic energy fluxes over the arid and semiarid zones of northwest India during the MONEX 79 summer monsoon months May to August at each level in the vertical up to 300 mb surface.

2. Data and method of analysis

The daily aerological data obtained from the MONEX 79 set of data at Ahmedabad, were subjected to spectral analysis in time domain following Blackman and Tukey (1958).

The heat, momentum and kinetic energy fluxes at any station may be expressed as

$$Q=\frac{C_P}{g}\int_0^{P_0}\bar{V}\bar{T}\,\mathrm{d}P+\frac{L}{g}\int_0^{P_0}\bar{V}\bar{X}\,\mathrm{d}P+\frac{C_P}{g}\int_0^{P_0}\overline{V'T'}\,\mathrm{d}P+\frac{L}{g}\int_0^{P_0}\overline{V'X'}\,\mathrm{d}P$$

$$M=\frac{1}{g}\int_0^{P_0}\bar{U}\bar{V}\,\mathrm{d}P+\frac{1}{g}\int_0^{P_0}\overline{U'V'}\,\mathrm{d}P$$

$$K=\bar{K}+K';\quad \bar{K}=\tfrac{1}{2}(\bar{U}^2+\bar{V}^2);\quad K'=\tfrac{1}{2}(U'^2+V'^2)$$

$$F_k=\int_0^{P_0}\bar{V}\bar{K}\,\mathrm{d}P+\int_0^{P_0}V'K'\,\mathrm{d}P,$$

where Q is the time-averaged northward flux of sensible and latent heat, M the momentum flux per unit time, X the humidity mixing ratio, K the kinetic energy and F_k the flux of kinetic energy per unit mass. The other parameters have their usual meaning. $(\bar{\ })$ denotes the time average and $(\ \ )'$ the deviation from the time average.

3. Discussion of the results

Of the several charts of power spectra, it has been considered adequate to present only the chart for vertical mean eddy flux in figures 1–5 for the purpose of illustration.

Tables 1 and 2 show the existing periodicities over the arid and semiarid regions of India for eddy sensible heat transport and eddy momentum transport at Ahmedabad, Jodhpur, Gwalior, New Delhi and Patiala. The vertical distribution of periodicity in eddy kinetic energy and flux of eddy kinetic energies do not show any significant changes other than those periodicities in tables 1 and 2. The computation of periodicity in eddy latent heat transport could not be performed from 700 to 300 mb because of lack of suitable number of data in the time series. Hence they are not presented here. However, the results are summarized below.

The vertical mean eddy sensible heat transport (table 1) does not show any remarkable periodicity over Ahmedabad, Jodhpur and Gwalior. However, at New Delhi and Patiala the presence of a short-range (<5-day) or medium-range (5–10-day) periodicity in the vertical mean eddy sensible heat transport is observed. The vertical mean eddy latent heat transport shows the presence of medium-range periodicity over Ahmedabad, Jodhpur and Patiala and besides that a short-range periodicity is present at Gwalior and New Delhi. The observed periodicity in vertical mean eddy momentum transport varies from 4·7 to 5·6 days over these stations (table 2). Thus, a fluctuation at an average of about 5 days can be considered to be present in the vertical mean eddy momentum transport over these regions. The vertical mean eddy kinetic energy shows the presence of medium-range periodicity over Ahmedabad, Jodhpur and New Delhi whereas the vertical mean flux of kinetic energy shows periodicity of short range at Jodhpur and of medium range over New Delhi and

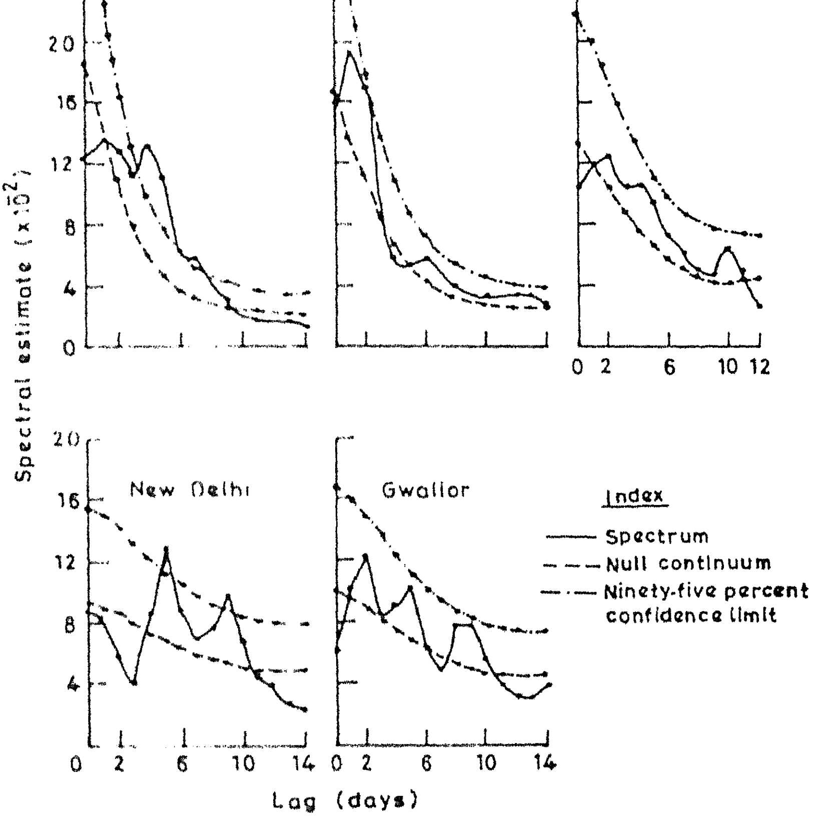

Figure 1. Spectra of vertical mean eddy sensible heat flux.

do not show their periodic occurrence whereas the vertical mean of eddy ntum transport, eddy latent heat transport, eddy kinetic energy and eddy kinetic flux usually seem to be governed by atmospheric processes that have varying dicity in short and medium ranges, more closely around 5 days. This 5-day dicity in different meteorological parameters, studied by several investigators thakrishnan and Keshavamurty 1970; Bhalme and Parasnis 1975; Murakami is most prominent in northern India and is related to the frequency of monsoon ravelling from the Bay of Bengal to northern India. Yanai *et al* (1968) found a ard-propagating wave with a 4 5-day period in certain regions of the tropics in eridional component of the wind at lower tropospheric levels. Wallace and Chang found an easterly wave with a period of 4 5 days and also a 4-day period of ary scale pressure fluctuation at the equator. Misra (1972) observed the ard-propagating planetary pressure wave of 4 5-day period in the tropics. Rao amanamurty (1972) observed a 4 8-day periodicity in tropical wave disturbances Singapore.

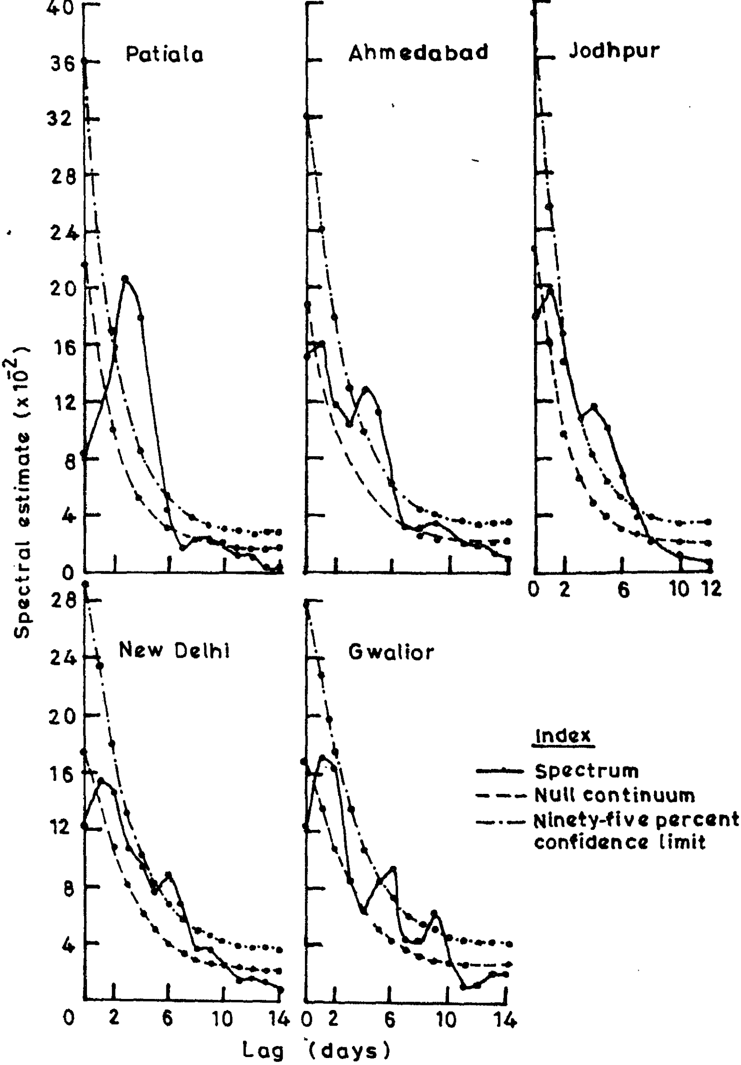

Figure 2. Spectra of vertical mean eddy latent heat flux.

We conclude that except in the eddy sensible heat transport over Ahmedabad, Jodhpur and Gwalior, a generally 3–7-day periodicity is present over the arid and semiarid zones of northwest India in vertical mean eddy latent heat transport, vertical mean eddy momentum transport and vertical mean eddy kinetic energy and vertical mean eddy flux of kinetic energy. Figure 6 and tables 1 and 2 show the vertical distribution of periodicities in eddy transport of heat, momentum and kinetic energy. In eddy latent heat transport short-, medium- and long-range (> 10-day) periodicity has been observed over the region. The eddy latent heat transport is dominated by short- and long-range periodic fluctuations of atomspheric processes in the layer below 800 mb surface over Ahmedabad, Jodhpur, Gwalior and New Delhi. In the layer from

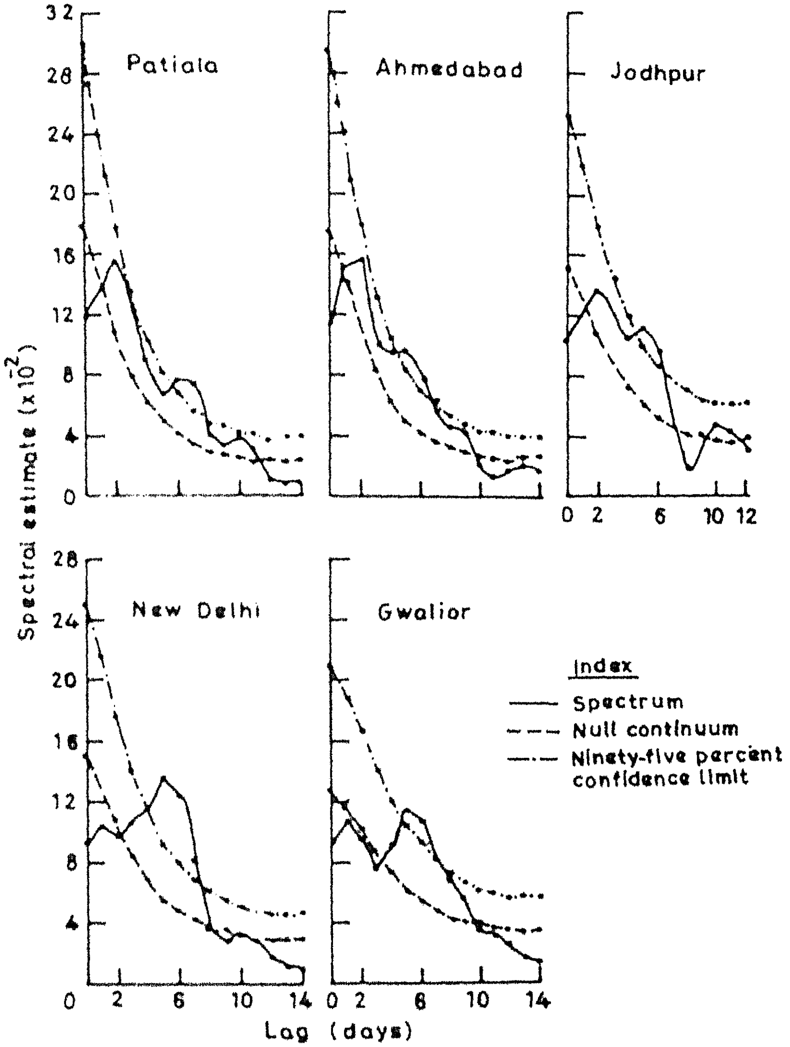

Figure 3. Spectra of vertical mean eddy momentum flux.

b to 950 mb surface over Gwalior and New Delhi, the eddy transport of latent s dominated by long-range periodicity.

eddy sensible heat transport, eddy momentum transport, eddy kinetic energy ddy flux of kinetic energy seem to be mainly controlled by short- and medium- fluctuations of atmospheric processes throughout the layer up to 300 mb surface. ng-range periodicity is occasionally present below 700 mb surface in these fluxes hmedabad, Jodhpur, Gwalior and New Delhi. However, at Patiala we observe esence of long-range periodicity at 900, 850, 700 and 300 mb in eddy momentum ort: at 850 and 900 mb in eddy kinetic energy and at 900, 700, 400 and 300 mb in

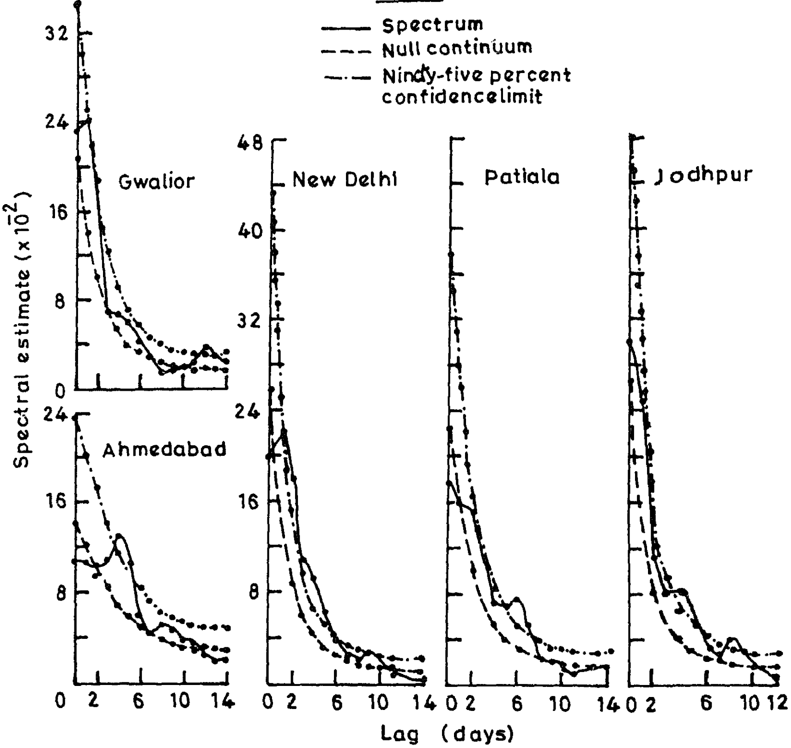

Figure 4. Spectra of vertical mean eddy kinetic energy.

troposphere around 700 mb surface at Patiala, New Delhi and sometimes at Jodhpur in some of the fluxes, and at upper troposphere around 300–400 mb surface.

At Ahmedabad and Gwalior, the long-range periodicity in eddy sensible heat transport is observed at about 300–400 mb surface and at Patiala at about 650–750 mb. This shows that with increasing latitude, the long-range periodicity, if present at upper surfaces (below 300 mb surface), shifts to higher pressure surfaces (lower heights) over these regions. This is observed more clearly in eddy sensible heat transport and less clearly in other fluxes. These shifts seem to be due to the influence of western disturbances which passed through extreme northern Indian subcontinent during MONEX 79. As 1979 was an abnormal monsoon year, these fluxes may not be very representative of average monsoon conditions but still they throw much light on this area of research. Information on absolute and relative values of these fluxes can be useful for modelling studies. The noted periodicities in the range of 5–7 days and 12–15 days are in agreement with periodicities noted in the monsoon system by many earlier studies.

4. Conclusions

(i) A periodicity of around 5 days is substantiated over arid and semiarid zones of northwest Indian subcontinent in vertical mean eddy latent heat and momentum

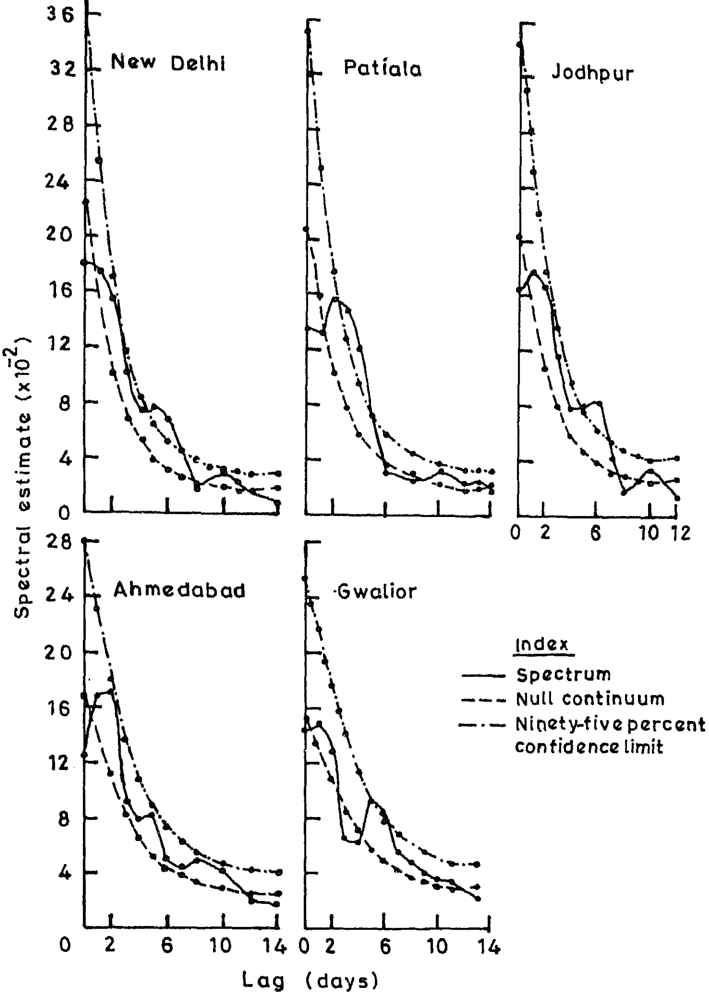

Figure 5. Spectra of vertical mean eddy kinetic energy flux.

transport. However, the vertical mean eddy sensible heat transport is not governed by any periodic oscillations over Ahmedabad, Jodhpur and Gwalior.

(ii) Medium-range periodicity usually dominates in eddy sensible heat, momentum, kinetic energy and flux of eddy kinetic energy in the lower troposphere. The eddy latent heat transport is essentially governed by short- and long-range periodicities over arid and semiarid zones of northwest India.

(iii) Long-range periodicity, if present at any surface, usually shifts to lower altitude pressure surface with increasing latitude over these regions of northwest India.

(iv) The dominance of medium-range periodicity in most of the fluxes in the lower troposphere as well as the shift of long-range periodicity to lower altitude with increasing latitude over northwest India seem to be associated with drought monsoon year..

Table 1. Periodicity (in days) in eddy sensible heat flux at different levels in the troposphere during MONEX 79.

on ure (mb)	Ahmedabad			Jodhpur			Gwalior			New Delhi			Patiala		
	Short	Med.	Long	Short	Med.	Long	Short	Med.	Long	Short	Med.	Long	Short	Med.	Long
rated ce to b)	×	×	×	×	×	×	×	×	×	3·1	5·6	×	×	7·0	×
ce ure	2·2	×	×	×	×	×	×	×	×	3·1	×	×	2·0	×	×
	×	×	×	×	×	×	4·0	×	×	4·0	×	×	×	9·3	×
	2·8	×	×	×	×	×	×	×	×	2·3 to 4·0	×	14·0	×	9·3	×
	2·5	×	×	×	×	×	×	×	×	4·0	×	×	2·8	9·3	×
	×	5·6	×	3·4	×	×	4·0	×	×	4·0	×	×	4·7	×	×
	4·7	×	×	2·4	×	12·0	×	×	×	×	7·0	×	2·8	×	14·0
	×	×	×	×	×	×	4·7	×	×	×	7·0	×	×	×	14·0
	×	×	×	×	6·0	×	×	×	×	×	7·0	×	×	7·0	12·0
	×	×	×	×	×	×	3·5	×	×	×	5·6	×	3·5	7·0	×
	4·0	×	×	×	6·0	×	×	7·0	×	4·0	×	×	×	7·0	×
	3·1	×	×	×	×	×	3·1	×	×	×	×	×	×	5·6	×
	4·7	×	×	—	—	—	3·1	×	14·0	3·1	×	×	×	5·6	×
	4·7	×	14·0	—	—	—	3·1	×	×	×	5·6	×	4·7	×	×
	4·7	×	14·0	—	—	—	3·5	×	12·0	×	5·6	×	4·0	×	×
	×	5·6	14·0	—	—	—	×	×	12·0	×	5·6	×	×	7·0	×

not computed due to lack of data; '×' no periodicity is present.

Table 2. Periodicity (in days) in eddy momentum flux at different levels in the troposphere during MONEX 79.

	Ahmedabad			Jodhpur			Gwalior			New Delhi			Patiala		
b)	Short	Med.	Long	Short	Med	Long	Short	Med	Long	Short	Med.	Long	Short	Med.	Long
ed to	×	5·6	×	4·8	×	×	×	5·6	×	×	5·6	×	4·7	×	×
	3·1	×	×	×	×	×	×	×	×	4·0	×	×	×	5·6	×
	4·7	×	×	×	×	×	×	×	×	×	×	×	×	5·6	×
	3·1 to 4·7	×	×	2·7	×	×	×	×	×	3·1	×	×	4·0	×	14·0
	3·5 to 4·7	×	×	3·4	×	×	4·7	×	×	×	5·6	×	×	×	14·0
	×	5·6	×	×	6·0	×	×	×	×	×	5·6	×	×	×	×
	×	5·6	×	×	×	12·0	3·5	×	×	×	5·6	×	×	9·3	×
	4·7	×	×	×	8·0	×	4·0	×	×	×	5·6	×	×	×	14·0
	4·0	×	×	×	8·0	×	×	×	×	×	5·6	×	×	×	×
	×	×	×	×	×	×	×	5·6	×	×	5·6	×	×	×	×
	×	7·0	×	×	×	×	×	5·6	×	4·7	×	×	4·0	×	×
	×	5·6	×	×	×	×	×	×	×	×	×	×	2·6	×	×
	4·7	×	×	—	—	—	4·7	×	×	4·0	×	×	4·0	×	×
	×	×	×	—	—	—	3·1	×	×	×	9·3	×	×	9·3	×
	3·5	×	14·0	—	—	—	3·1	×	×	4·7	9·3	×	4·7	×	×
	3·5	×	×	—	—	—	×	×	14·0	×	5·6	×	×	×	14·0

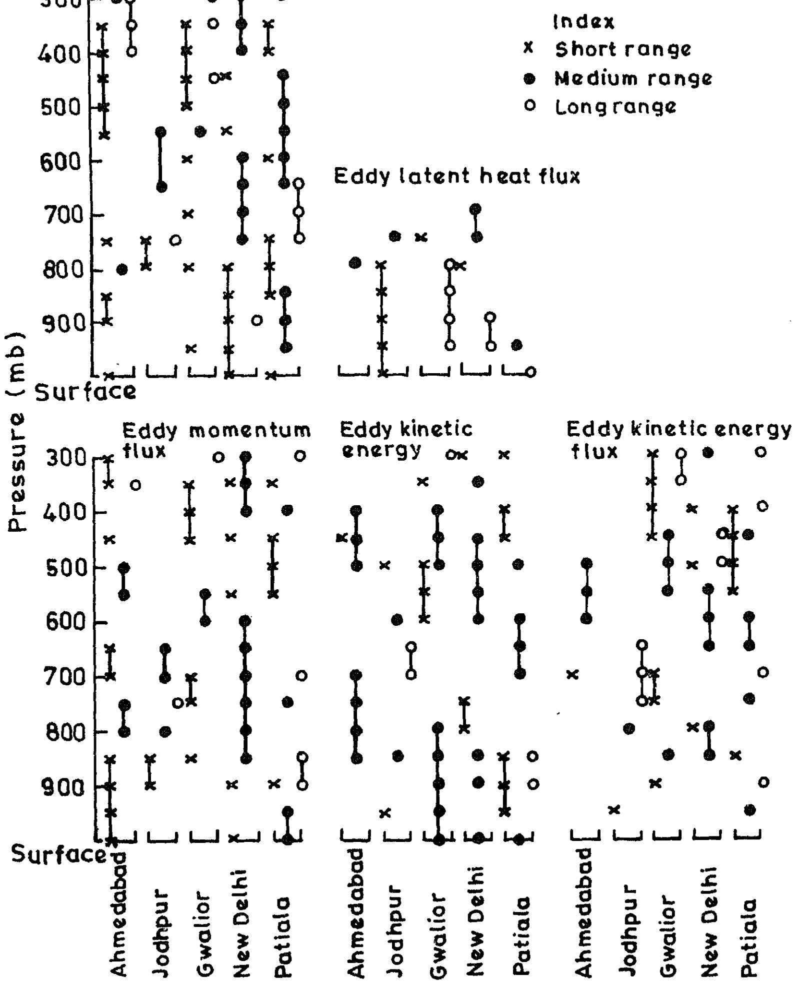

Figure 6. Periodicity in different fluxes at various stations in the vertical.

Acknowledgement

The financial support provided by UGC, New Delhi, is gratefully acknowledged.

References

Ananthakrishnan R and Keshavamurty R N 1970 On some aspects of the fluctuations in the pressure and wind fields over India during the summer and winter monsoon season; *Proc. Symp. Tropical Meteorology*, Honolulu, Hawaii, June 2–11, 1970, University of Hawaii, *Am. Meteorol. Soc.* (ed.) Paul H Kutschenreuter

Bavadekar S N and Mooley D A 1978 Computation of average precipitation over the eastern part of peninsular India during the summer monsoon from the continuity equation for atmospheric water vapour; *Tellus* **30** 537–541

Bhalme H N and Parasnis S S 1975 5–6 day oscillations in the pressure gradients over India during SW monsoon; *Indian J. Meteorol. Hydrol. Geophys.* **26** 77–80

Blackman R B and Tukey J W 1958 *The measurement of power spectrum* (New York: Dover) p. 190

Ghosh S K, Pant M C and Dewan B N 1978 Influence of Arabian Sea on the Indian summer monsoon; *Tellus* **30** 117–125

Gupta B R D 1972 Periodicity in the average daily strength of Siberian anticyclone from November 1967 to April 1968; *Tellus* **24** 380–381

Gupta B R D and Singh B 1977 A power spectrum analysis of the mean daily pressure over the Mediterranean and neighbourhood during November 1967 to April 1968; *Tellus* **29** 382–384

Madden R A and Julian P R 1972 Further evidence of global scale 5-day pressure waves; *J. Atmos. Sci.* **29** 1464–1469

Misra B M 1972 Planetary pressure wave of 4–5 day period in the tropics; *Mon. Weather Rev.* **100** 313–316

Murakami M 1976 Analysis of summer monsoon fluctuations over India; *J. Meteorol. Soc. Jpn.* **54** 15–31

Rao G Appa 1981 Atmospheric energetics over India during drought and normal monsoon; *Mausam* **32** 67–78

Rao G Appa and Ramanamurty Bh V 1972 Tropical wave disturbance over the region east of Indian Ocean; *J. Meteorol. Soc. Jpn.* **50** 325–331

Rao G Appa and Ramanamurty Bh V 1977 Water vapour transport and vergence patterns over India during two contrasting summer monsoons; *Pure Appl. Geophys.* **115** 491–501

Saha K R 1970 Air and water vapour transport across the equator in the western Indian Ocean during the northern summer; *Tellus* **22** 681–687

Saha K R and Bavadekar S N 1973 Water vapour budget and precipitation over the Arabian Sea during the northern summer; *Q. J. R. Meteorol. Soc.* **99** 273–278

Saha K R and Bavadekar S N 1977 Moisture flux across west coast of India and rainfall during southwest monsoon; *Q. J. R. Meteorol. Soc.* **103** 370–374

Sankar Rao M 1962 On the meridional local eddy flux of heat over India; *J. Atmos. Sci.* **19** 468–473

Sankar Rao M and Ramanadham R 1963 On the meridional local eddy flux of relative angular momentum over India; *J. Atmos. Sci.* **20** 350–353

Singh U S and Singh R S 1987 Spectra of heat and momentum fluxes over the east coast of India during MONEX 1979; *Mausam* **38** 411–414

Wallace J M and Chang C P 1969 Spectrum analysis of large-scale wave disturbances in the tropical lower troposphere; *J. Atmos. Sci.* **26** 1010–1025

Yanai M, Nitta T and Hayashi Y 1968 Power spectra of large-scale disturbances over the tropical Pacific; *J. Meteorol. Soc. Jpn.* **46** 308–323

Satellite-tracked drifting buoy observations in the south equatorial current in the Indian Ocean

S R SHETYE and G S MICHAEL
National Institute of Oceanography, Dona Paula 403 004, India

MS received 30 December 1987; revised 5 July 1988

Abstract. Three satellite-tracked drifting buoys released in the south equatorial current in the Indian Ocean followed the path of the current moving westward approximately zonally in the vicinity of 10 S latitude. On nearing the east coast of Africa two buoys moved north and the third moved south. Over the open sea regime the buoys moved with a speed of approximately 30 cm/s at an angle of about 35° to the left of the wind. The overall tendencies seen in the buoy drift are similar to those observed elsewhere in the world oceans.

Keywords. Drifting buoys; south equatorial current; Indian Ocean; surface drift; mixed layer.

1. Introduction

In April 1983 three satellite-tracked drifting buoys were released at about 77 E and 10–15 S in the Indian Ocean by the National Institute of Oceanography, Goa, using the vessels MV *Farnella* and MV *Skandi Surveyor*. During their lifetime the buoys crossed a zonal band stretching from about 80 E to the east coast of Africa, and from 5 S to 15 S. The south equatorial current flows in this region.

The drifting buoys used in this study were TOD's manufactured by the Polar Research Laboratory, California, USA. The ARGOS System, France, was used to track the buoys and to collect data recorded by the onboard sensors. On an average about six fixes and data transmissions were obtained per day. The following sensors were onboard: air temperature, atmospheric pressure, wind speed and direction (15 min average, sampled once per sec) and buoy compartment temperature. In this paper we restrict our attention to the observed drift, and to the surface winds measured by using the onboard sensors.

2. Data

The wind sensor was located about 90 cm above the sea surface. During launching, all the three buoys had a 24 m drogue tethered with its centre about 40 m below the ocean surface. A drogue sensor sensed whether the drogue stayed attached or not. The design of the buoy is given in figure 1.

The drifters were launched during the second week of April 1983. By November 1983 all the three buoys had reached the east coast of Africa. The drogues came unattached during the early part of the westward journey. The overall performance of the buoys is summarized in table 1.

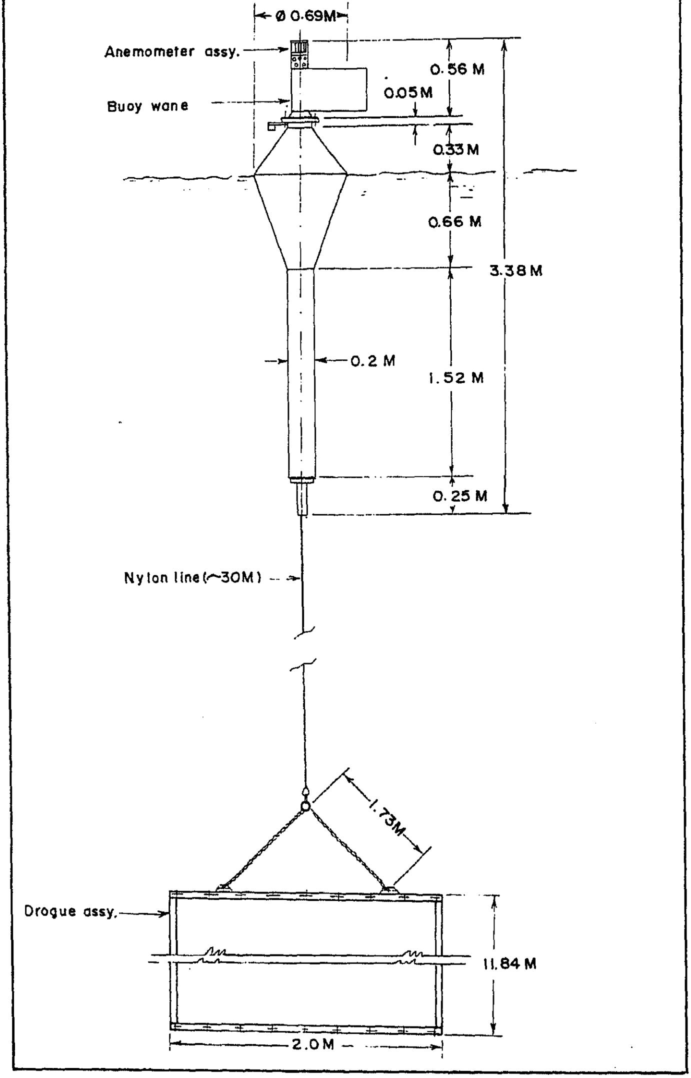

Figure 1. Vertical cross-sectional view of the drifting buoys used in this study.

Figure 2 gives the locations of the buoys with time. As seen from this figure, before entering the coastal current system off Africa, the buoys generally moved westward. The speed of buoys 1730 and 1733 showed little change when the drogues got detached. Buoy 1732, on the other hand, moved noticeably slower when the drogue was attached, and picked up speed when it got detached. The mean and the standard deviation of the magnitude of the drift of each of the three buoys during each fortnight of their lifetime are summarized in table 2.

Buoy 1732 showed a strong tendency to exhibit damped inertial motions when the drouge was attached. An extreme case of such motions occurred during 17–22 June.

Table 1. Dates and locations of interest in the performance of the three buoys.

	Buoys		
	1730	1732	1733
Deployment	15 April 1983	24 April 1983	18 April 1983
Latitude	11·907 S	9·812 S	14·473 S
Longitude	77·079 E	76·869 E	76·763 E
Last report	8 Oct. 1983	18 Nov. 1983	28 Sept. 1983
Latitude	0·111 S	5·876 S	13·148 S
Longitude	42·780 E	39·256 E	40·579 E
Date drogue detached	28 May 1983	1 August 1983	10 June 1983
Date wind magnitude Sensor broke down	3 July 1983	16 Nov. 1983	16 Sept. 1983

Details of the motion during this time are given in figure 3. On 16th June the winds recorded by the buoy were of the order of 10 m/s, and decreased rapidly later. At 10 S the inertial period was 69 h. Inertial motions similar to, but weaker than, those exhibited by buoy 1732 were also observed in the other two buoys during 17–22 June.

The wind sensor performed best on buoy 1733. Figure 4 has wind vectors plotted at buoy locations along 1733's path. A striking feature revealed by the figure is the buoy's tendency to move to the left of the wind direction. To explore this feature further we computed the angle between the drift over two consecutive buoy locations and the vector mean of the winds reported at the two locations for many such pairs of locations. Only those values for which the magnitude of the vector mean exceeded 1·7 m/s, the threshold value of the wind sensor, were used. The results for the period after the drogue was detached are summarized in figure 5. The mean of the angle between the drift and the wind was found to be 35° with a standard deviation of 44°. The angle did not show any marked dependence on the wind speed.

3. Discussion

Studies on drifting buoys carried out over the past decade in different regions of the world oceans have shown that undrogued buoys in the open ocean regime move at an angle to the right of the wind in the northern hemisphere (see McNally 1981, for example). This angle is close to the angle of 45° predicted by Ekman's theory for wind-driven surface flow in the oceans (Ekman 1905). However, doubts about this explanation arise because the present empirical evidence supports the idea of a slab-like mixed layer (Niiler and Kraus 1977) in which the velocity remains unchanged through the depth of the slab. These models predict that the surface velocity will be at an angle of 90° to the right (left) in the northern (southern) hemisphere, i.e. there will be no downwind component of the surface velocity (McNally and White 1985). Buoys, on the other hand, show a well-defined downwind component. Different explanations have been put forth to account for this component. McNally and White (1985) argued that it is caused by the stress exerted by the wind directly on the buoy (windage). Kirwan *et al* (1979) explained it by invoking Stokes drift. They also pointed out that large-scale geostrophic flow would tend to make the buoys move downwind.

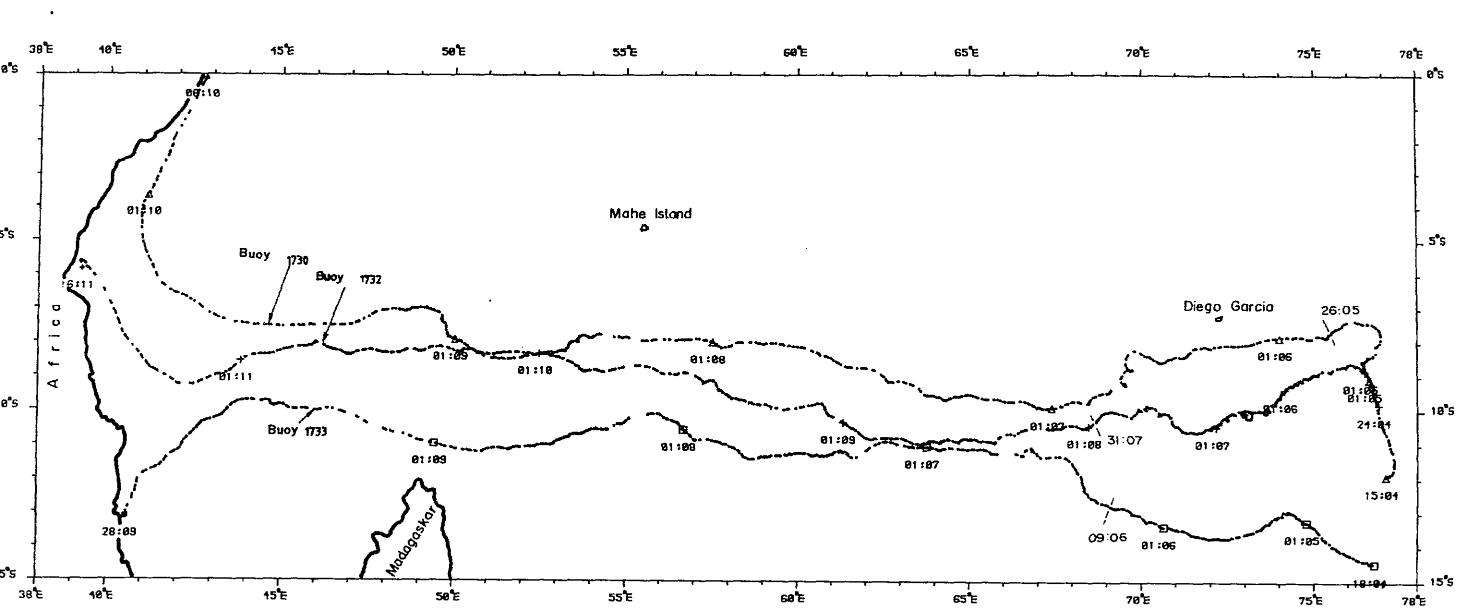

Figure 2. Locations of the three buoys (....) at the beginning of each month for buoy 1730 (Δ), buoy 1732 (+) and buoy 1733 (□). Time when drogue got detached is shown (26th May for buoy 1730, for example) with a line perpendicular to the buoy path.

Table 2. Mean and standard deviation (in brackets) of buoy drift in cm/s.

	Buoys		
Period	1730	1732	1733
16–30 April	26·2 (8·8)	20·6 (10·3)	23·6 (7·8)
1–15 May	13·4 (8·8)	14·7 (9·5)	13·1 (7·1)
16–31 May	29·7 (11·6)	12·7 (7·3)	26·0 (10·5)
1–15 June	35·5 (15·9)	14·3 (8·2)	33·4 (12·7)
16–30 June	38·0 (17·1)	22·4 (11·8)	39·0 (17·9)
1–15 July	35·3 (12·5)	18·3 (9·0)	33·2 (20·4)
16–31 July	51·6 (17·4)	25·2 (11·6)	33·3 (16·1)
1–15 August	35·3 (19·7)	32·3 (12·1)	28·5 (14·6)
16–31 August	33·2 (15·9)	31·6 (12·7)	36·1 (19·4)
1–15 September	39·5 (22·0)	39·4 (19·3)	55·7 (37·6)
16–30 September	67·1 (13·3)	44·9 (18·5)	45·8 (18·3)
1–15 October	73·5 (35·2)	38·3 (15·3)	
16–31 October		38·1 (14·8)	
1–15 November		59·8 (21·0)	

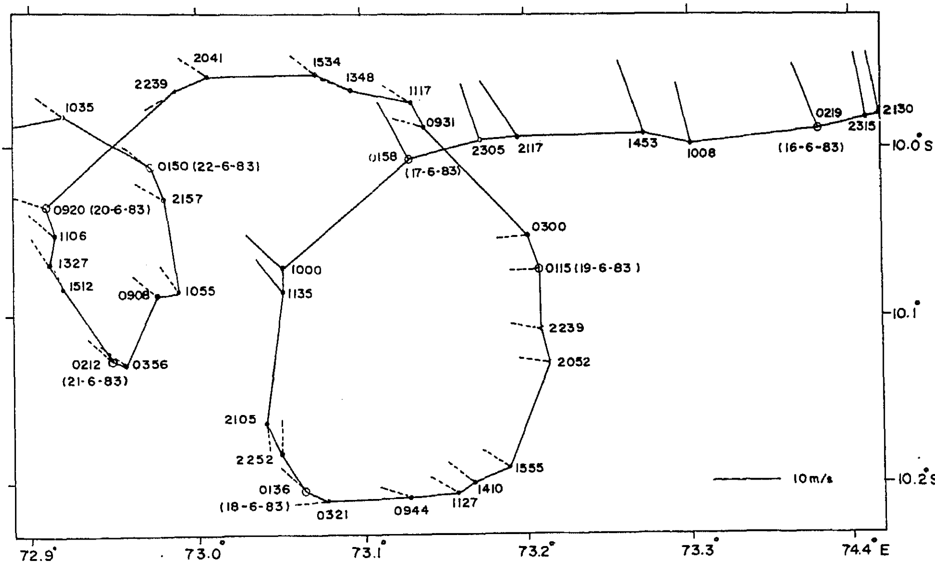

Figure 3. Locations of buoy 1732 during 16–22 June are shown with dots. Times (GMT at these locations are also shown. Wind sticks start from the location of the buoy and poin in the direction of the winds. Wind sticks are drawn as dashed line where magnitude of th winds is less than the threshold value of 5 m/s. The stick in the lower right hand corne corresponds to 10 m/s.

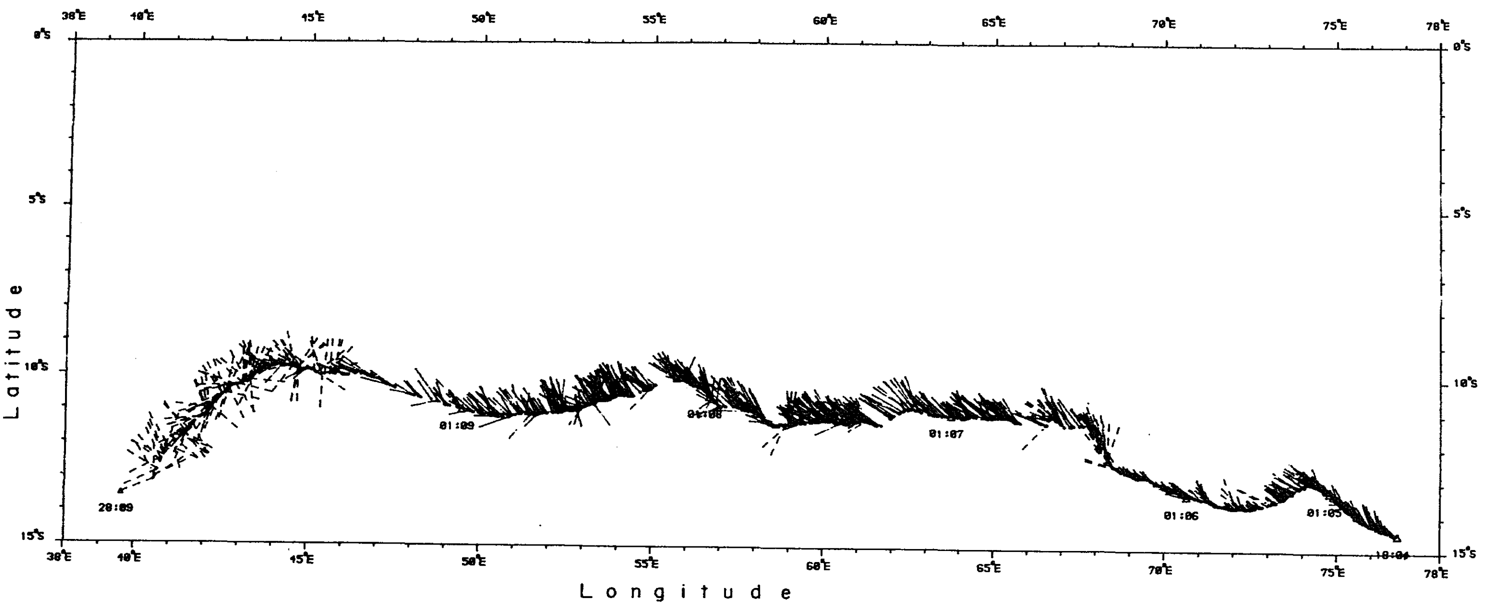

Figure 4. Winds recorded by buoy 1733 are shown by a stick starting at the buoy location and pointing in the direction of the wind. Magnitude of the wind corresponding to the stick in the upper right hand corner is 20 m/s. A dashed stick signifies that no wind magnitude value was available.

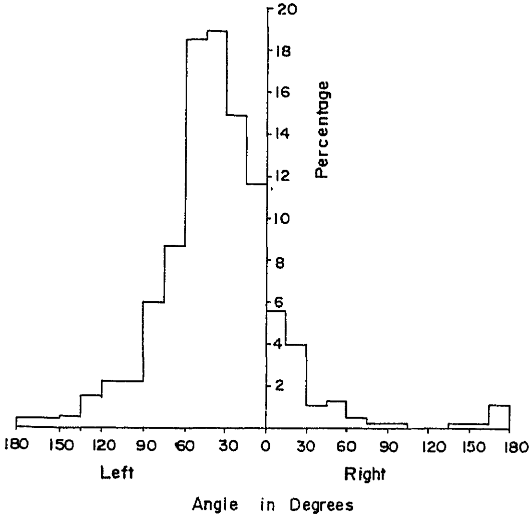

Figure 5. Histogram (from 551 observations) of angles between drift and winds for buoy 1733 after the drogue was detached.

The observed angle between the winds and buoy drift can also be explained by taking into account the friction at the bottom of the mixed layer. In slab mixed layer models the depth h of the mixed layer and surface temperature can be computed using air–sea fluxes of heat and momentum. The velocity can then be computed (see eqn (4.2) of Davies *etal* (1981)) from the following equations:

$$\frac{\partial u}{\partial t} = fv + \frac{1}{\rho h}(\tau_0^x - \tau_b^x) - \frac{1}{h}(u - \tilde{u})\frac{\partial h}{\partial t}, \tag{1a}$$

$$\frac{\partial v}{\partial t} = -fu + \frac{1}{\rho h}(\tau_0^y - \tau_b^y) - \frac{1}{h}(v - \tilde{v})\frac{\partial h}{\partial t}. \tag{1b}$$

Here u and v are respectively the eastward and northward velocity components in the slab. f is the Coriolis parameter, ρ the density, (τ_0^x, τ_0^y) the wind stress, (τ_b^x, τ_b^y) the stress at interface between the mixed layer and the underlying ocean, $(\tilde{u}, \tilde{v})$ the velocity just below the slab, and t the time.

If the time scale of interest is much longer than the inertial period, as is generally the case with drifting buoy data, the terms on the left-hand side of (1a) and (1b) can be safely ignored. The same argument can be used to ignore the last terms on the right-hand side. We now assume that the bottom stress terms can be written as

$$\tau_b^x = K_1 u, \quad \tau_b^y = K_1 v, \tag{2}$$

where K_1 is a constant. The solution to the velocity field can then be given by

$$(u^2 + v^2)^{1/2} = \frac{\tau_0}{[(\rho f h)^2 + K_1^2]^{1/2}}, \tag{3}$$

of the wind stress. $U = [u^2 + v^2]$ is the magnitude of the surface current. Equation (3) implies that in the northern (southern) hemisphere the drift angle θ will be negative (positive), i.e. clockwise (counter clockwise) with respect to the wind vector. It further implies that the magnitude of the angle will increase with latitude and with depth of the mixed layer. At the equator the angle vanishes.

On the whole, the existence of the downwind component can be explained by invoking one or more of the following influences: windage, Stokes drift, influence of interior geostrophic flow and friction at the bottom of the mixed layer. It is not possible at present to determine the relative magnitudes of these effects. Complicating the issue further are the recent data presented by Richman *et al* (1987) showing the presence of current shear in the uppermost 15 m of the water column during six days of observation off the west coast of North America. It is not known how common is the occurrence of such shears.

The geostrophic interior flow in the region crossed by the three buoys discussed here is dominated by the south equatorial current (SEC) which is a part of the southern hemispheric subtropical anticyclonic gyre (Wyrtki 1973). As seen in figure 6, a characteristic feature of this gyre is the long high-pressure ridge that extends from the Agulhas current system at the western edge to the Timor Sea on the east. The westward SEC is located north of the ridge. The current, on reaching the latitude of about 50 E, near the northern tip of Madagascar, bifurcates, one branch flowing southward along the east coast of Madagascar and the other continues westward. The latter, on approaching the coast of Africa bifurcates again, one branch flowing northward and the other southward into the Agulhas current system. It appears that the separation of the buoys, on reaching the coast of Africa, one moving south and the other two moving north occurred in response to the bifurcation of the SEC near the coast. As seen from table 2 the buoys picked up speed on moving into the coastal region.

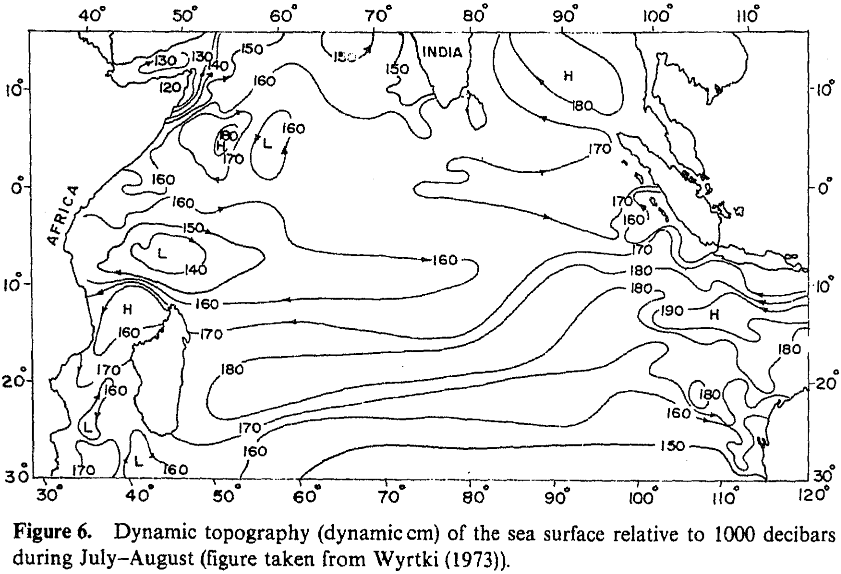

Figure 6. Dynamic topography (dynamic cm) of the sea surface relative to 1000 decibars during July–August (figure taken from Wyrtki (1973)).

vailable data suggest that the mixed-layer depth around 75 E and 10 S during y June is in the range of 20 to 60 m (Wyrtki 1971). It is possible that in the region sed by buoy 1732 during June July the mixed layer was less than 40 m, the depth of buoy drogue. In such a case the buoy would move much slower with the lower cities below the mixed layer.

onclusions

ummary, the three buoys generally followed the path of the SEC moving westward roximately zonally in the vicinity of 10 S. On reaching the west coast of Africa the ys separated, two moving north and the third moving south apparently in response ne bifurcation of the SEC. Over the open ocean regime the buoys moved at an angle bout 35° to the left of the winds, with a speed of about 30 cm/s. Though it is not sible at present to determine the precise dynamical reasons behind the movement bited by the buoys, the overall tendencies shown by them are similar to those erved in other parts of the world oceans.

nowledgements

s research has been supported by grants from the Department of Ocean elopment, Government of India, New Delhi. Programming support during the rse of the data analyses was provided by the Ocean Engineering and Pipeline ion and the Computer Section of MECON, Ranchi.

erences

es R E, de Szoeke R and Niiler P 1981 Variability in the upper ocean during MILE. Part II: Modelling nd mixed layer response; *Deep-Sea Res.* **A28** 1453–1475
an V W 1905 On the influence of earth's rotation on ocean currents; *Ark. Mat. Astron. Fys.* **2** 1–53
an A D Jr., McNally G, Pazan S and Wert R 1979 Analysis of surface current response to winds; *J. hys. Oceanogr.* **9** 401–412
lally G J 1981 Satellite-tracked drift buoy observations of the near-surface flow in the eastern nid-latitude north Pacific; *J. Geophys. Res.* **86** 8022–8030
lally G J and White W B 1985 Wind-driven flow in the mixed layer observed by drifting buoys during utumn winter in the mid-latitude north Pacific; *J. Phys. Oceanogr.* **15** 684–694
r P P and Kraus E B 1977 One-dimensional models of the upper ocean. In *Modelling and prediction f the upper layers of the ocean* (ed.) E B Kraus (Oxford: Pergamon Press)
man J G, de Szoeke R A and Davis R E 1987 Measurement of near-surface shear in the ocean; *J. eophys. Res.* **92** 2857–2858
ki K 1971 *Oceanographic atlas of the international Indian Ocean expedition* (Washington DC: US iovernment Printing Office)
ki K 1973 Physical oceanography of the Indian Ocean. In *Biology of the Indian Ocean* (ed.) B Zietzschel New York: Springer-Verlag) pp. 18–36

oc. Indian Acad. Sci. (Earth Planet. Sci.), Vol. 97, No. 2, December 1988, pp. 159–171.
Printed in India.

etrieval of cloud classification parameters using two-dimensional fast ourier transform

M MOHAN, LAKSHMI BHADURI and VIJAY K AGARWAL
Meteorology and Oceanography Division, Remote Sensing Area, Space Applications Centre, Ahmedabad 380 053, India

MS received 21 July 1987; revised 14 April 1988

Abstract. A method is presented for the retrieval of classification parameters of clouds observed by satellite-borne imaging systems. It is based on a two-dimensional fast Fourier transform of cloud images and an analysis of their power spectra. The parameters retrieved provide quantitative information on mean brightness, size, shape and directional properties of clouds. The efficacy of the subdivision of the original cloud image into smaller regions and the determination of individual parameters is demonstrated by applying this procedure to some NOAA and INSAT cloud images.

Keywords. Cloud classification parameters; satellite cloud images; two-dimensional fast Fourier transform; power spectrum; Laplacian filter.

Introduction

antitative analyses of cloud patterns and their relationship to cloud radiative operties have many useful applications ranging from their usefulness in studying nospheric dynamics to introducing corrections in remote-sensing observations for ud interferences (Cho 1976; Hobbs and Deepak 1981; Henderson-Sellers 1984). hough a rigorous solution to the problem of radiative transfer in realistic cloud ds is a formidable one, there have been attempts to tackle it numerically by model-g such situations with geometrically simple forms for the shapes of clouds and their tial distributions and simple microphysical properties for their constituents. (Cox 81; Harshvardhan *et al* 1981; Harshvardhan and Weinman 1982; Naber and einman 1984; Welch and Weilicki 1984). These studies have strongly indicated that th cloud mesoscale features and the microphysical nature of their internal nstituents are equally decisive in controlling the transport of heat and radiation ergy in an assembly of clouds. Highlighting this conclusion, the International tellite Cloud Climatology Project (Schiffer 1982) decided to look into it further by ordinating all available satellite cloud observations collected over the world during period 1983–1988.

The two-dimensional fast Fourier transform (2DFFT) is a very quick and effective y of retrieving average cloud mesoscale parameters (Bunting and Fournier 1980; ldalagi and Lebow 1982; Logan *et al* 1983) that can be used for modelling cloudy . Besides, it provides a means of classifying cloud fields in a quantitative fashion for mparisons. The power spectrum generated from it contains information on average observed by NOAA and INSAT satellites over the Arabian Sea and the Indian Ocean. We have introduced some modifications to the original scheme to simplify the computations. Our method is outlined in § 2. The description of its application to the NOAA and INSAT images and the results obtained are discussed in § 3. The generated 2DFFT power spectra are displayed in the form of images and the derived parameters are presented in tables.

2. Retrieval of cloud gross parameters

In a satellite image, clouds appear as patches of brightness against a darker and uniform background of vast stretches of oceans or land masses. Usually clouds in the visible channel images are sharper than in the thermal infrared images, in which low-lying water vapour, which also emits in the infrared, produces cloud-like impressions.

One can define the Fourier transform of a satellite cloud image discretized into an $N \times N$ array of pixels (Rosenfeld and Kak 1976; Logan *et al* 1983) as

$$F(k,l) = \frac{1}{N^2} \sum_{m,n=0}^{N-1} f(m,n) \exp\left[\frac{-2\pi i}{N}(mk+nl)\right]; \quad (k,l) = 0 \text{ to } N-1, \tag{1}$$

where (m, n) are the (x, y) coordinates of a pixel whose gray level is $f(m, n)$. To carry out the arithmetical operations involved in (1), we have employed the fast Fourier transform (FFT) technique (Bergland 1969; Cooley *et al* 1969; Bracewell 1978). From the real and imaginary parts of $F(k, l)$, the power spectrum of the image can be computed as

$$P(k,l) = [\mathrm{Re}\, F(k,l)]^2 + [\mathrm{Im}\, F(k,l)]^2. \tag{2}$$

Since $f(m,n)$ is a real quantity, it can be easily seen from (1) and (2) that $P(k,l)$ will exhibit the property

$$P(k,l) = P(N-k, N-l). \tag{3}$$

This implies that half of $P(k,l)$ will be same as the other half, except for a rotation through 180°.

One can notice in this spectrum that all the low-frequency components will be placed at the four corners of the array $P(k,l)$, by virtue of definition (1). This is rather inconvenient for the computation of the cloud parameters. So we divide the spectrum into four quadrants and rearrange them as shown in figure 1, whereby all the low-frequency components are brought to the middle of the frame (Logan *et al* 1983). This new power spectrum will henceforth be referred to as $P'(k,l)$. The relationship between $P(k,l)$ and $P'(k,l)$ can also be expressed as, $P'(k,l) = P(k - N/2, l - N/2)$.

In most cases, the actual numerical values of $P'(k,l)$ will span several orders of magnitude, making it impossible to display it as an image. In a computer display or a photographic image, the gray level can range only over a finite and small range of values. So in order to reduce the span of $P'(k,l)$, we transform it as

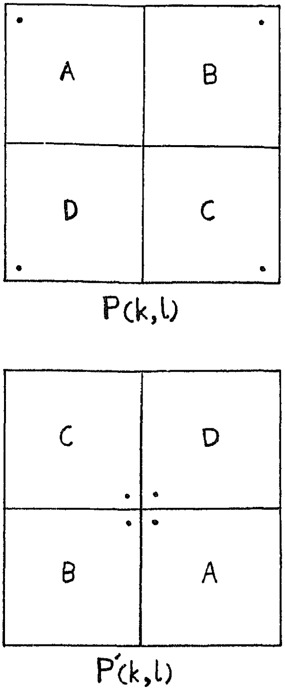

Figure 1. Rearrangement of the power spectrum to effect the transformation $P(k,l) \Rightarrow P'(k,l)$.

sformation is only to display the power spectrum as a visual image. For the putations of the cloud parameters, however, we will use $P'(k,l)$ and not $G(k,l)$. he different cloud parameters like average brightness, average size, average shape general orientation are determined from the power spectrum as follows:

verage brightness. The average brightness of clouds in an image is given by

$$\langle B \rangle = \frac{1}{a} \sum_{m,n} f(m,n), \tag{5}$$

re a is the total cloud coverage and the summation is carried out only over those ls where clouds are present. The presence of cloud at a pixel is decided by its htness if it exceeds a certain threshold. This threshold value is determined from the tering of points in the brightness distribution histogram of the image. In all the equent analyses, we have put $f(m,n) = 0$ whenever it is lower than the threshold.

Average cloud size. The width of the power spectrum is inversely related to the n cloud size. We define the width of a spectrum by averaging over all directions as

$$\langle W \rangle = \frac{\left\{ \sum_{k,l=0}^{N-1} P'(k,l) \left[\left(k - \frac{N}{2} \right)^2 + \left(l - \frac{N}{2} \right)^2 \right] \right\}^{1/2}}{\left\{ \sum_{k,l=0}^{N-1} P'(k,l) \right\}^{1/2}}, \tag{6}$$

where $P'(k,l)$ is given by (2). From this, one can compute the average cloud size as

$$\langle L\rangle = \frac{N}{\langle W\rangle}. \tag{7}$$

This procedure of determining the average cloud size is less time-consuming than the one described by Logan *et al* (1983) which involves a transformation into polar coordinates.

(iii) *Average orientation.* If the clouds in the original scene are elongated, the corresponding power spectrum will be anisotropic. In most cases this anisotropy can be approximated by a best-fitting elliptical shape whose major axis will be at right angles to the elongation of the clouds. Accordingly, we define the average cloud orientation as

$$\langle\alpha\rangle = \tan^{-1}(S/C) + 90^\circ, \tag{8}$$

where

$$S = 2\sum_{k,l=0}^{N-1}\left[\frac{P'(k,l)\left(k-\frac{N}{2}\right)\left(l-\frac{N}{2}\right)}{\left(k-\frac{N}{2}\right)^2+\left(l-\frac{N}{2}\right)^2}\right] \tag{9}$$

and

$$C = \sum_{k,l=0}^{N-1}\left[\frac{P'(k,l)\left[\left(k-\frac{N}{2}\right)^2-\left(l-\frac{N}{2}\right)^2\right]}{\left(k-\frac{N}{2}\right)^2+\left(l-\frac{N}{2}\right)^2}\right]. \tag{10}$$

If the clouds do not have any preferred orientation, then $P'(k,l)$ will be isotropic. In such cases, both S and C given by (9) and (10) will become zero and the definition of $\langle\alpha\rangle$ would be rendered meaningless.

(iv) *Average shape.* The shape parameter of elongated clouds is defined as the average of the ratios of their minor to major axes. Although clouds in general do not have very well defined elliptical shapes to define this parameter in a precise sense, the amount of anisotropy of the power spectrum is a measure of the average elongation of clouds. This is determined as

$$\langle\beta\rangle = \left\langle\frac{\text{minor axes}}{\text{major axes}}\right\rangle = \frac{A-(C^2+S^2)^{1/2}}{A+(C^2+S^2)^{1/2}}, \tag{11}$$

where

$$A = \frac{1}{2}\sum_{k,l=0}^{N-1} P'(k,l), \tag{12}$$

cloud scene around the Indian subcontinent taken on November 10 1984 by the geosynchronous satellite INSAT-1B in the visible channel 0·55–0·75 μm. All the three images are of size 512 × 512 pixels with resolutions of 1·1 km and 2·75 km for the NOAA and the INSAT respectively. Figures 5–7 are the Laplacian filtered images of figures 2–4, showing some cloud features enhanced. Such filtered images are useful in identifying certain types of cloud features while comparing the original images with their power spectra. The technique of Laplacian filtering for image enhancement is described in the appendix.

A visual inspection of these images themselves can very easily point out a number of regional differences in the general appearance of clouds. Cloud brightness, amount of elongation, direction of orientation, etc. all show marked changes from region to region in all these images. If one were to inspect the thermal infrared counterparts of these images, similar regional variations in brightness and other features characteristic of different cloud groups would show up. These infrared brightness variations are because of clouds lying at different altitudes giving off infrared radiation according to the local atmospheric temperature.

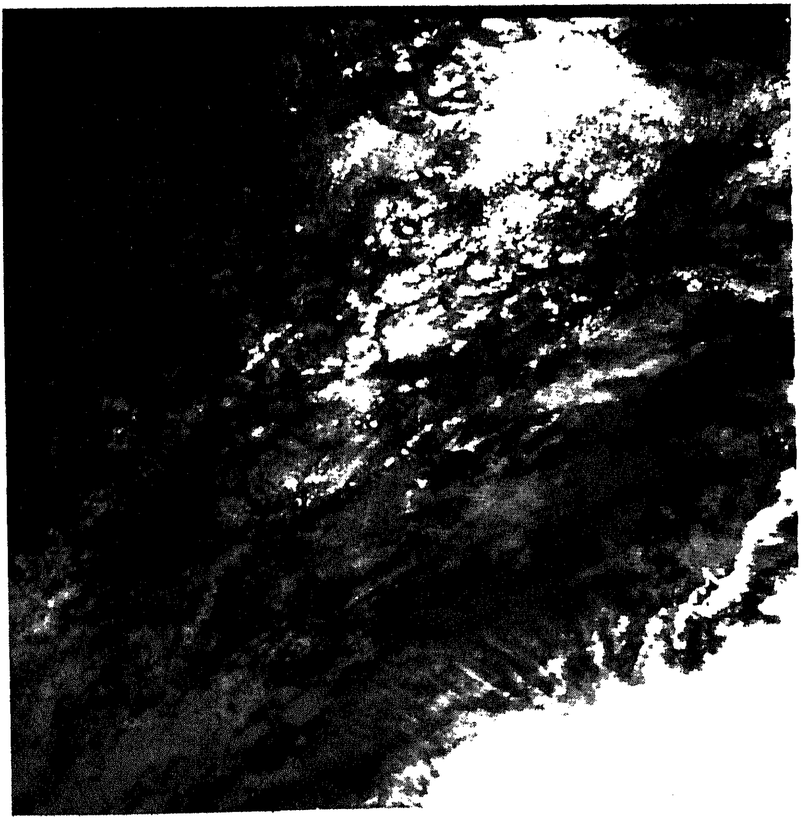

Figure 2. NOAA-6 visible channel (0·58 to 0·68 μm) cloud image of a region in the Arabian Sea taken on November 20 1980.

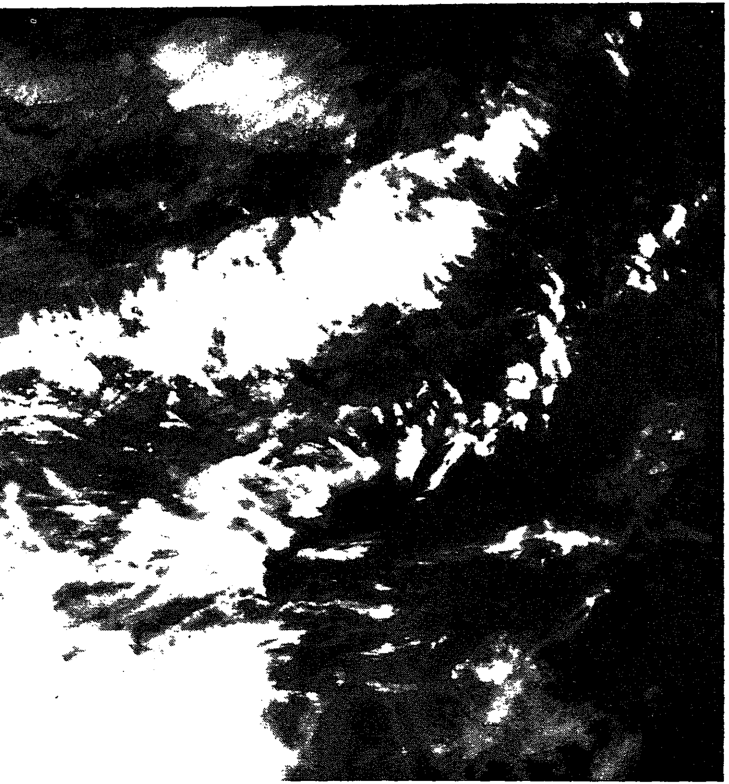

Figure 3. NOAA-6 visible channel (0·58 to 0·68 μm) image of a region adjacent to the one shown in figure 2 taken on November 20 1980.

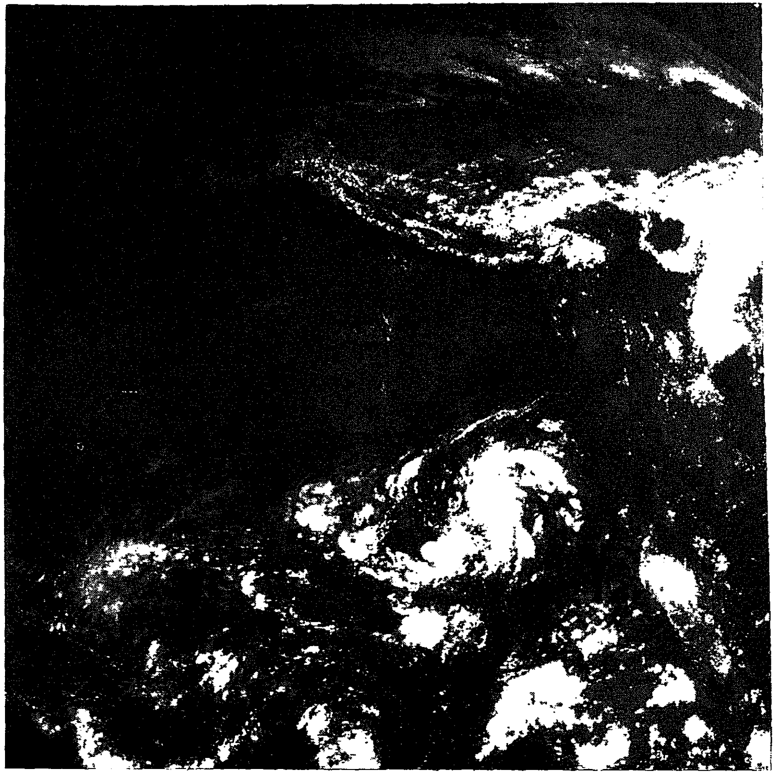

Figure 4. INSAT-IB visible channel (0·55 to 0·75 μm) image over the Indian subcontinent taken on November 10 1984.

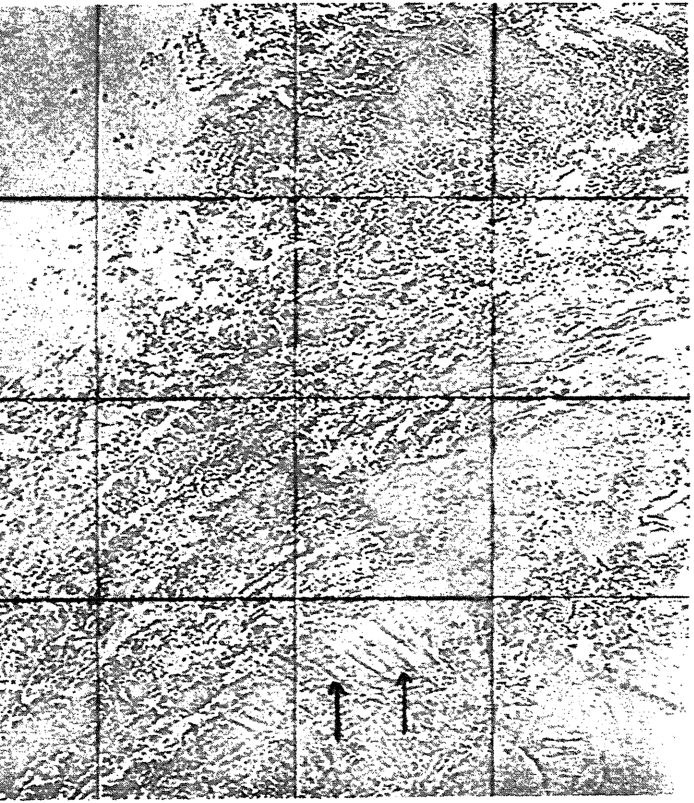

Figure 5. Laplacian-filtered image of the NOAA-6 visible channel image shown in figure 2. Note the wave-like structure (marked with arrows) in the bottom right part of the image.

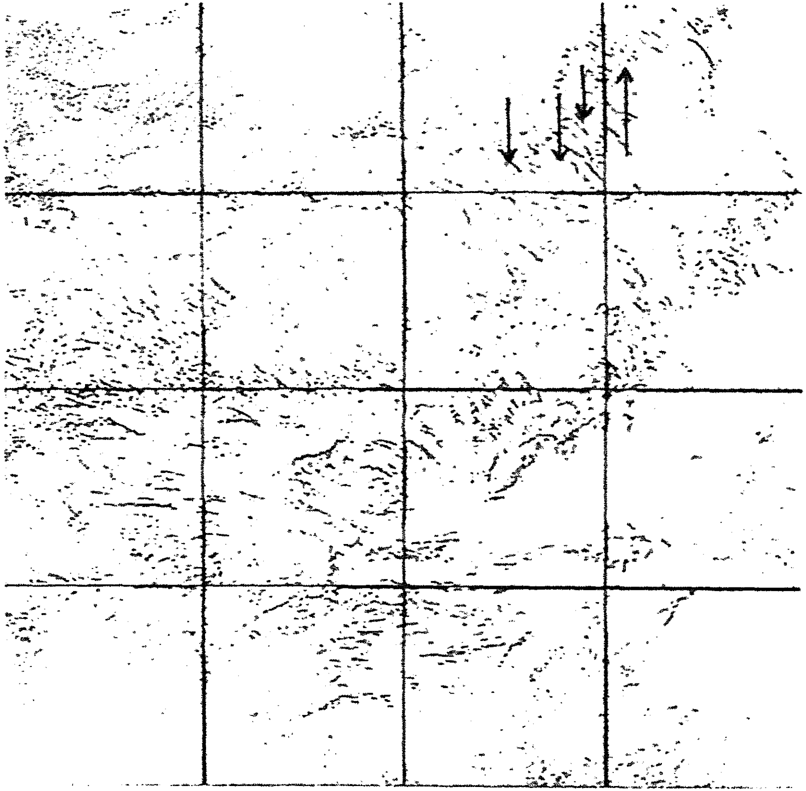

Figure 6. Laplacian-filtered image of the NOAA-6 visible channel image shown in figure 3. Note the wave-like structure (marked with arrows) in the upper right part of the image.

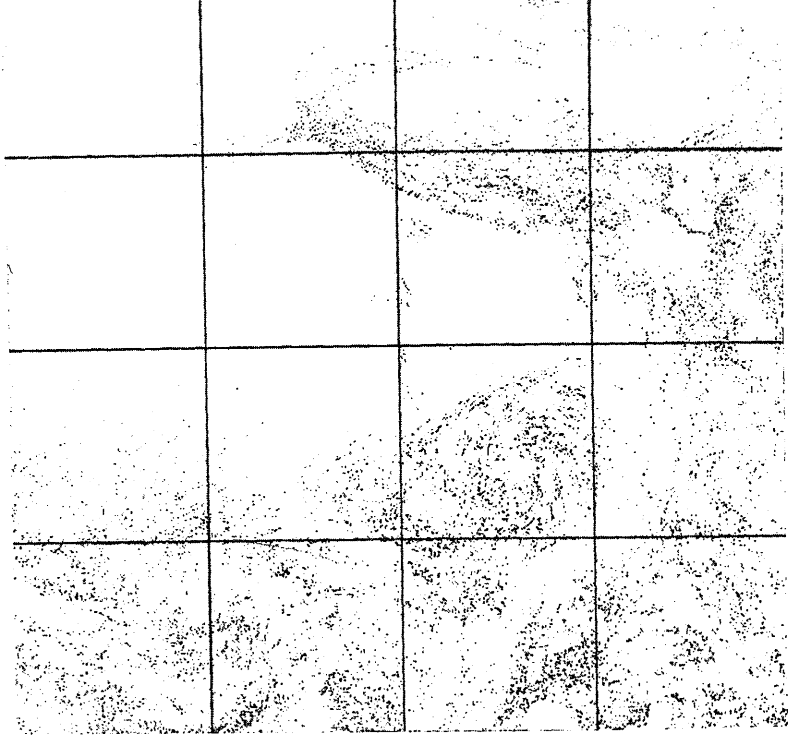

Figure 7. Laplacian-filtered image of the INSAT-1B visible channel image shown in figure 4.

In order to follow the regional variations of clouds in each image, we divide the images into sixteen subsections and carry out the 2DFFT analysis on each subsection individually. The size of the subsections is 128 × 128 pixels, which is small enough to detect the regional variations of the parameters fairly well, yet large enough to contain clouds of all scale sizes. The number and the size of the subsections have been selected to keep computation time minimum. The computed power spectra are then put together after the transformation (4) to form a single image with each spectrum occupying the position of its subsection in the original image.

Figures 8–10 are the power spectra composites of figures 2–4. As expected, the spectra have a lot of differences among them. The regions corresponding to large-size clouds have produced spectra concentrated towards the centre and those with smaller clouds have produced spectra that are spread out. Most of the spectra are anisotropic with their anisotropies at right angles to the orientation of the clouds. Some images have clouds that are spread over a few subsections with approximately the same orientation. This is reflected in their spectral anisotropies all pointing in a common direction.

Some spectra have bright thin spikes passing through their centres along x and y axes. These spikes are spuriously generated by the large differences between the brightnesses of clouds lying on the x-parallel boundaries or y-parallel boundaries of the corresponding subsection (Logan *et al* 1983). One has to take care that these spikes do

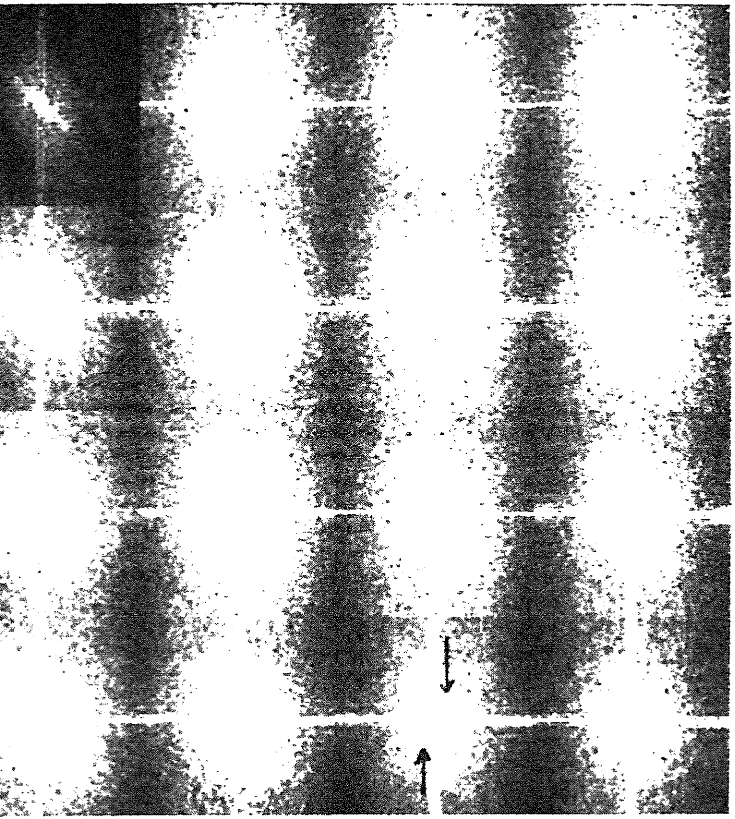

Figure 8. A 4 × 4 matrix of the 2DFFT power spectra of the image shown in figure 2. Each element of this matrix represents the corresponding subsection in figure 2. The bright dots in the spectrum corresponding to the wavy structure of figure 2 are shown by arrows.

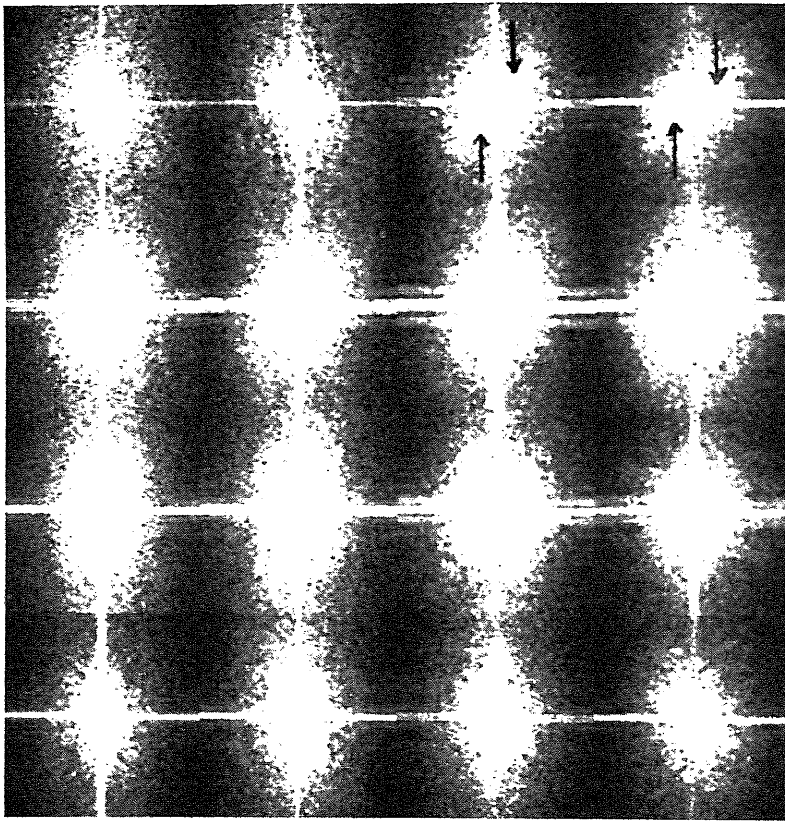

Figure 9. A 4 × 4 matrix of the 2DFFT power spectra of the image shown in figure 3. Each element of this matrix represents the corresponding subsection in figure 3. The bright patches in the spectrum corresponding to the wavy structure of figure 3 are shown by arrows.

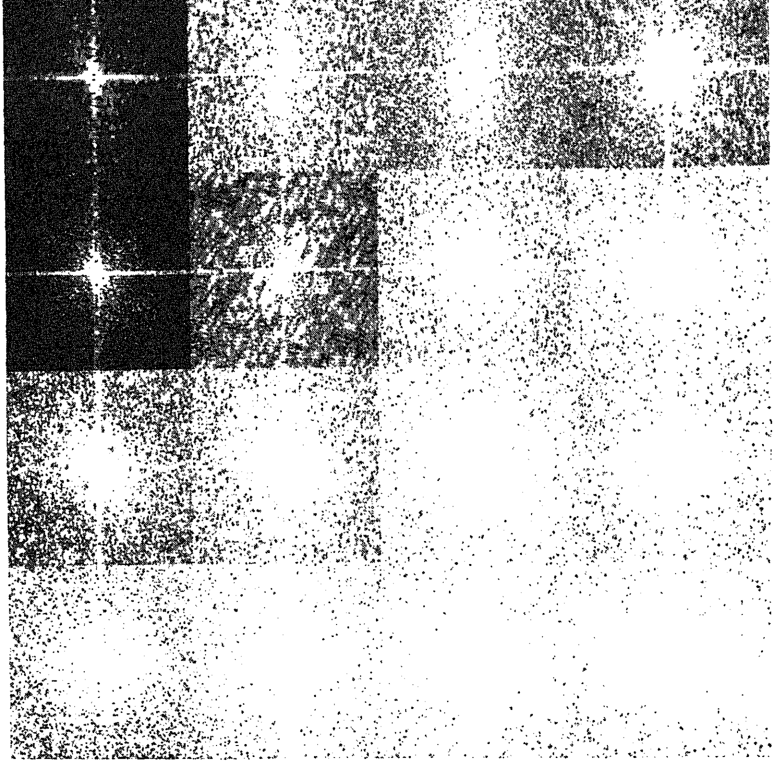

Figure 10. A 4 × 4 matrix of the 2DFFT power spectra of the image shown in figure 4. Each element of this matrix represents the corresponding subsection in figure 4.

not interfere with the estimation of the cloud parameters. We have chosen to exclude the portions of the spectra occupied by the spurious spikes.

The regularly spaced periodic wave-like streaks near the bottom right half of figure 2 (shown more enhanced in figure 5) have produced a series of bright dots in the spectrum of the corresponding region in figure 8. Similarly, the wave-like pattern in the upper half of figure 3 (shown enhanced in figure 6) has also produced a characteristic spectrum with well-defined, isolated bright patches in figure 9. From the positions of these patches, one can estimate the wavelength of the waves as

$$\lambda = \frac{N}{R}, \tag{13}$$

where $N = 128$ pixels is the length of the side of a subsection and R the distance of the first bright patch from the centre of the spectrum. In our case, the wavelength turns out to be around 9 to 14 pixels, equivalent to 10 to 15 km.

Table 1 gives the mean brightness, scale size, orientation and shape parameter of the clouds of each subsection of figure 2 calculated according to the formulae (5)–(12). Comparing with the original image, these derived parameters agree reasonably well with the visual appearances of the clouds. Similarly tables 2 and 3 give the computed cloud parameters for the images in figures 3 and 4.

Table 1. Average parameters of clouds in the NOAA-6 image shown in figure 2. ⟨B⟩, ⟨L⟩, ⟨α⟩ and ⟨β⟩ are the cloud mean brightness, average size, average angle of orientation and average shape respectively.

⟨B⟩	4·78	⟨B⟩	6·26	⟨B⟩	10·01	⟨B⟩ =	8·67
⟨L⟩	4·94	⟨L⟩	6·98	⟨L⟩	6·93	⟨L⟩ =	7·44
⟨α⟩	20·98	⟨α⟩	14·18	⟨α⟩	40·14	⟨α⟩ =	31·40°
⟨β⟩	0·88	⟨β⟩	0·68	⟨β⟩	0·53	⟨β⟩ =	0·56
⟨B⟩	8·26	⟨B⟩	7·29	⟨B⟩	8·86	⟨B⟩ =	7·70
⟨L⟩	6·70	⟨L⟩	7·49	⟨L⟩	7·31	⟨L⟩ =	8·15
⟨α⟩	49·61	⟨α⟩	3·99	⟨α⟩	20·84	⟨α⟩ =	27·62°
⟨β⟩	0·59	⟨β⟩	0·62	⟨β⟩	0·49	⟨β⟩ =	0·44
⟨B⟩	6·46	⟨B⟩	7·67	⟨B⟩	8·05	⟨B⟩ =	9·06
⟨L⟩	7·52	⟨L⟩	7·06	⟨L⟩	7·20	⟨L⟩ =	9·14
⟨α⟩	12·1	⟨α⟩	24·4	⟨α⟩	26·06	⟨α⟩ =	5·46°
⟨β⟩	0·88	⟨β⟩	0·81	⟨β⟩	0·44	⟨β⟩ =	0·54
⟨B⟩	8·09	⟨B⟩	7·63	⟨B⟩	10·93	⟨B⟩ =	14·54
⟨L⟩	7·30	⟨L⟩	7·69	⟨L⟩	8·15	⟨L⟩ =	11·99
⟨α⟩	12·32	⟨α⟩	12·22	⟨α⟩	21·39	⟨α⟩ =	0·56°
⟨β⟩	0·86	⟨β⟩	0·51	⟨β⟩	0·54	⟨β⟩ =	0·63

Table 2. Average parameters of clouds in the NOAA-6 image shown in figure 3.

⟨B⟩	8·21	⟨B⟩	9·12	⟨B⟩	8·19	⟨B⟩ =	6·05
⟨L⟩	7·88	⟨L⟩	8·01	⟨L⟩	11·96	⟨L⟩ =	11·86
⟨α⟩	60·59	⟨α⟩	19·87	⟨α⟩	14·89	⟨α⟩ =	154·30°
⟨β⟩	0·403	⟨β⟩	0·078	⟨β⟩	0·086	⟨β⟩ =	0·256
⟨B⟩	9·71	⟨B⟩	12·48	⟨B⟩	9·67	⟨B⟩ =	6·81
⟨L⟩	10·60	⟨L⟩	11·07	⟨L⟩	13·39	⟨L⟩ =	10·91
⟨α⟩	21·49	⟨α⟩	156·03	⟨α⟩	0·43	⟨α⟩ =	170·24°
⟨β⟩	0·40	⟨β⟩	0·191	⟨β⟩	0·027	⟨β⟩ =	0·141
⟨B⟩	10·48	⟨B⟩	10·79	⟨B⟩	7·63	⟨B⟩ =	6·94
⟨L⟩	8·84	⟨L⟩	11·17	⟨L⟩	10·64	⟨L⟩ =	11·76
⟨α⟩	21·01	⟨α⟩	18·41	⟨α⟩	5·39	⟨α⟩ =	5·564°
⟨β⟩	0·408	⟨β⟩	0·354	⟨β⟩	0·149	⟨β⟩ =	0·097
⟨B⟩	14·81	⟨B⟩	12·36	⟨B⟩	8·16	⟨B⟩ =	6·44
⟨L⟩	10·18	⟨L⟩	13·11	⟨L⟩	10·55	⟨L⟩ =	12·64
⟨α⟩	24·71	⟨α⟩	12·64	⟨α⟩	18·82	⟨α⟩ =	175·04°
⟨β⟩	0·102	⟨β⟩	0·097	⟨β⟩	0·103	⟨β⟩ =	0·002

. Conclusions

n this paper, we have described and demonstrated the use of 2DFFT in extracting

Table 3. Average parameters of clouds in the INSAT-1B image shown in figure 4.

$\langle B\rangle = 1{\cdot}49$	$\langle B\rangle = 13{\cdot}25$	$\langle B\rangle = 26{\cdot}73$	$\langle B\rangle = 30{\cdot}81$
$\langle L\rangle = 4{\cdot}89$	$\langle L\rangle = 3{\cdot}32$	$\langle L\rangle = 4{\cdot}20$	$\langle L\rangle = 6{\cdot}52$
$\langle \alpha\rangle = 10{\cdot}28^\circ$	$\langle \alpha\rangle = 99{\cdot}20^\circ$	$\langle \alpha\rangle = 110{\cdot}01^\circ$	$\langle \alpha\rangle = 129{\cdot}00^\circ$
$\langle \beta\rangle = 0{\cdot}17$	$\langle \beta\rangle = 0{\cdot}48$	$\langle \beta\rangle = 0{\cdot}23$	$\langle \beta\rangle = 0{\cdot}50$
$\langle B\rangle = 6{\cdot}24$	$\langle B\rangle = 12{\cdot}93$	$\langle B\rangle = 25{\cdot}19$	$\langle B\rangle = 50{\cdot}88$
$\langle L\rangle = 6{\cdot}48$	$\langle L\rangle = 3{\cdot}83$	$\langle L\rangle = 4{\cdot}34$	$\langle L\rangle = 5{\cdot}55$
$\langle \alpha\rangle = 18{\cdot}58^\circ$	$\langle \alpha\rangle = 156{\cdot}84^\circ$	$\langle \alpha\rangle = 27{\cdot}26^\circ$	$\langle \alpha\rangle = 158{\cdot}33^\circ$
$\langle \beta\rangle = 0{\cdot}05$	$\langle \beta\rangle = 0{\cdot}32$	$\langle \beta\rangle = 0{\cdot}40$	$\langle \beta\rangle = 0{\cdot}34$
$\langle B\rangle = 13{\cdot}20$	$\langle B\rangle = 18{\cdot}56$	$\langle B\rangle = 41{\cdot}47$	$\langle B\rangle = 20{\cdot}54$
$\langle L\rangle = 4{\cdot}97$	$\langle L\rangle = 4{\cdot}92$	$\langle L\rangle = 6{\cdot}28$	$\langle L\rangle = 4{\cdot}44$
$\langle \alpha\rangle = 30{\cdot}97^\circ$	$\langle \alpha\rangle = 22{\cdot}53^\circ$	$\langle \alpha\rangle = 0{\cdot}051^\circ$	$\langle \alpha\rangle = 112{\cdot}72^\circ$
$\langle \beta\rangle = 0{\cdot}14$	$\langle \beta\rangle = 0{\cdot}54$	$\langle \beta\rangle = 0{\cdot}15$	$\langle \beta\rangle = 0{\cdot}73$
$\langle B\rangle = 16{\cdot}77$	$\langle B\rangle = 22{\cdot}15$	$\langle B\rangle = 35{\cdot}21$	$\langle B\rangle = 42{\cdot}84$
$\langle L\rangle = 4{\cdot}28$	$\langle L\rangle = 4{\cdot}79$	$\langle L\rangle = 6{\cdot}63$	$\langle L\rangle = 6{\cdot}42$
$\langle \alpha\rangle = 56{\cdot}69^\circ$	$\langle \alpha\rangle = 35{\cdot}80^\circ$	$\langle \alpha\rangle = 2{\cdot}78^\circ$	$\langle \alpha\rangle = 47{\cdot}84^\circ$
$\langle \beta\rangle = 0{\cdot}74$	$\langle \beta\rangle = 0{\cdot}64$	$\langle \beta\rangle = 0{\cdot}02$	$\langle \beta\rangle = 0{\cdot}56$

earth by regulating the transport of heat and radiation which constitute the main sources of energy for all weather processes.

Acknowledgements

The authors thank Dr T A Hariharan for insisting on this study. One of the authors (V K Agarwal) is grateful to Dr Coakley of NCAR, USA, and Dr Huning of JPL, NASA, USA, for very useful discussions and providing us valuable information. Discussions with colleagues, especially Dr S M Bhandari, is gratefully acknowledged.

Appendix

The techniques usually employed for image enhancement primarily depend on the ability to detect spatial changes in the gray levels of an image. For instance, in enhancing the bondaries of clouds in a cloud image, the technique has to efficiently detect gray level changes across the edges of clouds. The Laplacian operator, which is a two-dimensional second order differential operator (Rosenfeld and Kak 1976), is well suited for meeting this objective. It is also called the Laplacian filter and is defined by

$$\nabla^2 f = \frac{\partial^2 f}{\partial x^2} + \frac{\partial^2 f}{\partial y^2}, \tag{A.1}$$

For our use, we discretize the Laplacian filter as

$$\nabla^2 f(k,l) = f(k-a,l) + f(k+a,l) + f(k,l-a) + f(k,l+a) - 4f(k,l), \tag{A.2}$$

where a is the distance to the side of the filter area from its centre. The value of (A.2) can sometimes become negative depending upon the nature of $f(k,l)$ at a particular locality. This negative value cannot be represented in the enhanced image in terms of a gray level, since gray levels can take only positive values. So we add to (A.2) a constant z, large enough to make the former's value positive at all the sites in an image. In the cases discussed in this paper, we have chosen $z = 128$ and $a = 1$.

The Laplacian filter, being a second order derivative operator, will amplify gray level gradients with small-scale sizes much more than those with larger-scale sizes. This can be seen in figures 5–7, where structures like small clouds, small holes and gaps in large clouds, wavy patterns represented by series of regularly spaced bright lines, etc. have all got enhanced much above some of the diffuse cloud boundaries where the gradients are slow.

References

Bergland G D 1969 A guided tour of the fast Fourier transform; *IEEE Spectrum* **6** 41–52

Bracewell R N 1978 *The Fourier transform and its applications* (McGraw-Hill Kogakusha) pp. 370–384

Bunting J T and Fournier R F 1980 Tests of spectral cloud classification using DMSP fine mode satellite data: Air Force Geophysical Laboratory, Hanscom AFB, Mass. AFGL-Tr-80-0181, Env. Res. Paper No. 704

Cho H R 1976 *Int. Conf. Cloud Phys.*, (Massachusetts: Am. Meteorol. Soc.) 45 pp. 428–433

Cooley J W, Lewis P A W and Welch P D 1969 The fast Fourier transform and its applications; *IEEE Trans. Education* **12** Special Issue

Cox S K 1981 *Clouds—their formation, optical properties and effects* (eds) P V Hobbs and A Deepak (New York: Academic Press), pp. 241–280

Harshvardhan, Weinman J A and Roger Davies 1981 Transport of infrared radiation in cuboidal clouds; *J. Atmos. Sci.* **38** 2500–2513

Harshvardhan and Weinman J A 1982 Infrared radiative transfer through a regular array of cuboidal clouds; *J. Atmos. Sci.* **39** 431–439

Henderson-Sellers A 1984 *Satellite sensing of a cloudy atmosphere: Observing the third planet* (London: Taylor and Francis)

Hobbs P V and Deepak A 1981 *Clouds—their formation, optical properties and effects* (eds) P V Hobbs and A Deepak (New York: Academic Press)

Logan T L, Huning J R and Glackin D L 1983 Cloud cover typing from environment satellite imagery—discriminating cloud structure with fast Fourier transforms. Report No. 84/17 Jet Propulsion Laboratory, Pasadena, USA

Naber P S and Weinman J A 1984 The angular distribution of infrared radiances emerging from broken fields of cumulus clouds; *J. Geophys. Res.* **89** 1249–1257

Rosenfeld A and Kak A C 1976 *Digital picture processing* (New York: Academic Press) pp. 184, 275, 278 and 281

Schiffer R A 1982 The international satellite cloud climatology project (ISCCP), Preliminary Implementation Plan; World Climate Programme, World Meteorological Organisation, WCP-35

Toldalagi P M and Lebow W M 1982 Survey and analysis of satellite cloud classification research techniques; Naval Environmental Prediction Research Facility, Monterey, CA, USA, NEPRF Contract 81-C-H155, p. 43

Welch R M and Weilicki B A 1984 Stratocumulus cloud field reflected fluxes: The effect of cloud shape; *J. Atmos. Sci.* **41** 3085–3103

Spectral width parameter for wind-generated ocean waves

C V K PRASADA RAO
Naval Physical and Oceanographic Laboratory, Cochin 682004, India

MS received 5 December 1986; revised 8 June 1988

Abstract. An evaluation of the spectral width parameter for wind-generated ocean waves is presented based on the analysis of wave data obtained through the ship-borne wave recorder fitted to RV *Gaveshani*. The coverage of wave data includes deep as well as shallow waters on the east and west coasts of India. Considering that the spectral width parameter ε_0 derived from Tucker's wave analysis provides a reasonably accurate estimate, a comparative study has been made for the other band-width definitions available in the literature. The results indicate some bias in the estimation of spectral width information using higher-order moments, e.g. ε_s and ν, and with the alteration of spectral forms that are usually associated with multiple- or single-peaked wave spectra. Such a bias is not seen in the case of Goda's peakedness parameter Q_p with variation of spectral form. The effect of the ratio of the high-frequency cut-off to the spectral peak period on ε_s, ν and Q_p is also investigated.

Keywords. Spectral width parameter; ship-borne wave recorder.

1. Introduction

Longuet-Higgins (1952, 1975) derived theoretical distributions of wave heights as well as the joint distribution of wave heights and periods based on the assumption that the wave frequencies lie in a narrow band with random phase values. In general it is accepted that the sea surface elevations follow a 'Gaussian' distribution and the wave heights follow a 'Rayleigh' distribution. These theoretical concepts have been tested earlier using a few wave observations made off the Indian coast (Dattatri 1973; Dattatri *et al* 1976, 1979; John 1977; Narasimhan and Deo 1981; Fernandes *et al* 1981; Baba and Harish 1985). Since the narrow-band criterion is adopted for theoretical considerations, it is essential to quantify the spectra band-width for ocean waves for testing and validation of the theory against observations. Thus the spectral width parameter assumes importance for ocean wave studies as it provides a clue to the composition of sea state, viz. 'sea' and 'swell' conditions. The shape of the wave engery spectrum is also determined by using spectral width information and often the estimates of wave spectral shapes are considered important for ocean engineering applications. Attempts are therefore made in this investigation to study the spectral width parameter in detail by analysing some wave data collected off the east and west coasts of India.

2. Analytical consideration

From the zero-upcrossing method of wave analysis (Tucker 1963; Draper 1967) one can respectively. The parameter ε_0 varies from 0 to 1 depending on the prevailing sea state, and $\varepsilon_0 \rightarrow 1$ (approaching unity) implies broad-band wave conditions with smaller waves (short-period) riding on top of the larger waves (long-period). On the other hand $\varepsilon_0 \rightarrow 0$ represents narrow-band characteristics which can be attributed to the presence of more regular waves, i.e. 'swell'. The spectral width values obtained through (1) can be considered as fairly accurate as careful estimations were made of T_z and T_c from the wave records.

However, it is often viewed by many users of wave information that the wave parameters derived by the Tucker/Draper method are just not adequate for complete description of the sea state and the use of spectral techniques is recommended for several coastal and offshore engineering works. In the wave spectrum approach the required significant wave parameters are derived from spectral moments and spectral density estimates. Any nth moment can be computed using the relationship

$$m_n = \int_{\mathrm{LF}}^{\mathrm{HF}} f^n s(f)\, \mathrm{d}f, \tag{2}$$

where LF and HF are lower and higher cut-off frequencies, and f and $s(f)$ are the frequency and the corresponding spectral density estimates. The zeroth (m_0), 1st (m_1), 2nd (m_2), and 4th (m_4) are the most commonly used moments for computation of wave parameters. The moment m_0 is referred to as the variance of sea surface and is proportional to the total energy of a wave spectrum.

Cartwright and Longuet-Higgins (1956) and Longuet-Higgins (1975) have suggested the following relationships for obtaining the values of spectral width parameter from the moments:

$$\varepsilon_s = [(m_0 m_4 - m_2^2)/m_0 m_4]^{1/2}, \tag{3}$$

$$\nu = [(m_2 m_0 - m_1^2)/m_1^2]^{1/2}. \tag{4}$$

Both ε_s and ν have the same range of numerical values as ε_0. The parameter ε_s is also known as the spectral width parameter but ν is sometimes referred to as 'spectral narrowness parameter' in the literature (Rye 1976). Goda (1970) proposed another parameter called the 'peakedness parameter', defined as

$$Q_p = (2/m_0^2) \int_{\mathrm{LF}}^{\mathrm{HF}} f[s(f)]^2\, \mathrm{d}f. \tag{5}$$

Unlike the other three parameters, i.e. ε_0, ε_s and ν, the numerical values of Q_p are normally more than 1·0 and a larger magnitude implies a more sharply peaked wave spectrum (or narrow-band condition) and vice versa.

3. Materials and methods

The data used for this study were collected on board RV *Gaveshani* during two of her cruises—the 79th and the 82nd—using a ship-borne wave recording system (IOS

Model 5254, Institute of Oceanographic Sciences, UK) installed on the vessel. The 79th cruise was conducted in the Bay of Bengal during the period 24th September to 4th October 1980. The wave measurements were made in this cruise at two locations south of Visakhapatnam, on the east coast of India, where the station depths are 250 and 500 m. Vethamony *et al* (1982, 1984) had processed the wave data collected in this cruise following spectral and statistical methods (zero-upcrossing analysis). Data on spectral width information as well as various other wave statistics, e.g. wave heights, periods, etc., were presented (tables 1 and 2 of Vethamony *et al* 1982). For this investigation the author selected 59 wave records from the above for extracting necessary data on spectral width parameters. Apart from these data another 20 wave records collected during the 82nd cruise between 12th and 15th November 1980 were also utilized for this study. The locations of wave measurements in this case lie in the shallow as well as deep waters off Goa, on the west coast of India. These data were analysed by the author (Prasada Rao 1984, 1985). The relevant data on spectral width parameters from the author's earlier works are also incorporated in this study. Thus, in total, 79 wave records have been considered for this investigation.

Regarding the methods of wave data analysis adopted, the following points may be noted. Each wave record is of approximately 15 min duration. For spectral analysis, the data were digitized with a sampling interval Δt of 1 s. An auto-correlation method was employed and a 'Hanning' window was used for smoothing raw spectral estimates (Bendat and Piersol 1971). As $\Delta t = 1$ s the Nyquist frequency ($1/2\Delta t$) is 0·5 Hz. But due to the limitations of the ship-borne wave recorder used in the study, the lower limiting period was fixed as 3 s or 0·33 Hz. It may be noted that the wave sensors were fitted to the ship's hull at 2 m below the water surface and very short period waves, i.e. waves of period < 3 s, are therefore usually disregarded. Similarly the upper limiting wave period was chosen as 25 s from the point of instrument sensitivity. Spectral moments were computed (2) and these inputs were used for deriving values of ε_s, ν and Q_p. The band-width parameter ε_0 was arrived at following the zero-upcrossing method of wave analysis (Tucker 1963; Draper 1967).

4. Results and discussion

From section 2 one can see that, except ε_0 the spectral width parameters are based on moments. Spectral moments in general and higher-order moments in particular are somewhat unstable owing to their dependence on several factors, viz. energy density values on the high-frequency side of the spectrum, cut-off frequency choice, etc. These are again related to the accuracy of the instrument and the data sampling interval used for any study. On the other hand, as the ε_0 is defined based on the number of zero-upcrossings N_z and the number of crests N_c for a given wave record, this parameter is relatively better. Goda (1974) discussed these aspects in detail. Similar arguments which give more weightage to ε_0 compared to other spectral width definitions might be seen from Haring *et al* (1976). Therefore an attempt is made to evaluate the spectral width parameter values of ε_s, ν and Q_p by comparing the same with those of ε_0.

Spectral analysis of wave data revealed the following aspects. By and large the spectra consisted of either a single peak or multiple peaks. The primary spectral peaks are noticed on the low-frequency side of the spectrum approximately around 'swells'. The subsequent peaks other than 'swell' peaks might have been caused by the locally generated 'seas'. Thus the actual shape of the spectrum depends on the sea state. Since different types of spectral forms are encountered the observed spectra are classified as follows. Spectra possessing conspicuously a single peak represent the narrow-band condition and those with two or multiple peaks represent the broad-band condition. Some typical wave spectra identified for narrow-band and broad-band conditions are shown in figure 1(a, b). The classification was based on visual examination of spectral shapes.

Comparison of ε_0 and ε_s is given in figure 2a. From this it can be seen that ε_s values are higher for narrow-band spectra and lower for broad-band spectra compared to ε_0. Earlier investigators found that ε_s was either higher or lower than ε_0. Hoffman and Karst (1975) found that ε_s estimates were higher than ε_0 by 15–20%. Results obtained by Dattatri *et al* (1979) show that ε_s values were consistently lower compared to ε_0. On the contrary Chakrabarty and Snider (1974), Haring *et al* (1976) and

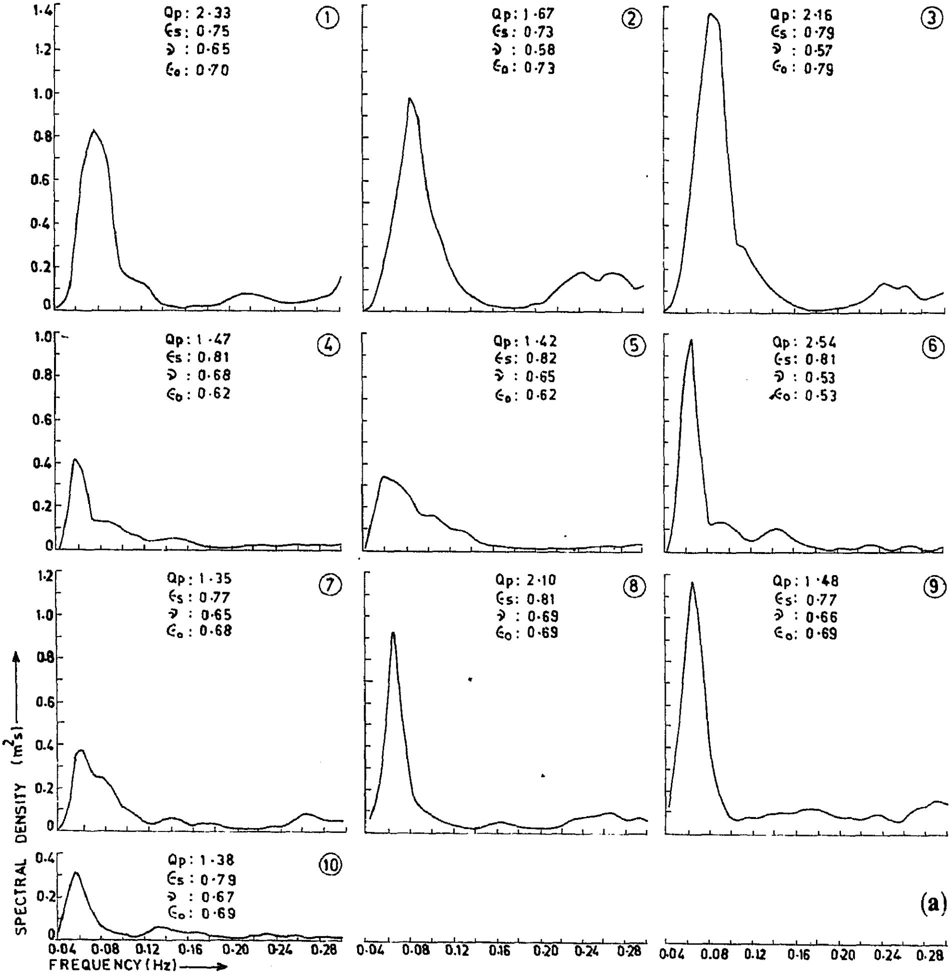

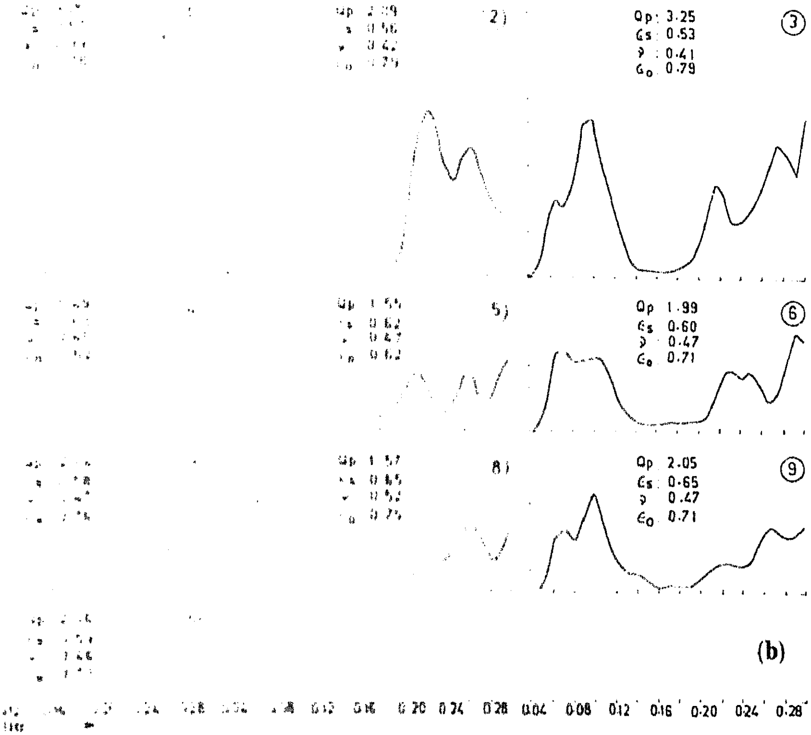

igure 1. Some typical wave spectra consisting of (a) single peak and (b) multiple peaks.

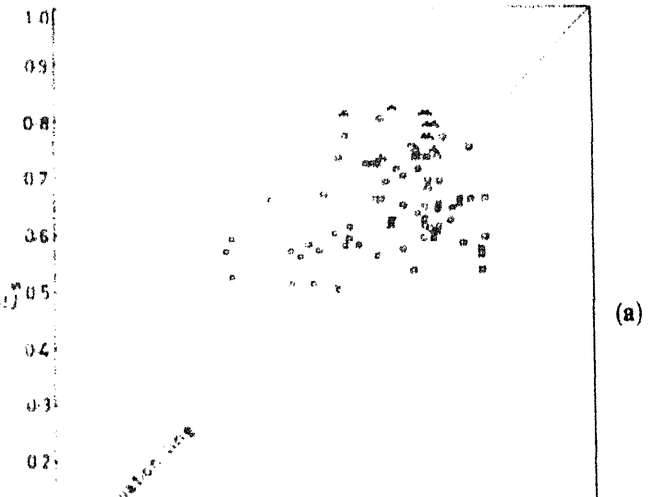

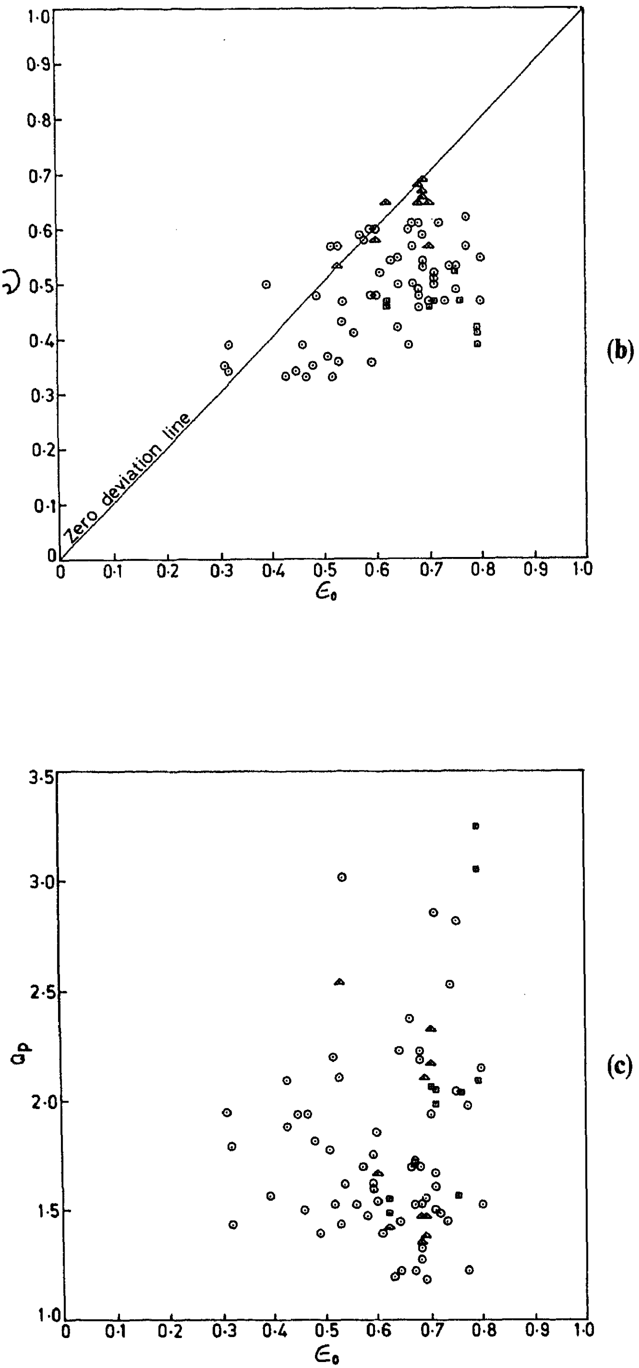

Figure 2. Comparison of the estimates of spectral width parameter obtained from the zero-upcrossing method with those derived from spectral analysis. Data points 'Δ' represent single-peaked spectra (as in figure 1a), '□' represent multiple-peaked spectra (as in figure 1b) and '○' represent the rest of the observations. (a) ε_0 vs ε_s (b) ε_0 vs ν and (c) ε_0 vs Q_p.

andes *et al* (1981) pointed out that no consistent relation was observed between
ad ε_s. Vethamony *et al* (1984) reported that ε_s was greater for 45% of spectra (out
l observations) and the same was found to be lower for spectra with multiple
s. Thus there exist divergent opinions as regards ε_s estimates but the main debate
hether it is an overestimate or an underestimate. Nevertheless it is evident from
discussion presented above that ε_s is less reliable and shows various anomalies.
present study substantiates this point and further following inferences may be
vn. Apparently ε_s does not necessarily give overestimate. Overestimation through
ght be expected for the narrow-band condition or for spectra with a single peak
h might occur because of the presence of a 'swell'. Multiple peaks in wave spectra
also occur when the growth of waves takes place along with existing swells and
such a case may cause underestimation of spectral width.

gure 2b presents a comparison between the spectral narrowness parameter ν and
Though the trend in the figure confirms that ν is in general less compared to ε_0, it is
h mentioning that the estimates of this parameter are relatively better for narrow-
d wave spectra. Hence ν offers a better estimate than ε_s in the case of narrow-band
ditions. However, the spectral narrowness parameter ν seems to fail to give correct
nates for broad-band spectra and its value is found to be reduced by almost a half of
value of ε_0 for some such cases. Dattatri (1979) also reported that ν was
roximately $0.8\,\varepsilon_0$. But it must be noted that such an approximation might be invalid
er narrow band conditions.

mong the spectrally derived band-width parameters, Goda's peakedness
ameter Q_p is more widely accepted. The reasons for this are: (i) Q_p is more reliable as
le quantities like m_0 and $S(f)$ are used for its computation, and (ii) it is independent
ut-off frequency choice. The peakedness parameter is a measure of the sharpness of
wave spectrum and hence higher values of Q_p imply more sharply peaked spectra,
vice versa. Further one can expect the higher values of Q_p are associated with
ow-band wave spectra and the lower values of Q_p with broad-band wave spectra.
aspect has been studied by comparing Q_p and ε_0 (figure 2c). The data reveal this
of trend ($\varepsilon_0 \propto 1/Q_p$) only for $Q_p < 2$; above this threshold such a relation is not seen
veen these two parameters. However, this needs further investigation. On the
tive side, the variation in Q_p does not seem to depend on the narrow-band or wide-
d criterion. It may be considered as a plus point as far as Q_p is concerned. Moreover,
dependence of Q_p on spectral form is also evident from figure 1(a, b).

he selection of cut-off frequency for spectral computations is also considered
ortant as it influences estimates of the spectral width parameter. The non-
ensional frequency values are obtained by taking the ratio of high-frequency cut-off
) to the spectral peak frequency (f_p). These are compared with ε_s, ν and Q_p in
re 3. Both ε_s and ν show clear indication of an increasing trend as the CF/f_p ratio
eases. Thus, for a given wave spectrum, by changing the value of CF one may obtain
rent results for ε_s as well as ν. Hence Q_p is better as it shows less dependence on
f_p. These findings are in agreement with those of Rye and Svee (1976) and Haring
(1976). Rye and Svee (1976) have opined that Q_p is a more convenient parameter for

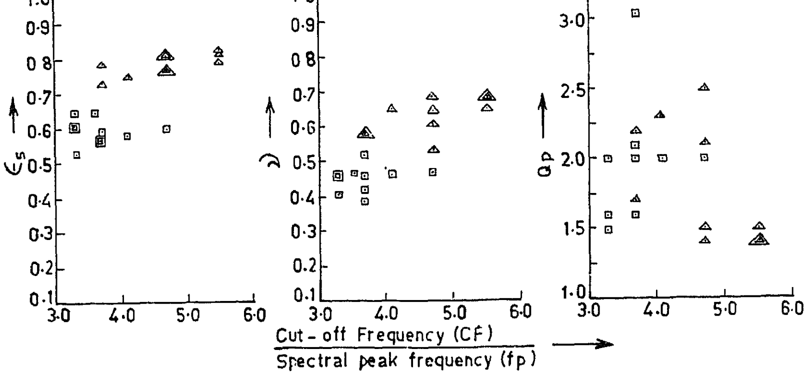

Figure 3. Influence of high-frequency cut-off (CF) on the spectral width estimates ν, ε_s and Q_p. CF is normalized to the spectral peak frequency, f_p. Data points 'Δ' and '$\square$' are as in figure 2.

5. Summary and conclusions

Spectral estimates of band-width parameters for ocean waves largely appear to be influenced by the nature of the wave spectrum. The occurrence of multiple peaks in spectra can alter the estimates and the effect of the same is very significant for ε_s and ν. If a choice is to be made between these two, ν is recommended for narrow-band/single-peaked spectra and ε_s for broad-band/multiple-peaked spectra. Goda's peakedness parameter Q_p can be considered to be relatively better as it appears to be independent of the spectral form. Also the estimates of Q_p are uncorrelated with the ratio of the high-frequency cut-off to the spectral peak frequency, whereas ε_s and ν show an increasing trend with increase in CF/f_p.

Acknowledgements

The author wishes to acknowledge the valuable comments and suggestions offered by the referees, which contributed significantly to this work.

References

Baba M and Harish C M 1985 Wave height and period distribution off the southwest coast of India; *Indian J. Mar. Sci.* **14** 1–8

Bendat J S and Piersol A G 1971 *Random data—analysis and measurement procedures* (New York: John Wiley & Sons)

Cartwright D E and Longuet-Higgins M S 1956 The statistical distribution of the maxima of a random function; *Proc. R. Soc. London* **A237** 212–232

Chakrabarti S K and Snider R N 1974 Wave statistics for March 1968 North Atlantic storm; *J. Geophys. Res.* **79** 3449–3458

Dattatri J 1973 Waves off Mangalore harbour, west coast of India; *J. Waterways Harbors Div. Am. Soc. Civil Eng.* **99** 39–58

Dattatri J, Jothi Shankar N and Raman H 1976 Comments on Hoffman and Karst: the theory of the Rayleigh distribution and some of its applications; *J. Ship Res.* **20** 235–238

Dattatri J, Raman H and Jothi Shankar N 1979 Height and period distributions for waves off Mangalore harbour, west coat of India; *J. Geophys. Res.* **84** 3767–3772

Draper L 1967 The analysis and presentation of wave data—a plea for uniformity; in *Proc. 10th Conf. on Coastal Engineering ASCE* **1** 1–11

Fernandes A A, Gouveia A D, Sathe P V and Nagarajan R 1981 Wave observations in the Mahanadi Basin (Bay of Bengal) during September 1980; *Mahasagar, Bull. Natl. Inst. Oceanogr.* **14** 239–249

Goda T 1970 Numerical experiments on wave statistics with spectral simulation; *Rep. Port Harbour Res. Inst. Jpn.* **9** 3–57

Goda T 1974 Estimation of wave statistics from spectral simulation; in *Proc. Intl. Symp. on Ocean Wave Measurement and Analysis*, New Orleans

Haring R E, Osborne A R and Spencer L P 1976 Extreme wave parameters based on continental shelf storm wave records; in *Proc. 15th Conf. on Coastal Engineering ASCE* **I** 151–170

Hoffman D and Karst O J 1975 The theory of Rayleigh distribution and some of its applications; *J. Ship Res.* **19** 172–191

John V C 1977 Distributions and relationships of height and period of ocean waves off Mangalore; *Indian J. Mar. Sci.* **6** 49–54

Longuet-Higgins M S 1952 On the statistical distribution of the heights of sea waves; *J. Mar. Res.* **11** 245–266

Longuet-Higgins M S 1975 On the joint distribution of the periods and amplitudes of sea waves; *J. Geophys. Res.* **80** 1688–1694

Narasimhan S and Deo M C 1981 Behaviour of ocean waves at Bombay High and their statistical predictions; First Indian National Conf. on Ocean Engineering, Madras 1981 **I** 67–74

Prasada Rao C V K 1984 Spectral characteristics of wind-generated ocean gravity waves—a case study; NPOL Dept. Rep. No. RR–1/84 1–16

Prasada Rao C V K 1985 Comparative study of wave parameters derived from spectral and zero-crossing methods; *Indian J. Mar. Sci.* **14** 202–205

Rye H 1976 Discussion of a statistical relationship between individual heights and periods of storm waves; in *Proc. 1st Intl. Conf. on Behaviour of Off-shore Structures* **2** 361–362

Rye H and Svee R 1976 Parametric representation of a wind-wave field; in *Proc. 15th Conf. on Coastal Engineering ASCE* **I** 183–201

Tucker M J 1963 Analysis of records of sea waves; *Proc. Inst. Civ. Eng.* **26** 305–316

Vethamony P, Gopalakrishna V V and Varkey M J 1982 Computation of wave statistics and spectra from records collected with a ship-borne wave recorder off the Godavari Basin (Bay of Bengal) during Sept/Oct 1980; NIO Tech. Rep. No. POD/1/82 1–9

Vethamony P, Gopalakrishna V V and Varkey M J 1984 Wave spectra and statistics off Godavari during Sept/Oct 1980; *Mausam* **35** 199–204

ndian Acad. Sci. (Earth Planet. Sci.), Vol. 97, No. 2, December 1988, pp. 183–191.
ated in India

er characteristics and transport of the Antarctic circumpolar ent in the Indian Ocean

P M MURALEEDHARAN and BASIL MATHEW*

National Institute of Oceanography, Dona Paula 403004, India
*Naval Physical and Oceanographic Laboratory, Cochin 682004, India

MS received 14 April 1988; revised 22 August 1988

Abstract. Geostrophic velocities are computed across meridians 37°E and 105°E using hydrographic data. The estimated mass transport is represented on a temperature–salinity diagram. The characteristics of the water within the Antarctic circumpolar current at 37°E and 105°E are discussed. The computed transport agrees with the previous estimates. Transports due to the current between 45°S and the Antarctic continent at these two meridians are comparable. The westerly flow south of 42°S at 105°E is associated with a cyclonic eddy which appears to be a permanent feature, whereas the one at 50°S is related to the topography of the region.

Keywords. Antarctic circumpolar current; mass transport; bivariate distribution; Indian Ocean

roduction

ntarctic circumpolar current (ACC) is the only ocean current circling the entire . Although the average speed of this eastward current is much lower oximately 15 cm s^{-1}) than that of the equatorial currents, it transports a large nt of water because of its considerable horizontal and vertical extents. From rophic computations and direct current measurements it is well established that CC extends down to the bottom of the ocean (Callahan 1971). Attempts have been in the past to estimate the net transport of the ACC by assuming geostrophic ce (Sverdrup *et al* 1942, Jacobs and Georgi 1977; Nowlin *et al* 1977) and by direct rements. The direct measurements were mostly made in the Drake Passage (Reid owlin 1971; Nowlin *et al* 1977; Whitworth *et al* 1982; Whitworth 1983) and along ion south of Australia (Callahan 1971). However, very little effort was made to the modal properties of the waters carried by the ACC. In the present study, we ried to find out the geostrophic transport across two sections in the Indian Ocean epresent it in bivariate classes of potential temperature and salinity.

aterial and method

ydrographic sections consisting of 26 stations were used for the present study.

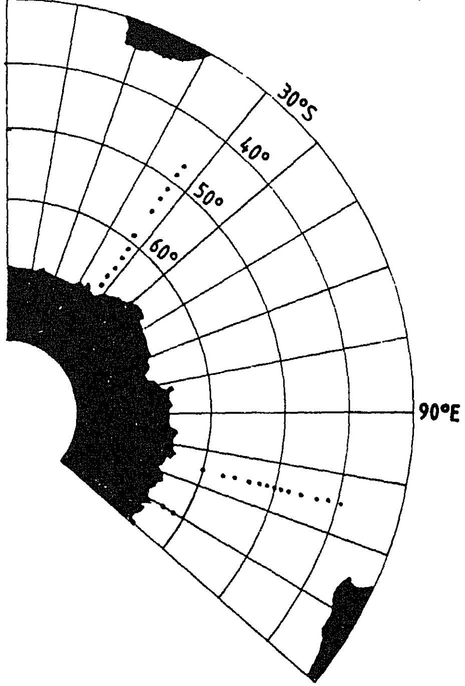

Figure 1. Track chart and station positions.

37°E represents only a part of the ACC. As the section at 105°E extends only up to 60°S, two additional stations to the south of 60°S were taken along 120°E. The latter were covered in the same cruise. It was assumed that this would not cause any appreciable error as the ACC is fairly steady south of the polar front (PF).

The geostrophic velocities were computed between station pairs relative to the deepest common observed depths following Callahan (1971) (figures 2 and 3). Vertical sections of potential temperature, salinity and geostrophic velocity were used for computing the transport and representing it in bivariate classes of potential temperature and salinity. In order to get the minute details, classes of potential temperature and salinity were chosen with smaller intervals, of 0·5°C and 0·1‰ respectively. The transports were computed through each solenoid formed by potential temperature and station pairs and integrated to get the total transport. This is achieved by superimposing potential temperature and salinity diagrams. The transport (flux) in each solenoid is differentiated again with respect to salinity in order to represent it on a temperature–salinity (T–S) diagram.

Figures 4 and 5 represent the net transport in bivariate classes of potential temperature (0·5°C intervals) and salinity (0·1‰ intervals). This method has the added advantage of giving the properties of the waters carried by the current and their contribution to the net flux.

To facilitate easy comparison, the geographical boundaries are chosen in such a way that the domains west of 50°E and east of 90°E represent, respectively, the western and eastern regions of the Indian Ocean sector of the Southern Ocean.

esults and discussion

he current structure

ical sections of geostrophic currents across the two sections (37°E and 105°E) are
n in figures 2 and 3. The velocity structure across 37°E (figure 2) shows a weak
l eastward component between 55°S and 60°S in the upper 1500 m. Beyond 60°S it
on decreasing, and the flow becomes westward south of 67°S. The eastward flow is
rated into two distinct zones: a narrow high-velocity core (> 15 cm/s) just south of
ndia–Antarctica Ridge and the less intense belt further south (near 57°S) already
tioned. At the surface, the polar front is located north of 50°S. Lutjeharms (1985)
rved that the polar front was around 50°S in the western Indian Ocean. Here the
imum velocity exceeds 15 cm/s. The westward flow is confined to the extreme
hern boundary of the section. This suggests a narrow and weak contribution from

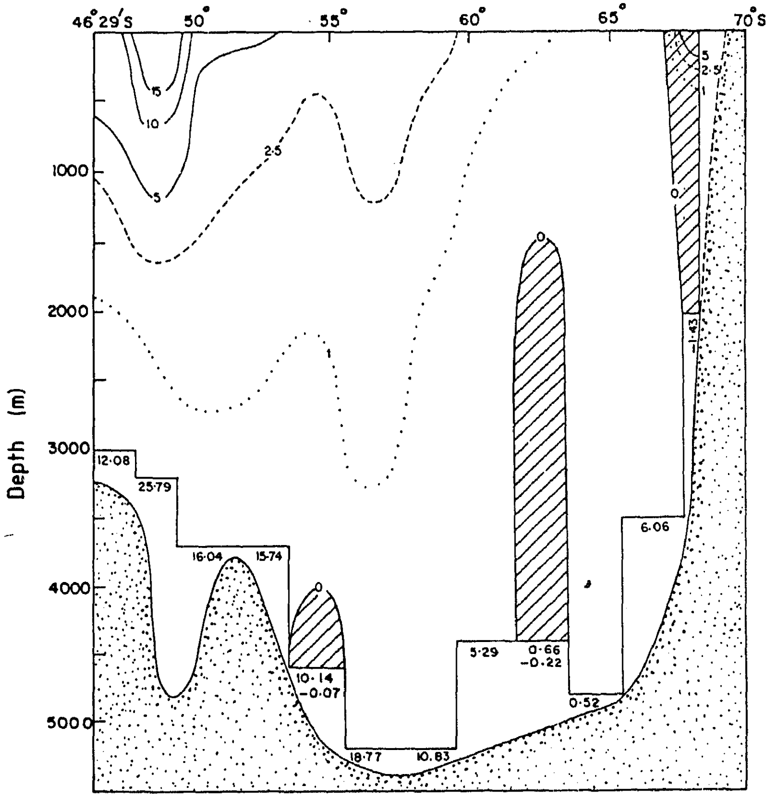

Figure 2. Geostrophic flow and transport across 37°E relative to the greatest common observed depths. Straight horizontal lines show the greatest common observed depth for station pairs. Westward flows are hatched and velocity contours are shown by solid lines for velocities at 5 cm/s intervals and dashed/dotted lines for velocites with smaller intervals between them. Quantities of mass transport ($10^6\, m^3 s^{-1}$) between station pairs are shown

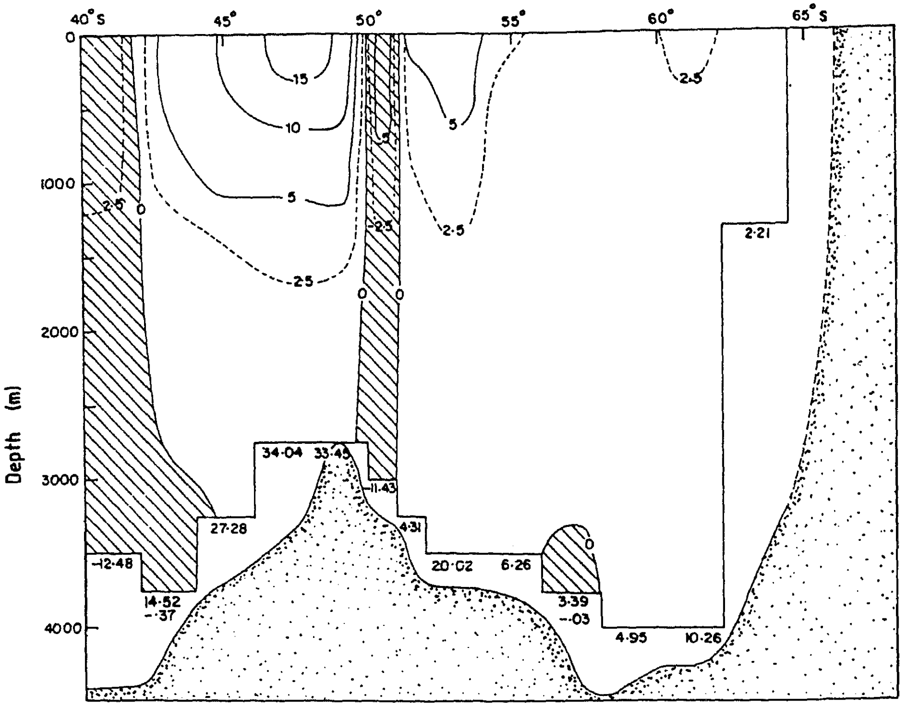

Figure 3. Geostrophic flow and transport across 105°E relative to the greatest common observed depths. See legend to figure 2 for details.

the east wind drift in this region. The zone of the Antarctic front is thus situated roughly around 67°S, slightly south of the position observed by Lutjeharms (1985).

A sub-Antarctic front (SAF) and a polar front are observed in the eastern section (figure 3). A westward flow, which separates these two fronts, extends down to the crest of the India–Antarctica Ridge. Callahan (1971) also found the same feature. He suggested that the zone over the ridge was characterized by extremely weak vertical shear throughout the water column. This could result in a westward flow or vanishing of the zonal component. The dynamics behind the westward countercurrent embedded in the ACC exactly over the India–Antarctica Ridge are still unknown. Callahan (1971) believed that the ACC was affected by major topographic features. According to him the position of the countercurrent is an indication of the influence of topography on the upper westward flow. He also felt, however, that the part played by the wind stress distribution could not be ignored. Interestingly, the zone of maximum westerly winds in the southern ocean (50°S) exactly coincides with the latitude of the countercurrent (Von Arx 1957). This strengthens the case for a topographic influence on the westward flow. Quoting Sverdrup *et al* (1942), Callahan (1971) pointed out that large-scale meanders in the ACC have been observed repeatedly over the meridional ridge system. This can be explained qualitatively by the conservation of potential vorticity (Pond and Pickard 1983), but a more complete dynamical model will help one to understand the real cause of this westward flow.

The westward flow at 40°S (figure 3) could be associated with a cyclonic eddy. Its presence has been confirmed between Antarctica and the region south of Australia by Sarchenko *et al* (1978). A similar cyclonic circulation was noticed in the vicinity of the polar front at the Drake Passage by Joyce and Patterson (1977). Wyrtki (1962) observed a cyclonic circulation between 105°E and 110°E, centred at 35°S all along the depths that were investigated. This appears to be a permanent feature.

Thus, the net eastward flux of the ACC is mostly derived from the sub-Antarctic zone (SAZ) and the polar frontal zone (PFZ). The contribution of SAZ is the more dominant of the two. The core velocities of these two zones are 15 and 5 cm/s respectively. A less intense belt is also seen around 61°S, which could be either an extension of the PFZ or the Antarctic zone (AZ).

From the data collected during the *Melville, Yelcho* and *Atlantis II* cruises Whitworth *et al* (1982) calculated the maximum velocity of the ACC in both SAF and PF and the values exceed 40 cm/s. However, such high velocities could not be seen along 132°E, at 115°E (Callahan 1971), or along 145°E (Sverdrup 1940), where the velocities were less than half the values reported by Whitworth *et al* (1982). In the present study, the velocity of the ACC never exceeded 20 cm/s. The high velocity at the Drake Passage was mainly due to the narrowness of the path of the ACC.

3.2 *Transport*

The zonal transports computed within the ACC across 37°E and 105°E amount to $122 \times 10^6\,\mathrm{m^3\,s^{-1}}$ and $160 \times 10^6\,\mathrm{m^3\,s^{-1}}$ respectively. The excess transport at 105°E may be attributed to the greater meridional coverage of this section compared to that at 37°E; otherwise, both the values are comparable. The westward flux is more conspicuous in the eastern section, while it is almost absent to the west.

The previous measurements of transport within the ACC in all the three sectors of the southern ocean correlate well with the present estimates. Nowlin *et al* (1977) computed a transport of $124 \times 10^6\,\mathrm{m^3\,s^{-1}}$ across the Drake Passage and his estimate is comparable with that of Whitworth (1983), who estimated an average transport of $121 \times 10^6\,\mathrm{m^3\,s^{-1}}$ from a 370-day current record. Bryden and Pillsbury's (1977) estimate of $262 \times 10^6\,\mathrm{m^3\,s^{-1}}$ at the Drake Passage (based on one year's records from 6 m) deviates considerably from the normal value and the extremes, according to Nowlin *et al* (1977), might have been the result of a longer observation period.

The present estimates of $122 \times 10^6\,\mathrm{m^3s^{-1}}$ at 37°E and $160 \times 10^6\,\mathrm{m^3s^{-1}}$ at 105°E are supported by the values of Jacobs and Georgi (1977) and Callahan (1971). Jacobs and Georgi have calculated the transport between Cape Agulhas and Antarctica and these values slightly exceed the present ones, while Callahan's estimates at 115°E and 132°E are $149 \times 10^6\,\mathrm{m^3s^{-1}}$ and $156 \times 10^6\,\mathrm{m^3s^{-1}}$ respectively.

3.3 *Bivariate distribution of the flux*

The distribution of the total transport among classes of potential temperature (0·5°C intervals) and salinity (0·1‰ intervals) is shown in figures 4 and 5. The transport values enclosed by the solid lines are of those classes that together contribute 50% of the total transport and are said to be within the 50% boundary. Similarly the 75% boundary (dashed lines) is defined as that which encloses transport values of classes that contribute 75% of the total transport. The following are the numbers of classes enclosed

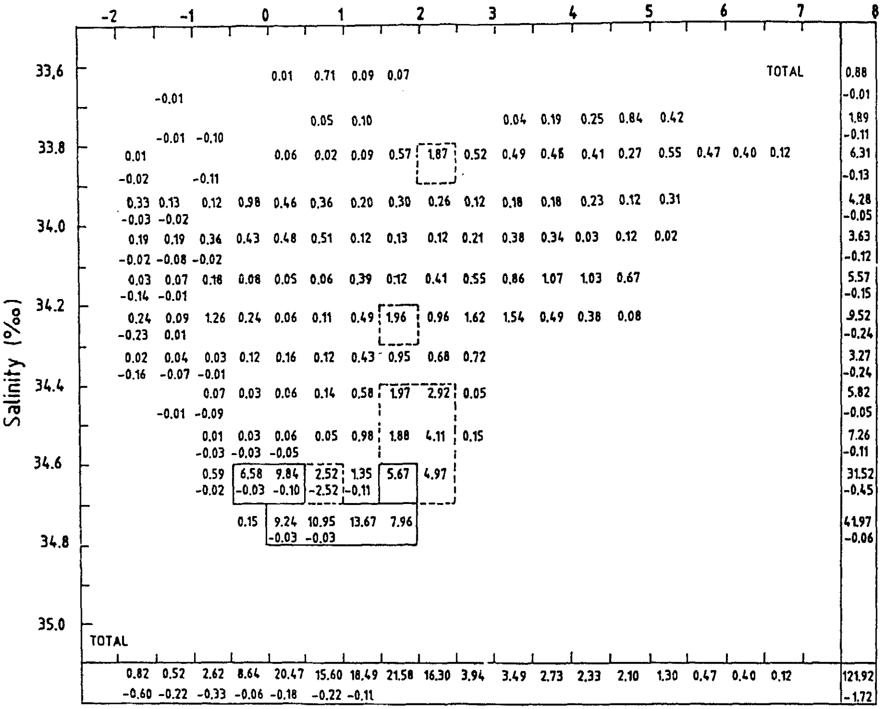

Figure 4. Distribution of the total transport across 37°E in bivariate classes of potential temperature and salinity. The solid-line boundary encloses classes that together contribute 50% of the total transport; the dashed-line boundary encloses classes that contribute 75%. The totals at bottom give distribution by potential temperature and those at right distributions by salinity. The total in the box in the bottom right-hand corner gives total transport ($10^6\,m^3\,s^{-1}$) across 37°E. Negative values indicate westward transport.

Region	50%	75%
Western (figure 4)	7	15
Eastern (figure 5)	12	31

The two regions can be compared with regard to the number of classes enclosed by the 50% and 75% boundaries. Both 50% and 75% boundaries reveal that the eastern region of the southern Indian Ocean is more heterogeneous than the western region. Along 105°E the primary, secondary and tertiary modes are very prominent, both at the 50% and 75% levels, and are widely scattered throughout the water column (figure 5). At 37°E, 75% of the circumpolar current has a salinity >34.2‰ and a potential temperature ranging from $-0{\cdot}5$°C to 2·5°C. The highly saline primary mode within the 50% boundary has only 7 classes while the additional 25% includes 8 classes, probably because of the admixture of water mass from the north (figure 4). Similar mixing of water masses is also inferred at the eastern region from the additional 19 classes within the 75% boundary. It is also presumed that the water in this region is comparatively stratified.

The less saline ($<34{\cdot}3$‰) warm water (3–7°C) noticed in the ACÇ at 37°E (figure 4) can be attributed to the southward advection of the Agulhas current. This accounts for

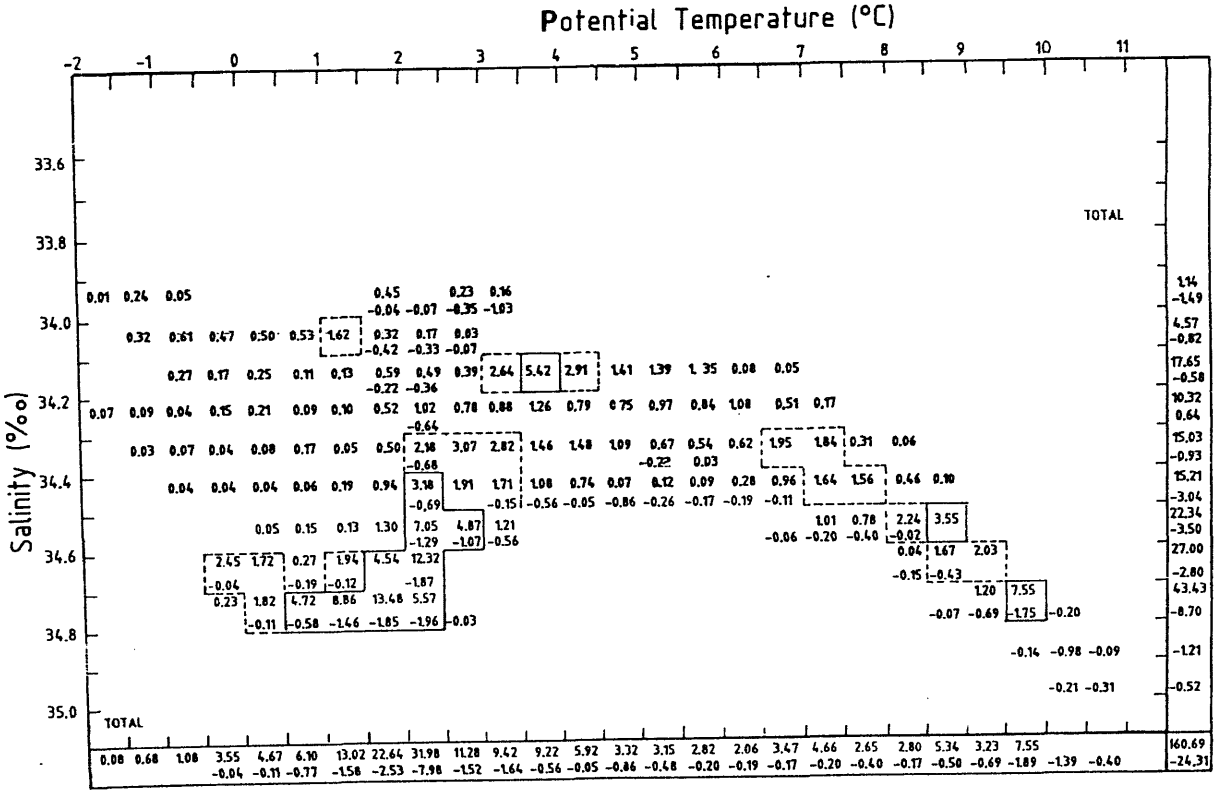

Figure 5. Distribution of the total transport across 105°E. See legend to figure 4 for details.

satellite-tracking device, observed a southerly flow in the Agulhas current around 37°E and thought it to be the recycling of the Agulhas current. He could also locate the rapid eastward return of the Agulhas current west of 20°E and its path towards the east along 40°S. Therefore the warm, less saline water at 37°E and 45°S in the present section must be due to the influence of the Agulhas current. Similarly, the presence of saline water within the potential temperature range 7–11°C at 105°E (figure 5) is a clear evidence of the northward-flowing West Australian current. The secondary mode within the 50% level occupies this part of the current. There is an indication of this northward current in the figures of Hamon (1965) for the period October 16 to November 15 1960. An analogous current structure was observed by Wyrtki (1957) and Rochford (1969) at the extreme west and east of the Indian Ocean sector of the Southern Ocean during the Austral summer.

4. Conclusions

In the present study the velocity of the ACC never exceeded 20 cm/s. Two westward flows were noticed at 50°S and 40°S across the meridian 105°E. The westward flow at 40°S was found to be associated with a cyclonic eddy. The computed geostrophic transport across 37°E and 105°E amounts to $122 \times 10^6\,\mathrm{m^3s^{-1}}$ and $160 \times 10^6\,\mathrm{m^3s^{-1}}$ respectively. The distribution of the total transport in bivariate classes of potential temperature and salinity indicates that the eastern region of the Southern Ocean is more heterogeneous than the western region. The influence of a less saline Agulhas current and a saline West Australian current may be inferred from the frequency distribution.

References

Bryden H L and Pillsbury R D 1977 Variability of deep flow in the Drake Passage from year-long current measurements; *J. Phys. Oceanogr.* **7** 803–810

Callahan J E 1971 Velocity structure and flux of the Antarctic circumpolar current south of Australia; *J. Geophys. Res.* **76** 5859–5864

Grundlingh M L 1978 Drift of a satellite-tracked buoy in the southern Agulhas current and Agulhas return current; *Deep Sea Res.* **25** 1209–1224

Hamon B V 1965 Geostrophic current in the southeastern Indian Ocean; *Aust. J. Mar. Freshwater Res.* **16** 255–271

Jacobs S S and Georgi D T 1977 Observations on the southwest Indian/Antarctic Ocean. In *A voyage of discovery* (ed.) M. Angel (Oxford: Pergamon Press) pp. 43–84

Joyce T M and Patterson S L 1977 Cyclonic ring formation at the polar front in the Drake Passage; *Nature (London)* **265** 181–233

Lutjeharms J R E 1985 Location of frontal systems between Africa and Antarctica: some preliminary results; *Deep Sea Res.* **32** 1499–1509

Nowlin W D, Whitworth T III and Pillsbury R D 1977 Structure and transport of the Antarctic circumpolar current at Drake Passage from short-term measurements; *J. Phys. Oceanogr.* **7** 768–802

Pond S and Pickard G 1983 *Introductory dynamical oceanography* (Oxford: Pergamon Press) p. 329

Reid J L and Nowlin Jr W D 1971 Transport of water through the Drake Passage; *Deep Sea Res.* **18** 51–64

Rochford D J 1969 Seasonal variations in the Indian Ocean along 110°E. 1. Hydrological structure of the upper 500 m; *Aust. J. Mar. Freshwater Res.* **13** 1–17

Sarchenko V G, Emery W J and Vladimirov D A 1978 A cyclonic eddy in the Antarctic circumpolar

Oceanogr 8 [illegible]

H U 1940 British, Australian, New Zealand Antarctic research expedition: Hydrology discussion; ZARE Report Ser. A, Vol. 3, part 2, sect. 2

H U, Johnson M W and Fleming R H 1942 *The oceans* (Englewood Cliffs NJ, USA: Prentice-Hall) 087

W 1957 An experimental approach to problems in physical oceanography. In *Physics and chemistry e earth* (eds) L H Ahrens, F Press, K Rankama and S K Runcorn (New York: Pergamon Press) 2, p 1

rth T III 1983 Monitoring the transport of the Antarctic circumpolar current at Drake passage; ys *Oceanogr* 13 2048 2057

rth T III, Nowlin Jr W D and Worly S J 1982 The net transport of the Antarctic circumpolar ent through Drake Passage, *J Phys. Oceanogr.* **12** 960 971

K 1957 Die zirkulation an der oberflache der sudostasiatischen gewässer; *Dt. Hydrog. Z.* **10** 1–13

K 1962 Geopotential topographies and associated circulation in the southeastern Indian Ocean; *J Mar. Freshwater Res* 13 1 17

Erratum

Paper entitled "Selection of optimum frequency of a wind scatterometer" by Abhijit Sarkar, Raj Kumar and Mannil Mohan, **96** 259–266.

The first equation in the Appendix, i.e. (A.1) should read as

$$\tau = 10^{-\int [K(Z)/10]\, \mathrm{d}Z, (\mathrm{d}B)}$$

Proceedings (Earth and Planetary Sciences)

Volume 97, 1988

SUBJECT INDEX

Antarctic circumpolar current
  Water characteristics and transport of the antarctic circumpolar current in the Indian Ocean 183
Arabian Sea
  Distribution of particulate organic carbon in the central Arabian Sea 35
Atmospheric flux
  Spectra of different fluxes over the arid and semiarid zones of northwest India during MONEX 1979 137

Basalts
  Magnetic studies on the remanence carriers in igneous rocks of different ages 81
Bivariate distribution
  Water characteristics and transport of the antarctic circumpolar current in the Indian Ocean 183
Break-monsoon days
  Hydroclimatic fluctuations of the Upper Narmada catchment and its association with break-monsoon days over India 87

Calcic amphiboles
  Chemistry of calcic amphiboles from the area around Terakanambi, southern Karnataka 1
Chemical analyses
  Chemistry of calcic amphiboles from the area around Terakanambi, southern Karnataka 1
Chlorophyll *a*
  Distribution of particulate organic carbon in the central Arabian Sea 35
Clockwise gyre
  On the observed synoptic variability in the thermal structure of the upper northern Bay of Bengal during MONEX-79 21
Cloud classification parameters
  Retrieval of cloud classification parameters using two-dimensional fast Fourier transform 159
Coastal currents
  Seasonal cycle of surface circulation in the coastal North Indian Ocean 53
Coherent rainfall zones
  Coherent rainfall zones: Case study for

Cretaceous dykes
  Late Cretaceous mafic dykes in the Dharwar craton 107

Deccan volcanism
  Late Cretaceous mafic dykes in the Dharwar craton 107
Deterministic chaos
  Is there an attractor for the Indian summer monsoon? 49
Dissolved oxygen
  Distribution of particulate organic carbon in the central Arabian Sea 35
Domain states
  Magnetic studies on the remanence carriers in igneous rocks of different ages 81
Drifting buoys
  Satellite-tracked drifting buoy observations in the south equatorial current in the Indian Ocean 149

Effective rainfall
  Upland erosion in a mixed pine forest ecosystem 193
Effective shear stress
  Upland erosion in a mixed pine forest ecosystem 193

Flow erosion
  Upland erosion in a mixed pine forest ecosystem 193

Galactic cosmic rays
  Cosmic-ray production rates of neon isotopes in meteorite minerals 117
Geochemistry
  Late Cretaceous mafic dykes in the Dharwar craton 107
Geochronology
  Late Cretaceous mafic dykes in the Dharwar craton 107

Heat budget
  On the observed synoptic variability in the thermal structure of the upper northern Bay of

thermal structure of the upper northern Bay of Bengal during MONEX-79 21
High grade terrain
  Chemistry of calcic amphiboles from the area around Terakanambi, southern Karnataka 1
Hydrological floods and droughts
  Hydroclimatic fluctuations of the Upper Narmada catchment and its association with break-monsoon days over India 87

Indian monsoon region
  Northward propagation of the 30–50 day mode in the Indian monsoon region 127
Indian Ocean
  Satellite-tracked drifting buoy observations in the south equatorial current in the Indian Ocean 149
  Water characteristics and transport of the antarctic circumpolar current in the Indian Ocean 183

Laplacian filter
  Retrieval of cloud classification parameters using two-dimensional fast Fourier transform 159

Magnetic parameters
  Magnetic studies on the remanence carriers in igneous rocks of different ages 81
Mass transport
  Water characteristics and transport of the Antarctic circumpolar current in the Indian Ocean 183
Maxwell model
  Quasi-static deformation of a layered half-space by a long strike-slip fault 11
Meteorites
  Cosmic-ray production rates of neon isotopes in meteorite minerals 117
Mixed layer
  On the observed synoptic variability in the thermal structure of the upper northern Bay of Bengal during MONEX-79 21
  Satellite-tracked drifting buoy observations in the south equatorial current in the Indian Ocean 149
MONEX
  Spectra of different fluxes over the arid and semiarid zones of northwest India during MONEX 1979 137
Monsoon climate and variability
  Is there an attractor for the Indian summer monsoon? 49
Monsoons
  Seasonal cycle of surface circulation in the coastal North Indian Ocean 53
Monsoon variability
  Coherent rainfall zones: Case study for Karnataka 63
Munk layer
  Seasonal cycle of surface circulation in the coastal North Indian Ocean 53

Neon isotopes
  Cosmic-ray production rates of neon isotopes in meteorite minerals 117
North Indian Ocean
  Seasonal cycle of surface circulation in the coastal North Indian Ocean 53
Northward propagation
  Northward propagation of the 30–50 day mode in the Indian monsoon region 127

Oscillations
  Spectra of different fluxes over the arid and semiarid zones of northwest India during MONEX 1979 137

Palaeomagnetism
  Late Cretaceous mafic dykes in the Dharwar craton 107
Particulate organic carbon
  Distribution of particulate organic carbon in the central Arabian Sea 35
Periodicity
  Spectra of different fluxes over the arid and semiarid zones of northwest India during MONEX 1979 137
Phase space analysis
  Is there an attractor for the Indian summer monsoon? 49
Power spectrum
  Retrieval of cloud classification parameters using two-dimensional fast Fourier transform 159
Precipitation concentration index
  Hydroclimatic fluctuations of the Upper Narmada catchment and its association with break-monsoon days over India 87

Quasi-static deformation
  Quasi-static deformation of a layered half-space by a long strike-slip fault 11

Rainfall period
  Hydroclimatic fluctuations of the Upper Narmada catchment and its association with break-monsoon days over India 87
Remanence carriers
  Magnetic studies on the remanence carriers in igneous rocks of different ages 81

Satellite cloud images
  Retrieval of cloud classification parameters using two-dimensional fast Fourier transform 159
Saturation overland flow
  Upland erosion in a mixed pine forest ecosystem 193

roclimatic fluctuations of the Upper
nada catchment and its association with
k-monsoon days over India 87
stress
si-static deformation of a layered half-space
long strike-slip fault 11
orne wave recorder
tral width parameter for wind-generated
n waves 173
lares
mic-ray production rates of neon isotopes in
orite minerals 117
equatorial current
llite-tracked drifting buoy observations in the
h equatorial current in the Indian
an 149
al width parameter
tral width parameter for wind-generated
n waves 173
e attractors
here an attractor for the Indian summer
soon? 49
slip fault
si-static deformation of a layered half-space
long strike-slip fault 11
e displacement
si-static deformation of a layered half-space
long strike-slip fault 11
e drift
llite-tracked drifting buoy observations in the
h equatorial current in the Indian
an 149

Seasonal cycle of surface circulation in the coastal North Indian Ocean 53
Synoptic variability
On the observed synoptic variability in the thermal structure of the upper northern Bay of Bengal during MONEX-79 21

Terakanambi
Chemistry of calcic amphiboles from the area around Terakanambi, southern Karnataka 1
Thermal structure
On the observed synoptic variability in the thermal structure of the upper northern Bay of Bengal during MONEX-79 21
Two-dimensional fast Fourier transform
Retrieval of cloud classification parameters using two-dimensional fast Fourier transform 159

Vertical distribution
Spectra of different fluxes over the arid and semiarid zones of northwest India during MONEX 1979 137

Wind stress
Seasonal cycle of surface circulation in the coastal North Indian Ocean 53

30–50 day oscillation
Northward propagation of the 30–50 day mode in the Indian monsoon region 127

AUTHOR INDEX

Agarwal K Vijay
  see Mohan M 159

Bhandari N
  Cosmic-ray production rates of neon isotopes in meteorite minerals 117
Bhosle N B
  Distribution of particulate organic carbon in the central Arabian Sea 35

Correia J F
  see Sharma K D 193

Dayal A M
  see Kumar Anil 107
Dhople V M
  see Bhosle N B 35

Gadgil Sulochana
  Coherent rainfall zones: Case study for Karnataka 63
Garg Nat Ram
  Quasi-static deformation of a layered half-space by a long strike-slip fault 11
Gopalan K
  see Kumar Anil 107
Gowri R
  see Gadgil Sulochana 63

Kasture S V
  see Keshavamurty R N 127
Keshavamurty R N
  Northward propagation of the 30–50 day mode in the Indian monsoon region 127
Krishnakumar V
  see Keshavamurty R N 127
Kumar Anil
  Late Cretaceous mafic dykes in the Dharwar craton 107
Kumar K Krishna
  see Singh Nityanand 87
Kumari V M Padma
  see Kumar Anil 107

Lakshmi Bhaduri
  see Mohan M 159

Mahabaleswar B
  see Swamy N Shadakshara 1
Mathew Basil
  see Muraleedharan P M 183
  see Rao R R 21
Michael G S
  see Shetye S R 149
Mohan M
  Retrieval of cloud classification parameters using two-dimensional fast Fourier transform 159
Muraleedharan P M
  Water characteristics and transport of the antarctic circumpolar current in the Indian Ocean 183
Murthy G S
  see Radhakrishnamurty C 81

Radhakrishnamurty C
  Magnetic studies on the remanence carriers in igneous rocks of different ages 81
Rao C V K Prasada
  Spectral width parameter for wind-generated ocean waves 173
Rao R R
  On the observed synoptic variability in the thermal structure of the upper northern Bay of Bengal during MONEX-79 21
Rao Y J Bhaskar
  see Kumar Anil 107

Satyan V
  Is there an attractor for the Indian summer monsoon? 49
Shanker Daya
  see Singh U S 137
Sharma K D
  Upland erosion in a mixed pine forest ecosystem 193
Shenoi S Satheesh Chandra
  see Shetye S R 53
Shetye S R
  Satellite-tracked drifting buoy observation in the south equatorial current in the Indian Ocean 149
  Seasonal cycle of surface circulation in the coastal North Indian Ocean 53

Narmada catchment and its association with break-monsoon days over India 87
gh R K
ee Singh U S 137
gh Sarva Jit
ee Garg Nat Ram 11
gh U S
Spectra of different fluxes over the arid and emiarid zones of northwest India during MONEX 1979 137

Soman M K
see Singh Nityanand 87
Swamy N Shadakshara
Chemistry of calcic amphiboles from the area around Terakanambi, southern Karnataka 1

Wagh A B
see Bhosle N B 35

Yadumani
see Gadgil Sulochana 63

roceedings

h and Planetary Sciences

tes on the preparation of papers

ors wishing to have papers published in the *Proceedings* should send them to

e Editor, Proceedings (Earth and Planetary Sciences), Indian Academy of Sciences,
ngalore 560 080, India.

copies of the paper must be submitted.
apers must normally present results of original work. Critical reviews of important fields
lso be considered for publication. Submission of the script will be held to imply that it
ot been previously published and is not under consideration for publication elsewhere;
urther that, if accepted, it will not be published elsewhere.

cript:

rs should be typed double spaced with ample margin on all sides on white bond paper
215 mm. This also applies to the abstract, tables, figure captions and the list of references
are to be typed on separate sheets.

page:

he title of the paper must be short and contain words useful for indexing.
he names with initials of authors and the name and address of the institution, where the
was done must be given.
n *abbreviated running title* of not more than 50 letters including spaces must also be given.

act:

apers must have an abstract of not more than 200 words of the significant results reported
paper.

ords:

een 3 and 6 keywords must be provided for indexing and information retrieval.

ext:

aper must be divided into sections starting, preferably with 'Introduction' and ending
Conclusions'. The main sections should be numbered 1, 2, etc., sub-sections 1.1, 1.2, etc.,
urther sub-sections (if necessary) 1.1a, 1.1b, etc.

s:

bles must be numbered consecutively in arabic numerals in the order of appearance in
xt. The tables should be self-contained and have a descriptive title.

- Line drawings must be in Indian ink on good quality tracing paper or on white card of a size smaller than that of text paper. Structural formulae of compounds must be drawn in Indian ink on tracing paper. Lines must be drawn sufficiently thick for reduction to a half or third of the original size (0·3 mm for axes and 0·6 mm for curves are suggested).

List of symbols:

For the convenience of the printers, authors should attach to the manuscript the complete list of symbols identified typographically.

Mathematical material:

Equations must be clearly written, each on its own line, well away from the text. All equations must be numbered consecutively in arabic numerals with the number in parentheses near the right hand margin. Indices or superscripts must be indicated in pencil with a $\surd$ sign and subscripts with $\wedge$ sign; 'oh' and 'zero', K, k, and kappa, 'ell' and one, etc., must be clearly distinguished. For example, the following scheme of (single respectively double) underlining in colour may be used to denote (lower case respectively capital) characters—blue for Greek, red for German (gothic), green for script and brown for bold face. Authors must indicate wherever special characters (Greek, German, script, scalar, vector, tensor, matrix, etc.) are required. All other letters will be set in italic types. Vectors must be underlined by a wavy line and tensors by two wavy lines. The SI system of units and symbols is recommended.

References:

References should be cited in the text by authors and year. If there are more than two authors, reference should be to the first author followed by *et. al* in the text. References at the end of the paper should be listed alphabetically by authors' names, followed by initials, year of publication, title of the paper, name of the journal (abbreviated according to the World List of Scientific Periodicals, Butterworths, London), volume number and starting and ending page numbers. References to books should include: name(s) of author(s), initials, year of publication, title of the book, edition if not the first, initials and name(s) of editor(s) if any, preceded by ed(s), place of publication, publisher and chapter or pages referred to. References to thesis must include the year, the title of the thesis, the degree for which submitted and the University.

Footnotes:

Footnotes to the text should be avoided if possible but when necessary should be numbered consecutively, and typed on a separate sheet.

Appendices:

All appendices should be numbered consecutively in arabic numerals.

Proofs:

Authors are requested to prepare the manuscript carefully before submitting it for publication to minimise corrections and alterations in the proof stage which increase publication costs. Galley proofs sent to the authors together with the reprint order form must be returned to the editorial office within two days of their receipt.

Reprints:

50 reprints of each article will be supplied free of charge.